ABSTRACT

Title of Dissertation: Study of Transverse Density Waves in an Electron Beam Experiment

Santiago Bernal, Doctor of Philosophy, 1999

Dissertation directed by: Martin Reiser, Professor

Electrical Engineering Department

The physics of the transport of intense charged-particle beams is characterized by the evolution of the beam particle distribution in phase space. The internal structure of an intense beam, which comprises both density and temperature profiles, changes in response to the combined action of external focusing and the self-electric field. The present work explores beam evolution in experiments conducted in a number of focusing channels over a distance of about one meter. The initial experiments with one short solenoid and five printed-circuit (PC) magnetostatic quadrupole lenses constitute prototype matching experiments for the University of Maryland Electron Ring, or *UMER*. The latter will be a machine designed to explore beam physics issues associated with circular machines, over an entirely new regime of beam intensities with potential applications for future accelerators.

In all experiments, the beam profiles along the channel are obtained from phosphor screen pictures. A linear beam envelope code is used for section design, while particle-in-cell simulations provide important clues for beam evolution. During the course of the initial matching experiments, a wavelike phenomenon was discovered that led to additional experiments in three-solenoid and six-PC quadrupole channels. It was found that the waves are induced by an aperture located a few centimeters from the electron gun cathode. Simulations suggest that the beam phase-space particle distribution relaxes to an equilibrium distribution after a few plasma periods. Furthermore, a simple particle-tracking model reproduces well the onset of the perturbation in all experiments.

Simulations also show a small decrease of beam root-mean-square emittance, a beam quality factor, over a few plasma periods. Furthermore, the irreversible character and associated entropy increase of the beam relaxation are reconciled with the reduction in emittance.

Several questions remain concerning the stability and scaling of the oscillations. An important issue is the possible connection to the known Gluckstern modes of a K-V distribution, a model distribution with uniform particle densities in both space and velocity.

STUDY OF TRANSVERSE DENSITY WAVES

IN AN

ELECTRON BEAM EXPERIMENT

by

Santiago Bernal

Dissertation submitted to the Faculty of the Graduate School of the
University of Maryland, College Park in partial fulfillment
of the requirements for the degree of
Doctor of Philosophy
1999

Advisory Committee:

Professor Martin Reiser, Chair/Advisor
Professor Alex J. Dragt
Professor Richard F. Ellis
Professor Robert L. Gluckstern
Professor Patrick G. O'Shea

UMI Number: 9964809

UMI Microform 9964809

Bell & Howell Information and Learning Company
300 North Zeeb Road
P.O. Box 1346
Ann Arbor, MI 48106-1346

DEDICATION

To Dr. Clara, my wife, with all my love and admiration.

ACKNOWLEDGEMENTS

This dissertation benefited greatly from the help and assistance of several people, all of whom I hope to include here.

Professor Martin Reiser provided an incomparably positive working environment, with continuous encouragement and constructive criticism at every stage of the project. I am very thankful for finding an advisor who understands students and recognizes that the only trademarks for success in any endeavor are persistence and passion for understanding.

Dr. R.A. Kishek made key contributions with his masterful use of the code WARP. We disagreed on occasions on the merits of simple methods vs. WARP, but additional insights were always the result of the many discussions we had. Dr. Kishek also wrote a MATLAB program for image analysis that saved me countless hours in processing the experiment pictures. I am forever in debt to Dr. Kishek.

Dr. J.G. Wang helped me during the initial stage of the experiments and was always a source of encouragement and support.

Dr. T. Godlove designed the first printed-circuit quadrupoles ever used. His enthusiasm for the UMER project and constant help are appreciated.

Dr. I. Haber was instrumental in implementing WARP for direct use at IPR and provided numerous insights for understanding the experiment results. His idea to display the results from WARP as simulated phosphor screen pictures facilitated the comparison with experiment.

Dr. M. Venturini taught me through his detailed work the mysteries of quadrupole design and multipole expansions.

Dr. D. Kehne helped me with the code E-GUN and gave me important information on the Hughes electron gun.

W.W. Zhang conducted the measurements with the rotating coil and assembled the quadrupoles for the bend experiments.

I am thankful to professors A. Dragt, R.F. Ellis, R.L. Gluckstern and P.G. O'Shea for serving on my dissertation committee.

I am also indebted to the mechanical "gurus" Ken Diller, Victor Yun, Jay Pyle and Paul Chin. Their expertise was crucial for the successful design and construction of key components of the experiments. Also important was the timely assistance received from J. Rodgers and E. Condon on electronics and computer matters.

The committed work of a number of undergraduate students is also acknowledged, with a special mention of M. Pruessner and A. Yiri.

Last, and not least, the support from my mother in Colombia was essential. Without my family's help, specially that from Daniel, my 3-1/2-year old son, this work would have been completed at least one year earlier. However, without my family, no real meaning could have been attached to this effort.

TABLE OF CONTENTS

Section		Page
List of Tables		x
List of Figures		xi
I.	Introduction	1
	1.1 The University of Maryland Electron Ring (UMER) Project	1
	1.2 Beam Transport in a Magnetic FODO Lattice	7
	1.2.1 Single-particle Dynamics	7
	1.2.2 K-V Envelope Equations and the Smooth Approximation	13
II.	Beam Equilibrium and the K-V Distribution	16
	2.1 Introduction	16
	2.2 Vlasov Equation, Metaequilibria and Thermal Equilibrium	17
	2.3 The Kapchinskij-Vladimirskij (K-V) Distribution	21
	2.4 Emittance Growth	26
	2.4.1 Definitions	26
	2.4.2 Phenomenological Theory	28
	2.4.3 Additional Mechanisms	33
	2.4.4 Stability of the K-V Distribution	35
	2.4.5 Emittance, Entropy and Reversibility	40

III. Experimental Facility for Electron Beam Transport Experiments 44

3.1 Introduction 44

3.2 Electron Gun 45

3.3 Vacuum System 46

3.4 Solenoid Lenses 52

3.5 Elements for Beam Centroid Corrections 58

3.5.1 Steering Dipoles 58

3.5.2 Helmholtz Coils 58

3.6 Beam Diagnostics 60

3.7 Image Processing and Analysis 63

3.8 Rotating Coil Magnetometer 67

IV. Design and Field Measurements of Printed-Circuit Quadrupole Lenses 70

4.1 Introduction 70

4.2 Multipole Expansion in a Magnetic Lens 71

4.2.1 Long Lens 71

4.2.2 Short Lens 74

4.2.3 Single-Particle Equations of Motion to Third Order 76

4.3 Empirical Design (Small-Aperture -SA- Quadrupole) 77

4.4 Formal Design (UMER Quadrupole) 79

4.5 Field Measurements of a Scaled Prototype Quadrupole 88

4.6 Integrated-Multipole Measurements of PC Quadrupoles 95

4.6.1 Rotating Coil Magnetometer 95

4.6.2 Multipole Content - Calculations 99

4.6.3 Multipole Content - Measurements 100

4.7 Summary and Conclusions 106

V. RMS Matching Experiments in a Straight Solenoid-Quadrupole System 108

5.1 Introduction 108

5.2 Matching Section Design: General Considerations 109

5.3 Experimental Procedure 112

5.3.1 Measurement of Initial Beam Slope 115

5.3.2 Solenoid Focusing 119

5.3.3 Quadrupole Focusing and RMS Matching 125

5.4 Results 129

5.5 Summary and Conclusions 137

VI. Additional Matching Experiments: 20 deg. Bend and All-Quadrupole Sections 139

6.1 Introduction 139

6.2 20 degree Bend Section 139

6.3 Characterization of Bend Dipoles 144

6.4 Results of Bend Experiments 149

6.5 Matching with an All-quadrupole Section 153

6.6 Additional Calculations 159

6.6.1 Matching with $\sigma_{0x} \neq \sigma_{0y}$ 159

6.6.2 Round-to-Round Transformation 160

6.7 Summary and Conclusions 160

VII. Evolution of Particle Distribution in a Collimated Beam 164

7.1 Introduction 164

7.2 Experimental Results 165

7.2.1 Single Solenoid 165

7.2.2 Three Solenoids 166

7.2.3 Experiments in Quadrupole Channels 170

7.2.4 Mismatched Beams 170

7.3 Discussion 176

7.3.1 Electron Gun Aberrations 177

7.3.2 External Focusing 178

7.3.3 Aperture "Imaging" 179

7.3.4 Semi-Gaussian Distribution and WARP Simulations 182

7.3.5 Beam-Edge Particle Tracking 189

7.3.6 Emittance Change in Simulations 194

7.3.7 An Irreversible Process with No RMS Emittance Growth 201

7.3.8 Other Perturbation Mechanisms and Gluckstern-Mode Analysis 204

7.4 Conclusions and Suggestions for Future Work 207

Appendix A: Effects of an Aperture - General Considerations 209

A.1 Effect on tune depression 209

A.2 Scaling of Emittance 211

A.3 Representation of Collimated Distribution 215

Appendix B: Computer Codes 217

B.1 K-V Envelope Code SPOT 217

B.2 Matrix Codes TRACE 2D-3D 221

B.3 Particle-in-cell Code WARP 228

Appendix C: Rotated Quadrupoles and Matching 230

C.1 Single-Particle Effects 230

C.2 Matching Section with Rotated Quadrupoles 231

References 237

LIST OF TABLES

Number		Page
1.1	University of Maryland Electron Ring (UMER) parameters	5
2.1	Length and time scales relevant to transport experiments of this work	22
3.1	Physical and magnetic parameters of main solenoid	55
4.1	Parameters of small-aperture and UMER printed-circuit (PC) quadrupoles	87
4.2	Calculation of lowest-order harmonics for concentric-loops model of PC quadrupoles	101
5.1	Beam and lattice parameters for solenoid - five PC quadrupole experiment	111
5.2	Parameters of focusing elements in solenoid - five PC quadrupole experiment	114
6.1	Prototype bend experiment vs. UMER	143
6.2	Parameters of UMER bend dipole	146
6.3	Parameters for all-quadrupole matching	155
7.1	Solenoid parameters (three-solenoid experiments)	168
7.2	Matching parameters from SPOT calculations (three-solenoid experiments)	168
A.1	Effects of aperture size on UMER's tune depression and average beam size	213
B.1	Results of FODO matching ("matcher") with SPOT	218
B.2	Results of FODO matching with TRACE2D-3D	223

LIST OF FIGURES

Number		Page
1.1	University of Maryland Electron Ring (UMER) layout	2
1.2	Beam physics regimes	4
1.3	FODO lattice parameters	9
1.4	Trace space ellipse	11
2.1	Emittance growth due to mismatch vs. mismatch ratio	31
2.2	Beam radius ratio vs. mismatch ratio	32
3.1	Hughes electron gun	47
3.2	Cathode voltage and beam current waveforms	48
3.3	Hughes gun setup	49
3.4	EGUN calculations for Hughes gun	50
3.5	Phosphor screen transport and vacuum systems	51
3.6	Cutout view of solenoid housing	54
3.7	Solenoid on-axis field profiles and analytical fits	56
3.8	Steering printed-circuit dipole, conductor layout and measured field profile	59
3.9	Helmholtz coils, photo and calculated field profile	61
3.10	Effects of median filtering and background suppression	66
3.11	Parabolic model of beam intensity profile	68
3.12	Schematics of rotating coil setup	69
4.1	Geometry of a lens with quadrupole symmetry and circular cross section	73
4.2	Conductor layout of small-aperture printed-circuit quadrupole	80

4.3 Small-Aperture PC quadrupole, radial variation of axially-integrated field, and on-axis gradient profile 81

4.4 Conductor layout of UMER printed-circuit quadrupole 85

4.5 UMER PC quadrupole, radial variation of axially-integrated field, and on-axis gradient profile 86

4.6 Photograph of scaled quadrupole 90

4.7 Transverse and axial field measurements of scaled quadrupole vs. MAG-PC Calculations 91

4.8 Transverse and axial field measurements of scaled quadrupole vs. linear and nonlinear fits 93

4.9 Calculated (MAG-PC) gradient profiles vs. analytical fit for SA and UMER PC quadrupoles 94

4.10 Normalized gradient $g(z)$, and $g''(z)$ for SA and UMER PC quadrupoles 96

4.11 Calculated (MAG-PC) FFT for UMER and SA quadrupoles 102

4.12 Photograph of rotating coil setup 103

4.13 FFT of signal from rotating coil for UMER and SA quadrupoles 105

5.1 Schematics of Solenoid - five PC quadrupole experiment 113

5.2 Beam free expansion: pictures 117

5.3 Beam free expansion: intensity profiles and beam sizes 118

5.4 Solenoid focusing: phosphor screen pictures 120

5.5 Comparison of horizontal intensity profiles 121

5.6 Solenoid focusing: sensitivity to peak solenoid field and initial slope 123

5.7 Solenoid focusing: sensitivity to emittance and solenoid position 124

5.8 Layout of PC quadrupole connections 127

5.9 Matching experiment pictures: $\sigma_0 = 85^0$ 131

5.10 Beam profiles (pictures in Fig. 5.9) 132

5.11 Experiment results vs. K-V envelope solutions for $\sigma_0 = 85^0$ 133

5.12 Matching experiment pictures: $\sigma_0 = 76^0$ 134

5.13 Beam profiles (pictures in Fig. 5.13) 135

5.14 Experiment results vs. K-V envelope solutions for $\sigma_0 = 76^0$ 136

6.1 Schematics of 20 deg. bend experiment 141

6.2 Side and 3D views of 20-degree bend section 142

6.3 Conductor layout and field profile of UMER printed-circuit bending dipole 145

6.4 Reference orbit in bending dipole and UMER setup 148

6.5 Phosphor screen pictures of bend experiment 151

6.6 Summary of matching/bending experiments vs. calculations for $\sigma_0 = 85^0$ 152

6.7 Special setup for matching with six SA PC quadrupoles 154

6.8 Phosphor screen pictures of six - PC quadrupole matching experiments 156

6.9 Results of all-quadrupole matching experiments: hard-edge representation of quadrupole focusing function 157

6.10 Results of all-quadrupole matching experiments: smooth representation of quadrupole focusing function 158

6.11 SPOT calculations for matching with $\sigma_{0X} = 76^0$, $\sigma_{0Y} = 85^0$ 161

6.12 SPOT calculations for round-to-round transformation 162

7.1 Phosphor screen pictures from single-solenoid experiments 167

7.2 Pictures from Three-solenoid experiments 169

7.3 Mismatched beam envelope in six-quadrupole section - Strength of Q2 varying 172

7.4 Phosphor screen pictures for mismatched conditions - Strength of Q2 varying 173

7.5 Mismatched beam envelope in six-quadrupole section - Strength of Q1 varying 174

7.6 Phosphor screen pictures for mismatched conditions - Strength of Q1 varying 175

7.7 Single solenoid at 12.5 cm, 4.4 A: envelope and beam profiles 180

7.8 Three-solenoid experiment (σ_0=85^0): envelope calculation vs. experiment 181

7.9 Summary of experiments and simulations 185

7.10 Horizontal projection of trace space (WARP simulation) 187

7.11 Equivalent K-V beam ellipse downstream of aperture plane, experiment and Simulation 188

7.12 Beam-edge particle tracking: examples from single-solenoid and three-solenoid experiments 191

7.13 Size and location of first ring perturbation in single-solenoid experiment 192

7.14 Beam-edge particle tracking calculation for horizontal motion in six - PC quadrupole experiment 195

7.15 Beam-edge particle tracking calculation for vertical motion in six - PC quadrupole experiment 196

7.16 WARP simulation of evolution of (initial) S-G distribution in uniform focusing channel 197

7.17 WARP calculation of unnormalized transverse emittance over 20 m in uniform focusing channel 199

7.18 Particle-tracking calculation for uniform focusing channel: space-charge dominated and emittance dominated beams 203

A.1 Effect of aperture size on tune depression and average beam size in *UMER* 212

A.2 K-V beam horizontal trace-space ellipse and model of collimated region 214

B.1 Matched envelope in a unit FODO cell in *UMER* 219

B.2 Windows from SPOT 222

B.3 FODO matching in *UMER*: SPOT vs. TRACE 225

B.4 Matching in solenoid - five PC quadrupole section: SPOT vs. TRACE 227

C.1 TRACE3D calculations: effect of quadrupole rotations on matching: "systematic" errors 235

C.2 TRACE3D calculations: effect of quadrupole rotations on matching: "random" errors 236

CHAPTER I: Introduction

1.1 The University of Maryland Electron Ring (UMER) Project

The physics of the transport of intense particle beams is of great interest to basic research as well as to many areas of applied science: accelerators for high energy physics (e.g. the muon-muon collider), free electron lasers, heavy-ion fusion drivers, spallation neutron sources, and medical applications, among others. Many of the beam physics issues relevant to these applications can be addressed in a low-cost way by using low energy (< 10 kV), high current (~ 100 mA) electron beams. The physics of ion-beam transport and electron-beam transport are similar over a wide range of parameters provided that the tune depression, as defined below, is the same. Based on these ideas, the University of Maryland has started the construction of a small electron ring [1] to extend the beam physics experiments to a much longer time scale than was available with a 5-meter-long solenoid channel used for several years, and to investigate new beam physics issues in circular lattices [2]. Figure 1.1 shows the schematics of the electron ring. A similar small recirculator project is being pursued at the Lawrence Livermore National laboratory (LLNL) [3]. While *UMER* will address general beam physics issues, the LLNL ring will also address technology issues peculiar to ions.

Beam transport in most particle accelerators today is characterized by highly relativistic energies and low currents; under these conditions, the space charge repulsion from the self-electric fields inside the beam cancels almost exactly the focusing force from the self-magnetic fields. This is the regime of emittance-dominated beam

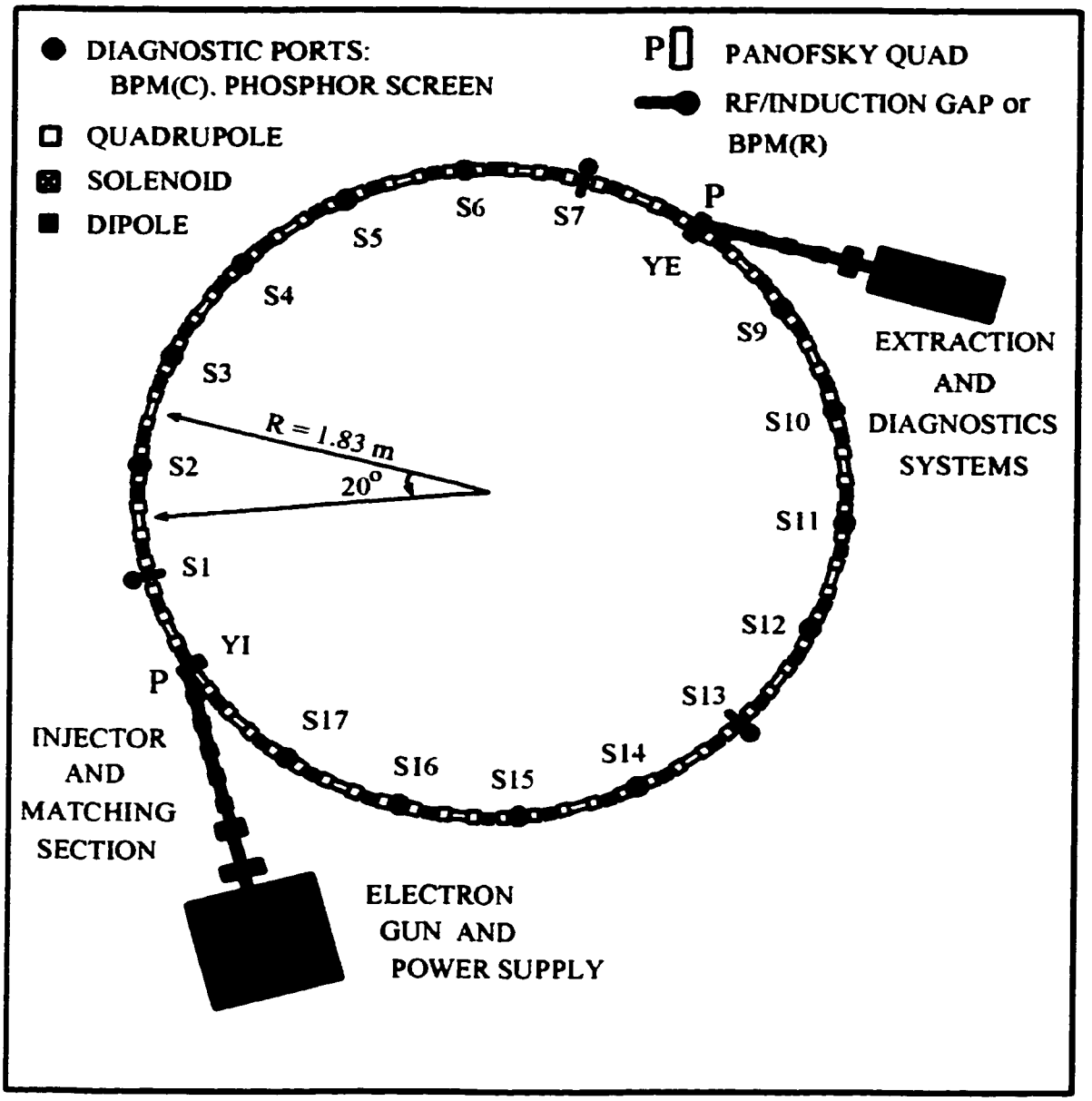

Fig. 1.1. University of Maryland Electron Ring (UMER) layout.

transport, where the dynamics is adequately described by single-particle equations of motion. By contrast, in some machines envisioned for the future, as well as in the low-energy injectors of many accelerators in existence, space charge may be the dominant factor. Figure 1.2 [4] illustrates the regimes of operation of *UMER* and existing rings. In the latter, the beams are so tenuous, and/or the energies so high, that the frequency of electrostatic plasma oscillations, ω_p , is small compared to the frequency of betatron oscillations, ω_0; in physical terms, the time for development of plasma waves is very long when compared to the transit time of the beam. In circular machines, the number of plasma oscillations per turn, and the number of betatron oscillations per turn define the "plasma" tune, ν_p , and the betatron tune, ν_0, respectively. When the current is increased, expressed by an increase in the intensity factor χ, defined below, space charge introduces a defocusing force that reduces the betatron tune to a value $\nu = \nu_0 - \Delta\nu$, where $\Delta\nu$ is known as the *tune shift*. Conventionally, the tune shift is chosen to satisfy $\Delta\nu \leq 0.25$ to avoid resonances. Although linear accelerators are not restricted by the tune shift, the cost of achieving high intensities with these machines in applications like heavy-ion fusion has been estimated to be higher than the cost associated with the more complex recirculators, where the same acceleration and focusing stages are used over and over to achieve the same energies. For circular machines, the ratio ν/ν_0 defines the *tune depression*, while $k/k_0=\sigma/\sigma_0$, in terms of wave numbers k, or phase advances per period σ, is used for linear machines. The value $\nu/\nu_0= \sqrt{0.5} \sim 0.7$ is the divide between emittance-dominated and space-charge dominated regimes (Fig. 1.2). *UMER* is designed to operate in a new regime of beam intensity where plasma physics is as relevant as accelerator physics. Table 1.1 presents *UMER*'s design parameters.

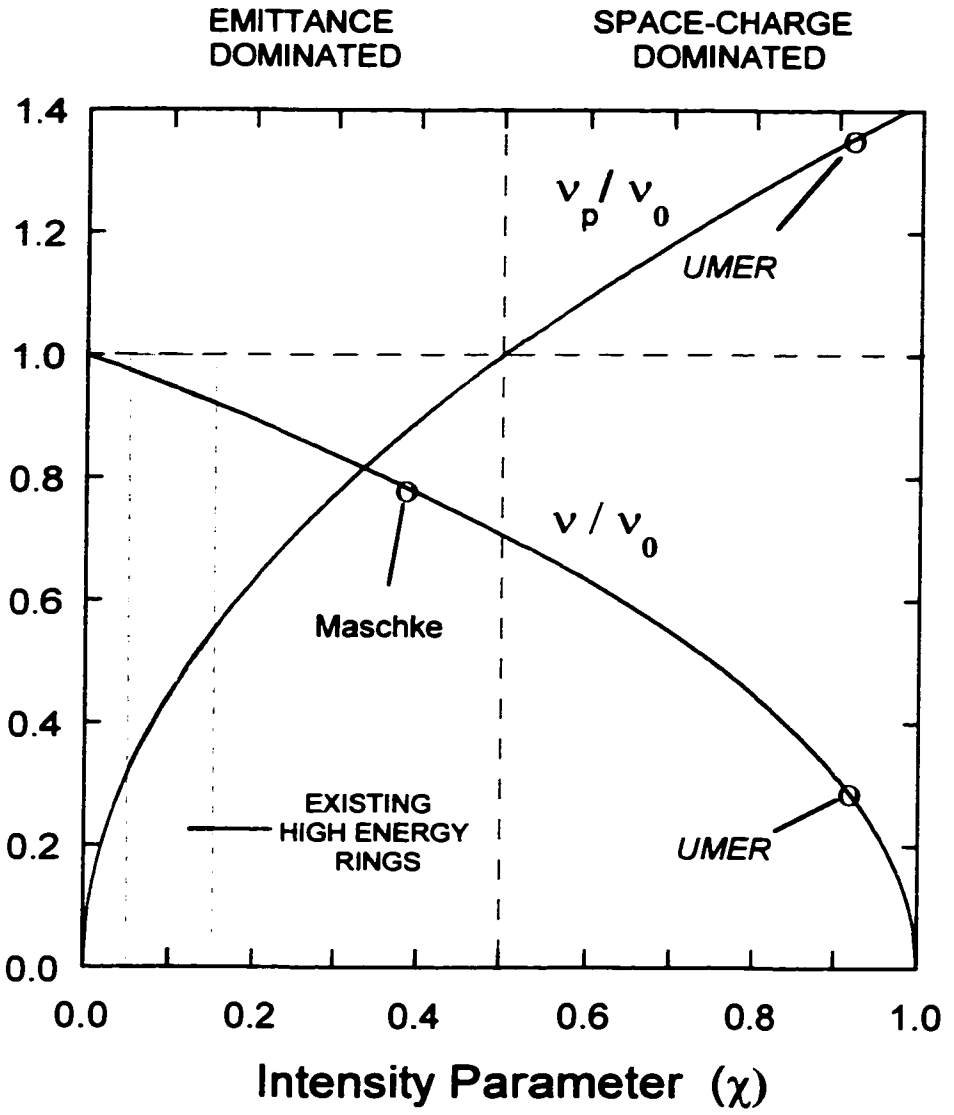

Fig. 1.2. Beam physics regimes [4]. The tune depression ν/ν_0 and the ratio ν_p/ν_0 are plotted as functions of the intensity parameter χ defined in Eq. [1.16]. In the space-charge dominated regime of UMER, the plasma period becomes smaller than the (undepressed) betatron period, leading to plasma processes not seen in ordinary beams.

Table 1.1: UMER design parameters.

Beam energy, electron speed: T , β	10 keV , 0.2
Beam Current, I	< 100 mA
Generalized Perveance, K	$< 1.5 \times 10^{-3}$
Emittance, rms, norm. $\epsilon_N = \beta\gamma\epsilon$	2.5 mm-mrad
Pulse Length	40 ns
Circumference	11.52 m
Lap Time	197 ns
FODO Period	0.32 m
Phase Advance, σ_0	76^0
Betatron Tune	7.6
Tune Depression	> 0.2

The successful operation of *UMER* (loosely defined as "multiturn" operation, or no less than 3-5 turns) depends critically on the design of the injection system, consisting of a straight matching section and an inflector; the former uses dc focusing elements, while the latter employs pulsed elements for focusing and deflection into the ring. The original motivation for the work of this dissertation was the design and test of a prototype matching section for the electron ring; the work included testing and characterization of focusing elements as well as design and construction of means to balance the Earth's magnetic field to reduce its effect in the low-energy electron beam. In the process of testing the matching section, however, new beam phenomena were observed that led to additional experiments and calculations that gave the work here presented a different character from the one originally intended. The main lesson of this experience is that new phenomena are not unexpected in short transport experiments with intense beams; extrapolating, we foresee new exciting results even before the completion of a single turn in *UMER*.

1.2 Beam Transport in a Magnetic FODO lattice

1.2.1 Single-particle Dynamics

A monochromatic beam of non-interacting particles moving in an external focusing field represented by (κ_x, κ_y) can be described by the paraxial (linear) equations of motion for a single particle:

$$x'' \equiv d^2x/ds^2 = -\kappa_x x, \tag{1.1a}$$

$$y'' \equiv d^2y/ds^2 = -\kappa_y y, \tag{1.1b}$$

where s measures distance along the reference trajectory ($s = z$, along the optical axis in a linear channel, and $s = R\theta$ in a circular channel of radius R, with positive θ measured counterclockwise relative to the fixed x-axis in the lab frame). In a focusing system with period S, $\kappa_{x,y}(s) = \kappa_{x,y}(s+S)$; if the system is an alternating-gradient or FODO system of quadrupoles, we have

$$\kappa_x(s) = \frac{+q}{p_0} g_x(s), \quad \kappa_y(s) = \frac{-q}{p_0} g_Y(s) \tag{1.2}$$

where q and $p_0 = \gamma m \beta c$ are the particle's charge and (design) linear momentum, respectively. The quadrupole field components are related to the quadrupole on-axis gradients $g_{x,y}$(s) through $(B_{qx}, B_{qy}) = \left(g_x(s)y,\ g_y(s)x\right)$. In many focusing systems, it is common practice to replace the smooth focusing function by a piecewise constant function consisting of "hard-edge" elements whose effective length l is defined by

$$l_{x,y} = \frac{1}{\kappa_{0_{x,y}}} \int_{-\infty}^{\infty} \kappa_{x,y}(s) ds, \tag{1.3}$$

where κ_0 is the peak value of the smooth profile (Eq. [1.2]). In the thin-lens approximation, the focal length of a quadrupole lens obeys

$$\frac{1}{f} = \pm \kappa_0 l, \tag{1.4}$$

where the positive sign applies to the focusing case. Figure 1.3 illustrates a typical FODO lattice geometry and all relevant parameters.

In the exact treatment of the Courant and Snyder theory (section 3.8.2 in Ref. [5]), the solution to Eq. [1.1] (a) is written as

$$x(s) = A_x \sqrt{\hat{\beta}_{0x}(s)}\, Cos[\psi_x(s) + \phi] \tag{1.5}$$

where $\hat{\beta}_{0x}(s)$ is the *betatron function*, ψ_x is obtained by integration of $\psi_x' = 1/\hat{\beta}_{0x}(s)$, and the quantities A_x and φ are determined from the initial conditions. Furthermore, the *phase advance* of a particle in one lattice period is $\sigma_{0x} = \int_{s_0}^{s_0+S} (1/\hat{\beta}_{0x}) ds$.

The amplitude coefficient A_x can be related to the (unnormalized) *x-emittance* of the beam by $A_x = \sqrt{\varepsilon_x}$. From Eq. [1.5] it is straightforward to show that particles follow ellipses in x-x' space, or trace space:

$$\hat{\gamma}_x x^2 + 2\hat{\alpha}_x x x' + \hat{\beta}_x x'^2 = A_x^2, \tag{1.6}$$

where the coefficients, or *Twiss parameters* satisfy the following relations:

$$x_m = \sqrt{\hat{\beta}_x \varepsilon_x}, \quad x_m' = \sqrt{\hat{\gamma}_x \varepsilon_x}, \quad (x_m)' = -\hat{\alpha}_x \sqrt{\frac{\varepsilon_x}{\hat{\beta}_x}}, \tag{1.7}$$

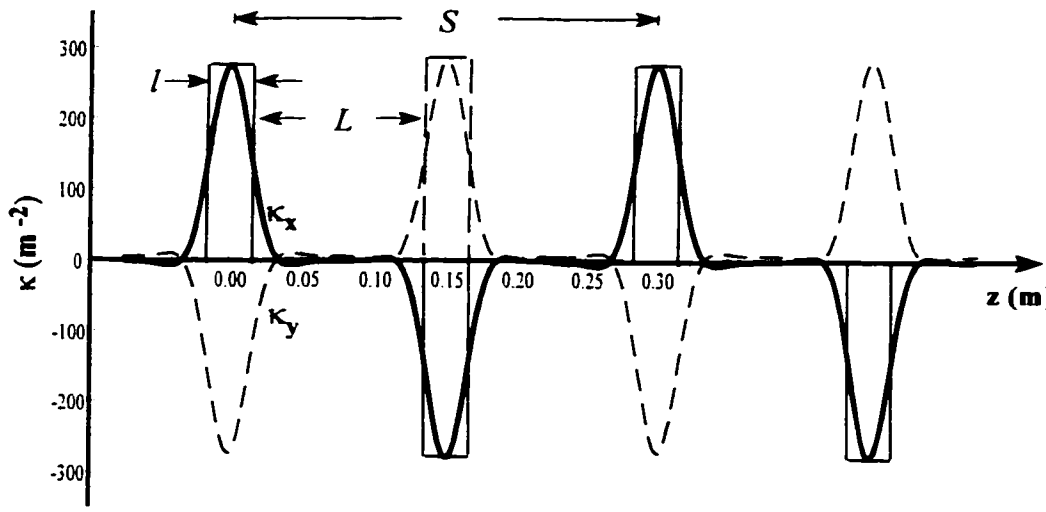

Fig. 1.3 Focusing function in a FODO channel. The quadrupole effective length is l, and the full-lattice period is $S=2(L+l)$.

where $x_m(s)$ is the maximum value of $x(s)$ at a given transverse plane at s, $x'_m(s)$ is the maximum value of the slope, and $(x_m)'$ is the slope at the maximum value of x(s) - See Fig. 1.4. The quantity ε_x is conserved and is proportional to the area of the largest trace space ellipse. Furthermore, the Twiss parameters obey $\hat{\beta}\hat{\gamma} - \hat{\alpha}^2 = 1$.

The solution to the linear second-order differential equations, Eqs. [1.1](a)-(b), can be conveniently expressed in matrix form. The initial conditions (x_0, x'_0), and (y_0, y'_0) at the entrance plane are propagated with a transform matrix representing the focusing system. The trace of the matrix for a FODO unit cell (see Fig.1.3) is proportional to $\cos(\sigma_0)$, where σ_0 is the zero-current phase advance defined before. By using the matrices for quadrupoles and drifts [5], and the notation illustrated in Fig. 1.3, and assuming the general case of alternating quadrupoles with different strengths, we get

$$\cos(\sigma_{0X}) = \cosh(\theta_Y)\left[\cos(\theta_X) - \frac{L}{l}\theta_X \sin(\theta_X)\right] + \sinh(\theta_Y)\sin(\theta_X)\left[\frac{1}{2}\left(\frac{\theta_Y}{\theta_X} - \frac{\theta_X}{\theta_Y}\right) - \frac{L^2}{2l^2}\theta_X\theta_Y + \frac{L}{l}\theta_Y \cot(\theta_X)\right], \tag{1.8a}$$

$$\cos(\sigma_{0Y}) = \cos(\theta_Y)\left[\cosh(\theta_X) + \frac{L}{l}\theta_X \sinh(\theta_X)\right] + \sinh(\theta_X)\sin(\theta_Y)\left[\frac{1}{2}\left(\frac{\theta_X}{\theta_Y} - \frac{\theta_Y}{\theta_X}\right) - \frac{L^2}{2l^2}\theta_X\theta_Y - \frac{L}{l}\theta_Y \coth(\theta_X)\right], \tag{1.8b}$$

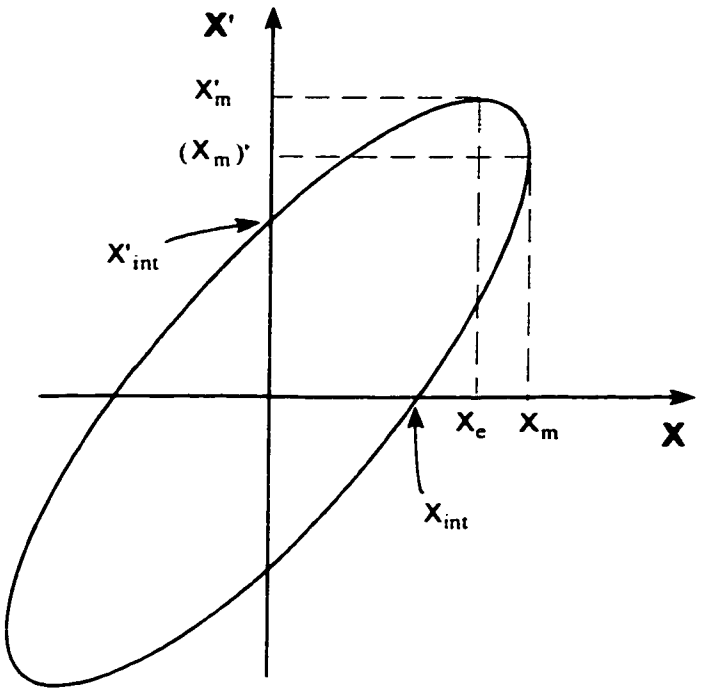

Fig. 1.4. Trace-space ellipse. The points shown are related to the Twiss parameters in Eqs. [1.6] and [1.7].

where, $\theta_X \equiv (\kappa_{0X})^{1/2} l$ and $\theta_Y \equiv (\kappa_{0Y})^{1/2} l$. Equations [1.8](a)-(b) reduce to Eqs. [3.354] and [3.555] of Ref [5] if $\sigma_{0X} = \sigma_{0Y}$. For *given* σ_{0X} and σ_{0Y}, and *filling ratio* l/L , Eqs. [1.8](a)-(b) are solved simultaneously for θ_X, θ_Y, which in turn yield the required peak quadrupole focusing strengths κ_{0X}, κ_{0Y} from the quadrupole effective length (Eq. [1.3]).

In a circular channel, a bending field is needed in addition to $\kappa_{x,y}(s)$. Thus, an ideal dipole field in the y-direction introduces an additional term to the right-hand-side of Eq. [1.1](a), $-qB_{dy}/p_0 = 1/R_0$, where R_0 is the reference path radius. If the bending is not uniform throughout the ring, but occurs over short distances l_d, equally spaced along the circumference and short compared with R_0, the strength of each dipole is

$$\int_{s_1}^{s_2 = s_1 + l_d} B(s)ds = \frac{p_0}{q}\Delta\theta, \tag{1.9}$$

where $\Delta\theta$ is the bend angle.

Finally, to complete the picture for non-interacting particles, the effect of a small momentum "error" $\Delta p \equiv p_0\delta$ yields the first order correction $(qB_{dy}/p_0)\delta = \delta/R_0$ to the right-hand-side of Eq. [1.1](a). The average (over a full lattice period S) deviation from the reference path is then equal to $\delta(R_0/\nu_o^2)$, where $\nu_o = N\sigma_0/2\pi$ is the *betatron tune* without space charge ($N = 2\pi R_0/S$ is the number of FODO periods in the ring). The average *dispersion function*, $\overline{D}$, is defined by the relation

$$\overline{D} = \frac{R_0}{\nu_o^2} \tag{1.10}$$

The betatron and dispersion functions characterize the dynamics of the circular focusing lattice. A good estimation of these functions can be made in the framework of Hamiltonian dynamics. Specifically, Lie algebra methods [6] can be employed to track the motion of single particles and determine the stability regions of the motion. The basic procedure is to derive maps (i.e. matrices and higher order terms connecting dynamical variables) for the bending and focusing elements, i.e. dipoles and quadrupoles, from the Taylor-expansion coefficients of their vector potentials, and from these maps construct the motion across one FODO cell and then the ring. A study of this nature using the elements of the proposed electron ring can be found in [7].

1.2.2 K-V Envelope Equations and the Smooth Approximation:

The inclusion of linear space-charge effects is straightforward in the framework of the K-V distribution to be discussed in the next chapter. Space charge introduces a linear defocusing force and a coupling, through the beam envelopes, of the two transverse components of the particle's motion. We can write [5],

$$x'' + \kappa_x x - \frac{2K}{X(X+Y)}x = 0, \tag{1.11a}$$

$$y'' + \kappa_y y - \frac{2K}{Y(X+Y)}y = 0, \tag{1.11b}$$

for the trajectories, and

$$X'' + \kappa_x X - \frac{2K}{X+Y} - \frac{\varepsilon_x^2}{X^3} = 0, \tag{1.12a}$$

$$Y'' + \kappa_y Y - \frac{2K}{X+Y} - \frac{\varepsilon_y^2}{Y^3} = 0, \tag{1.12b}$$

for the beam envelopes X(s), Y(s). The space-charge term in Eqs. [1.11] and Eqs. [1.12] contains K, the *generalized beam perveance*, defined as

$$K = \frac{2I}{I_0}\frac{1}{\beta^3\gamma^3}, \quad I_0 \equiv \frac{4\pi\varepsilon_0 mc^3}{q}, \tag{1.13}$$

where I is the beam current, $\beta = \upsilon/c$, $\gamma = (1-\beta^2)^{-1/2}$, c is the speed of light, and υ is the particle's velocity. For electrons, $I_0 \cong 17$ kA.

In the case of solenoid focusing, Eqs. [1.11] and [1.12] reduce to

$$r'' + \kappa r - \frac{K}{R^2}r = 0, \quad R'' + \kappa R - \frac{K}{R} - \frac{\varepsilon^2}{R^3} = 0 \tag{1.14}$$

A very useful approximation replaces the focusing functions $\kappa_x(z)$ and $\kappa_y(z)$ by an average uniform focusing constant $\kappa_0 = k_0^2$ (assuming $\sigma_{0x} = \sigma_{0y}$) and $X(s)$, $Y(s)$ by their average values, $\overline{X} = a = \overline{Y}$. Thus, we obtain from either Eqs. [1.12] or [1.14],

$$k_0^2 a - \frac{K}{a} - \frac{\varepsilon^2}{a^3} = 0, \text{ or } k^2 a - \frac{\varepsilon^2}{a^3} = 0, \tag{1.15}$$

with $k^2 = k_0^2 - \left(K/a^2\right)$. The ratio k/k_0 is called the *tune depression* and is equal to

$$\frac{k}{k_0} = \sqrt{1 - \frac{K}{k_0^2 a^2}} = \sqrt{1-\chi}, \tag{1.16}$$

where $\chi \equiv K/k_0^2 a^2$ defines the *intensity parameter*. In terms of phase advance per full-lattice period, $\sigma = kS$, the tune depression is $k/k_0 = \sigma/\sigma_0$. Furthermore, the average beam size is given by [eq. (4.93b) in Ref. [5]):

$$a = a_0\left(u + \sqrt{1+u^2}\right)^{1/2},\ u \equiv \frac{K}{2k_0\varepsilon}, \tag{1.17}$$

where $a_0 = \sqrt{\varepsilon/k_0}$ is the zero-current beam size.

Another expression that is useful for design problems, gives the envelope *ripple*, defined here as the ratio $a/a_{\max}$ [eq. (4.183) in [5]):

$$\frac{a}{a_{\max}} \cong \left(1 - \frac{1.2\sigma_0}{\pi}\right)^{1/2}, \tag{1.18}$$

which is a good approximation for $\sigma_0 < 90^0$.

Finally, an improved, empirical formula for the average beam size that is a good approximation in all regimes of space charge is the following [eq. (5.293) in [5]):

$$a \cong \left(\frac{S}{\sigma_0}\right)\left(\frac{\varepsilon\sigma_0}{S} + K\right)^{1/2}. \tag{1.19}$$

Equations [1.15] through [1.18] constitute the basic relations of the *smooth approximation* of periodic focusing channels [5]. For a space-charge dominated beam we have $K >> \epsilon^2/a^2$.

Additional useful relations are presented in Appendix A.

CHAPTER II

Beam Equilibrium and the K-V Distribution

2.1 Introduction

While in Chapter I the basic equations of beam transport in a FODO lattice are reviewed, the physics behind them requires a more thorough discussion. The first issue to consider, beam equilibrium, is reviewed in general terms in Section 2.2. The length and time scales relevant to the transport dynamics of the electron beam used in our experiments are summarized in Table 2.1. Section 2.3 introduces the K-V distribution, a widely used mathematical construct to model real intense beams; also reviewed is the concept of the equivalence between uniform electric (or magnetic quadrupole) focusing and uniform solenoid focusing when the latter is viewed from a rotating reference frame, the Larmor frame. The fundamental topic of emittance growth is then addressed in Section 2.4, starting with general definitions and the idea of equivalent beams, followed by a phenomenological theory and an example of calculations for mismatched beams. The second part of Section 2.4 briefly reviews recent developments and summarizes the general question of beam stability in the K-V model from the point of view of an envelope-stability analysis, and the more general approach of the linearized Vlasov equation. We conclude with general comments on entropy change and emittance growth.

2.2 Vlasov Equation, Metaequilibria and Thermal Equilibrium

The phase space of a system of N particles has $6N$ dimensions, $3N$ generalized coordinates and the corresponding $3N$ conjugate momenta. From the continuity equation in $6N$ dimensions, and assuming that the system is Hamiltonian, i.e. that it obeys Hamilton's equations of motion, it is straightforward to prove that an ensemble of systems evolves in phase space like an incompressible fluid, i.e. that a given initial volume remains constant although its shape may change. This conservation of volume in phase space is known as *Liouville's theorem*. In the *Vlasov approximation*, a single particle evolves in the average electric and magnetic fields produced by the rest of the distribution; thus, the $6N$-dimensional space, or *Γ-space*, can be replaced by the six-dimensional phase space of a *single* particle (*μ-space*). A region in *μ-space* then represents the phase space of a system of N "non-interacting" particles evolving under the action of average fields. Since the dynamics is Hamiltonian as before, Liouville's theorem is also valid in *μ-space*.

It is customary to consider Vlasov or *collisionless* plasmas (neutral or non-neutral) in *thermal equilibrium*. In this case, the action of an individual particle is screened over distances of the order of the *Debye length* λ_D, defined as

$$\lambda_D = \left(\frac{\varepsilon_0 \gamma k_B T}{q^2 n} \right)^{1/2}, \tag{2.1}$$

where n is the density of electrons or ions of charge q, T is the absolute temperature, k_B is Boltzmann's constant, and γ is the relativistic mass factor.

The normalized phase-space distribution function for a single particle, $f(q,p,t)$, is defined so that $Nf\,dpdq$ is the number of particles in a 6-dimensional volume element $dpdq$. From Maxwell equations, the Lorentz force equation and Liouville's theorem in μ-*space*, it follows that [5,8,11]

$$\left[\frac{\partial}{\partial t}+\vec{\upsilon}\cdot\vec{\nabla}-e\left(\vec{E}+\vec{\upsilon}\times\vec{B}\right)\cdot\vec{\nabla}_{\upsilon}\right]f(q,p,t)=0, \tag{2.2}$$

for the case of non-relativistic electrons. Equation [2.2] is known as the Vlasov equation, or the *collisionless* Boltzmann equation, which together with the Maxwell equations $\nabla\times\vec{E}=0$, $\nabla\times\vec{B}=-\mu_{o}e\int\vec{\upsilon}f(q,p,t)d^{3}P$, $\nabla\cdot\vec{E}=(-e/\varepsilon_{o})\int f(q,p,t)d^{3}P$, and $\nabla\cdot\vec{B}=0$ for the average self-fields (in the electrostatic limit), constitute a set of closed equations for $f(q,p,t)$.

An important distribution function that represents both a thermal equilibrium state and a Vlasov equilibrium is the *Maxwell-Boltzmann* (M-B) distribution:

$$f=\left(\frac{m}{2\pi k_{B}T}\right)^{3/2}\exp\left(-\frac{m}{2k_{B}T}\upsilon^{2}\right). \tag{2.3}$$

In general, any function of the single-particle constants of the motion such as the total energy, angular or linear momentum can be shown to be a stationary solution of Vlasov's equation. An important example is the *rigid-rotor* equilibrium, where total energy and both angular and linear momentum, perpendicular to and along the direction of an externally applied magnetic field, are conserved; this applies to a plasma column [8] or to a trapped non-neutral plasma [9]. Another example is the Kapchinskij-

Vladimirskij (K-V) distribution [10] widely used for modeling of intense beams. Since the K-V distribution is the most relevant to this work, we will consider it in detail in the next Section.

When the distribution function is non-M-B, an effective temperature characterizing the average kinetic energy can still be defined:

$$\frac{3}{2}k_B T = \left\langle \frac{m\upsilon^2}{2} \right\rangle, \tag{2.4}$$

where < > indicates average over the particle distribution. Furthermore, the effective temperature can be considered as a function of position, meaning that the condition of *local thermal equilibrium* applies, as opposed to *global thermal equilibrium*. (Local thermal equilibrium implies, naturally, that the local distribution function is not too far from a M-B distribution.).

Relevant to this discussion is the question of *thermalization*, i.e. evolution towards thermal equilibrium, and entropy increase. Since the Vlasov equation does not include the effects of collisions, the Boltzmann entropy, which in the "information theory" form reads

$$S(t) = -\int f(q,p,t)\ln\left(f(q,p,t)\Delta\mu\right)d^3q\,d^3p, \tag{2.5}$$

in terms of the *single-particle* distribution function *f and an unspecified phase-space volume element*, $\Delta\mu$, remains constant [11]. Therefore, the average interaction between particles is not enough to drive a system towards thermal equilibrium, an evolution

which involves entropy increase and associated irreversibility. As a matter of fact, stable metaequilibria can be constructed that have less entropy than the corresponding M-B distribution [11]. Apparently, it is still possible for a system to evolve towards a M-B distribution in the absence of collisions. Collective phenomena involving *nonlinear forces* and *instabilities*, most notably *Landau damping* [11], are often mentioned as feasible mechanisms.

To conclude this section, we present a summary of quantities that give an idea of the time and length scales involved in the evolution of the electron beams in the experiments of this work. The *space scale* of charge separation, the *Debye length*, was already introduced in Eq. [2.1]. The *time scale* of charge separation is easily derived from the restoring force produced when two electrons are separated by an average distance equal to $[3/(4\pi n)]^{1/3}$, where n is the electron number density. The time scale is the inverse of the *plasma frequency* given by:

$$\omega_p = \left(\frac{q^2 n}{\gamma^3 m \varepsilon_0} \right)^{1/2}, \tag{2.6}$$

Another time scale associated with Vlasov's equation is provided by the *cyclotron frequency*:

$$\omega_c = \frac{|q|B}{\gamma m}, \tag{2.7}$$

The *Larmor frequency* is defined as one-half the cyclotron frequency; it plays a fundamental role in the description of beam propagation under the action of axial B

fields. Table 2.1 summarizes the time and length scales and some additional typical parameters relevant to the experiments of this work.

2.3 The Kapchinskij-Vladimirskij (K-V) Distribution

In the K-V distribution, all particles have the same total transverse energy H_0, and the same longitudinal velocity $v_z = v_0$; the distribution can be written in the form

$$f_{KV} = \frac{n_0}{2\pi m}\delta(H_\perp - H_0), \tag{2.8}$$

where δ is a Dirac delta function, H_0 is constant, and

$$H_\perp(p_x, p_y, x, y, t) = \frac{1}{2m}\left(p_x^2 + p_y^2\right) + \frac{1}{2}m\omega_0^2\left(x^2 + y^2\right) + q\phi(x, y, t), \tag{2.9}$$

is the non-relativistic Hamiltonian for the *transverse* motion of a single particle of mass m and charge q, with position (x,y) and transverse velocity $(1/m)(p_x,p_y)$. The second term represents *external linear focusing*, where ω_0 is the betatron frequency of a particle in the absence of space-charge, and the last term contains the self-potential. To proceed further, we will assume that external focusing is provided by a uniform background of opposite charge; this assumption is made only to provide a physical basis for the model. (We will consider magnetic focusing below.) The K-V distribution is then restricted to axisymmetric linear external and internal forces, in which case the distribution is the only known self-consistent solution of the Vlasov-Maxwell system of equations. Under these conditions the self potential is

Table 2.1: Length and time scales relevant to the transport dynamics of a 4 keV, 17 mA, 67 mm mrad[a] electron beam in a focusing channel with $\sigma_0=85^0$ (7.6 mm avg. radius).

Debye Length	0.74 mm
Plasma Frequency, ω_p	$2\pi \times 3.5 \times 10^7$ s^{-1}
Plasma Wavelength, λ_p	4×0.27 m
Undepressed Betatron Frequency, ω_0	$2\pi \times 2.7 \times 10^7$ s^{-1}
Undepressed Betatron Wavelength, λ_0	1.4 m
Lattice Filling Factor[b], l_{eff}/L	0.26
Electron Bunch Duration	$\sim 5\ \mu$s
Bunch Length	$\sim$ 190 m

[a]Effective, 4 × rms emittance.

[b]For small-aperture quadrupoles (See Fig. 1.3 and Chapter IV).

$$\phi(r)=\begin{cases} -\dfrac{qn_0}{4\varepsilon_0}r^2, & 0\le r\le a, \\ -\dfrac{qn_0}{4\varepsilon_0}a^2\left[1+2\ln\left(\dfrac{r}{a}\right)\right], & a\le r\le a_w \end{cases} \tag{2.10}$$

The total number of particles per unit length of the beam is $N=\pi n_0 a^2$, where a is the beam radius. For simplicity, the potential is chosen to be zero on the beam axis. Alternatively, and more commonly (p. 194 in Ref. [5]), the potential is chosen to be zero on the surface of a cylindrical boundary (radius a_w), with a straightforward rewriting of Eq. [2.10]. The *potential depression* across the beam is $\phi(r=a)-\phi(r=0)=-(qn_0a^2/4\varepsilon_0)$, while the beam edge potential relative to the wall is $\phi(r=a)-\phi(r=a_w)=(qn_0a^2/2\varepsilon_0)\ln(a_w/a)$.

If the definition of plasma frequency (Eq. [2.6], with $\gamma = 1$) is used to rewrite the expression for the self-potential *energy* inside the beam, the Hamiltonian can be put in the form

$$H_\perp(p,r)=\frac{p^2}{2m}+H_0\left(\frac{r}{a}\right)^2, \tag{2.11}$$

where

$$H_0=\frac{1}{2}ma^2\left(\omega_0^2-\frac{\omega_p^2}{2}\right)\equiv\frac{1}{2}mra^2\omega^2. \tag{2.12}$$

Above, ω is the frequency of transverse oscillations resulting from the combined action of linear external focusing and linear space charge forces.

Taking advantage of the definitions above, the K-V density distribution can be written explicitly as $f_{KV} = (n_0/2\pi m)\delta\left[p^2/2m - H_0(1 - r^2/a^2)\right]$, which is consistent with a uniform density $2\pi\int f_{KV}\,pdp = n_0$, for $0 \le r \le a$, and a *parabolic temperature profile*,

$$T = \frac{2\pi}{n_0}\int\left(\frac{p^2}{2m}\right)f_{KV}\,pdp = H_0\left(1 - \frac{r^2}{a^2}\right). \tag{2.13}$$

It should be stressed that this temperature is an example of an effective or kinetic equilibrium (non-thermal) temperature; the temperature is constant when the system is in thermal equilibrium and is related to the density through the *pressure tensor* (isotropic in thermal equilibrium) by $\bar{P}(r) = n(r)T$, with T in energy units [8]. In this latter case, $n(r)$ assumes the form of a Boltzmann distribution, which leads to a Gaussian density profile in the high temperature limit, and to a K-V distribution in the $T \to 0$ limit. For intermediate temperatures, the beam profiles have no analytical form, but all display relatively broad bell-shaped cores with tails that extend over lengths of the order of the Debye length (Sec. 5.4.4 in Ref. [5]). Of course, the K-V distribution cannot be considered to have, *literally*, a thermal temperature $T = 0$, since the Boltzmann distribution, being a classical distribution, is no longer valid in that limit. Besides, a zero temperature for the *distribution* would imply zero emittance, which is only a special case, the case of laminar or Brillouin flow. (In fact, a K-V distribution *can* be defined for *any* combination of emittance and perveance.) For the K-V distribution, the kinetic temperature, with its parabolic profile, is more meaningful, having $T = 0$ only at the beam edge.

Let's consider now the Hamiltonian for the *transverse* motion of a particle in the presence of a constant and uniform magnetic field in the $+z$ direction, $\vec{B} = B\hat{z}$, i.e. $\vec{A} = A_\theta\hat{\theta} = (rB_z/2)\hat{\theta}$, since $\vec{B} = \vec{\nabla} \times \vec{A}$. In cylindrical coordinates we have:

$$H(p_r, p_\theta, r, \theta, t) = \frac{1}{2m}\left[p_r^2 + \left(\frac{p_\theta - qrA_\theta}{r}\right)^2\right] + q\phi(r, \theta, t). \tag{2.14}$$

In a reference frame that rotates clockwise about the $+z$-axis at half the *cyclotron* frequency (Eq. [2.7]), i.e. at the *Larmor* frequency, the Hamiltonian transforms to [12]:

$$H(p_r, p_{\theta_L}, r, \theta_L, t) = \frac{1}{2m}\left(p_r^2 + \frac{p_{\theta_L}}{r^2}\right) + \frac{1}{4}m\omega_c^2 r^2 + q\phi(r, \theta_L, t), \tag{2.15}$$

where $\dot{\theta}_L = \dot{\theta} \pm (\omega_c/2)$ is the particle's frequency as seen in the rotating frame, and the negative sign applies for negatively charged particles. Comparison of Eqs. [2.15] and [2.9] shows that uniform electrical focusing in the laboratory frame is mathematically equivalent to uniform magnetic focusing in a frame rotating at the Larmor frequency, if the substitution $\nu_0 \rightarrow \omega_c/2$ is made. Furthermore, the effective transverse temperature in the rotating frame is given by

$$H_0 = \frac{1}{2}ma^2\left[\frac{\omega_c^2}{4} - \frac{\omega_p^2}{2}\right]. \tag{2.16}$$

For a cold beam, i.e. if H_0=0, we obtain the condition for ideal Brillouin flow: $\omega_L^2 = \omega_p^2/2$.

If we introduce the *generalized beam perveance* K, unnormalized transverse *emittance* ϵ, and the *focusing function* κ (constant in the present case), defined by

$$K=\frac{\omega_p^2}{2}\frac{a^2}{v^2},\quad \varepsilon=\sqrt{\frac{2H_0}{m}}\frac{a}{v},\quad \kappa=\frac{\nu_0^2}{v^2}, \tag{2.17}$$

we can cast Equation [2.12] in a very useful form:

$$\kappa a-\frac{K}{a}-\frac{\varepsilon^2}{a^3}=0. \tag{2.18}$$

This is a form of the transverse K-V envelope equation that represents an average force-thermal balance relation when all forces are linear. The focusing function can represent average focusing from a periodic lattice of electrical or magnetic quadrupoles, in which case the reference frame is the laboratory frame, or average focusing from a periodic lattice of solenoids, in which case the reference frame is the Larmor frame. Equation [2.18] is a statement of the *smooth approximation* for beam transport in a periodic focusing channel, reviewed in Chapter I (Eq. [1.15] with $k_0^2 \equiv \kappa$).

2.4 Emittance Growth

2.4.1 Definitions:

A beam with an arbitrary charge distribution can be approximated by an *equivalent K-V beam* having the same current, energy and second moments of the distribution. An *effective beam emittance* is defined ([13], and eq. (5.206 in Ref. [5]),

$$\varepsilon_{x\,eff}=4\left[\langle x^2\rangle\langle x'^2\rangle-\langle xx'\rangle^2\right]^{1/2}=4\varepsilon_{rms} \tag{2.19}$$

where <> denotes average over the actual phase-space distribution, and primes mean d/ds. For a K-V beam, the emittance defined by Eq. [2.19] is equal to the area in x-x' space divided by π; this is not the case for a general distribution, because the projected phase-space in x-x' space may not have elliptical symmetry and/or may not be uniformly filled. Other relevant definitions are the *effective beam size* and *effective slope*:

$$x_{eff} = 2\langle x^2 \rangle^{1/2}, \quad x'_{eff} = 2\langle x'^2 \rangle^{1/2}. \tag{2.20}$$

For a K-V distribution, the effective beam size is just equal to the beam edge radius a, while the effective slope is the maximum slope a', not to be confused with the slope at the beam edge (see also Eqs. [1.7] and Fig. 1.4). With the above definitions, the envelope equations, Eqs. [1.12], are valid with the substitutions $X = x_{eff}$, $Y = y_{eff}$, and $\epsilon_{x,y} = \epsilon_{x,y\,eff}$.

Since $x' = (1/v)dx/dt$, emittance, as defined in Eq. [2.19], will depend on the beam energy. The normalized emittance is defined to make possible a comparison between emitttances corresponding to beams of different energies:

$$\varepsilon_N = \gamma\beta\varepsilon \tag{2.21}$$

Although, according to Liouville's theorem, the volume in phase space is preserved in the absence of collisions, or other stochastic processes, a system's phase space may develop distortions or filamentations under the action of non-linear forces. From the definition of rms emittance in Eq. [2.20], extra weight is given to particles in the outer regions in trace space, relative to the situation when the trace space is more regular, leading to an increase in rms emittance. In mathematical terms, it can be shown that the

rms emittance is invariant under time-independent linear symplectic transformations [14]; if acceleration is involved, the normalized emittance (Eq. [2.21]) is conserved [15].

2.4.2 Phenomenological Theory:

The propagation of a continuous beam in a uniform focusing channel or, equivalently, in a periodic channel, in the smooth approximation, is characterized by a constant average beam size and a constant rms emittance. Another way of expressing this is to say that the average total energy per unit length is conserved. The total energy has contributions from the self electrostatic field energy, the potential energy associated with the focusing force, and the average kinetic energy per particle associated with the transverse motion.

In a real situation, a beam may have an initially non-uniform particle distribution, or it may be mismatched for transport in a periodic or uniform focusing channel, or have an asymmetric envelope, i.e. an elliptical cross section. In the first two cases, at least, the charge density will redistribute, in response to internal nonlinear forces and the externally applied field, so the beam will assume eventually a more uniform distribution; in the process, the rms emittance will grow, accompanied in most cases by halo formation. Other processes that may lead to rms emittance growth, especially in space-charge dominated beams, are dispersion in rings, coupling between the transverse motions (from rotated quadrupoles or misalignments), and kinetic energy exchange

between longitudinal and transverse motions (equipartioning). Some of these are considered later in the chapter.

A phenomenological theory has been developed by a number of authors [16, 17, and Chap. 6 in Ref. 5] that allows one to calculate the rms emittance growth to be expected. The theory is based on the idea that the non-equilibrium initial state of a beam has extra energy, relative to the energy of the equivalent stationary beam, which thermalizes as the beam relaxes towards M-B equilibrium. The extra energy, or "free energy", translates into additional thermal energy, i.e. rms emittance growth; this growth can be calculated using the equivalent uniform beam model [16, 5].

From the smooth approximation, Eq. [1.15], applied to both the evolving beam distribution, with final *equivalent* radius a_f, and emittance ϵ_f, and the initial *equivalent* uniform distribution (radius a_i and emittance ϵ_i), we can write (eq. 6.12b in Ref. [5]):

$$\frac{\varepsilon_f}{\varepsilon_i} = \frac{a_f}{a_i}\left[1 + \frac{k_0^2}{k_i^2}\left(\frac{a_f^2}{a_i^2} - 1\right)\right]^{1/2}, \tag{2.22}$$

where k_i/k_0 is the tune depression of the initial equivalent uniform beam. If one assumes that the radius a remains constant, one can derive a differential equation for the evolution of emittance in the form [17]:

$$\frac{d\varepsilon^2}{dz} = -a_i^2 K \frac{1}{2W_0}\frac{dU(z)}{dz}, \tag{2.23}$$

where $U(z) = W(z) - W_u$ is the difference between self-field energies per unit length, with $W_u = W_0[1+4ln(a_w/a_i)]$, and a_w = pipe radius. Using the smooth approximation, Eq. [1.14] , Eq. [2.23] can be integrated *if we assume* $a_i \approx a_f$:

$$\frac{\varepsilon_f}{\varepsilon_i}=\left[1-\frac{(U_f-U_i)}{2W_0}\left(\frac{k_0^2}{k_i^2}-1\right)\right]^{1/2}\rightarrow\left[1+\frac{U_i}{2W_0}\left(\frac{k_0^2}{k_i^2}-1\right)\right]^{1/2}, \tag{2.24}$$

where the space-charge dominated limit is taken on the right-hand side, so U_f/W_0=0, corresponding to a uniform distribution.

The general treatment by Reiser [16, 5] which yielded Eq. [2.22] for the emittance growth, has no restrictions on the radius a_f, so an equation for the change of radius can be obtained in the form (eq. 6.8 in Ref. [5]):

$$\left(\frac{a_f}{a_i}\right)^2-\left(1-\frac{k_i^2}{k_0^2}\right)\ln\left(\frac{a_f}{a_i}\right)-1=h, \tag{2.25}$$

where h, called the free-energy parameter, is related to U_i/W_0 through $h=(1/4)\left[1-(k_i/k_0)^2\right](U_i/W_0)$. As an example of the application of the theory, we present calculations for the case of mismatched beams. Equations [2.22] and [2.25] are solved using an expression for h derived in [16, 5] for mismatched beams. Figure 2.1 is a plot of the emittance ratio vs. the mismatch ratio a_0/a_i, where a_0 is the minimum beam radius of an initially mismatched beam, the latter being represented by a rotating ellipse in trace-space, and a_i is the beam radius of the initial, stationary (ΔE=0) equivalent uniform beam. Furthermore, Figure 2.2 shows the beam size ratio of Eq. [2.25] vs. the mismatch ratio a_0/a_i. In both Fig. 2.1 and Fig. 2.2, the curves are plotted for tune depressions k_i/k_0 =0.25, 0.5, 0.75 and 1.0. From Fig. 2.1 we can see that emittance growth is largely insensitive to current in the emittance-dominated regime, i.e. for tune depressions near 1, regardless of mismatch ratio. For relatively large or small mismatch

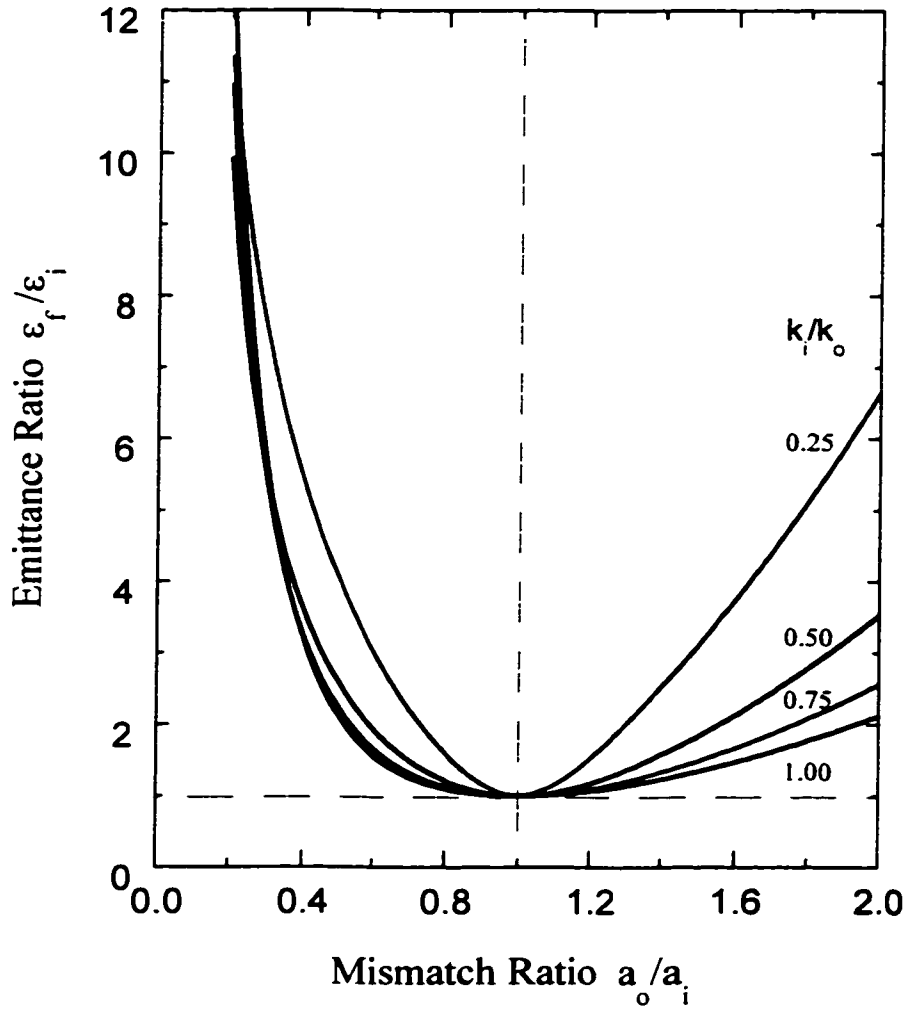

Fig. 2.1 Emittance growth due to mismatch. a_0 is the initial beam radius of the mismatched beam, and a_i is the radius of the equivalent matched beam.

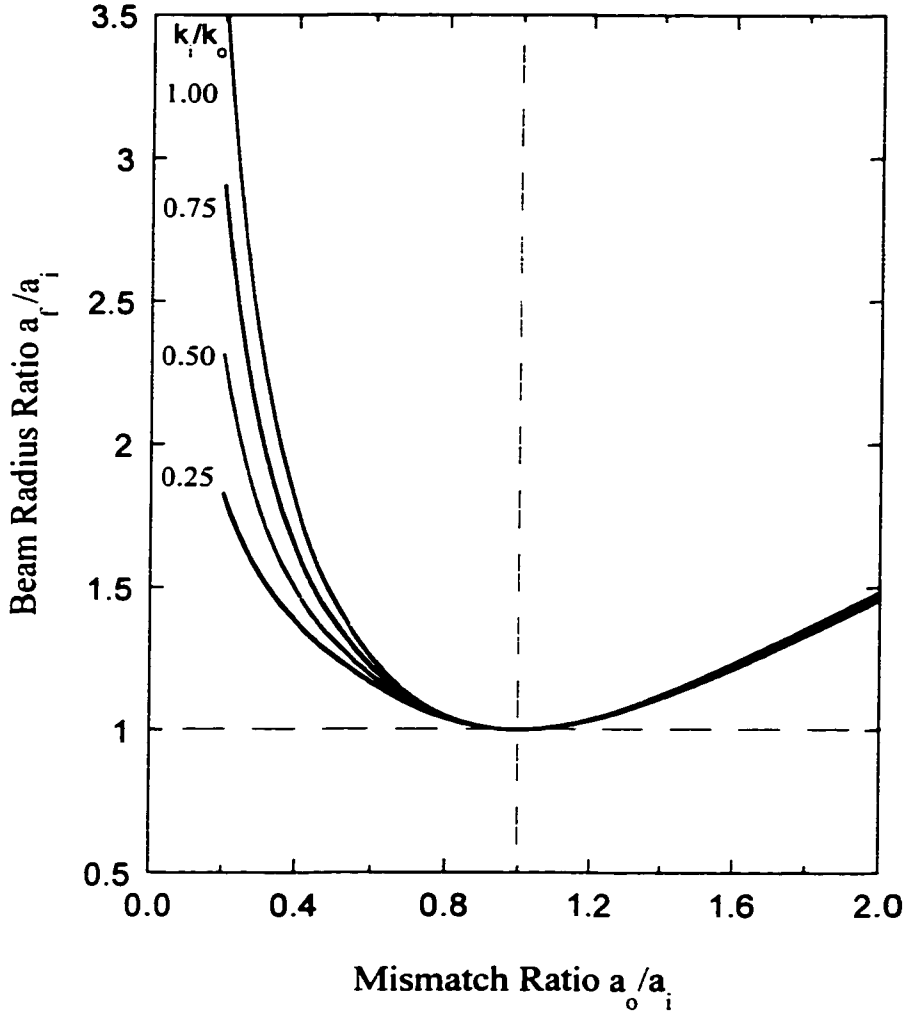

Fig. 2.2. Increase in effective beam radius due to mismatch. a_0 is the initial beam radius of the mismatched beam, and a_i is the radius of the equivalent matched beam.

ratios and strong space charge, on the other hand, a large increase in emittance is predicted. This is consistent with a change in the free energy parameter h related to the envelope oscillations of a mismatched beam (to be reviewed at the beginning of the next section): the oscillations *eventually* relax by the action of collective forces so that the beam fills an effective upright ellipse with effective radius a_f greater than the radius a_i of the initial stationary beam (i.e. the beam without the mismatch).

The theory reviewed above does not give a time scale for the relaxation process. However, simplified models [18] and/or computer simulations provide important clues: the relaxation process is fastest for initially non-uniform charge distributions, of the order of a quarter plasma period, $\lambda_p/4$; for mismatched beams, the relaxation scale is more complicated and involves the growth rate of the envelope instability [19, 20 and Sec. 2.4.4 in 5] to be discussed below.

2.4.3 Additional Mechanisms:

So far, "mismatch" has referred to rms envelope, or betatron function, mismatch. Another type of matching, dispersion function matching, is necessary in circular machines like *UMER* if the beam has a significant non-zero longitudinal energy spread. The dispersion function (defined in Chapter I for low current) gives the deviation, per unit fractional momentum spread, from the reference orbit. In general terms, dispersion introduces a coupling of the longitudinal and betatron motions that is complicated if space charge is also present. To tackle the problem, Venturini and Reiser [21] have recently developed a self-consistent theory for continuous beams; furthermore, a set of

rms envelope equations similar to the K-V envelope equations (Eqs. [1.12]), supplemented with a third equation for the dispersion function [22] have made possible calculations of dispersion matching [23]. A major feature of the new theory is the introduction of a generalized emittance that is invariant in the presence of linear dispersion in the same sense that the regular rms emittance is under linear forces. Particle-in-cell calculations for *UMER* have shown [23] that lack of dispersion matching leads to a large initial increase in the horizontal rms emittance followed by rapid oscillations that eventually subside; further, the vertical emittance also increases because of nonlinear coupling between the transverse directions of motion. When both betatron and dispersion function matching are employed, however, the calculations show significantly smaller final emittances in both transverse directions; moreover, if proper matching is extended to the extraction section (see Fig. 1.1), the original horizontal emittance is recovered.

Another mechanism of emittance growth of interest arises from errors in the orientation of quadrupoles in a FODO lattice. Rotated quadrupoles cause a coupling of the x and y motions that, even for initial K-V distributions, leads to rms emittance growth. As in the dispersion case, however, generalized emittances can be defined that are conserved in a linear model [24,25]. Particle-in-cell simulations for *UMER* by R. Kishek [25] using an initially semi-Gaussian distribution (see Chapter VII for a definition) have shown that even a moderate rms error in quadrupole orientation (0.2^0) can cause the regular rms emittances to increase by 20% approx. after 10 turns, with oscillations that reflect the periodicity in the errors. The emittance oscillations correspond to reversible changes from linear forces in the beam, while the observed

steady increase in a generalized emittance (actually the lower bound to the oscillations) indicates the presence of an irreversible component from nonlinear space-charge forces. By contrast, in a straight lattice the steady increase in the generalized emittance is followed by a sudden large increase, associated with halo formation. In both cases, the rotated quadrupoles lead to rotated beams which in turn translate into mismatches in the rms envelopes X and Y. Initial observations of this nature are reported in Chapter V and Appendix C.

Finally, charge redistribution may occur even when the initial charge distribution is uniform, if the initial transverse *velocity* distribution is sufficiently non-uniform, i.e. if a strong temperature profile is present. Furthermore, in this special case, no rms emittance change is seen in simulations as the beam evolves towards a stationary distribution. The phenomenon has been reported in simulations using a semi-Gaussian distribution [17, and p. 496 in Ref. 5], and the first experimental evidence, with additional simulations, has been the subject of a recent paper [26]. A detailed discussion is presented in Chapter VII.

2.4.4 Stability of the K-V distribution:

A. Envelope Analysis:

The study of beam instabilities plays a crucial role in the design of accelerators, as beam instability is one of the main factors leading to emittance growth and halo formation. We start this section with a brief description of envelope oscillations of mismatched beams.

A simple matrix formulation of single-particle motion through a periodic linear-focusing lattice shows that the phase advance per cell is restricted to $\sigma_0 \leq 180^0$ to ensure confined, i.e. stable, periodic motion; this is similar to the problem in optics of ray stability in a quadratic-index medium. When particle beams are considered, the simplest stability analysis is done in a uniform, axisymmetric focusing channel. It is found (pp. 217-221 in [5]) that for a small mismatch, i.e. if the beam size is initially close to but not identical to the matched-beam value, the beam envelope undergoes *in-phase* sinusoidal oscillations whose frequency depends on the mode structure and beam intensity. For zero intensity the envelope ripples at twice the single-particle frequency, while at high intensity (laminar flow) the envelope oscillates at the plasma frequency ω_p for the in-phase (breathing) mode.

For periodic focusing channels, the smooth approximation provides a natural simplification of the stability problem. For small deviations from matching in both X and Y envelopes, assuming a quadrupole system, the solutions to the linearized equations for the deviations yield two normal modes of oscillation, as for two coupled linear harmonic oscillators. The first mode is an *in-phase* mode where the ripples in X and Y add up, identical to the envelope mode in the uniform, axisymmetric channel. In the second mode, an *out-of-phase* mode, the deviations oscillate with a 180^0 phase difference. "Beating" can occur between the modes, leading to fast oscillations at a frequency equal to the sum of the mode frequencies, with a slow-varying amplitude oscillating at the difference frequency. For zero current the two modes become one with a frequency equal to twice the single-particle frequency. In the high intensity limit ($\nu \to 0$

in Eq. [2.12]), on the other hand, the mode frequency is $\sqrt{2}$ times the single-particle frequency, i.e. the plasma frequency.

The case where the full periodic nature of focusing is included was investigated by Struckmeier and Reiser [20] and is discussed in Sec. 4.4.3 of Ref. [5]. Mathematically, it is similar to the Courant-Snyder theory with the addition of linear space charge forces. Again, *in-phase* and *180^0-out-of-pase* quadrupole modes are found. For zero current, both modes converge and have a phase advance $\phi = 2\sigma_0$ as before; for a given $\sigma_0 \geq 90^0$, and as the beam intensity is increased, the modes separate and can become unstable when $\phi_{\text{in-phase}}$ or $\phi_{\text{out-of-phase}}$ passes through 180^0. The analysis is similar for both solenoid and quadrupole channels, although the regions of instability (in σ_0-σ space) in the quadrupole channel seem broader and more severe than in the equivalent solenoid channel.

B. Kinetic Analysis - Gluckstern Modes:

The quadrupole envelope modes just mentioned are not the only modes of a K-V distribution. A more general analysis, based on the K-V distribution, uses the linearized Vlasov equation [8]. Gluckstern [27] has derived the transverse kinetic oscillation modes that result from a sinusoidal, axisymmetric perturbation on a continuous, matched K-V beam in a uniform focusing channel. The modes correspond to distortions of the hyper-ellipsoidal surface in phase space that K-V beam particles populate; the modes are labeled by radial and azimuthal mode numbers, n and m, respectively. The (n,m)=(1,0) mode, for example, coincides with the "breathing" mode derived from the above envelope analysis, i.e. the stable oscillations of the beam radius at frequency

$\omega_{10}=(2\omega_0^2+2\omega^2)^{1/2}$, or $\omega_{10}\rightarrow\omega_p$ in the high current limit. As another example, the (0,2) mode is the same as the quadrupole mode from envelope analysis, with frequency $\omega_{02}=(\omega_0^2+3\omega^2)^{1/2}$. The normalized mode frequencies ω_{nm}/ω_0 depend on the tune depression ν/ν_0, and are real, i.e. the modes are stable, for tune depressions $\nu/\nu_0 > 0.4$, approximately. The modes with $n > 1$ exhibit high and low frequency branches; the former are stable for all tune depressions, but the latter exhibit instabilities whose maximum growth rates increase for larger radial mode numbers n and increasing tune depressions, being maximum at $n = 4$. When the K-V beam is sufficiently mismatched, instabilities are seen even for relatively large values of tune depressions [28]. However, the high-order K-V mode instabilities ($n>2$), are not significant in more realistic distributions which do not exhibit the singular nature of the K-V distribution where all particles oscillate with the same betatron frequency [29].

To complement the kinetic approach, Lund and Davidson [30] have shown that the high frequency branches of Gluckstern modes, which are stable, can be obtained with a "warm fluid" model of a continuous beam in a uniform focusing channel. In this model, moments of the Vlasov equation are used to derive equations containing macroscopic quantities (flow velocity, pressure and heat tensors); the equations are simplified under the assumptions of zero heat flow, a diagonal pressure tensor, and a small perturbation, so the linearized equations for the perturbed macroscopic quantities can be employed to find dispersion relations and eigenfunctions. Lund and Davidson conclude that the high frequency branch of Gluckstern modes must represent universal behavior in beams, beyond the K-V beam model. Furthermore, Lund and Davidson show how a small, but otherwise arbitrary, radial perturbation in beam density or potential can be written as a

superposition of axially symmetric (m=0) Gluckstern modes. This has potential applications for the study of actual beam perturbations like the one discussed in Chapter VII.

An extension of Gluckstern's work to periodic solenoid and quadrupole focusing by Hofmann *et al.* [19] has revealed additional instabilities associated with resonances with the periodic focusing structure. More recent work by Hofmann [31] has considered the stability of continuous anisotropic beams, i.e. when $\sigma_{0x} \neq \sigma_{0y}$, and/or $\epsilon_x \neq \epsilon_y$, in the context of the smooth approximation; in addition to tune depression, Hofmann has found it necessary to use two additional parameters to express the results of the stability analysis: the ratio of depressed betatron frequencies, and the beam ellipticity in real space. The product of tune ratio and emittance ratio defines the degree of transverse anisotropy; instabilities are seen at tune depressions less than 0.6, with maximum growth rates for tune depressions of 0.3, approximately, and relatively high anisotropy (>5). Beams in linacs are predicted to be stable despite a combination of high degree of anisotropy (or "non-equipartitioning") and moderate space-charge.

C. Chaos:

A complementary approach to the study of beam stability is provided by the particle-core analysis and the Poincaré surface-of-section plot technique [32,33]. Using the latter, Chen and Davidson [34] have shown that unstable beam oscillations in a periodic solenoid channel develop chaotic behavior, as displayed by densely populated regions on the Poincaré plots, for sufficiently low tune depressions. Ikegami [35] has

recently extended the studies to FODO lattices and shown that global chaos exists in these channels over a wider parameter range than for the equivalent solenoid channels. These results may be very important, but the connections between chaotic behavior in beams, emittance growth and halo formation remain to be worked out in detail, not to mention the need for experimental evidence of such connections.

2.5 Emittance, Entropy and Reversibility:

A simple equation relating the Boltzmann entropy in the microcanonical ensemble form $S = k_B \ln W$ (which is equivalent to Eq. [2.5], the "information theory" version) and rms emittance was first proposed in 1973 by Lawson, Lapostolle and Gluckstern [36]. The model shows that emittance growth from phase space filamentation is consistent with entropy increase or more "disorder" in the beam. However, as pointed out more recently by Lawson [37], the connection between emittance and disorder is far from general: a simple one-dimensional K-V distribution, where the contour of a x-x' space ellipse is uniformly populated, is more ordered than a uniformly filled ellipse (i.e. a one-dimensional waterbag) and yet has four times as much rms emittance.

The situation is complicated by the fact that there is no general consensus on the statistical definition of entropy that better represents the thermodynamic or experimental entropy. Equation [2.5] is a definition of entropy based on the *single-particle* phase-space distribution function $f(q,p,t)$; a different definition, the *Gibbs entropy*, uses the multi-particle distribution function, so all interactions are implicit. Liouville's theorem in *Γ-space* (Section 2.2) shows that the Gibbs entropy is an

invariant in *any* process, in exact analogy to the constancy of Boltzmann entropy in μ-space for collisionless processes. Furthermore, according to a school in statistical mechanics founded by E.T. Jaynes [38], the second law of thermodynamics, i.e. the increase in experimental entropy, disorder and associated irreversibility in a closed system, follows from the *constancy* of the Gibbs entropy, but not from the evolution of the "incomplete" Boltzmann entropy.

Whatever the true definition of entropy is, an *operational* concept is needed in beam physics that can shed some light on the question of emittance growth and reversibility. A development in this direction, specially applicable to bunched beams, appears in a recent paper by P.G. O'Shea [39]. The entropy is explicitly defined in terms of the experimental resolution for actual measurements of phase space (the factor $\Delta\mu$ in Eq. [2.5]); this "coarse graining" of the entropy, as it is sometimes called, is actually a way in which the Boltzmann entropy can be reconciled with the thermodynamic entropy [40]. Further, O'Shea generalizes the differential equation for emittance growth obtained by Wangler *et al.* (Eq. [2.23]) to include time-dependent linear and nonlinear forces; the time dependent part is contained in an "emittance correlation coefficient" that relates overall bunch transverse emittance to bunch "slice" emittance. The two emittances are equal if the phase space evolution of any slice characterizes the entire bunch, in which case non-linear *spatial* forces are responsible for the "correlated" change; otherwise, changes in the phase space of individual slices that are correlated with their position, as may be the result of a number of stochastic processes, lead to time-dependent emittance growth. The change in emittance is called reversible if the entropy change is zero, and conversely, it is called irreversible if

entropy increases. Another important implication for interpreting some of the results of our work (Chapter VII) is that *emittance growth is not always associated with entropy increase*, i.e., irreversible processes may exist without emittance change. To see this, we consider the equation $d\langle\epsilon_{xn}\rangle^2/dz \propto -\langle x^2\rangle dF/dz$, where ϵ_{xn} is the normalized emittance, $\langle x^2\rangle$ is related to the beam size, and $F \equiv U - TS$ is a generalized free energy function [39]. At constant kinetic temperature T, an entropy increase ΔS may be offset by an opposite change in U, which includes energy changes from non-linear forces. We will briefly revisit this issue near the end of Chapter VII.

A broader, related issue, that Lawson also addresses [37], is the existence of equilibrium in beam transport. In our opinion, this matter must be approached in practical terms: different kinds of equilibria may exist in different situations. For example, for reasonably "smooth" focusing, long pulses and long enough transport times, a beam should eventually approach three-dimensional thermal equipartitioning, i.e. true thermal equilibrium (see Sec. 6.4.2 in Ref. [5]). In another situation, when a large difference exists between the two transverse kinetic temperatures in a continuous beam, stable transport (over some distance) may be possible for moderate space charge, as shown by Hofmann, without the beam ever achieving thermal equilibrium. In this latter case, a sort of "dynamical" or "force equilibrium" may still be established where external focusing compels the beam particle distribution to assume a highly anisotropic but otherwise stationary ("meta-equilibrium") state. However, in the same continuous beam model and in the presence of thermal-diffusion type of processes, a difference in transverse temperatures may entail a non-reversible constant beam degradation [41]. As a third example, unequal transverse and longitudinal temperatures in a bunched beam

with non-negligible space charge are inconsistent, as proved by N. Brown [42], with the stationary Vlasov equation; in other words, meta-equilibria cannot exist in this case, so the beam will evolve in time even in the absence of collisions.

CHAPTER III

Experimental Facility for Electron Beam Transport Experiments

3.1 Introduction

One of the most important issues to be addressed before completion of the *UMER* design is the *beam transverse dynamics* in the matching section and in the main FODO lattice. Beam transport in a FODO lattice was reviewed in Chapter I; the current Chapter presents a detailed description of the main components used in experiments with a one-meter long (approx.) focusing channel. The experiments with the one-meter channel not only represent prototype tests for *UMER* but are also important on their own, as they explore beam evolution phenomena in a number of lattices. For these studies, a long-bunch electron beam is adequate, as provided by the electron gun described in the next section. The vacuum system and associated phosphor-screen transport are the subjects of sections 3.3 and 3.6, respectively. The first focusing element in the matching section for *UMER*, a short solenoid, is described in Section 3.4. Section 3.5 describes the elements for beam-centroid corrections: steering dipoles and Helmholtz coils. Another major component is the diagnostics, which must provide reliable output to determine the beam density profile at as many points as possible along the channel. Section 3.7 summarizes the techniques employed for analyzing the captured beam images; the discussion in this Section is particularly important, as it relates to the determination of beam size data in all experiments. Finally, the rotating

coil magnetometer (Sec. 3.8) is the principal tool used for characterizing both quadrupoles and bend dipoles, whose design is discussed in Chapter IV.

3.2 Electron Gun

The electron beam source is a Pierce-type, constant perveance gun which produces pulses in the microsecond range, with energies up to about 10 keV and currents ranging from a few mA to about 300 mA. The gun, model 245C manufactured by the Hughes Company, is a scaled-down replica (2.54 cm cathode) of the SLAC PEP gun (see Figure 3.1). Following the gun, 5.7 cm from the cathode, is a 2.3 mm thick round plate with a number of apertures that can be positioned to allow passage of the full beam or fractions of it. A second aperture (6.35 mm in diameter) is located 6.7 cm from the aperture plate; it is cut out on a blank copper gasket and permits obtaining additional beam currents at a given energy. A typical cathode voltage waveform and the corresponding beam current (from a Pearson transformer, model 2100) are shown in Figure 3.2. The pulse width is about 7 microseconds, with a repetition rate of 60 Hz. It is of special importance that the pulses be synchronized with nulls of the AC voltage applied to the cathode heater. Figure 3.3 illustrates the implementation of this synchronization, important to prevent the electron beam from acquiring significant angular momentum from the magnetic field of the heater coil.

An electrostatics simulation of the electron gun can be useful to check results of measured quantities important for design calculation of transport channels. Figure 3.4 shows the results of electron trajectory calculations with the code EGUN [43], under

conditions of space-charge limited emission. The geometry includes the concave cathode, electrodes, the transport pipe and an aperture used to collimate the electron beam. The code yields a total current of 178 mA at 4.0 kV, compared with 182 mA, reported in the electron gun manual for a 7.5 V heater voltage. In the experiments, a heater voltage of 8.0 V is used, with a typical measured beam return current of 165 mA at 4.0 kV; aging of the cathode is the most likely cause of the discrepancy. The beam current after the aperture (6.35 mm, diameter) can also be obtained from EGUN data: 26 mA, approximately. The result for the beam envelope slope right after the aperture is 30 mrad.

3.3 Vacuum System

When not in use, the electron gun is isolated from the main transport pipe with an in-line gate valve. The low pressure (high 10^{-9} to low 10^{-8} Torr) is maintained by an 8 l/s ion pump located in the front end, and a 30 l/s pump on the rear. Typical pressures in the transport system (approximately one-meter long) when the gun is in operation are low 10^{-8}- mid 10^{-8} Torr. This pressure is achieved with two ion pumps, a 20 l/s and a 40 l/s, attached to ports in a six-inch-flange, 8-inch long chamber on the upstream end of the transport system. Figure 3.5 shows the vacuum chamber (without the pumps) and the phosphor-screen transport system. The main components of the transport are a 1-1/4" pipe that holds the phosphor screen, and a slide-seal feedthrough fitted with a port for differential pumping. The phosphor screen pipe is guided inside the beam transport pipe by means of a Teflon O-ring secured near the end (bottom part of Fig. 3.5). A

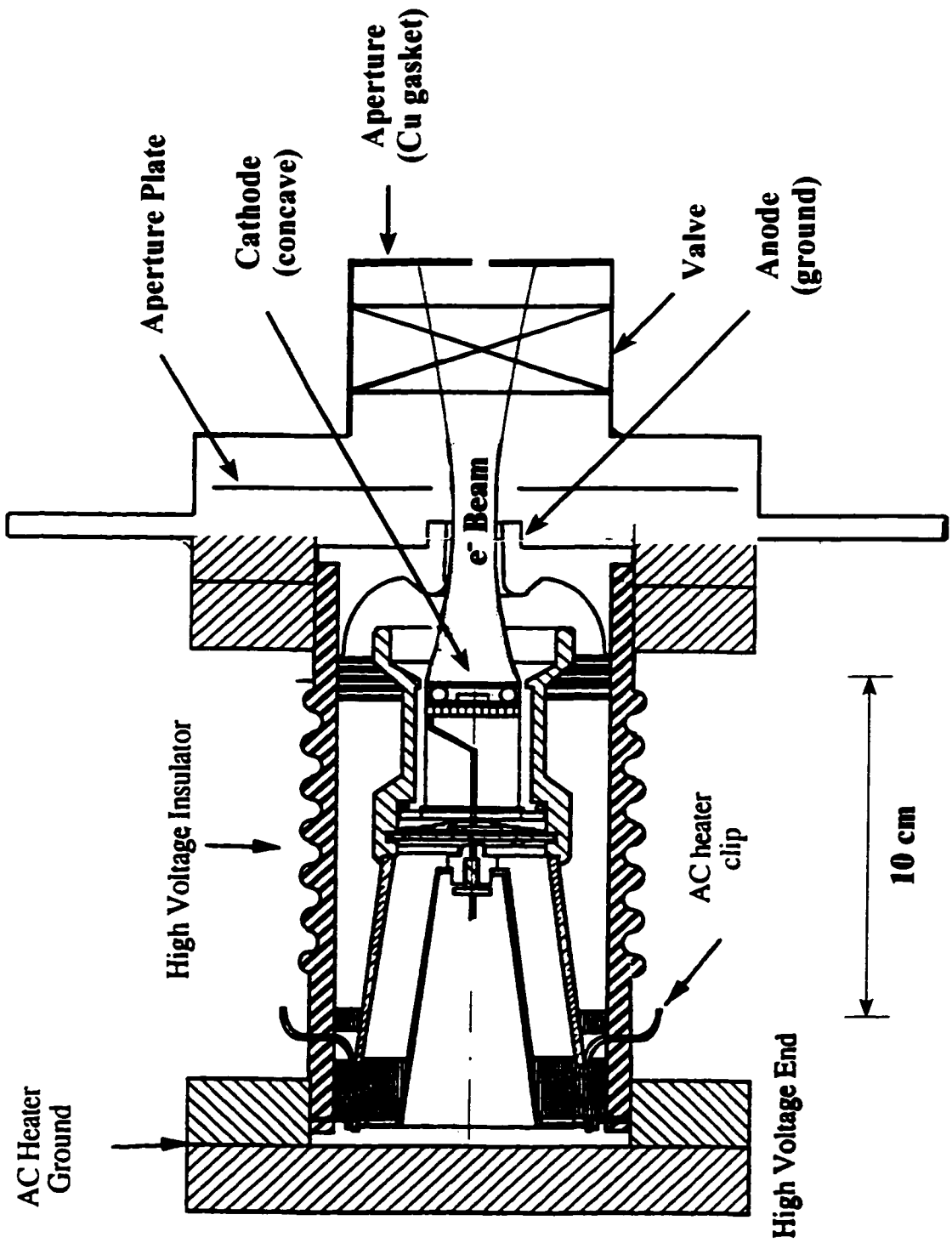

Fig. 3.1. Hughes electron gun.

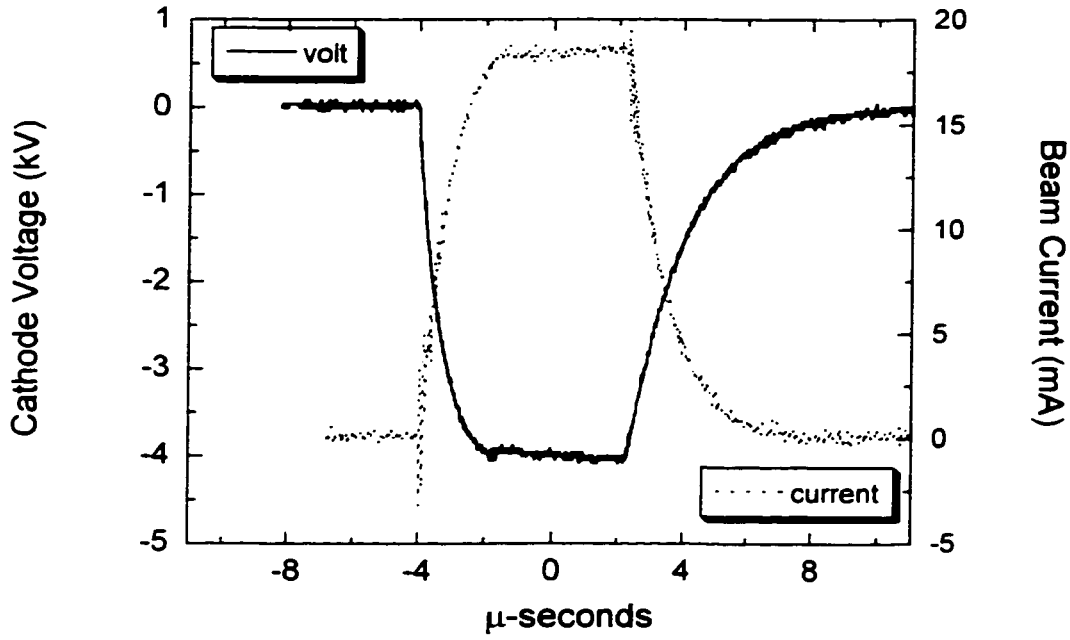

Fig. 3.2 High voltage applied to cathode as measured with HV, compensated Tektronix probe, and beam current from a 1.0 V/A Pearson transformer.

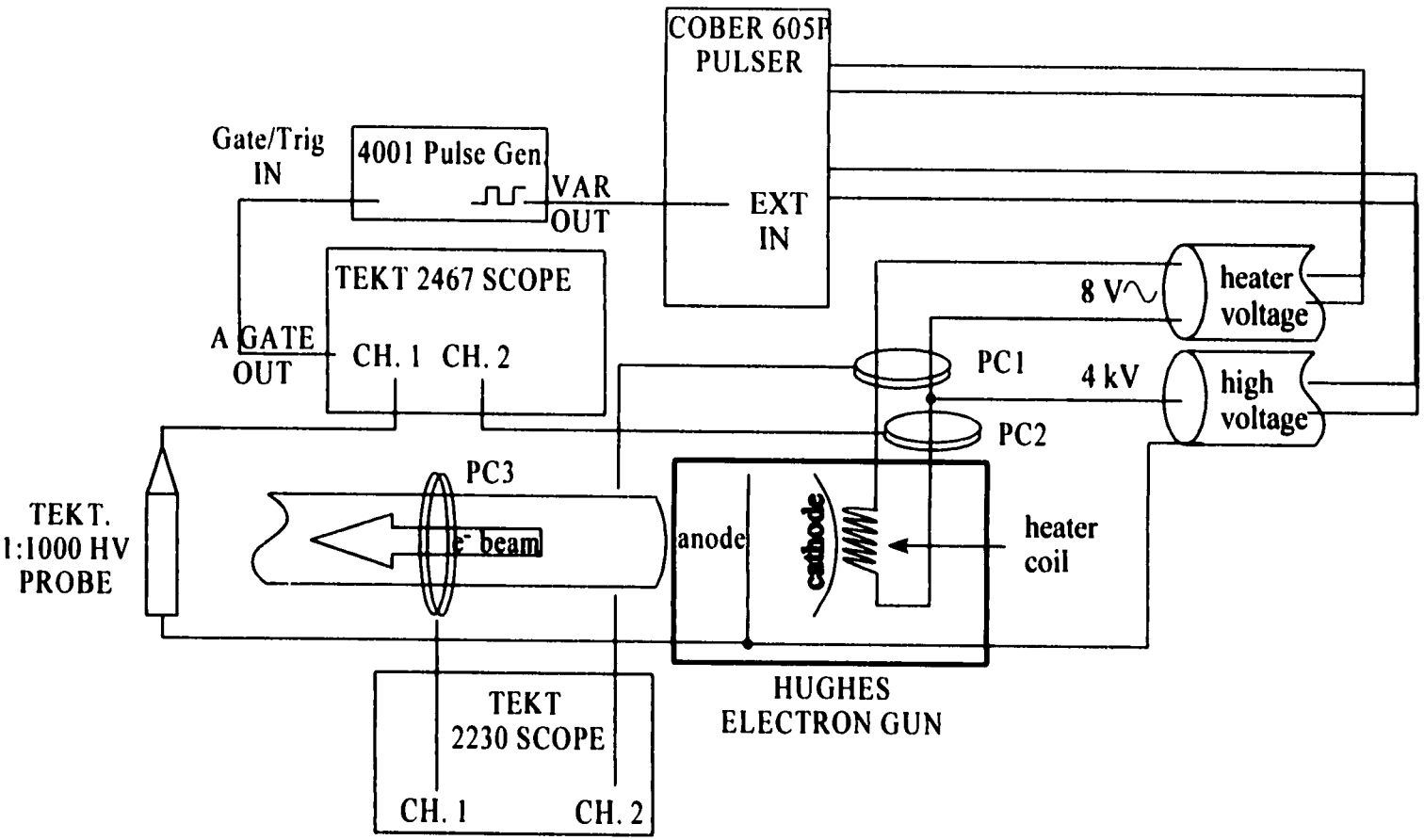

Fig. 3.3. Hughes gun setup, including synchronization of nulls of heater current with start of HV pulse. PC's represent Pearson transformers: PC1 measures the total beam return current (= output current), PC2 measures heater current, and PC3 the beam current in the transport system.

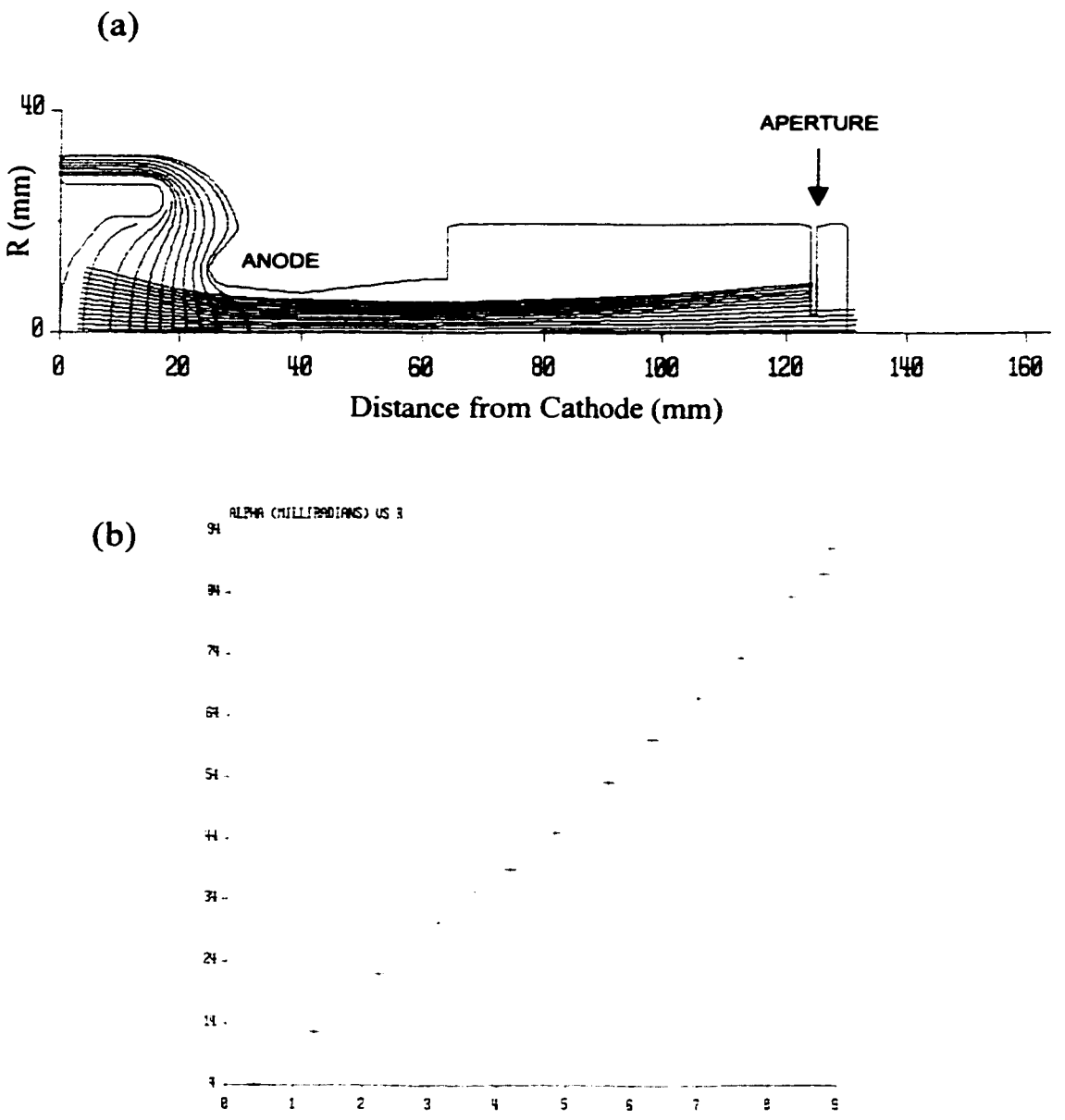

Fig. 3.4. EGUN calculations with the Hughes gun at 4 kV: (a) Trajectories of 13 rays starting at the cathode (some equipotential curves also shown), and (b) Ray slopes vs. radial distance at a plane13 cm from the cathode.

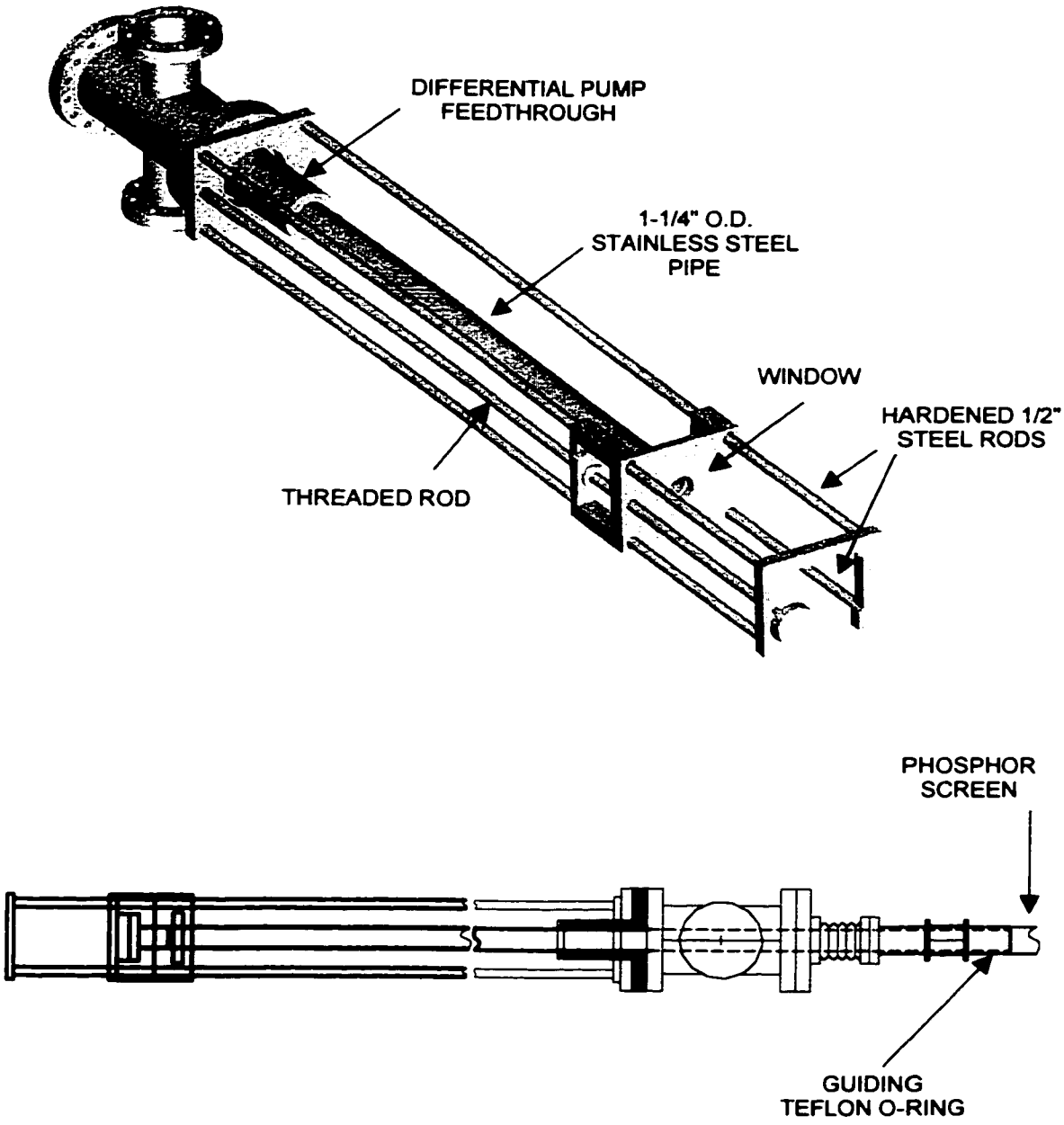

Fig. 3.5. 3D and Side views of phosphor screen transport and vacuum chamber systems.

mechanical pump is used for differential pumping while moving the phosphor screen pipe; during this latter operation, the electron gun gate valve is closed for safety.

Slight modifications of the basic setup were made for the three-solenoid experiment (Chapter VI) and subsequent experiments. A single 80 l/s ion pump, installed 80 cm under the chamber, replaced the two ion pumps around the six-inch chamber; in this way, the magnetic field from the pump magnets in the vicinity of the transport pipe was reduced to ambient field values.

3.4 Solenoid Lenses

A solenoid identical to the one intended for the electron ring injector was used in the beam matching experiments described in Chapter V. The solenoid is similar in construction to the solenoids employed in a 5 m channel used extensively for beam physics experiments at Maryland in the last 15 years (p. 484 in Ref. [5]). The main difference is the bore diameter: the solenoid used for the matching experiments has a bore of 76.0 mm, compared to 50.8 mm for the old solenoids. The schematics of the solenoid is shown in Figure 3.6. For reference, a summary of physical and magnetic parameters is given in Table 3.1.

The on-axis field profile can be represented very accurately by the function [44]

$$B_z(r=0,z) = B_0 \exp\left(-z^2/d^2\right)\left[sech(z/b) + C_0 \sinh^2(z/b)\right], \qquad (3.1)$$

where B_0 is the on-axis field on the middle plane of the solenoid, and d, b and C_0 are fit coefficients. This function allows us the direct computation of the solenoid off-axis nonlinear axial and radial field components, as given by the following expressions:

$$B_z(r,z) = B_z(0,z) - \frac{r^2}{4} B_z''(0,z) + \cdots, \tag{3.2}$$

$$B_r(r,z) = -\frac{1}{2} B_z'(0,z) r + \frac{1}{16} B_z'''(0,z) r^3 + \cdots, \tag{3.3}$$

where r is the radial distance from axis and primes indicate derivatives with respect to z. These expressions are carried out to fourth order in r for calculations with the particle-in-cell code WARP discussed in Appendix B.

The use of Equation [3.1] is preferable to a direct integration of the fields from the solenoid wires, because it is less prone to errors and, furthermore, makes possible the separation of linear and nonlinear contributions to the solenoid field. Equation [3.1] is an improvement over a simpler representation used before (p. 224 in Ref. [5]):

$$B_Z(r=0,z) = B_0 \exp\left(-z^2/d^2\right) / \left(1+z^2/b^2\right) \tag{3.4}$$

The (normalized) measured on-axis field of the solenoid is plotted in Figure 3.7, along with the two analytical fits, Eqs. [3.1] and [3.4]. Originally, $B_0 = 107.02$ G for a current of 6.00 amps. The effective length of the solenoid is equal to the integral of the normalized focusing function, κ_{SOL}; the latter is defined as (eq. (3.198) in [5]):

$$\kappa_{SOL}(z) = \left[\frac{qB_Z(r=0,z)}{2mc\beta\gamma}\right]^2. \tag{3.5}$$

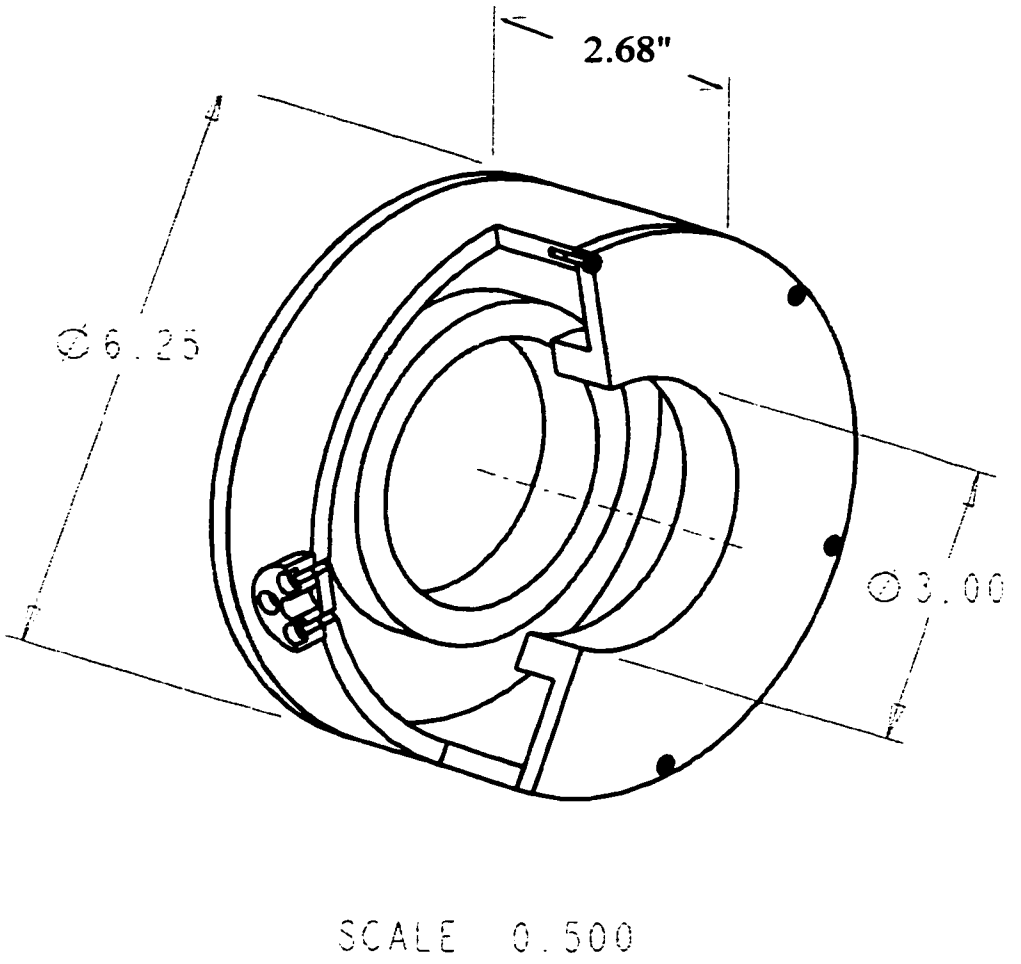

Fig. 3.6 Cutout view of housing of solenoid used in matching experiments. The material used is low-carbon steel. The magnet wire is wound on an inner aluminum spool (not shown). Dimensions are in inches.

Table 3.1: Physical and Magnetic Parameters of Main Solenoid in Matching Experiments

Bore Diameter and Length	7.6 cm, 6.8 cm
Field Profile Fit Coefficients (old formula Eq. [3.4])	d = 5.65 cm, b = 4.16 cm
Field Profile Fit Coefficients (improved formula Eq. [3.1])	d = 4.82 cm, b = 3.43 cm, C_0 = 0.017
Effective Length	4.46 cm
Peak Field per Amp	17.6 Gauss
Hysteresis	1 %

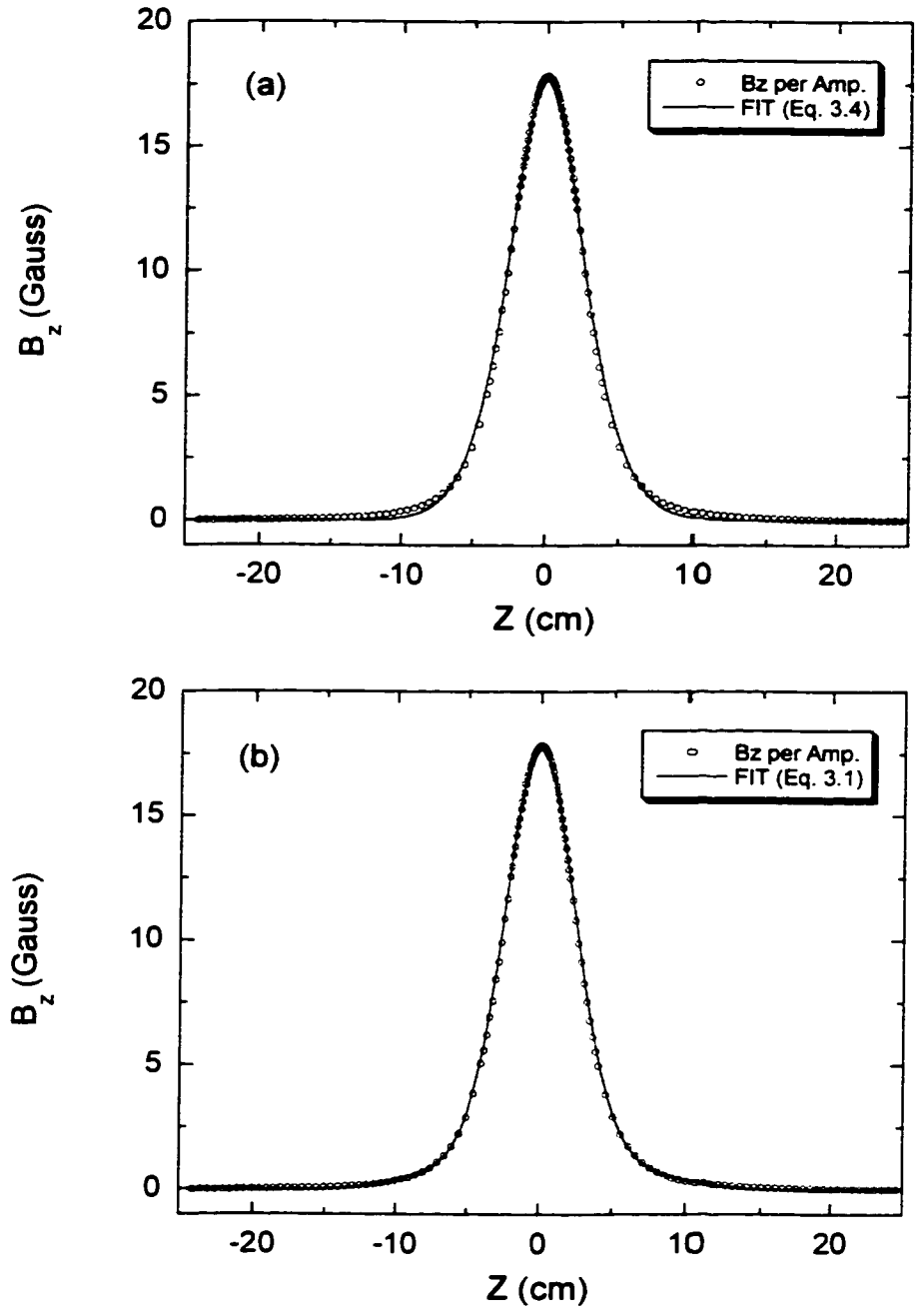

Fig. 3.7. Hall-probe measurements and fits of on-axis field profile, per amp, of wide-bore solenoid depicted in Fig. 3.6: (a) Fit based on old empirical formula, (b) Fit based on improved formula.

Direct numerical integration of the measured (normalized) axial field squared yields an effective length for the *UMER* solenoid equal to 4.46 cm. The use of Equation [3.1], on the other hand, yields an effective length of 4.50 cm. For the K-V beam envelope calculations with the code SPOT (Appendix B), the old formula in Eq. [3.4] can be used with improved coefficients d, b that yield the same effective length of 4.50 cm as the improved formula (Eq.[3.1]). It must be stressed that the exact analytical form of the field profile of a short lens is not important if a linear model is used, as long as the integrated field squared agrees with measurements [45]. Pitfalls may occur, however if a hard-edge profile is used, even with a width equal to the effective length of the smooth model, if the code does not handle the discontinuity in the profile with enough numerical accuracy. This is the case with the current (as of this writing) version of the code SPOT.

Another relevant characterization of the solenoid is the maximum on-axis field vs. current. A linear fit of data taken when the current is varied from zero to 6.5 A is B_z(Gauss)=1.35+17.6$\times I$ (A), while the fit for data taken when reducing the current from 6.5A to zero is B_z(Gauss)=2.01+17.6$\times I$ (A). These results are consistent with a quoted [46] hysteresis of about 1%, meaning that the remnant field (i.e. the field when I=0) is about 1% of the maximum field in the cycle. This hysteresis effect introduces an uncertainty in the actual field of the solenoid in the transport experiments, since once in place in the transport system, no "in site" magnetic field measurement is possible, and no attempts to demagnetize the solenoid or retrace the H vs. B curve were tried.

3.5 Elements for Beam Centroid Corrections

3.5.1 Steering Dipoles:

To aid in beam alignment, printed-circuit dipoles (D. Kehne's design) are used after the gasket aperture and between quadrupoles in the matching experiments (Chapters V and VI). The dipole effective length is 4.0 cm, and its flat top field is B_d(gauss)=3.5×current(A). Typical currents in the experiments are 50 - 380 mA, so the correction fields are of the order of the Earth's magnetic field, but over short distances, corresponding to angular displacements of around one degree, or 3 mm deflection at 12 cm from the dipole for a 4 keV electron beam. Both horizontal and vertical steering are possible with only one PC dipole by allowing rotation of its aluminum mount over the transport tube; although this procedure introduces some reproducibility problems, it is simpler and requires fewer dc power supplies. The conducting pattern of the one-layer printed-circuit is shown in Fig. 3.8 (a). The transverse field profile (measured) on the midplane (x=0=y) is shown in Figure 3.8 (b).

3.5.2 Helmholtz Coils:

Also important for beam alignment are a set of one-meter square Helmholtz coils (HC) introduced in most of the experiments to balance the vertical component of the Earth's field. The coils are 10-turn each, use gauge 22 magnet wire and require currents around 2.0 A. The square coils are 50 cm apart, to give a fairly uniform field configuration near the middle plane as in the more common circular HC. The effective length of the HC is 78.2 cm, and the flat top field is B_{HC}(gauss)=0.17×current(A).

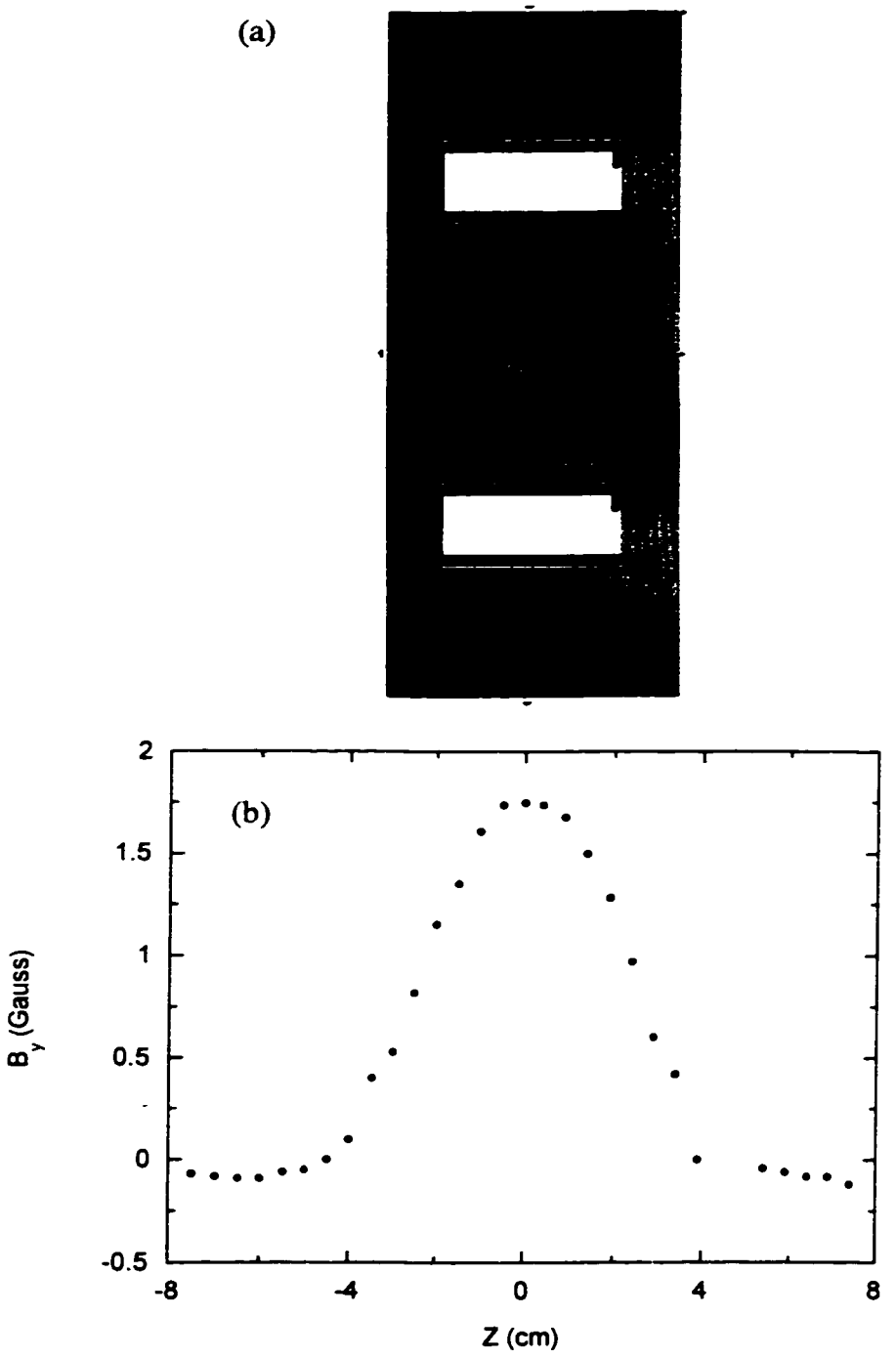

Fig. 3.8. (a) One-layer printed-circuit steering dipole (D. Kehne's design), and (b) Measured transverse field profile in the midplane for I=0.5 A.

Although no special provision is used for balancing the (smaller) horizontal component of the Earth's field, the steering PC dipoles produce sufficient compensation in the transport experiments. The transverse field profile (calculated) on the midplane of the HC, along the transport pipe (x=0=y) is shown in Figure 3.9.

3.6 Beam Diagnostics

The main beam diagnostics is a 2.54 cm (diameter) fluorescent screen manufactured by CRT Corporation, Van Nuys, CA. It is made with phosphor designated P43, whose peak emission is around 550 nm, i.e. "green", close to the peak sensitivity of the charge-coupled device (CCD) sensors used in modern video cameras. The phosphor screen has an aluminum coating for improved conductivity and grounding and responds without saturation or obvious damage at the beam parameters (energy, current, pulse width and rate) used, over several months of experiments. Its main advantages are very high light output (high quantum efficiency phosphor), very low outgassing (small increase in system pressure while the electron beam is on) and long lifetime.

The CCD camera employed (Panasonic GP-MF602, monochrome) has 570 lines of horizontal resolution and a 56db signal-to-noise ratio. Its CCD sensor (1/2 inch format) is an array of 768 (horizontal) × 494 (vertical) pixels. The camera provides for internal shutter speed control and can be used with regular C-mount lenses. This latter feature permits easy control of the light input to the CCD sensor to prevent saturation, crucial for obtaining reliable beam profiles. The distance from the window to the phosphor

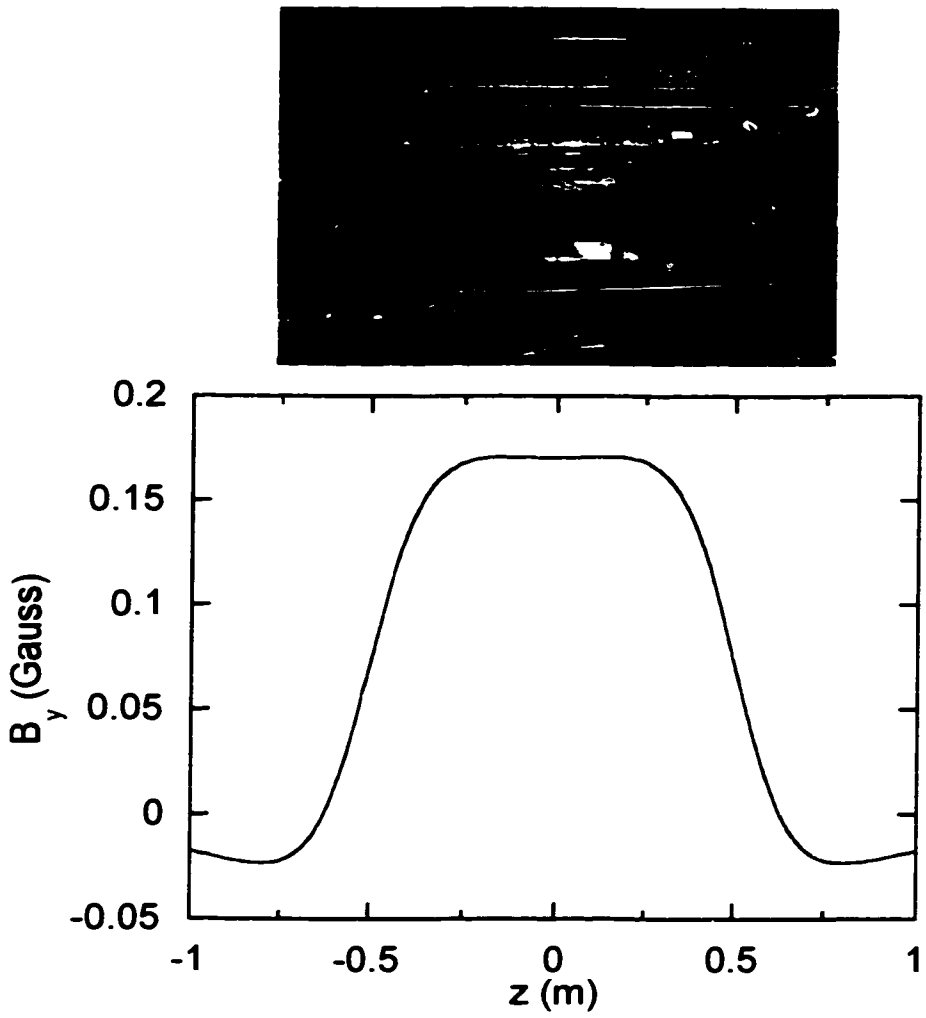

Fig. 3.9. One-meter square Helmholtz coils: photograph of setup in a matching experiment, and calculated vertical field profile per amp at the midplane, along the axis of the transport pipe.

screen is around 145 cm in most experiments, so a combination of two 2× teleconverters, Nikkon TC-201, and a normal lens (Nikkor 50 mm, f/1.8) yields a good field of view on an RCA monochrome monitor (TC1210). Although the phosphor screen is not calibrated (against a Faraday cup, for example) for obtaining accurate beam profiles, previous experience [45] with the relatively sharp-edged profiles of space-charge dominated beams has shown that the uncalibrated beam profiles are in most cases sufficient for determining the effective beam size along the channel. (Additional considerations are presented in the next Section.)

Another aspect of the beam diagnostics concerns the synchronization of the CCD camera and the beam pulses. The camera is operated in the "field integration" mode where the photodiodes accumulate the light signal over a period of 1/60 seconds. This is also the repetition period of the beam pulse, but no attempt is made to synchronize the camera integration with the electron beam, although possible in principle. The result of this lack of synchronization is that the signal to be digitized may vary from shot to shot; however, no significant differences are seen in pictures taken repeatedly under the same experimental conditions. Of course, the integration of the image digitizer, SNAPPY, would have to be considered as well for a complete understanding of the end results. SNAPPY is setup for a "moving object", meaning that the Analog-to-Digital (A/D) process has its own frame integration time to accommodate the changing light conditions. In conclusion, the combination electron-beam-pulse- phosphor-screen-CCD-camera- image-digitizer produces images that are reproducible enough to be processed for extracting accurate beam profiles. It is worth noticing, though, that an integrated image-acquisition system where the beam pulse is synchronized with the

sensor integration cycle as well as the digitizing process is advisable for future experiments with *UMER*.

3.7 Image Processing and Analysis

The analog video signal (RS-170) of the camera is digitized using a commercial device, SNAPPY (manufactured by Play Incorporated), connected to the parallel (printer) port of a Windows-based computer. The digitized pictures from SNAPPY are typically true-color (24-bit), 640×480 pixels; they are usually cropped to 300×300 or 350×350 pixels and converted to 8-bit grayscale with readily available software (e.g. PHOTOSTUDIO), and stored in a standard format like uncompressed Tagged Image File Format (TIFF). The *scale* in the pictures is easily determined from a known dimension (e.g., the inner diameter of the metal ring that covers the phosphor screen) and the corresponding number of pixels:

$$CALIBRATION: 67.5 \pm 0.5 \ \mu m/pixel. \tag{3.6}$$

At the end of an experiment run, the beam pictures are batch-processed using a convenient MATLAB program written by R.A. Kishek. The program calculates the beam centroid coordinates, the 2×rms beam size in the horizontal and vertical directions, and has options for plotting and displaying beam profiles. The beam centroid is calculated from

$$x_c = \frac{\iint x f(x,y)dxdy}{\iint f(x,y)dxdy} \cong \frac{\sum\sum xI(x,y)}{\sum\sum I(x,y)}, \tag{3.7}$$

and similarly for y_c. $I(x,y)$ is the gray-scale value of each pixel, from 0 to 255 for an 8-bit gray image, or from 0.0 to 1.0 when normalized. The effective beam size is calculated according to the following formula:

$$2x_{RMS} = 2\times\sqrt{\frac{\iint(x-x_c)^2 f(x,y)dxdy}{\iint f(x,y)dxdy}} \cong 2\times\sqrt{\frac{\sum\sum(x-x_c)^2 I(x,y)}{\sum\sum I(x,y)}}, \qquad (3.8)$$

and similarly for $2y_{RMS}$.

An important feature of the program is the use of *median filtering* for noise reduction. The filter consists of replacing the gray-scale value at the center of a specified small window (typically 7×7 pixels in our case) by the median of the gray-scale values within the window. Median filtering has the property of suppressing impulse noise, also called "salt and pepper" noise, while preserving edges. This latter feature is specially important for beam profiling. In addition to filtering random noise, an option exists for background suppression or reduction. For this, a threshold is automatically computed for each picture based on the average background light in a corner near the edge of the picture. The maximum threshold can be specified, between 0.0 and 1.0, with a default value of 0.13: any (normalized) gray-scale value smaller than the threshold is set to 0 (black).

An example of median filtering and background suppression is presented in Figure 3.10. For accurate beam size determination, background suppression is more important than smoothing of the profile, specially when the beam is relatively small and surrounded by significant background light as in Fig. 3.10. Background suppression

makes little difference only when the beam size is comparable to the phosphor screen size. In any case, it is good practice to minimize the background; for this, the aperture size (f/#) in the camera lens and possibly also the repetition rate of the beam pulse must be adjusted to prevent saturation of the phosphor screen or the CCD sensor. At the same time, enhanced sensor gain may be required, with unavoidable saturation, if special low-intensity features in the beam profile are to be studied. A simple solution that may work is to block the center part of the beam image (the apparent halo in Fig. 3.10 could be enhanced in this way).

Another issue that arises when calculating beam size is the possible effects of *beam hollowness* or other structure. This is worth considering in some detail, first because the response of the phosphor screen is not perfectly linear so the observed beam profiles are not exactly proportional to the true beam particle distributions, and secondly because saturation of the phosphor screen or the CCD sensor, or both, is sometimes unavoidable. In this latter case, the possibly hollow beam profile may be "flattened out" or distorted at the edges with implications to the calculation of beam size.

A simple model of a parabolic hollow beam profile (prob. 6.2 in Ref. [5]) can be defined by the function $f(r,\theta) = h + (1-h)(r/a_0)^2$, where $0 \le r \le a_0$, $h \le 1.0$, so a_0 defines the sharp-edge radius and h is the degree of hollowness. Then the effective beam size (2×rms) a can be calculated to be [47]:

$$a = \sqrt{\frac{2}{3}\frac{(h+2)}{(h+1)}}a_0. \tag{3.9}$$

Typically, h is around 0.8 (i.e. "20% hollowness"), so a=1.02a_0 from Eq. [3.9].

(a)

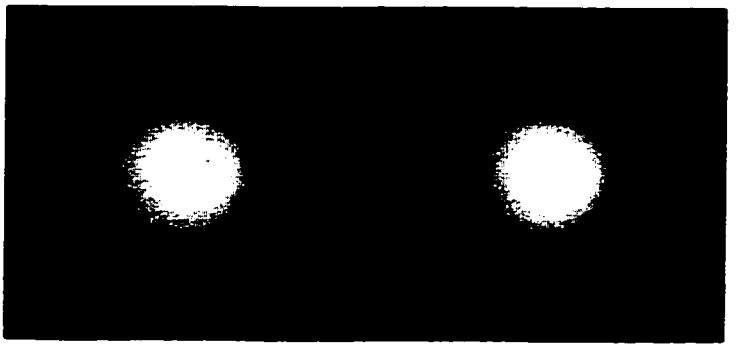

No Filter or Background Suppression

Median Filter (7×7) plus Background Suppression

(b)

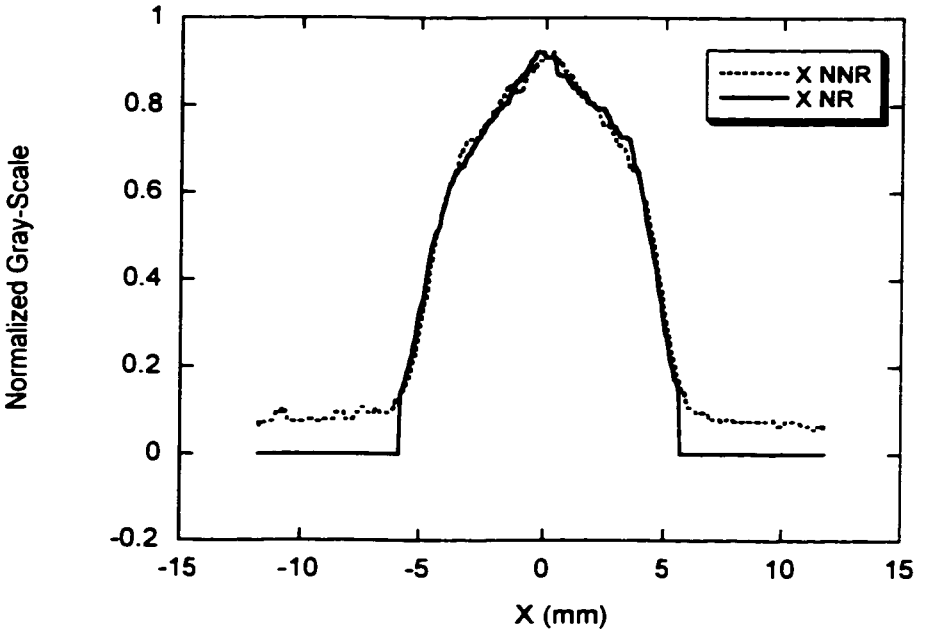

Fig. 3.10. Effects of median filtering and background suppression: (a) Beam pictures, and (b) Horizontal intensity profiles. The default maximum threshold (0.13) is used in the MATLAB program.

Figure 3.11 shows a hollow beam profile taken from Fig. 5.5 (Chapter V). The hard-edge, drawn approximately at the half-width at half-maximum points, yields a_0 =8.5 mm; the beam size computed from Eq. [3.8] and from Eq. [3.9] (with h=0.85) gives $2x_{RMS}$= a=8.8 mm, and a=8.6 mm, respectively. Of course, Eq. [3.8] implies that the entire distribution enters the beam size calculation, while Eq. [3.9] is based on a simplified model. In any case, the effect of moderate beam hollowness on beam size is of the order of 1%.

3.8 Rotating Coil Magnetometer

An accurate, widely used method of determination of the field quality of magnetic elements like quadrupoles and bend dipoles is the rotating coil [48]. It consists of a rectangular coil spinning so that one side of the coil is positioned along the axis of the magnets. The device used to characterize the quadrupoles used in this work has dimensions 1.50 cm by 12.7 cm; it is fabricated by winding 2,820 turns of very fine 44-gauge copper wire on a plastic spool. The coil is attached to a motor and spun at 6 ± 0.001 Hz. The induced voltage is then fast-Fourier transformed in a scope to get information on the harmonic content of the quadrupole-lens field. The phase of the rotation of the coil can be obtained by using a mechanical synchronous signal to trigger the scope. The Earth's field and environmental noise are carefully compensated, since otherwise they produce a dipole and possibly other spurious harmonic terms. To shield the effect of the Earth's field, a mu-metal box is employed that reduces de field to about 5 mG at the coil. An schematics of the rotating coil setup is shown in Figure 3.12. The theoretical background and results of measurements are presented in the next chapter.

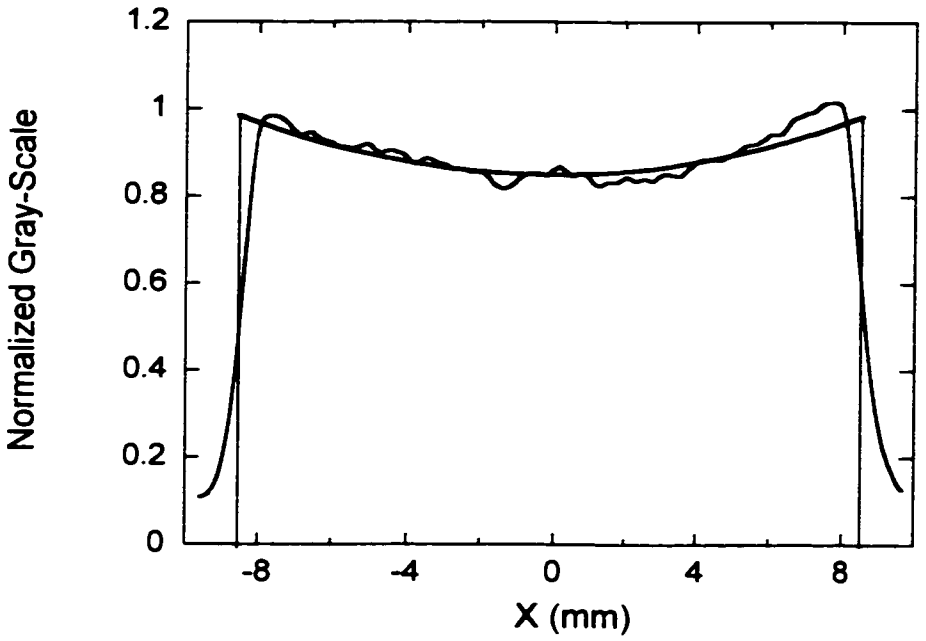

Fig. 3.11. Beam intensity profile from last phosphor screen picture in Fig. 5.4 (see also Fig. 5.5) of Chap. V, and simple parabolic model. Notice the slight saturation on the righ-hand side peak.

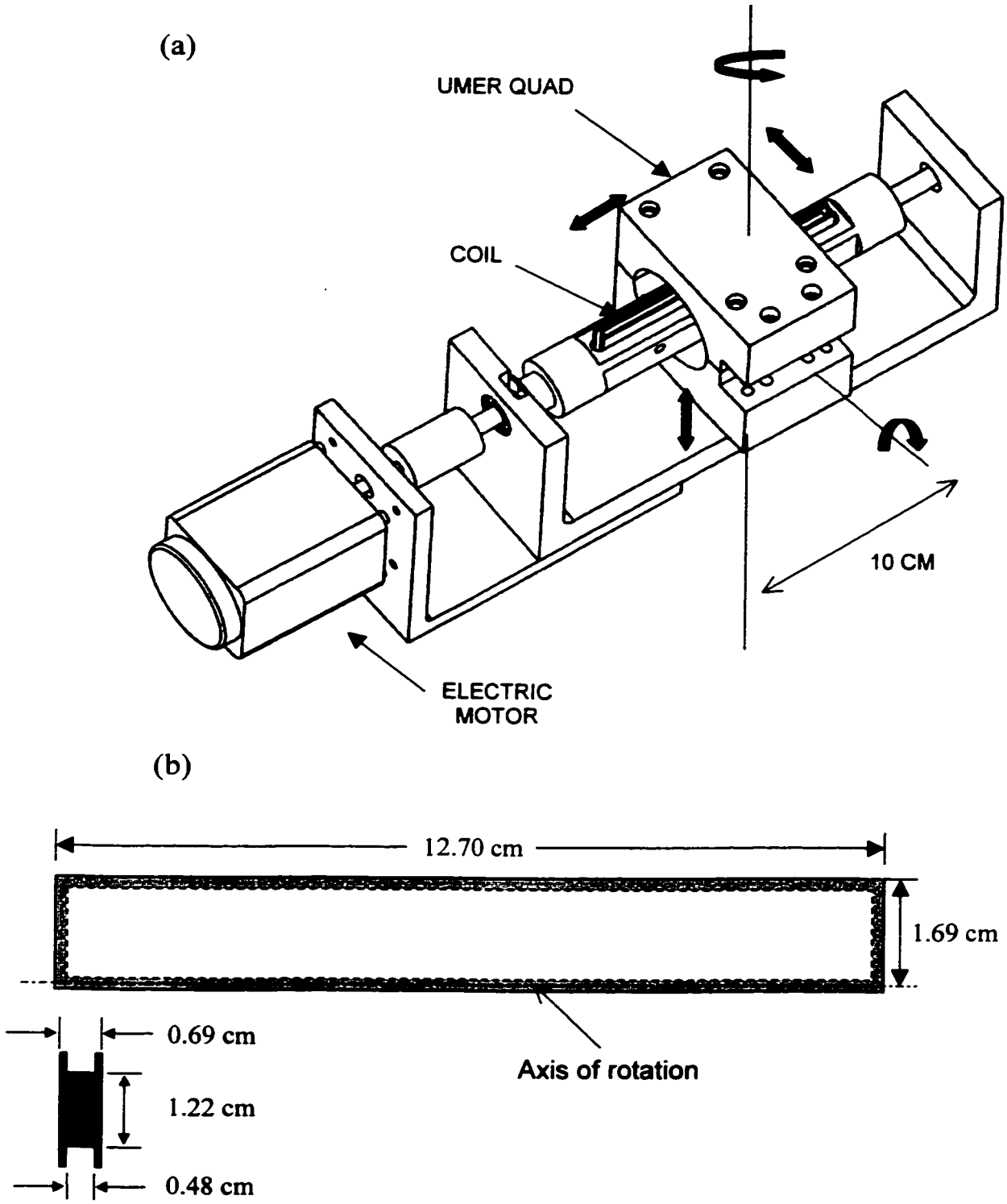

Fig. 3.12. (a) Rotating coil setup used to characterize the printed-circuit quadrupoles and dipoles. The solid arrows indicate the possible adjustments for alignment of the magnet relative to the coil. (b) Coil dimensions; 2820 turns of 44-gauge copper wire are used (about 6300 Ω).

CHAPTER IV

Design and Field Measurements of Printed-Circuit Quadrupole Lenses

4.1 Introduction

The transport of intense charged-particle beams in circular accelerators requires strong focusing. This focusing is provided in most cases by magnetostatic quadrupole lenses in a FODO geometry, as described in Chapter I. Electrostatic lenses, on the other hand, are used specially in the low-energy part of injector systems. In *UMER*, there is a special situation arising from two factors: the low, non-relativistic, beam energy, and the relatively large beam excursions, as much as 50 % of the pipe radius, expected in the space-charge dominated regime. The first factor implies that very low magnetic fields are sufficient for focusing (Eq. [3.5]), while the second means that effects from image forces, even for long bunches, must be minimized. Air-core, magnetostatic lenses of special design meet both requirements. For *UMER*, the main features of these lenses are their short aspect ratio (as demanded by stringent space requirements in the lattice), and a design based on a surface current pattern laid on a flexible printed circuit (PC). Other advantages of the magnetostatic PC design are cost and ease in manufacturing. Despite all these advantages, the short quadrupoles have raised concerns about the field quality and the implications for the beam dynamics. For this reason, a complete characterization of the field produced by the lenses is desired. To this effect, the study presented in this Chapter involves direct "point-by-point" field measurements, as well

as integrated-harmonics measurements. In both cases, comparisons with numerical and/or theoretical results are discussed.

Although the design of the short transport experiments described in latter chapters depends only on the lowest order calculations or measurements, an understanding of the higher order terms is required for realistic studies for *UMER*.

We begin this chapter with a review of the multipole expansion of the magnetic field components; this is followed by the derivation of the single-particle, third order equations of motion. The equations are cast in a form previously presented for the solenoid case. We also review the design of the PC quadrupole used in most of the prototype experiments (empirical, or small-aperture design) as well as the more formal design of the *UMER* quadrupole. To parallel the characterization of the solenoid field, an empirical function is introduced for the on-axis gradient of the quadrupoles; in this way, calculation of the lowest order non-linear field terms is simplified. Finally, we present results of direct field measurements on a scaled quadrupole, and measurements of the integrated multipole terms in the PC quadrupoles with a rotating coil magnetometer.

4.2 Multipole Expansion in a Magnetic Lens

4.2.1 Long Lens:

The cartesian components of the magnetic field can be expressed in terms of the cylindrical-coordinate components by:

$$B_x = B_r \cos\theta - B_\theta \sin\theta, \tag{4.1a}$$

$$B_y = B_r \sin\theta + B_\theta \cos\theta, \tag{4.1b}$$

with the azimuthal angle defined as in Figure 4.1. For a long magnet, it is reasonable to assume that $B_z = 0$ far from the ends, so the field is essentially two-dimensional.

For the discussion that follows, it is convenient to define a *complex cartesian* magnetic field

$$\hat{B}_{cart} \equiv B_x - iB_y = \hat{B}_{cyl} \exp[-i(\theta + \pi/2)], \tag{4.2}$$

where

$$\hat{B}_{cyl} = B_\theta + iB_r, \tag{4.3}$$

defines a *complex cylindrical* field, as can be easily verified from Eqs. [4.1].

From Laplace's equation for a potential $\Phi(r,\theta)$ in cylindrical coordinates, the magnetic field $\vec{B}_{cyl} = -\nabla\Phi$ *inside* a lens of aperture radius r_0 can be written as a generalized Fourier series:

$$\hat{B}_{cyl}(r,\theta) = \sum_{n=0}^{\infty} c_n (r/r_0)^n \exp[i(n+1)\theta], \; r < r_0. \tag{4.4}$$

In general, c_n is a complex quantity, $c_n = a_n + ib_n$. The terms associated with the coefficient a_n are called *"normal"*, so $B_{n\theta}^{norm} \propto \cos(n+1)\theta$, $B_{nr}^{norm} \propto \sin(n+1)\theta$, while those associated with b_n are called *"skew"*. To simplify the algebra, we will assume that only normal multipole components are present, so $c_n = a_n$.

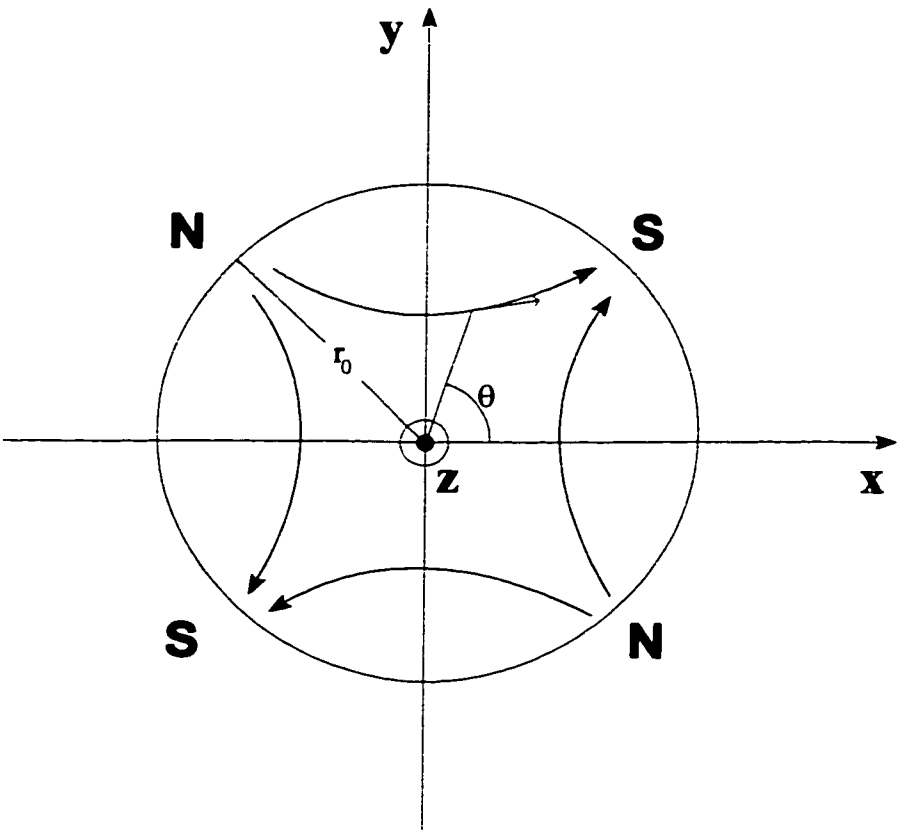

Fig. 4.1. Schematics of magnetic field geometry of a lens with quadrupole symmetry and circular cross section. The lens is focusing in the horizontal (x) direction for a positively charged particle moving in the +z direction (out of the plane of the paper).

Quadrupole symmetry requires that the magnetic field components in cylindrical coordinates change sign under a $\pm 90^0$ advance in θ (see Fig. 4.1). Therefore, from Eq. [4.4], the possible values of $n+1$ are restricted to $n+1 = 4k+2$, with $k = 0,1,2,\ldots$, so the multipole expansion can be rewritten as

$$\hat{B}_{cyl}(r,\theta) = \sum_{n=0}^{\infty} a_{4n+1} (r/r_0)^{4n+1} \exp[i(4n+2)\theta], \tag{4.5}$$

with $a_1 = gr_0$, and $g = \partial \hat{B}_{cyl} / \partial r \big|_{\substack{r=0, \\ \theta=0}}$, the *on-axis quadrupole gradient.*

The first term in Eq. [4.5], i.e. n=0, corresponds to the *quadrupole* component: linear radial dependence and exp(i2θ) angular dependence. The first higher multipole is the *duodecapole*: r^5 radial dependence, and exp(i6θ) angular dependence.

From Eq. [4.2], the cartesian components of the field with quadrupole symmetry are obtained using $\hat{B}_{cart}(r,z,\theta) = -i\sum_{n=0}^{\infty} a_{4n+1}(r/r_0)^{4n+1} \exp[i(4n+1)\theta]$, i.e.,

$$B_x(r,z,\theta) = \mathrm{Re}\{\hat{B}_{cart}\} = \sum_{n=0}^{\infty} a_{4n+1} (r/r_0)^{4n+1} \sin(4n+1)\theta, \tag{4.6a}$$

$$B_y(r,z,\theta) = -\mathrm{Im}\{\hat{B}_{cart}\} = \sum_{n=0}^{\infty} a_{4n+1} (r/r_0)^{4n+1} \cos(4n+1)\theta. \tag{4.6b}$$

4.2.2 Short Lens:

Equations [4.4] or [4.5] represent a 2D field. In a real lens, however, the magnetic field must be treated as 3D near the ends. There, additional "pseudo" multipoles are present that depend on the derivatives of the on-axis quadrupole gradient $g(r=0,z) \equiv g(z)$. In a short lens, i.e. one whose aperture is comparable to its length, as in the

quadrupole lenses used for this work, the pseudo multipoles may be the dominant nonlinearities. To third order we have [p. 48 in Ref. 49],

$$B_x(x,y,z) = y\left[g(z) - \frac{1}{12}\left(3x^2 + y^2\right)g''(z)\right], \tag{4.7a}$$

$$B_y(x,y,z) = x\left[g(z) - \frac{1}{12}\left(3y^2 + x^2\right)g''(z)\right], \tag{4.7b}$$

$$B_z(x,y,z) = xy\left[g'(z) - \frac{1}{12}\left(x^2 + y^2\right)g'''(z)\right], \tag{4.7c}$$

with $g'(z) \equiv dg/dz$, etc.

The cubic terms above introduce an additional term to $\hat{B}_{cyl}$ with angular dependence exp(i2θ), but r^3 radial dependence. This is the so-called pseudo-octupole. Another term, not included in Eqs. [4.7], with the same angular dependence exp(i2θ) but r^5 radial dependence gives rise to the pseudo-duodecapole term.

The axial component B_z (Eq. [4.7c]) is appreciable only near the edges of the quadrupole, and off the x and y axes. However, since the lens is assumed to be symmetric about the middle plane $z = 0$, the integration of B_z between points far away from this plane, along an axis parallel to the quad axis, is zero: $\int_{-z_1}^{z_1} g'dz = g(z_1) - g(-z_1) = 0.$ For the same reason, the pseudo-octupole and pseudo-duodecapole terms integrate to zero. Therefore, the field of a short lens is two-dimensional, as is the case for a long lens, but in an *axially-integrated* sense. Consequently, the first correction to the integrated quadrupole field is a fifth-order term.

Despite the vanishing, upon axial integration, of terms involving the derivatives of the quadrupole gradient, it does not follow that these terms do not contribute to the beam dynamics. Therefore, to parallel Loschialpo et al. [50], we consider the single-particle equations of motion that include the third-order terms.

4.2.3 Single-Particle Equations of Motion to Third Order:

In cartesian coordinates we have:

$$\ddot{x}=\frac{q}{\gamma m}\left(E_x+\dot{y}B_z-\dot{z}B_y\right), \tag{4.8a}$$

$$\ddot{y}=\frac{q}{\gamma m}\left(E_y+z\dot{B}_x-\dot{x}B_z\right), \tag{4.8b}$$

$$\ddot{z}=\frac{q}{\gamma m}\left(E_z+xB_y-\dot{y}B_x\right). \tag{4.8c}$$

Neglecting the effects of self magnetic fields (nonrelativistic case), we obtain to third order, after substituting Eqs. [4.7] (a)-(c) in Eqs. [4.8] (a)-(c),

$$x''=-\kappa x\left[1-\frac{1}{12}\frac{g''}{g}\left(x^2+3y^2\right)+\frac{1}{2}\left(y'^2+3x'^2\right)-yy'\frac{g'}{g}\right]+\kappa yy'x'+\frac{e}{\gamma m\beta_z^{\,2}c^2}E_x \tag{4.9a}$$

$$y''=\kappa y\left[1-\frac{1}{12}\frac{g''}{g}\left(y^2+3x^2\right)+\frac{1}{2}\left(x'^2+3y'^2\right)-xx'\frac{g'}{g}\right]-\kappa xy'x'+\frac{e}{\gamma m\beta_z^{\,2}c^2}E_y \tag{4.9b}$$

Above, E_x, E_y are the transverse electric self-fields (no field in the axial direction is assumed). The lens focusing strength is given by:

$$\kappa(z)=\frac{e}{\gamma m\upsilon}g(z), \tag{4.10}$$

defined as the *focusing* strength in the x-direction, or *defocusing* strength in the y-direction.

Equations [4.9] (a) and [4.9] (b) are put in a form reminiscent of equations derived by P. Loschialpo for the solenoid case [50]. The first nonlinear term, proportional to g'', is analogous to the spherical aberration term in the solenoid; as in the solenoid, the third order aberration coefficients in a quadrupole are defined in terms of the initial conditions of a particular trajectory, and depend, naturally, on the lens geometry through $g(z)$ [$B_z(r=0,z)$ for the solenoid] and its derivatives [51]. However, solenoid focusing, unlike quadrupole focusing, is essentially a fringe-field effect making solenoids inherently more nonlinear than quadrupoles.

The lens nonlinearities of the *UMER* focusing and bending elements are treated in detail by M. Venturini [7]. The dynamical aperture, i.e. the phase-space area of *stable* orbits, of *UMER* is calculated in the modern framework of Lie Algebra methods. Here we concentrate on the design and field measurement issues associated with the printed-circuit quadupoles. An empirical form of $g(z)$ will be sufficient for characterizing the quadrupoles for the calculations and studies in the short transport experiments of this work, but we will revisit the use of the function $g(z)$ and its derivatives in Section 4.5.

4.3 Empirical Design (Small Aperture -SA- Quadrupole)

The radial and azimuthal field components of a pure quadrupole are:

$$B_r(r,z,\theta)=gr\ sin(2\theta),\quad B_\theta(r,z,\theta)=gr\ cos(2\theta). \tag{4.11}$$

The infinitely long quadrupole field, i.e. where g = constant, can be produced with a surface current density given by

$$\vec{K} = -gr_0 \cos 2\theta \ \hat{z}, \tag{4.12}$$

over a cylindrical surface of radius r_0 , as can be easily proved by invoking the boundary conditions across the cylinder, and using Equations [4.11]. Similarly, a pure dipole field H_o in the x or y directions can be generated with a surface current density equal to $K=H_o sin\theta$, or $K=-H_o cos\theta$, along the z-axis.

Although the "cos2θ" current density distribution is in most cases a good approximation for long quadrupoles, the realization of an acceptable quadrupole field when the aspect ratio (length : diameter) is close to 1 or smaller requires that the current distribution deviates substantially from Eq. [4.12]. This is so mostly because conductors of varying lengths over a wide range have to be used for an efficient design (see Figures 4.2 and 4.4).

The design of the "first generation" quadrupole lens uses 20 straight (or "active") conductors per octant on a cylindrical surface, with angular placement following an empirical algorithm developed by T. Godlove [52] :

$$\theta_{n+1} - \theta_n = \Delta\theta / \left(1 + \theta_n^2 / k\right), \tag{4.13}$$

where n = 1..19. The adjustable parameters are the location of the first conductor $\theta_1 \equiv \Delta\theta/2$, the constant k, and the spacing between return conductors (arcs). The criterion for optimizing the parameters is that the integrated transverse field be as close as possible to a linear function of the radial distance from the quad axis. For a short

quadrupole of aspect ratio 1:1, i.e. radius = length/2, and spacing between return conductors equal to 0.023×length, and θ_1=1.17°, it is found that k=3.0 yields a deviation of the axially integrated field, from the value obtained if perfect linearity is assumed, of only 0.6 % at 70 % of the quadrupole radius. The conductor geometry of one-half printed-circuit quadrupole is shown in Figure 4.2. The radial variation of the axially integrated field (per amp) and the on-axis gradient (per-amp) are shown in Figures 4.3 (a) and (b), respectively. The calculations in Figs. 4.3 are based on a rectangular-loop geometry implemented in the iron-free magnetics code MAG-PC. Comparisons of actual field measurements on a prototype quadrupole with calculations are presented in Section 4.5.

4.4 Formal Design (*UMER* Quadrupole)

A new PC quadrupole and dipoles for bending and steering were designed based on the ideas introduced by Avery *et. al.* [53] for the design of PC steering coils. Since M. Venturini has reviewed these ideas in great detail and presented additional insights [7], we present here only a summary of results.

The basic idea behind the design of PC lenses is that the integrated transverse field of a *continuous* and *finite* current distribution on a given surface depends only on the *axial* (i.e. "z") component of the surface current density (units of A/m). If a vector $\vec{S}$ is defined whose components are the axially-integrated transverse (i.e. x and y) components of the magnetic field, i.e.,

$$\vec{S} = \int_{-\infty}^{\infty} \vec{B}_{\perp} dz \,, \tag{4.14}$$

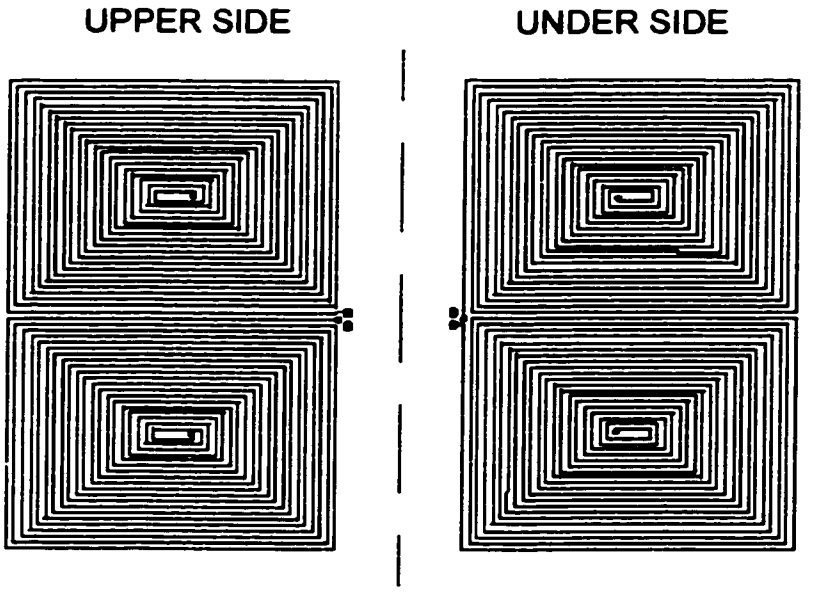

Figure 4.2. Double-sided printed circuit quadrupole (empirical design). One-half (0 to 180^0) of the circuit is shown. The other half is identical. The external twisted pair is connected to the two largest spots. The physical parameters are given in Table 4.1 (the scale of the illustration is close to 1:1).

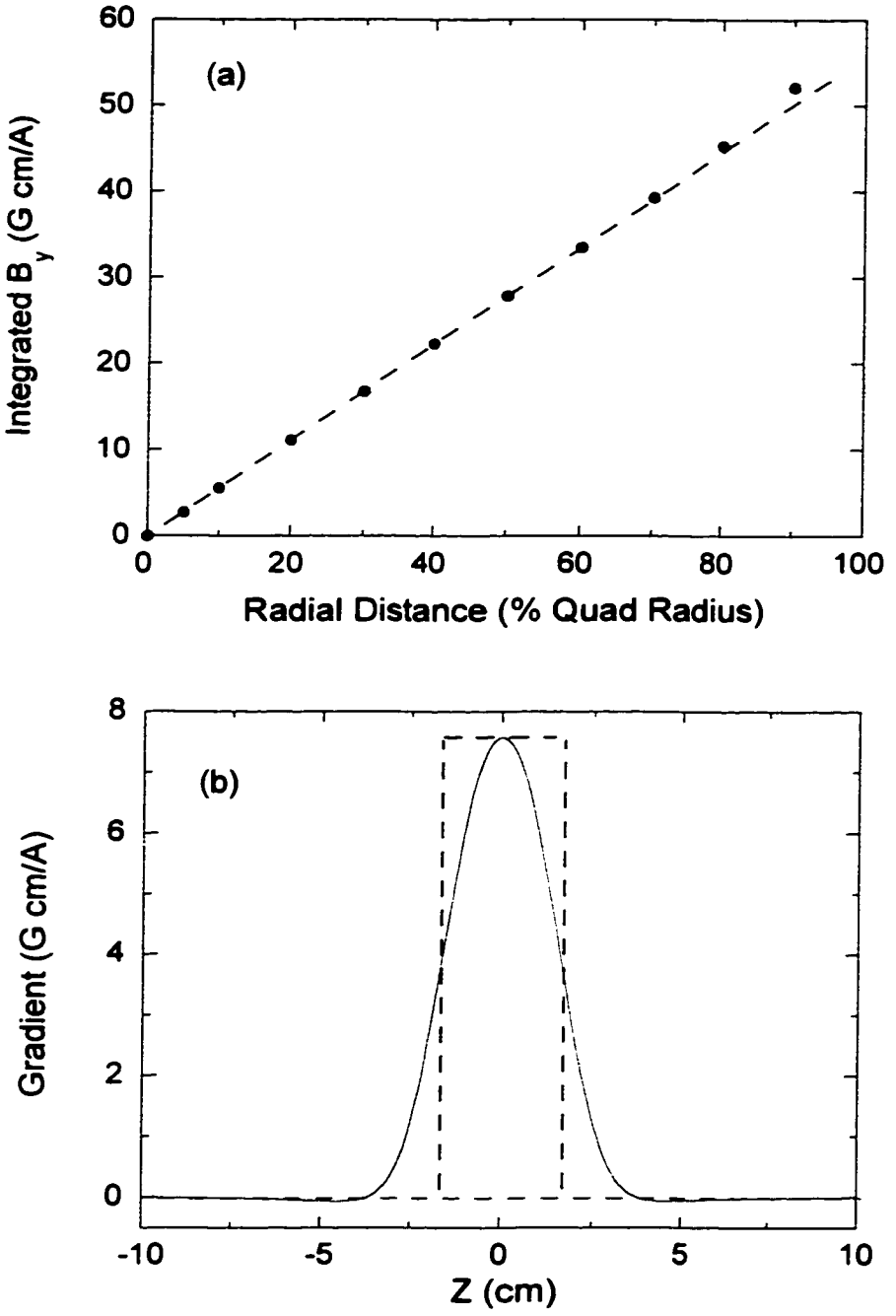

Fig. 4.3. Small-Aperture PC Quadrupole: (a) Radial variation of axially integrated field (per amp) at 0 deg. (x-axis), and (b) On-axis gradient (per amp). The dashed lines in (b) represent the hard-top model.

then it can be easily shown that the source of this vector field is the integrated axial component of the surface current density. In the absence of magnetic materials we have:

$$\vec{\nabla}_{\perp} \cdot \vec{S} = 0, \quad \vec{\nabla}_{\perp} \times \vec{S} = \mu_0 \int_{-\infty}^{\infty} K_z dz \, \hat{z}. \tag{4.15}$$

Thus, the problem of finding the integrated field inside the surface is a two dimensional problem. A "vector" potential F can be defined so that $\vec{S} = -(\partial/\partial y, \partial/\partial x)F$, and

$$\nabla_{\perp}^2 F = -\mu_0 \int_{-\infty}^{\infty} K_z dz. \tag{4.16}$$

We are interested in the current distribution over a cylindrical surface that results in an axially-integrated transverse field $\vec{S}$ in the form of a multipole field and having maximum strength. One possible way to accomplish this is to let the *axial* current density vary with azimuth angle in some way, while the current density in the *azimuthal* direction is constant. This is the same basic geometry of the empirical approach described above; however, an analytical solution is possible that yields an improved design. As in the empirical design, the current distribution is realized with straight conductors parallel to the lens axis, and return conductors or arcs equally spaced along z.

The axial surface current distribution in a cylindrical surface of radius r_0 and length l must be such that [7]:

$$\int_{-l/2}^{l/2} K_z dz = \int_{-l/2}^{l/2} \frac{\partial I(\theta)}{r_0 \partial \theta} dz = I_0 \delta(r - r_0)\cos(n\theta), \tag{4.17}$$

where $I(\theta)$ is the accumulated current up to an angle θ, r is the radial coordinate, δ

represents a Dirac-delta function, and I_0 is a constant. This current distribution in combination with Eq. [4.16] leads to a potential in cylindrical coordinates equal to

$$F_n(r,\theta)=\frac{\mu_0}{2}I_{0n}r_0\left(\frac{r}{r_0}\right)^n\frac{\cos(n\theta)}{n}, \tag{4.18}$$

with I_{0n} given by:

$$I_{0n}=\frac{nl^2}{4}\frac{I}{r_0\,\Delta z}, \tag{4.19}$$

where Δz is the constant spacing of return conductors, and I is the circuit current. Above, the explicit form of I_{0n} maximizes the strength of a given multipole. Furthermore, a *discrete* model for the current distribution is used where $K_\phi(z)\Delta z \approx I$.

From Eqs. [4.18] and [4.19], the axial integration of a dipole field ($n=1$) in the y-direction is:

$$S_{1y}=\left|\frac{-\partial F_1}{\partial x}\right|=\frac{\mu_0}{8}\frac{l^2 I}{r_0\,\Delta z}, \tag{4.20}$$

Similarly, the integrated gradient of a quadrupole ($n=2$) is:

$$\frac{S_{2y}}{x}=\frac{\left|-\partial F_2/\partial x\right|}{x}=\frac{\mu_0}{4}\frac{l^2 I}{r_0^{\,2}\Delta z}. \tag{4.21}$$

The ideal *continuous* distribution of current is obtained [7] from conservation of current and Eq. [4.17]: the half-length of axial conductors, z, is related to the azimuth angle θ by

$$z(\theta)=l\left[1-\frac{2k}{n}\sin(n\theta)\right]^{1/2}, \tag{4.22}$$

where $0 \leq \theta \leq \pi/2n$, and $k \leq 1$ is an adjustable parameter, set equal to $n/2$ in obtaining Eq. [4.19]. A variation of the prescription in Eq. [4.22] is used in the design of the *UMER* quadrupoles: the half-length of the i-th axial conductor, z_i , is related to the azimuth angle θ by

$$\sin(2\theta_i) = 1 - \left(\frac{2z_i}{k'l}\right)^2 . \tag{4.23}$$

The spacing between return conductors in the *UMER* quadrupole is $\Delta z = l/(N+2)$, where $N=40$ is the number of physical conductors per quadrant (90^0). The adjustable parameter is $k'=0.976$. The conductor geometry of one-half printed-circuit quadrupole is shown in Figure 4.4. The radial variation of the axially integrated field (per amp) and the on-axis gradient (per-amp) are shown in Figures 4.5 (a) and (b), respectively.

Table 4.1 summarizes the physical parameters and field properties of the SA and *UMER* PC quadrupoles. The parameters in the last three rows are the results of MAG-PC calculations based on a rectangular-loop geometry. For comparison, use of Eq. [4.21] for the integrated gradient of the *UMER* quad yields 14.7 G/A, or about 1% smaller than the value in Table 4.1. For the empirical quad, Eq. [4.21] yields an integrated gradient of 24.3 G/A, or 4% smaller than the MAG-PC value. Of course, Eq. [4.21] can only be valid approximately for the empirically designed quadrupole. The 1% difference in the case of the *UMER* quad, on the other hand, can be explained from the small deviation of the design from the ideal prescription that maximizes the strength of the quadrupole, and the effect of a discrete geometry vs. the ideal continuous geometry.

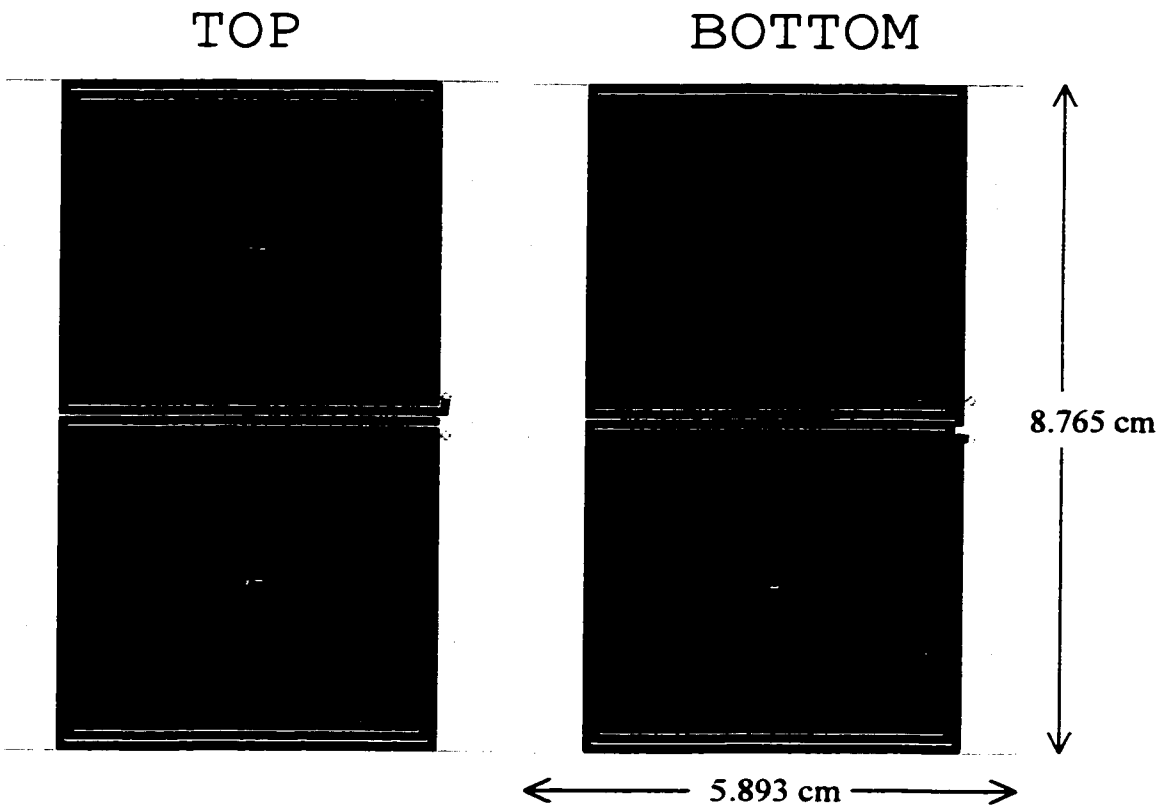

Fig. 4.4. Upper side (left) and underside (right) of the double-sided UMER printed-circuit quadrupole. The small holes near the edges, in the middle, are used for alignment pins; the bigger holes are used for attaching the circuits to an aluminum piece. More information is given in Table 4.1

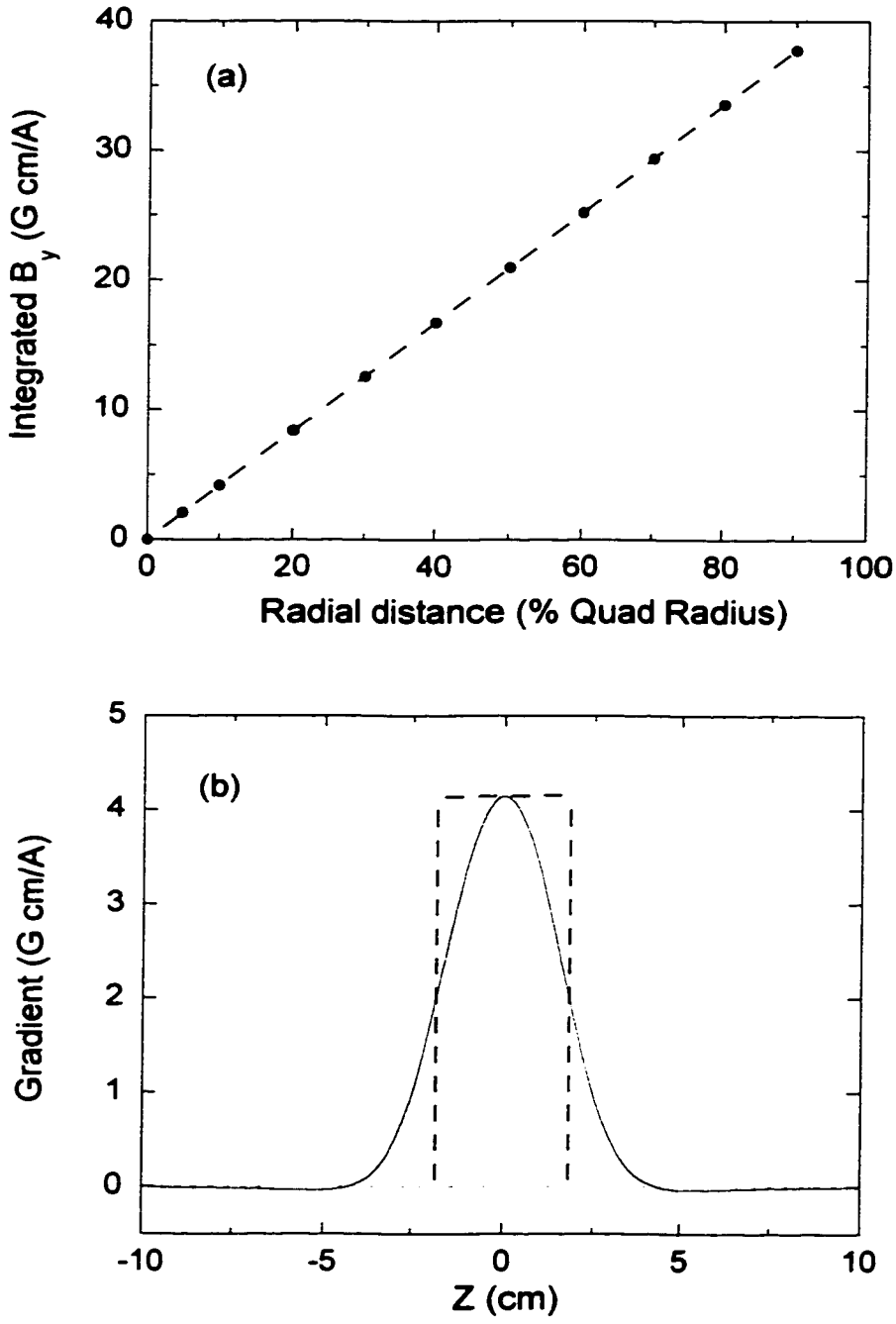

Fig. 4.5. UMER PC Quadrupole: (a) Radial variation of axially integrated field (per amp) at 0 deg. (x-axis), and (b) On-axis gradient (per amp). The dashed lines in (b) represent the hard-top model.

Table 4.1: Parameters of Old (Small-Aperture) and New Printed-Circuit Quadrupoles

	SA Quadrupole	UMER Quadrupole
Design	40 active conductors/quadrant Ref. [52]	40 active conductors/quadrant Ref. [53]
Algorithm	Equation [4.13]	Equation [4.23]
Radius and Length r_0 , l	2.2 cm; 4.4 cm	2.79 cm; 4.65 cm
Aspect Ratio (length:diameter)	1 : 1	0.833 : 1
Gradient Profile Fit Coefficients [Eq. 4.25]	d = 2.56 cm, b = 14.6 cm	d = 2.05 cm, $b = \infty$
Effective Length l_{eff}	3.35 cm	3.63 cm
On-axis Peak Gradient Per Amp: g_0	7.57 G/cm A	4.14 G/cm A
Integrated Field Gradient Per Amp: $g_0 \times l_{eff}$	25.3 G/A	14.9 G/A

From the theory in Ref. [7], a simple exact expression can be written for the integrated gradient of the PC quadrupoles in terms of the active conductor lengths l_i and the corresponding azimuth angles θ_i:

$$\int_{-\infty}^{\infty} g(z)dz = \frac{16I}{c}\frac{1}{r_0^2}\sum_{i=1}^{20} l_i \cos(2\theta_i) \tag{4.24}$$

Equation [4.24] is valid for the concentric loops model implemented in MAG-PC; the summation on the right hand side is over the conductors in the first octant. From Eq. [4.24] and the MAG-PC file, we find that the integrated gradient of the *UMER* and empirical quads are 15.0 and 25.3 G/A, respectively, closer to the values in Table 4.1 than the results in the continuous surface current density model. In the real quad, as opposed to the "MAG-PC quad" of Table 4.1, an additional contribution to the integrated gradient comes from the short (active) conductors that make possible the spiral geometry; this contribution is estimated to be around 0.1 % [7]. The presence of an underside layer introduces another contribution of the same order to the integrated gradient.

4.5 Field Measurements of a Scaled Prototype Quadrupole

A scaled model of the empirically-designed quadrupole was built to check the calculations done with the magnetics code MAG-PC, the same code employed later for the *UMER* quadrupole and dipole designs. The pattern of conductors was drawn using a CAD program, with the relevant dimensions derived from Eq. [4.13] for a lens of radius R = 12.8 cm. The conductor pattern uses magnet wire laid on a 10" ± 0.015" outer diameter, 1/4" wall, aluminum tube with a length of 27.88 ± 0.01 cm. Heavy armored,

gauge-18 magnet wire is tightly and accurately wound with the help of flat-head nylon screws inserted at the corners of each rectangle of the two-layer pattern (see Figs. 4.2 and 4.6). Hard copies of the conductor winding generated in the CAD program were taped to the aluminum tube and used as a guide in the winding. Figure 4.6 shows a photograph of the scaled quadrupole.

A Hall probe (spatial resolution = 0.5 mm, approximately) was used to make z-axis scans of the transverse field at four different radii, r/R = 0, 0.2, 0.4, 0.6, 0.8, and $\theta = 0$, 45^0, for a current of 10A ± 1 mA. The longitudinal component of the quadrupole field was also measured at $\theta = 45^0$. The vertical component of the Earth's field was balanced with large circular Helmholtz coils (radius = 50 cm, approximately), and corrections were made for the small horizontal component. Care was taken in probe positioning and zero drift of the gaussmeter. A z-axis scan at $x = 0.6R$, $y = 0$ is shown in Fig. 4.7 (a). Similarly, Fig 4.7 (b) compares results of MAG-PC calculations with measurements of the axial component of the quadrupole field at $x = 0.42R = y$. The agreement between MAG-PC calculations and measurements is excellent. Measurements indicated that the mechanical axis and the magnetic axis were coincident within about 1 mm. No evidence was found of significant differences between magnetic fields produced by the spiral geometry of Fig. 4.2 and the concentric loop geometry used in MAG-PC.

Finally, the calculated transverse field was fit to an analytical expression whose parameters are adjusted to obtain the same scaled effective length of the PC quadrupole (as obtained with MAG-PC), i.e. $L_{scaled} = l_{eff} \times (R/r_0) = 19.49$ cm, with the notation and values of Table 4.1. The expression is:

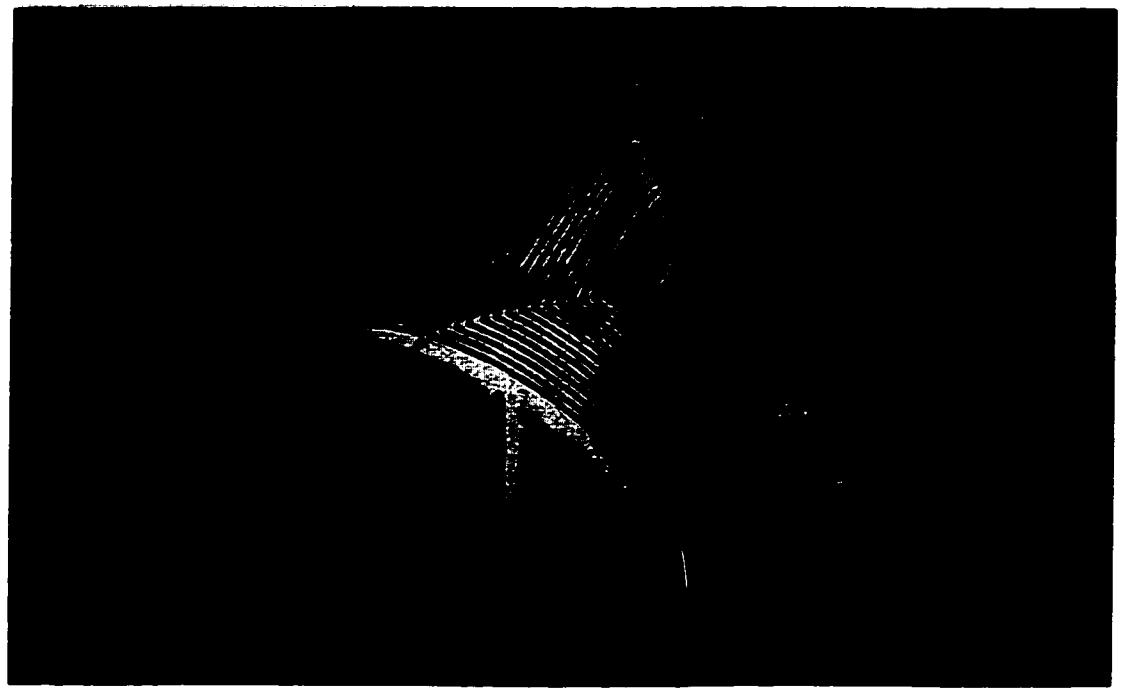

Fig. 4.6. Photograph of 25.6 cm diameter prototype quadrupole. One coil of the Helmholtz set and the Hall-probe setup can be seen in the picture.

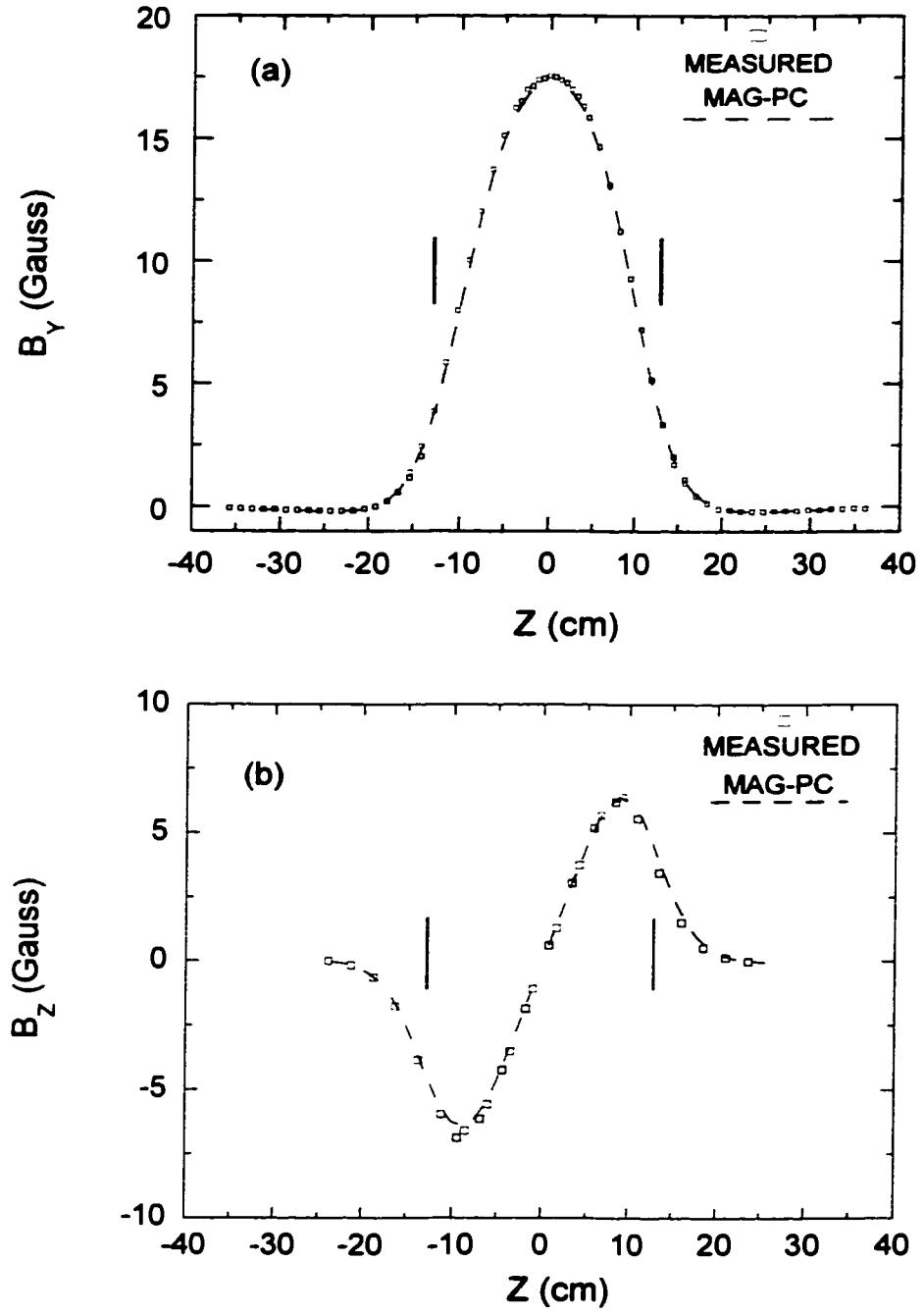

Fig. 4.7. Hall-probe measurements of transverse, (a) , and axial, (b), field components of scaled quadrupole at r=0.6R, θ=0, 45 deg. vs. calculations with MAG-PC. The quadrupole current is 10 A.

$$B_y(z) = xg(z) = x\, g_{0scaled}\, Exp\left(-z^2/d^2\right)\cos(2\pi z/b), \tag{4.25}$$

with $g_{0scaled} = g_0(10A/1A)(r_0/R)^2 = 2.24$ G/cm, and fit parameters $d = 14.7$ cm, and $b = 85.7$ cm. In the present case, $x = 0.6 \times R = 7.68$ cm.

In Figure 4.8, the measured transverse field component of the prototype quadrupole is compared with the linear field obtained from Eq. [4.25]; also, the longitudinal field is compared with the nonlinear field obtained using Eq. [4.7] (c). The derivatives of *g(z)* are obtained analytically from Eq. [4.25].

Equation [4.25] was implemented by C. K. Allen in the KV envelope code SPOT used for matching calculations (see Chap. V and App. B). The parameters *d, b* can be specified for the particular PC quad design, in a way similar to the use of Eq. [3.4] for the magnetic field profile of a solenoid. Table 4.1 includes the fit coefficients for both the SA and the new PC quadrupoles. As for the scaled quadrupole, the values of the fit coefficients are adjusted so the areas under the analytical and MAG-PC curves for the gradient profiles are the same.

To conclude this Section, a comparison is made between the two PC quadrupole designs described in this Chapter. Figures 4.9 (a) and 4.9 (b) present the analytical profiles of the on-axis gradients of the PC quadrupoles vs. calculations with MAG-PC; the analytical profiles follow Eq. [4.25] with the coefficients of Table 4.1. From the plots, it is seen that the empirical quadrupole has tails that intrude into the negative side more than in the *UMER* quadrupole; this justifies the presence of the cosine term in Eq. [4.25], and the infinite value given to *b* for the *UMER* lens (Table 4.1).

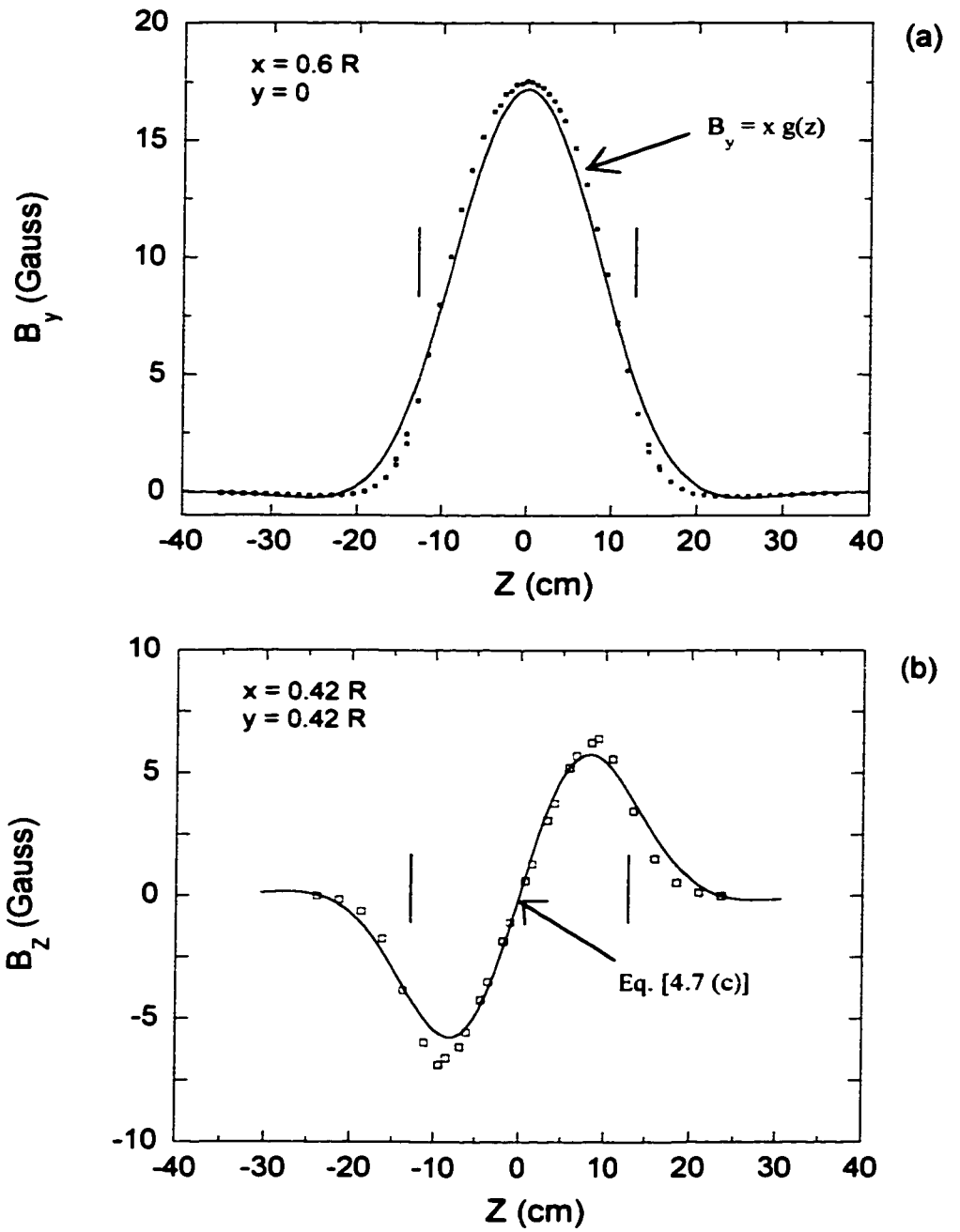

Fig. 4.8. (a) Measured transverse field in scaled quadrupole vs. linear fit B_y=xg(z) from Eq. [4.25], and (b) measured longitudinal field vs. nonlinear fit B_z=xy[g'(z)-(1/12)(x^2+y^2)g'''(z)].

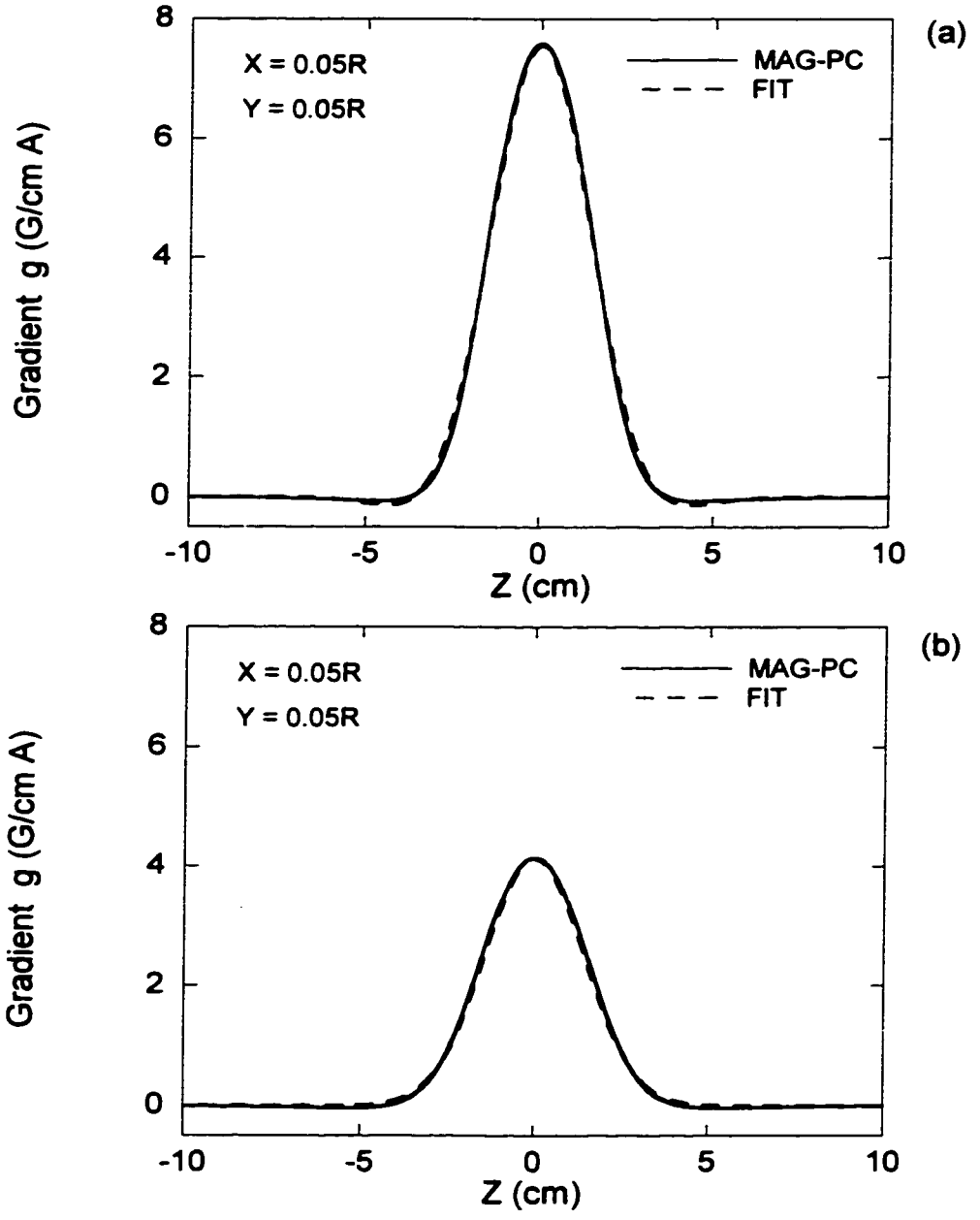

Fig. 4.9. (a) Calculated gradient profile of empirical PC quadrupole, and fit from Eq. [4.25] with coefficients from Table 4.1, and (b) results for UMER quad.

From Eqs. [4.9] (a)-(b), the first nonlinear contribution to the particle's equations of motion involves a cubic term in the cartesian coordinates with coefficient proportional to $g''(z)$. Since the numerical second derivative involves differences of small numbers near the points where the first derivative vanishes, i.e. at z=0 and at the minima on the tails of the profile (see Fig. 4.9), considerable error is expected at those points. Because of this latter fact, the analytical form of $g(z)$ is preferred for computation of the third order contribution to the transverse field components, or the longitudinal component. It should be emphasized, however, that this approach is an approximation that can only provide an insight of the importance of the lowest-order nonlinearities. A rigorous treatment that includes applications to the scaled quadrupole (prototype quad of Fig. 4.6) of this work and other quadrupoles can be found in References [7] and [54].

Figures 4.10 (a) and (b) show a comparison of the normalized gradients, $g(z)$, and second derivatives, $g''(z)$, for the two PC quadrupoles studied in this Chapter. From the figures, it is clear that, to third order at least, the two quadrupoles are not significantly different despite their different aspect ratios and design algorithms.

4.6 Integrated-Multipole Measurements of PC Quadrupoles

4.6.1 Rotating Coil Magnetometer:

A conducting rectangular loop, with dimensions, *length* = l, and *height* = fr_0 (r_0 = lens aperture radius, and $0 < f \leq 1$), rotating coaxially with a lens at an angular frequency ω, will yield an emf given by $\varepsilon = -(\partial / \partial t)\oint \vec{B} \cdot d\vec{s} = -(\partial / \partial t)\oint B_\theta ds$, where

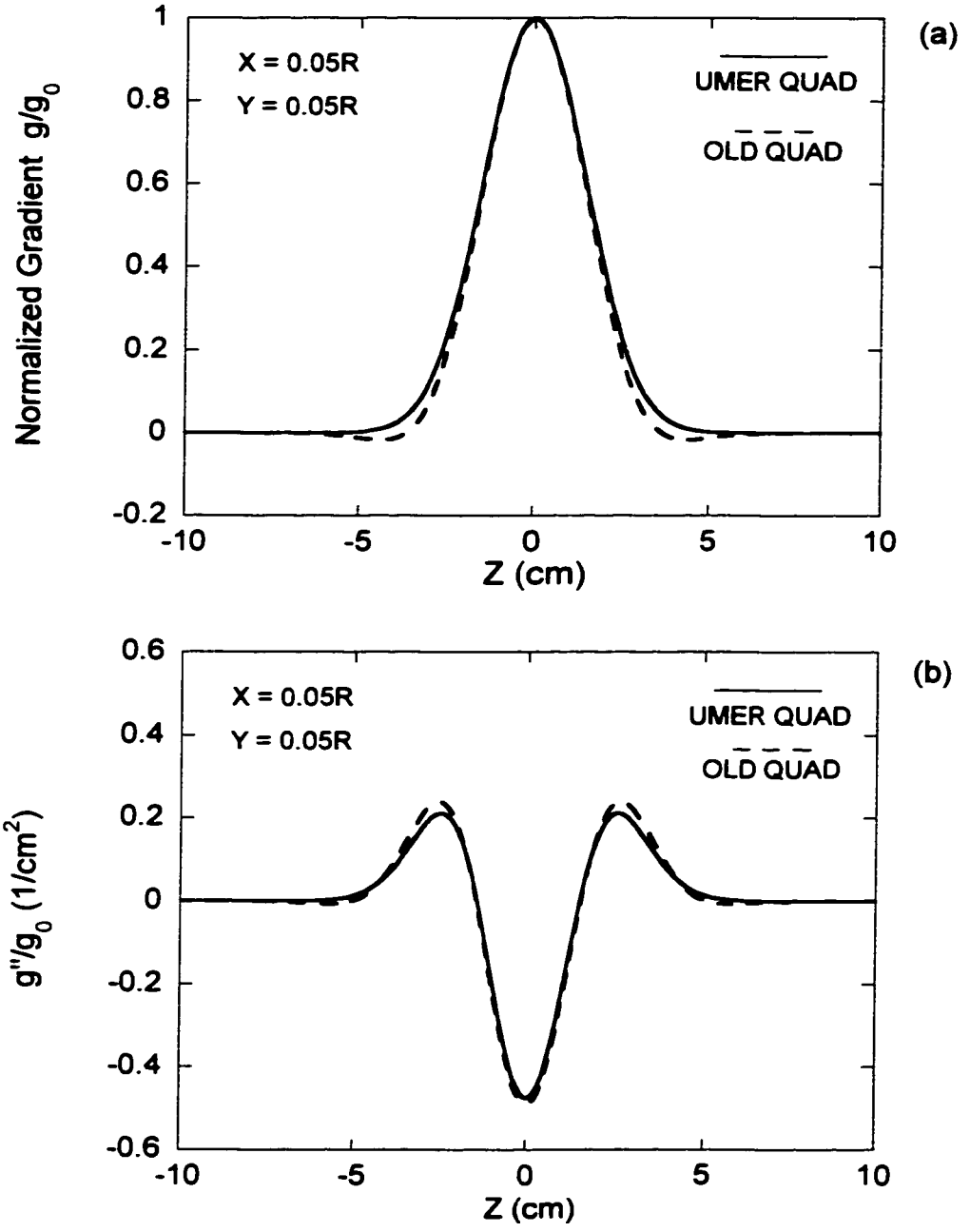

Fig. 4.10. (a) Normalized gradient profiles of SA and UMER PC quadrupoles (from Eq. [4.25] and Table 4.1), and (b) Normalized g"(z). Scans at 5% quad radius.

the integral is over the area of the loop. From Eqs. [4.3] and [4.4], and $cos(n+1)(\theta+\pi)=(-1)^{n+1}cos(n+1)\theta$, we find

$$\varepsilon(t)=\omega\int\int_0^{fr_0/2}\sum_{n=0}^{\infty}(n+1)\left[1-(-1)^{n+1}\right]a_n(r/r_0)^n\sin[(n+1)\omega t]drdz \tag{4.26}$$

Only the terms corresponding to $n+1$ = odd number (i.e. dipole, sextupole, decapole, etc) would yield a non-zero signal. To solve the problem, the rectangular probe must be used with its long side along the quadrupole axis [48], as in Fig. 3.12 (Chapter III); in this case, the induced voltage per loop is

$$\varepsilon(t)=\omega\int\int_0^{fr_0}\sum_{n=0}^{\infty}(n+1)a_n(r/r_0)^n\sin[(n+1)\omega t]drdz \tag{4.27}$$

If the lens is *short* compared to the probe's length l, as in our case, then we can define $(1/l)\int_{-l/2}^{l/2}a_n(z)dz\equiv\bar{a}_n$ and write, after carrying out the integration over r,

$$\varepsilon(t)=l\omega\sum_{n=0}^{\infty}\bar{a}_n f^{n+1}r_0\sin[(n+1)\omega t]\equiv\sum_{n=0}^{\infty}\varepsilon_n\sin[(n+1)\omega t] \tag{4.28}$$

(The factorization of the "z" and "r" dependences in Eqs. [4.5] or [4.27] is not possible in general because of the presence of the pseudo-multipoles [7], but the latter integrate out to zero, so Eq. (4.27) is valid with $\bar{a}_n$ as defined above).

From Eq. [4.28], the voltage amplitude of the $(n+1)$-multipole relative to the quadrupole term ε_1 is

$$\frac{\varepsilon_n}{\varepsilon_1}=\frac{\bar{a}_n}{\bar{a}_1}f^{n-1} \tag{4.29}$$

Since the average beam size in the prototype and future *UMER* experiments is of the order of 35% of the quadrupole half-aperture, f above should at least be equal to 0.35, if the measured integrated multipoles are to be used for realistic beam simulations. Furthermore, it is important to recall that the terms in the expansion of B_θ that depend on the derivatives of the on-axis quadrupole gradient (i.e the pseudo-octupole and pseudo-duodecapole terms) are integrated out by the rotating coil, as long as the coil "divides" the quadrupole into two equal halves along the z-axis. Therefore, the information provided by the multipole measurements must be complemented by calculations of pseudo-multipole terms.

As an example, the induced voltage associated with the quadrupole multipole is

$$\varepsilon_1(t) = f^2 l \omega \bar{a}_1 r_0 \sin(2\omega t). \tag{4.30}$$

The effective quantity $l\bar{a}_1$ can be approximated by $l\bar{a}_1 \approx a_1(z=0) l_{eff} = g r_0 l_{eff}$, where l_{eff} is the effective length of the quadrupole, and g is the on-axis gradient. A single rectangular loop in one of the coils used for the measurements has dimensions, height = 0.590" = 1.50 cm, and length = 12.7 cm (>> quad's effective length = 3.35 cm). The coil is rotated at 360 rpm with one side along the printed-circuit quadrupole axis (quad radius = r_0= 2.2 cm), so the *amplitude* of the signal induced from the quadrupole component is approximately equal to

$$\varepsilon_1 \approx (0.68)^2 (3.35\,cm)(6.28)(6)(7.57\,G/cm\,A)(2.2\,cm)^2 = 21\,\mu V/A, \tag{4.31}$$

per loop. The coil of the example has 2,820 turns, so the voltage amplitude from the quadrupole term is about 60 mV, easily measurable.

4.6.2 Multipole Content - Calculations:

An exact expression, within the concentric loops model, can be written for the voltage amplitudes measured relative to the quadrupole voltage [7]:

$$\frac{\varepsilon_m}{\varepsilon_2} = \frac{\bar{a}_m f^m}{\bar{a}_2 f^2} = f^{m-2} \frac{\sum_{i=1}^{20} l_i \cos(m\theta_i)}{\sum_{i=1}^{20} l_i \cos(2\theta_i)}. \tag{4.32}$$

where we have set $m \equiv n+1$, so $m=2$ corresponds to the quadrupole term. Equation [4.32] is used to obtain the relative signals from the rotating coil. Alternatively, a numerical calculation is possible using the magnetics code MAG-PC.

If $a_m(r)$ denotes the coefficients of the series of normal multipoles in Eq. [4.4], then

$$a_m(r) = \frac{1}{\pi} \int_0^{2\pi} B_\theta(r,\theta) \cos(m\theta) d\theta, \tag{4.33}$$

In practice, $B_{r,\theta}$ can be evaluated or measured at N discreet values $\theta_k = k\Delta\theta$, $\Delta\theta = 2\pi/N$, ($k = 0,1 \ldots N-1$), at a given z-plane and radial distance from the lens axis. Therefore, the integral above can be approximated by

$$a_m = \frac{1}{\pi} \Delta\theta \sum_{k=0}^{N-1} B_\theta(k\Delta\theta) \cos(mk\Delta\theta), \tag{4.34}$$

The summation in Eq. [4.34] corresponds, up to a factor of two, to the real part of the *Discreet Fourier Transform* (DFT) of $B_\theta(\theta_k)$, defined by $\mathrm{DFT}\{ B_\theta(\theta_k) \} = (1/N) \sum_{k=0}^{N-1} B_\theta(\theta_k) \exp(i2\pi km/N)$. Equation [4.34] can also represent the

DFT's of the *axially integrated* field if we redefine the quantities so that $a_m \rightarrow \int a_m(r,z)dz$, $B_\theta(\theta_k) \rightarrow \int B_\theta(r,z,\theta_k)dz$.

The calculations with MAG-PC proceed as follows: the azimuthal component of the B-field is calculated with 8 significant digits at 400 points along the length of the rotating coil (12.7 cm), at a radial distance from the quad axis equal to the coil's height (1.5 cm). This is done for 64 equally spaced azimuth angles starting with zero. For each angle the field is integrated numerically and the results are Fast-Fourier transformed. Table 4.2 contains the results of MAG-PC calculations and Eq. [4.32] for the lowest allowed harmonics ($m=6$ and 10) for both the empirical and *UMER* quadrupoles. Figure 4.11 displays the results of MAG-PC up to $m=24$. From the Table and Fig. 4.11, it is clear that beyond $m=10$ the accuracy of the numerical calculations is compromised.

4.6.3 Multipole Content - Measurements:

Figure 4.12 shows a photograph of the rotating coil setup with the smaller aperture quadrupole in place. (Additional information on the mechanical design can be found in Chapter III). The same coil was used for integrated-multipole analysis of both the SA and *UMER* PC quadrupoles. The analog signal from the coil was digitized and fast-Fourier analyzed in a HP- infinum digital oscilloscope. Spectrum measurements made with a larger coil for of a number of *UMER* quads and bending dipoles are reported elsewhere [55]. Here we report results of measurements with the small coil only.

Table 4.2: Calculation of lowest-order harmonics for concentric-loops model of PC quadrupoles

	SA Quadrupole $f = 0.682$ [a]	**UMER Quadrupole** $f = 0.538$ [a]
$\sum_{i=1}^{20} l_i Cos(2\theta_i)$ [b]	0.38307 m	0.36539 m
$\sum_{i=1}^{20} l_i Cos(6\theta_i)$ [b]	4.486×10^{-3} m	1.156×10^{-4} m
$\sum_{i=1}^{20} l_i Cos(10\theta_i)$ [b]	2.457×10^{-3} m	1.236×10^{-4} m
$\varepsilon_6/\varepsilon_2$ (%)	0.253 (Eq.[4.32]) 0.214 (MAG-PC + FFT)	0.0026 0.0024
$\varepsilon_{10}/\varepsilon_2$ (%)	0.300 0.169	2.4×10^{-4} 1.3×10^{-4}

[a] f = coil's height / quad radius.
[b] Evaluated from MAG-PC specification files.

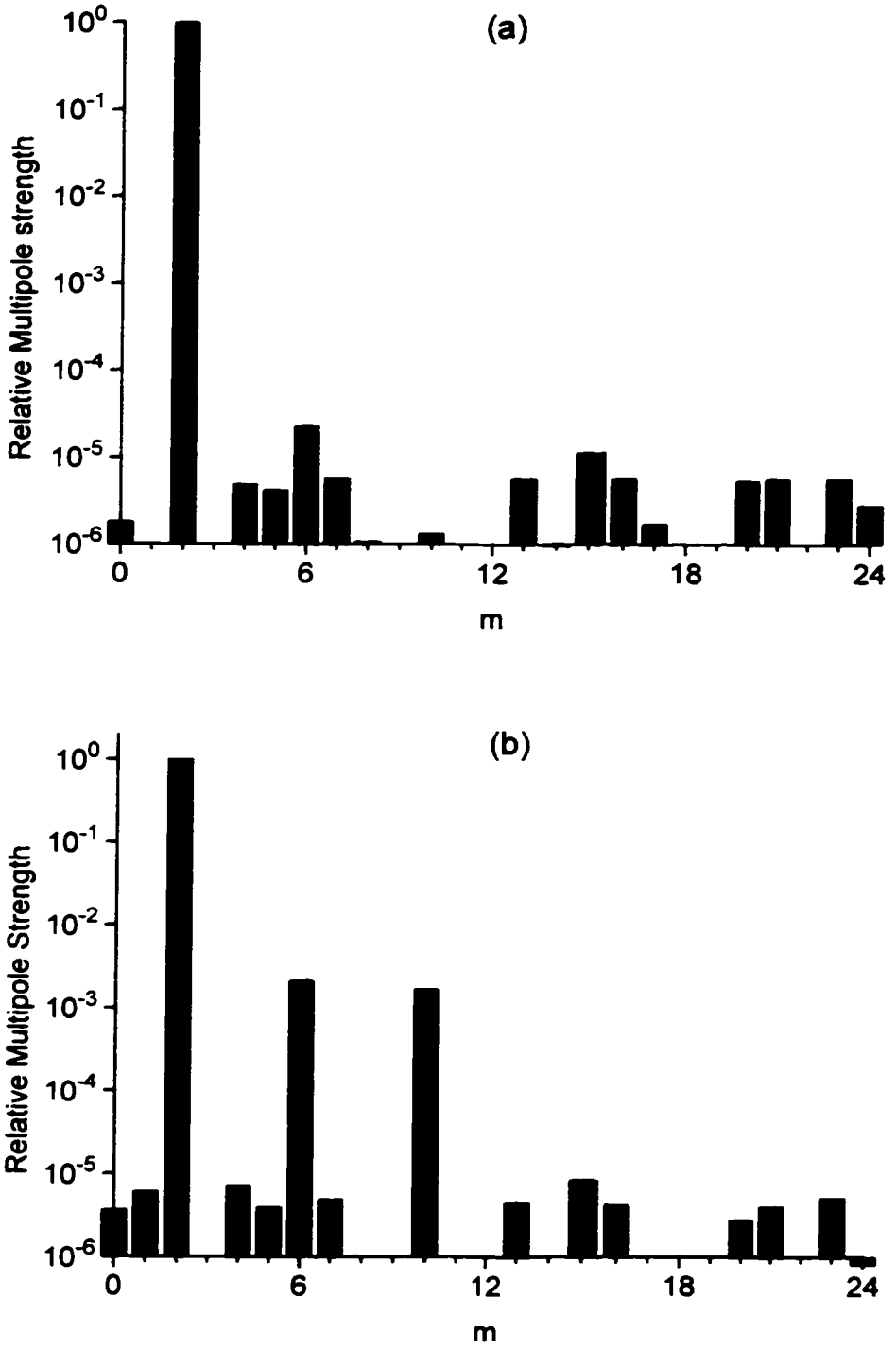

Fig. 4.11. FFT of axiall-integrated B_θ from MAG-PC (at r=1.50 cm) for (a) the UMER PC quadrupole, and (b) the old (small aperture) PC quadrupole.

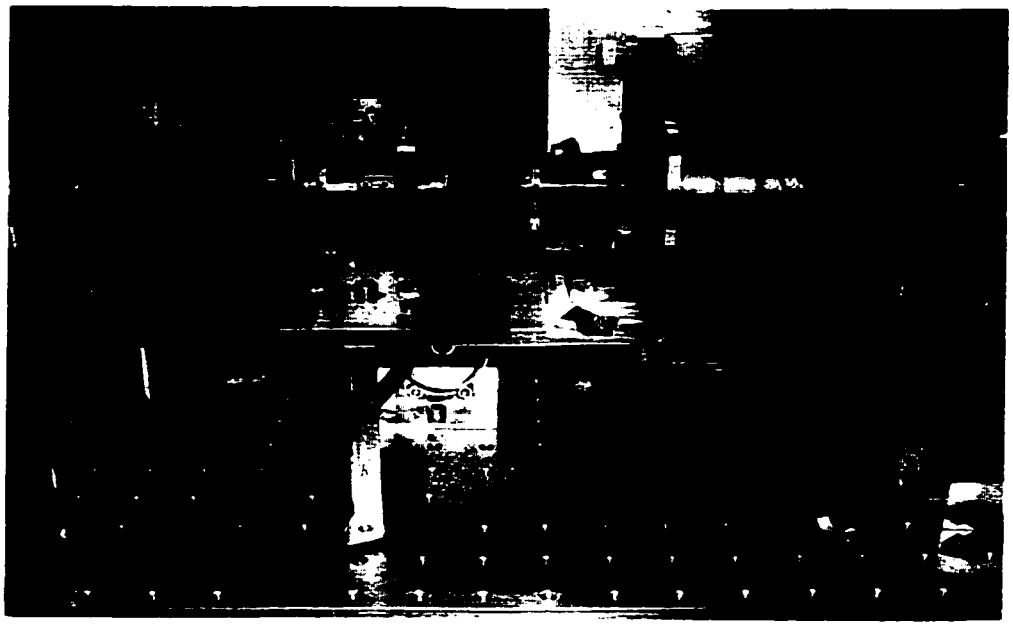

Fig. 4.12. Photograph of rotating coil set up with small-aperture PC quadrupole. Physical length of printed circuit quad is 4.4 cm, while the coil is 12.7 cm long. See also Fig. 3.12.

Results of spectra for the two types of PC quadrupoles are compared in Figures 4.13 (a)-(b). The first obvious feature from the measurements is the presence of strong "forbidden" multipoles : sextupole ($m=3$, or 18 Hz), octupole ($m=4$, or 24 Hz), and a decapole ($m=5$, or 30 Hz). Furthermore, the relative strength of the measured duodecapole term for the *UMER* quadrupole is about 100 times larger than the calculated one from the concentric-loops model (Table 4.2). The measured relative duodecapole for the small-aperture quad, on the other hand, is barely distinguishable from the noisy background; an upper value is 0.07 %, or three to four times smaller than the calculated value.

The analysis in Ref. [7] shows that the inclusion of the spiral geometry changes the harmonics spectrum. Most obvious is the presence of a new strong octupole term that can be easily understood from the eight-fold symmetry produced by the new geometry. The presence of the sextupole and decapole terms has been recently accounted for with MAG-PC calculations that include a tilt error in the assembly of the quadrupole halves [56]. The observed 1% relative strength of the sextupole term agrees with calculation involving a tilt angle between 0.5 and 1.0^0, which is a reasonable error in quadrupole assembly; furthermore, a linear dependence is observed between the sextupole harmonic and the tilt angle, for small angles.

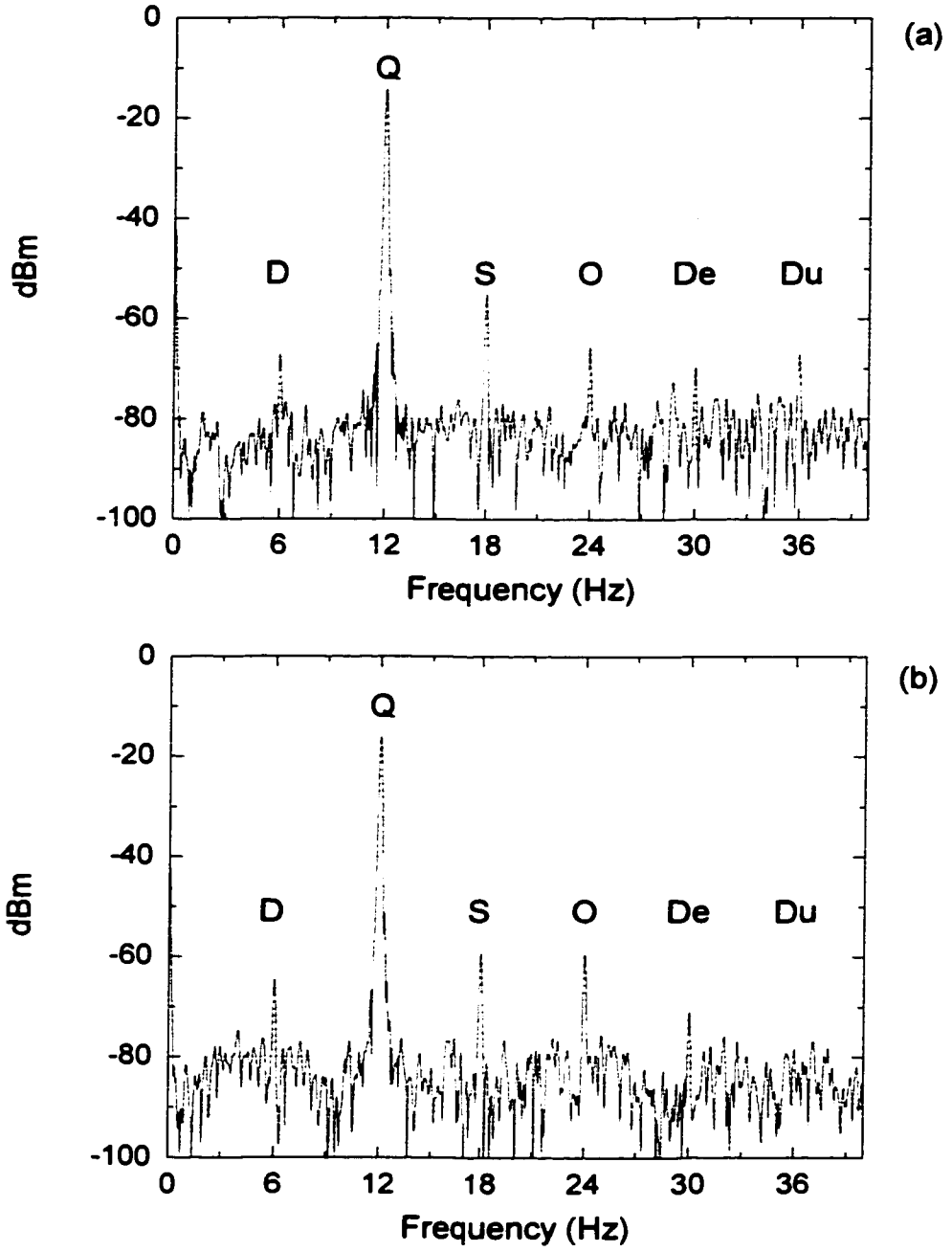

Fig. 4.13. FFT of signal from rotating coil (6 Hz) in the field of (a) the UMER quad with I = 2 A, and (b) the SA quad with I = 1 A. The spectrum shows D(ipole), Q(uadrupole), O(ctupole), De(capole) and Du(odecapole)

4.7 Summary and Conclusions

Comparison of two printed-circuit quadrupole designs, one based on a completely empirical approach that optimizes the linearity of the axially-integrated transverse field, and the other one based on a formal optimization of the integrated quadrupole term in the multipole expansion, reveals no essential differences in the transverse field axial profiles to third order in the transverse coordinates (Fig. 4.10, and Equations [4.7]). The third order term is related to the so-called pseudo-octupole component, which may play an important role for the beam dynamics, despite the fact that it vanishes in an axially-integrated sense.

"Point-by-point" field measurements of a scaled quadrupole agree well, within about 1 %, with calculations with a magnetics code based on a concentric-loop model for the printed-circuit conductor pattern. Furthermore, the axially-integrated gradients can be estimated in the framework of a model where the surface current distribution is continuous, so the details of the exact conductor pattern are not important (Equation [4.21]), or using an exact expression that is valid for a model of concentric loops (Equation [4.24]). The effects of the spiral geometry of the real quads introduce additional contributions to the integrated gradients of the order of 0.1 %.

Obvious differences are seen in calculations of the harmonics content of the two quadrupole designs, with the more formal design (the *UMER* quad) exhibiting significantly smaller integrated higher multipoles (Fig. 4.11 and Table 4.2). The comparison of results from these numerical calculations and from exact expressions for

the same concentric-loops model (Equation [4.32]) also serve to test the accuracy of the numerical computations with MAG-PC, the code used for the original quad design. It is concluded that not only additional accuracy is required, but also a more realistic model that incorporates the spiral geometry. Measurements with a rotating coil display unexpected results that are accounted for by recent calculations that incorporate a relative rotation error between the two quadrupole halves. For the studies that follow, only the lowest order calculations/measurements are important, but refinements of the integrated-multipole measurements may be necessary for realistic beam transport simulations of *UMER*.

CHAPTER V

RMS Matching Experiments in a Straight Solenoid-Quadrupole System

5.1 Introduction

As mentioned in Chapter IV, the criterion for the design of the printed-circuit quadrupoles is based on single-particle dynamics considerations. Since we are interested in the transport of space-charge dominated beams, for which no simple approach exists for quadrupole design, a thorough check is required, both experimentally and with computer simulations that include the effects of lens nonlinearities and space-charge. To this effect, an experiment was designed involving a solenoid and five printed-circuit quadrupoles in a straight channel [57,58]. The purpose of the experiment was to test not only the basic PC quadrupole lens with intense beams, but also the lattice design for the future electron ring, and to demonstrate beam envelope matching in an rms sense. The experiment described in [58] uses a geometry based on the original ring lattice parameters [1] with quadrupole spacing equal to 15 cm; the experiments presented here use a variation of this geometry whereby the last three quadrupoles are spaced at 16 cm, as in the final design of the *UMER* lattice. Matching into such a FODO lattice is studied for σ_0=85^0, and 76^0, values of zero-current phase advance that lead to maximum beam sizes (for the beam parameters in table 5.1) roughly fitting the available diagnostics; they are also within the range envisioned for the future matching experiments in *UMER*.

The next Section is a brief discussion of general considerations for the design of the matching section. A detailed description of the experiment is presented in Section 5.3. In the last section, the experiment results are compared with calculations performed with the computer codes discussed in Appendix B.

5.2 Matching Section Design: General Considerations

There are four conditions that the rms envelopes of a matched beam in a periodic FODO lattice must satisfy: $X(z + S) = X(z)$, $Y(z + S) = Y(z)$, $X'(z + S) = X'(z)$, and $Y'(z + S) = Y'(z)$, where S is the lattice period. We take $z = 0$ to be at the midplane of the *last* quadrupole in the matching section, so $X(l + L/2) = Y(l + L/2) = a$, and $X'(l + L/2) = - Y'(l + L/2) = a'$, where l is the quadrupole's effective length, and L is the drift space length between quadrupoles (see Fig. 1.3).

With four constraints and a matching section consisting of a solenoid and five quadrupoles, the problem is under-constrained. In other words, we have more "knobs" than we strictly need. Not only can the strengths of the six elements be varied, but also their location. Thus, a very large number of matched solutions exists; in practice, however, mechanical constraints reduce the solution space considerably. As an example, an obvious practical constraint imposes a limit to the *total length* of the matching section; additional constraints could include the fixed locations or even strengths of one or more focusing elements.

Out of the possible matched solutions, some must be preferable to others because of better *stability* under changes of lens currents, or initial beam parameters, or simply because the solutions provide better "treatment" of the beam in the sense that a smooth, "adiabatic" change of the beam particle distribution from the source to the main FODO lattice is realized. Although these are important issues that must be considered for a complete understanding of the beam dynamics in the matching section and the FODO lattice that follows, they are very specific to the system at hand and can only be addressed in an extended experiment. (Examples of matching sections in a low-energy ion ring and in an electron injection line are discussed in Refs. [59] and [60], respectively.) Therefore, the scope of the matching experiments described in the following sections is limited to finding the focusing function and corresponding matched envelope solutions that satisfy the mechanical constraints, although care is taken to design the section so the resulting envelope is as uniform as possible, as explained later.

The envelope and focusing function solutions are obtained from the K-V envelope equations (Chap. I), following a procedure explained in detail in Appendix B. Additional checks are performed with a particle-in-cell code with a more realistic implementation of focusing elements and initial particle distribution.

The beam and lattice parameters relevant to our matching problem are summarized in Table 5.1. "Lattice" refers here to the straight matching section, employing a solenoid and PC quadrupoles of the early, small-aperture, design, followed by a prototype, 20^0 bend section, described in Chapter VI. "FODO lattice" will be used to

Table 5.1: Beam and Lattice Parameters for Solenoid-Five PC quadrupole Experiment

Beam energy /particle's speed , T/β	$4 \times 10^3 \pm 20$ eV / 0.12
Beam Current, I	17 ± 0.5 mA
Generalized perveance, K	1.01×10^{-3}
Emittance (normalized), $\epsilon_N = \beta\gamma\epsilon$	8.4 mm mrad
Effective emittance (4 rms), ϵ	67 mm mrad
Initial beam slope, R_0'	32 ± 2 mrad
Transport pipe radius - straight section	1.90 cm
Half-lattice period* (20^0 bend section), $S/2$	16 cm
Tune Depression	0.3

*Matching into FODO lattice of UMER quads

mean the alternating gradient geometry formed with the *UMER* PC quadrupoles. All the quantities in Table 5.1 are experimentally determined, with the exception of the emittance. A lower limit to the emittance is estimated from previous measurements at 5 kV [45], while the final value for matching calculations is obtained from beam expansion data (Sec. 5.3.1).

Using results from the review in Chapter I for the transport of space-charge dominated beams, we can estimate the average and maximum beam radii in the FODO lattice (Eqs. [1.19] and [1.18], respectively), corresponding to zero-current phase advances of σ_0=85^0, and 76^0: a = 7.85, 8.67 mm, a_{max}= 11.9, 12.3 mm. These latter values are close to the radius of the fluorescent screen used for beam diagnostics in the experiments. Similar approximations (Eq. [1.16]), give a tune depression σ/σ_0 in the infinite FODO lattice equal to 0.27, for both σ_0=85^0, and 76^0. This value is within the design range of *UMER*.

5.3 Experimental Procedure

Figure 5.1 illustrates the schematics of the experiment. The electron beam, originating 12 cm behind the aperture, is allowed to expand before entering the solenoid field. The first PC quadrupole is located near the beam waist, 9.8 cm from the middle plane of the solenoid. Four more PC quadrupoles, with locations given in Table 5.2, focus the beam to a distance of almost one meter from the aperture. PC steering dipoles

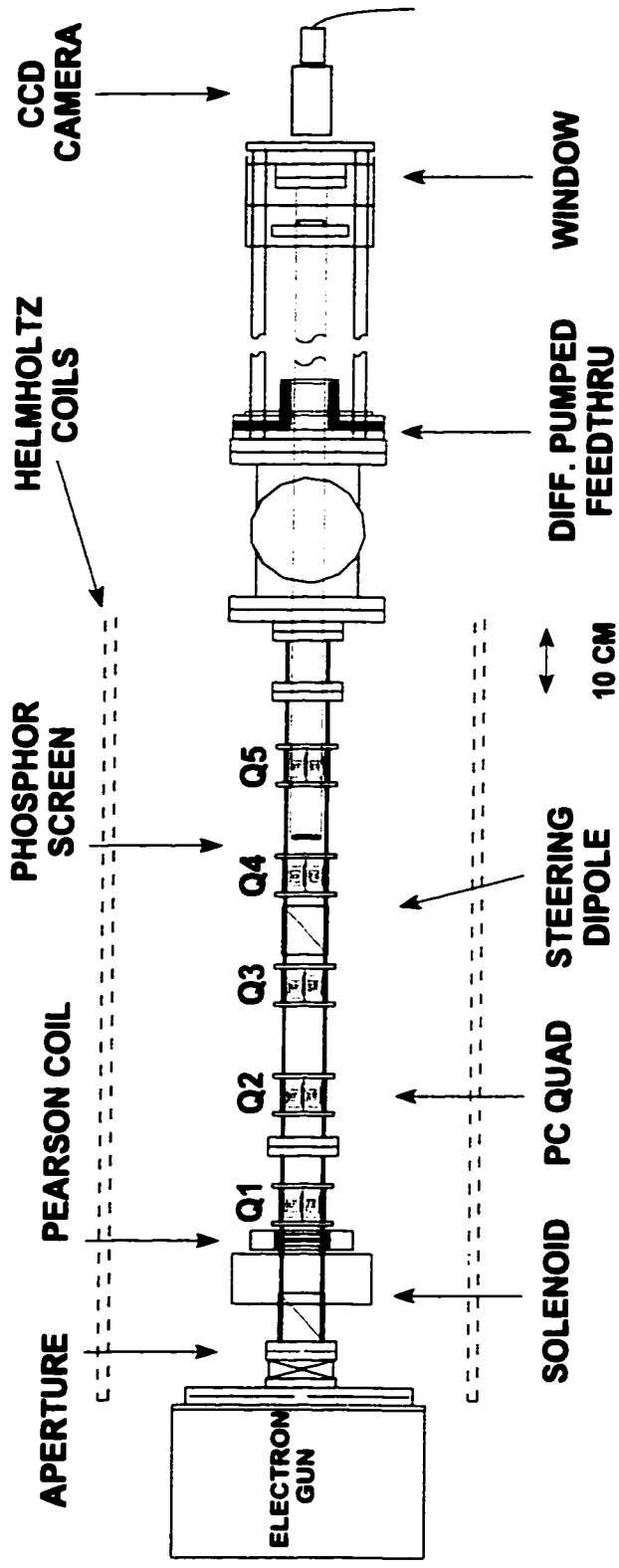

Fig. 5.1. Schematics of the solenoid - five PC quadrupole experiment. The PC quadrupoles are of the small-aperture type. The locations of focusing elements are given in Table 5.2

Table 5.2: Parameters of Focusing Elements in Solenoid[a] - Five SA[b] Quadrupole Experiments. (Optimized Focusing from SPOT)

	Zero-Current Phase Advance $\sigma_0 = 85^0$	Zero-Current Phase Advance $\sigma_0 = 76^0$
Distance Aperture - Solenoid	12.5 ± 0.1 cm	12.5 ± 0.1 cm
Solenoid Peak Focusing κ_0 (Eq. [3.5])	218.8 m^{-2}	200.0 m^{-2}
Solenoid On-axis Field	63.2 ± 1 G	60.4 ± 1 G
Solenoid Current	3.52 ± 0.05 A	3.36 ± 0.05 A
Quad Distances from Aperture	22.3, 37.3, 52.8, 68.8, 84.8, 100.8[c] ± 0.1 cm	22.3, 37.3, 52.8, 68.8, 84.8, 100.8[c] ± 0.1 cm
Quad Peak Focusing κ (Eq. [4.10])	-77.2, 232.0, -286.5, 276.5, -271.0, 252.7[c] m^{-2}	-65.45, 210.7, -257.2, 244.0, -235.5, 230.2[c] m^{-2}
Quad Peak Gradients	-1.65, 4.96, -6.12, 5.91, -5.79, 5.40[c] G/cm	-1.40, 4.50, -5.50, 5.21, -5.03, 4.92[c] G/cm
Quad Currents	218, 655, 809, 780, 765, 1,300[c] mA	185, 595, 726, 689, 665, 1,190[c] mA

[a] Solenoid parameters given in Chapter III.
[b] Small-Aperture quads - parameters given in Chapter IV.
[c] "Q6" is a UMER quadrupole.

and a set of Helmholtz coils assist in beam alignment. Differential pumping allows the use of a movable phosphor screen for beam diagnostics anywhere in the channel. Details of the steering elements and mechanical design are given in Chapter III.

The experiment proceeded in three stages. In the first step, the initial beam slope was determined from beam size data for the free expansion of the beam near the aperture. Then solenoid focusing was studied over a distance of about 40 cm from the aperture. In the last step, quadrupole focusing and rms envelope matching are studied. Details of how the initial beam slope is determined, and measurements of solenoid focusing are given in the next two subsections. Quadrupole focusing and matching are dealt with in the last subsection.

5.3.1 Measurement of Initial Beam Slope:

An accurate determination of the initial slope of the beam envelope is crucial for design calculations. The simplest way to determine the initial beam slope is to measure the beam size at two *closely* spaced points, one being at the aperture plane. In this method, a laminar beam (i.e. with zero emittance) can be assumed, so the beam evolution between the two planes can be easily modeled using the equations in section 4.2 of Ref. [5]. However, errors in the distance from the aperture to the second point and, specially, in the beam size, yield significant errors in the slope. An alternative, trying a point farther out from the aperture so the relative errors in both the beam size at the point and in the distance are reduced, does not work well because the emittance becomes an important factor for the evolution of the beam over the extended distance.

The solution is to fit a number of experimentally determined beam sizes, over the extended distance, to a solution of the full K-V envelope equations. In the process, the emittance plays the role of a fit parameter whose value for initial calculations is estimated from previous measurements without the aperture.

Measurements on the full beam by D. Kehne [45] at points not far from the location of the aperture yield a value of 95 mm mrad for the effective, unnormalized emittance at 5 keV. At 4 keV, the corresponding emittance without the aperture is 106 mm mrad. The aperture reduces the emittance; an estimation of the new emittance using the simple model presented in Appendix A (Eq. [A.6]) and beam size data from D. Kehne and the aperture radius (3.18 mm) yields 48 mm mrad.

Beam size data for the free expansion of the beam were obtained at six points over a distance of about 12 cm from the aperture. Figures 5.2 and 5.3(a) show the pictures and corresponding beam profiles in the horizontal direction. In order to obtain a peak intensity signal in the digitized beam pictures safely away from saturation, but still strong enough to minimize the effects of noise, specially from spurious background and reflected light, the aperture (f/#) of the normal lens attached to the camera was varied from picture to picture. Thus the profiles shown in Fig. 5.3(a) are not normalized, in the sense that the areas under the different curves are not the same. This, however, has little or no effect on the rms beam size, as has been checked by trying different lens apertures in a particular case. The final beam sizes at each plane along the channel are obtained by averaging the rms "x" and "y" sizes (these sizes differ by no more than about 3%.) For comparison, the beam envelope is calculated with the K-V envelope code SPOT

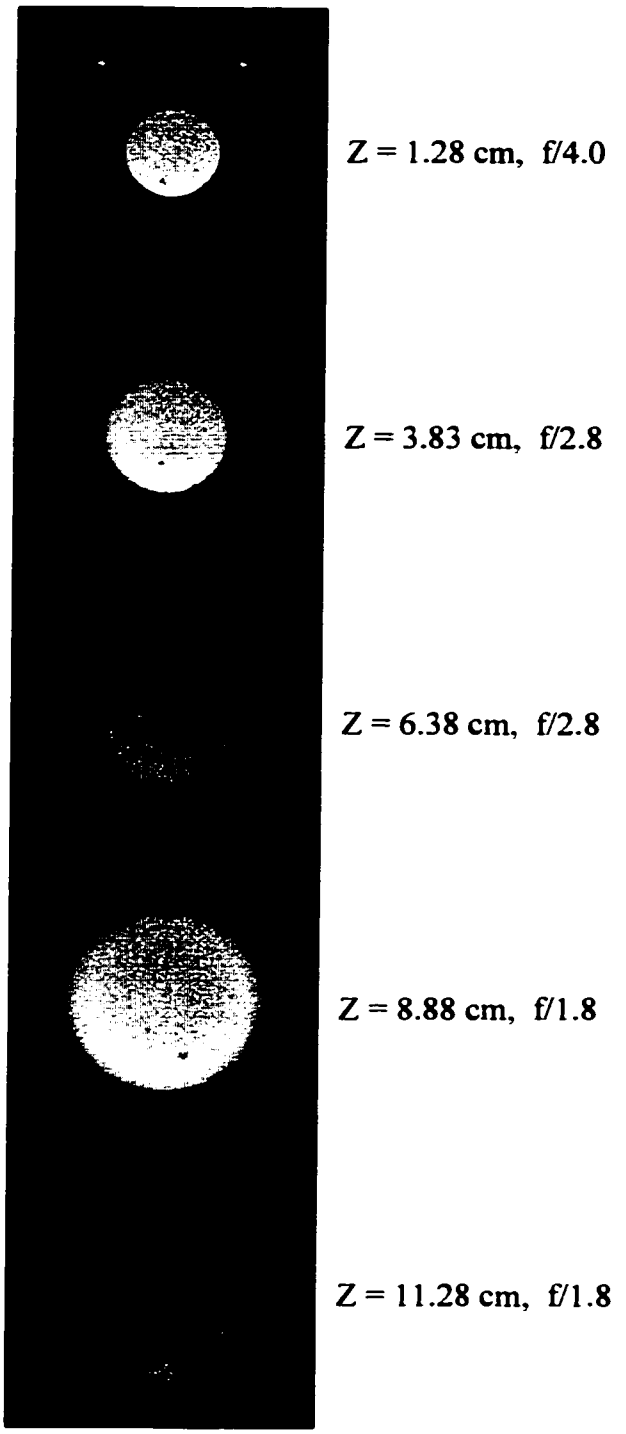

Fig. 5.2. Beam free expansion: phosphor screen pictures near the aperture midplane (z = 0). The f/# values are adjusted for optimum light gathering at the CCD sensor, and to prevent saturation.

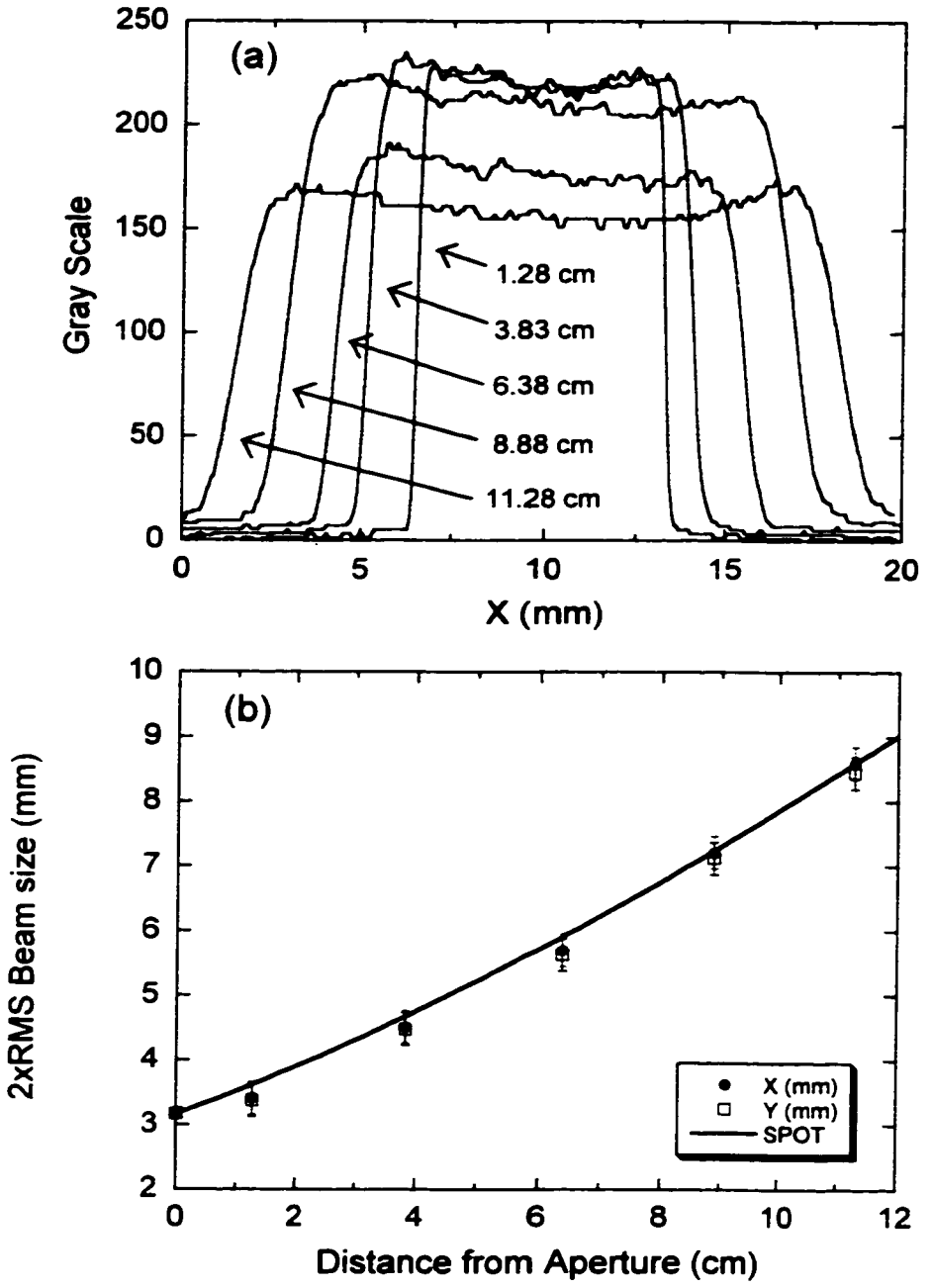

Fig. 5.3. Beam free expansion: (a) horizontal intensity profiles from phosphor screen pictures (Fig. 5.2), and (b) twice RMS horizontal and vertical beam sizes.

described later in Appendix B. The results of measurements and calculations are shown in Figure 5.3(b); the best fit, in a least-squares sense, is obtained for an initial beam slope of $R'_0 = 32$ mrad, and an effective, unnormalized emittance of $\epsilon = 67$ mm mrad.

5.3.2 Solenoid Focusing:

Solenoid focusing was studied in detail before attempting the matching experiments. Figure 5.4 is a montage of beam pictures obtained with the solenoid located at 12.5±0.1 cm from the aperture, with a solenoid current of 3.53±0.07 A. (The uncertainty in the solenoid current translates into an uncertainty of about 1.3 G in the peak field of the solenoid, comparable with the error from hysteresis.) The first picture is taken near the aperture, while the last one is taken about 40 cm downstream. The framed picture is obtained near the middle plane of the solenoid, where the beam is close to its maximum size; when compared with the last picture, the sizes are about the same, but there is a definite difference in internal structure. While the beam particle density is fairly uniform over 30 cm or so from the aperture, a thin bright ring appears near the beam edge in the last two or three pictures, accompanied by beam hollowing. This is also seen in the beam profiles of Figure 5.5, obtained from pictures (also shown) taken with the *same f/#* = 1.8. The beam at 11.9 cm is fuzzy at the edges, in contrast with the sharp-edged and more hollow beam at 43.2 cm. The observed asymmetry in the profile of the fuzzy beam is thought to be an artifact (a similar asymmetry would be

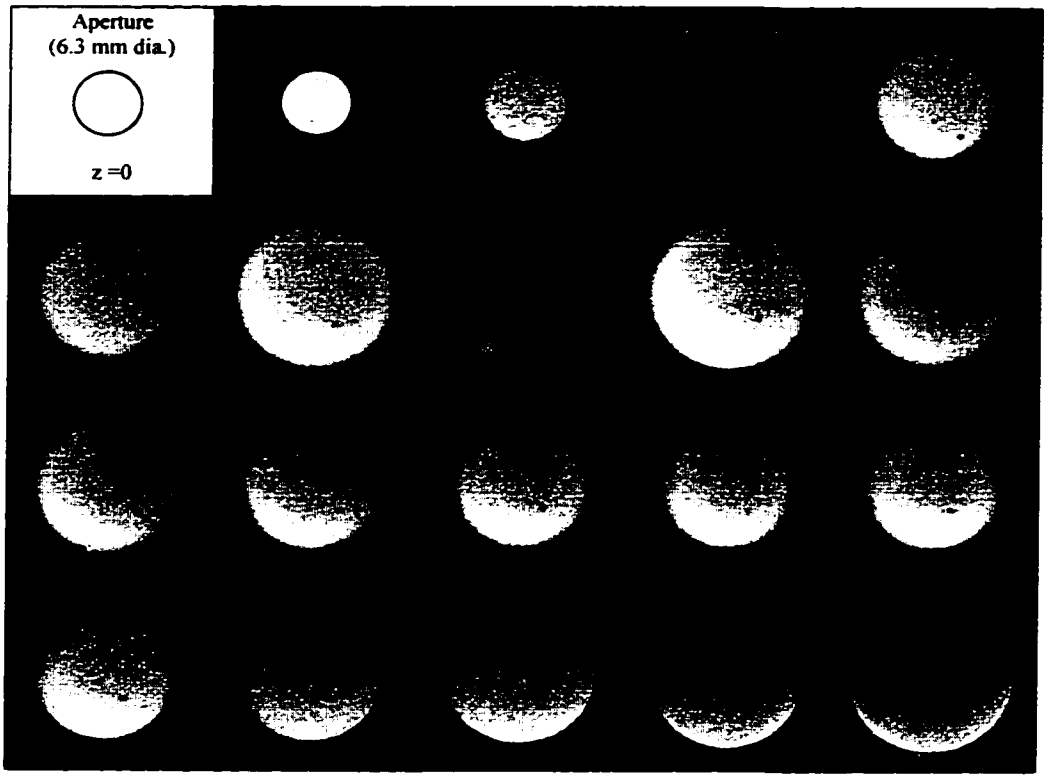

Fig. 5.4. Solenoid focusing: beam evolution from near the aperture out to a distance of 43.2 cm from it. The solenoid is located at 12.5 cm from the aperture; the solenoid current is 3.53 A (63.46 G).

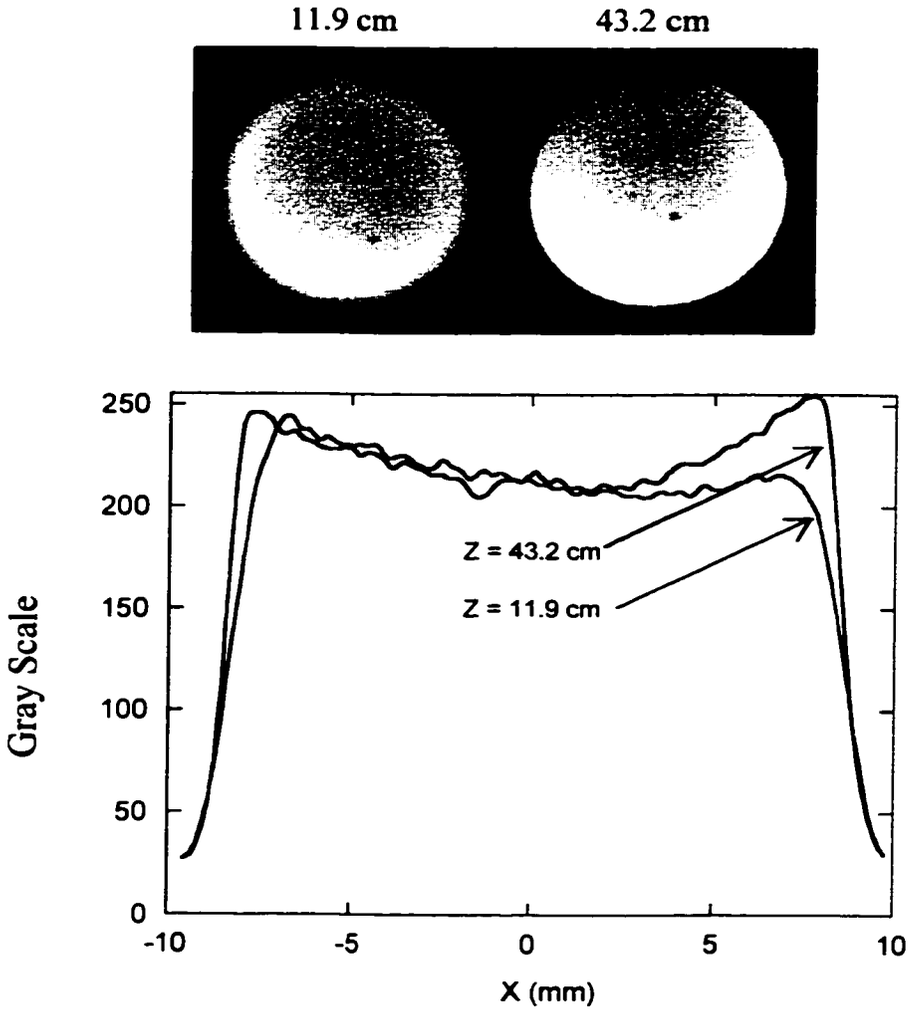

Fig. 5.5. Comparison of horizontal intensity profiles of beam pictures near the midplane of the solenoid and at 43.2 cm downstream of the aperture.

obtained for the vertical profile of the sharp beam, as seen from the picture on the right-hand side.) These observations will be qualified in Chap. VII.

Beam envelope calculations with the K-V code SPOT are in excellent agreement with experimental results. The solenoid on-axis field profile is modeled with Eq. [3.4] and the corresponding fit coefficients of Table 3.1. We are interested in the sensitivity of the calculated envelope to the peak solenoid field, initial beam slope, effective emittance and solenoid location. Figure 5.6 shows the calculated envelope vs. experiment for two values of peak solenoid field: the nominal 63.46 G (close to the final value for matching) and a field 1% smaller. The initial beam slope and effective emittance are $R'_0 = 32$ mrad and $\epsilon = 67$ mm mrad (these latter values correspond to the best fit parameters for the free expansion of the beam, as explained before). From Fig. 5.6(a), it is clear that the maximum beam excursion, near the midplane of the solenoid, is fairly independent of peak solenoid field, and that the beam waist is smaller for larger solenoid fields (as expected for increased focusing). The nominal peak field of 63.46 G ($\kappa_0 = 220.5$ m^{-2}) reproduces the experimental results best. Figure 5.6(b), on the other hand, presents the results for two values of initial beam slope, and a peak field of 63.46 G; from the figure, the beam envelope size downstream of the beam waist is largely independent of initial beam slope; however, the exact location and size of the beam waist is sensitive to the initial beam slope. The calculation with R'_0=32 mrad [Fig. 5.6(a)] best reproduces the experiment. Finally, sensitivity to emittance and solenoid location is studied in Figures 5.7(a)-(b). Based on the curves shown in Figs. 5.6 and 5.7,

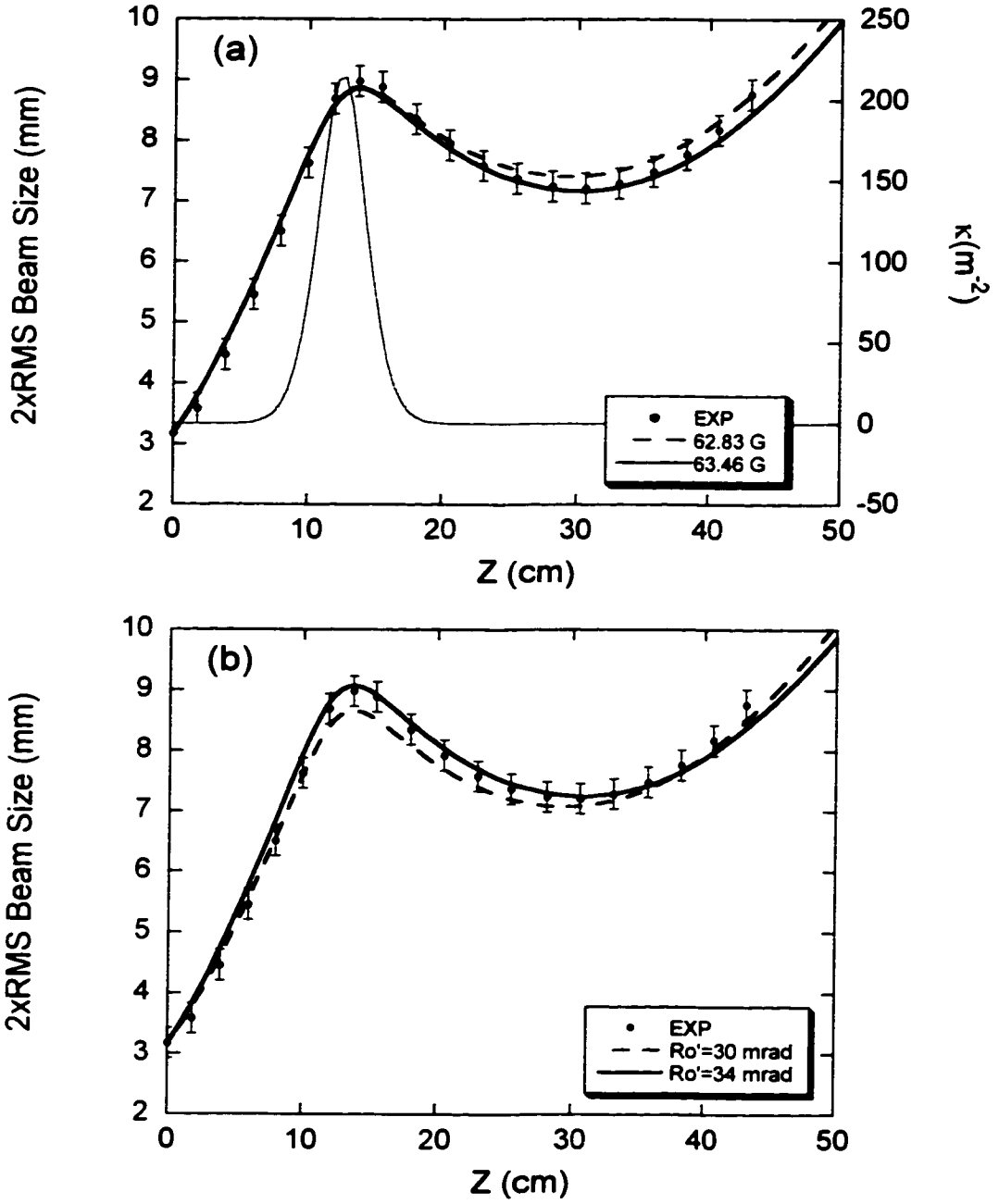

Fig. 5.6. Solenoid Focusing - Experiment vs. SPOT calculations:
(a) Dependence of K-V envelope solution on peak solenoid field,
(b) Dependence on initial slope (peak field = 63.46 G).

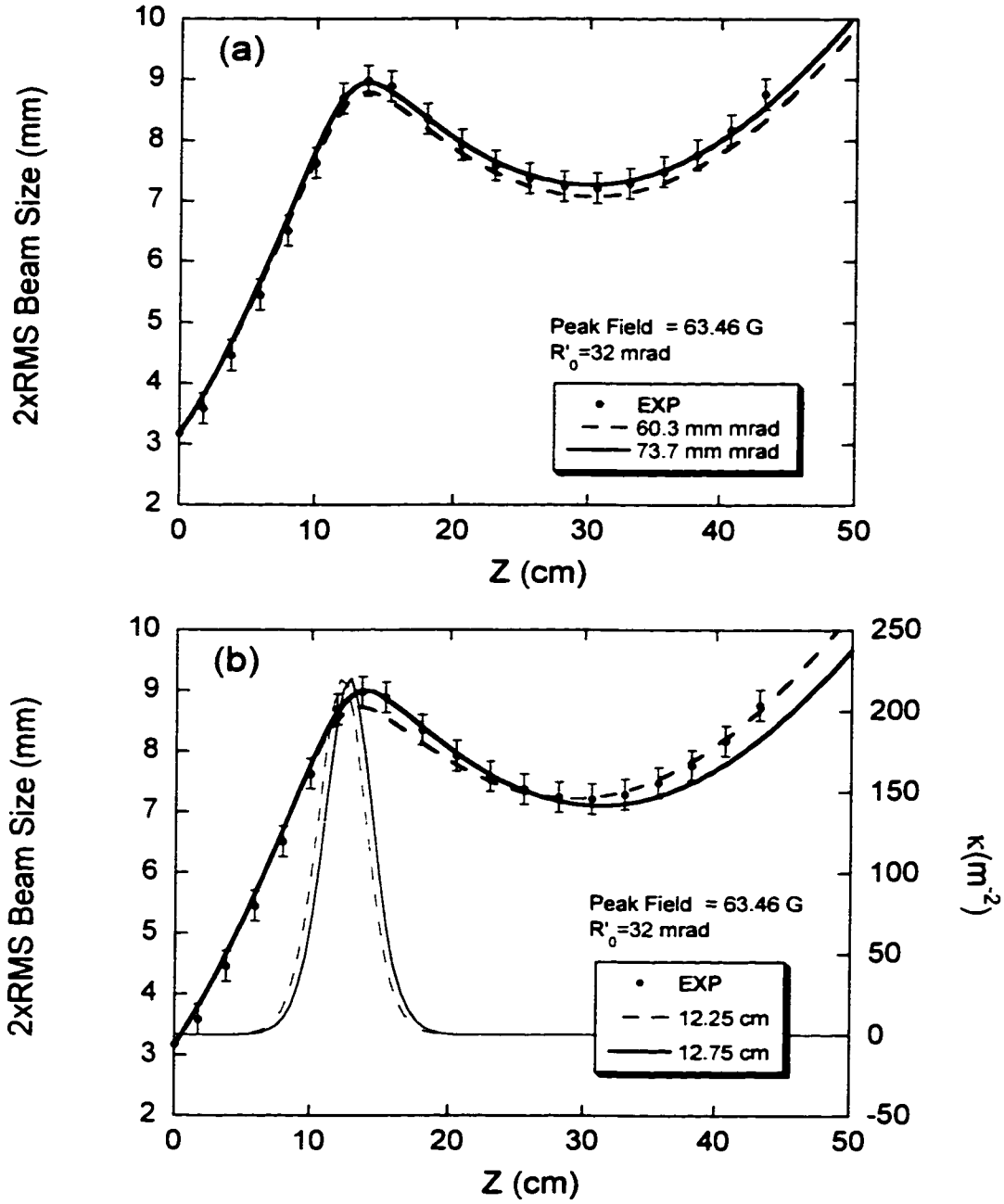

Fig. 5.7. Solenoid Focusing - Experiment vs. SPOT calculations: (a) Dependence of K-V envelope solution on effective emittance (4xrms), (b) Dependence on solenoid position.

the best fit parameters are $B_0 = 63.46$ G, $R'_0 = 32$ mrad, $\epsilon = 67$ mm mrad, and $Z_{sol} = 12.5$ cm. Figure 5.6 (a) includes the solution corresponding to these parameters.

Calculations with the particle-in-cell code WARP of solenoid focusing with no aberrations and a K-V beam agree with SPOT results when both codes use exactly the same conditions, i.e. same field profile and step size. When the nonlinearities of the solenoid are included through the derivatives of the field profile (Eqs. [3.2] and [3.3]), the envelope calculations extracted from WARP differ very little from the linear calculations. Thus, for all practical purposes, solenoid focusing in the experiments of this work can be characterized as *linear*.

5.3.3 Quadrupole Focusing and RMS Matching:

With the solenoid at 12.5 cm from the aperture and the PC quadrupoles located as given in Table 5.2, calculations with the K-V envelope code SPOT yield the required quadrupole strengths.

The particular lattice geometry chosen can be understood in simple terms. The solenoid is placed at a distance such that the beam is allowed to expand to a radius roughly equal to the average radius in the FODO lattice. This value is small compared to the solenoid bore radius (38 mm), so the role of solenoid nonlinearities is minimized. The first quadrupole, on the other hand, is located so the beam envelope splits as "evenly" as possible, i.e. with lobes in X and Y that resemble as much as possible those in the FODO lattice. This even "envelope split" is not possible if the solenoid is too

close or too far from the aperture; in the first case, a "neck" is produced at Q2 in one direction from overfocusing, while a large excursion is produced (also at Q2) in the other transverse direction from over-defocusing. (The experiment reported in Ref. [58] suffers somewhat from this.) The existence of the envelope "neck" is the result of two factors: the extra focusing needed from the solenoid to prevent the rapidly expanding beam from "overshooting" the first quad (in this case the beam size at the first quad is relatively small compared to the average FODO lattice value), and the additional action of that quad, at the split point, that induces a large difference between the X and Y envelopes at Q2. If the solenoid is too far from the aperture, on the other hand, not only is the maximum beam size increased, with the risk of solenoid nonlinearities starting to play a role, but also the waist (from solenoid focusing) is pushed farther downstream forcing a relocation of the first quad (if even split is still desired); even with this relocation, the difference between the maximum and minimum envelope sizes at Q2 is still rather large.

The first quadrupole is powered by an individual dc power supply (HP-E3610A); the other four are connected in series, and each one connected in parallel to a power rheostat. A single dc power supply (Kepco ATE 100-2.5M) powers the series combination of four quadrupoles, adjustment of the rheostats permitting independent variation of the quadrupole currents. There is also provision for inverting the quadrupole currents individually, through the use of double-pole-double-throw switches. The electrical diagram of the PC quadrupole connections is shown in Figure 5.8. Quadrupole heating, initially thought to be a potential problem, is moderate: at a current of 0.810 A,

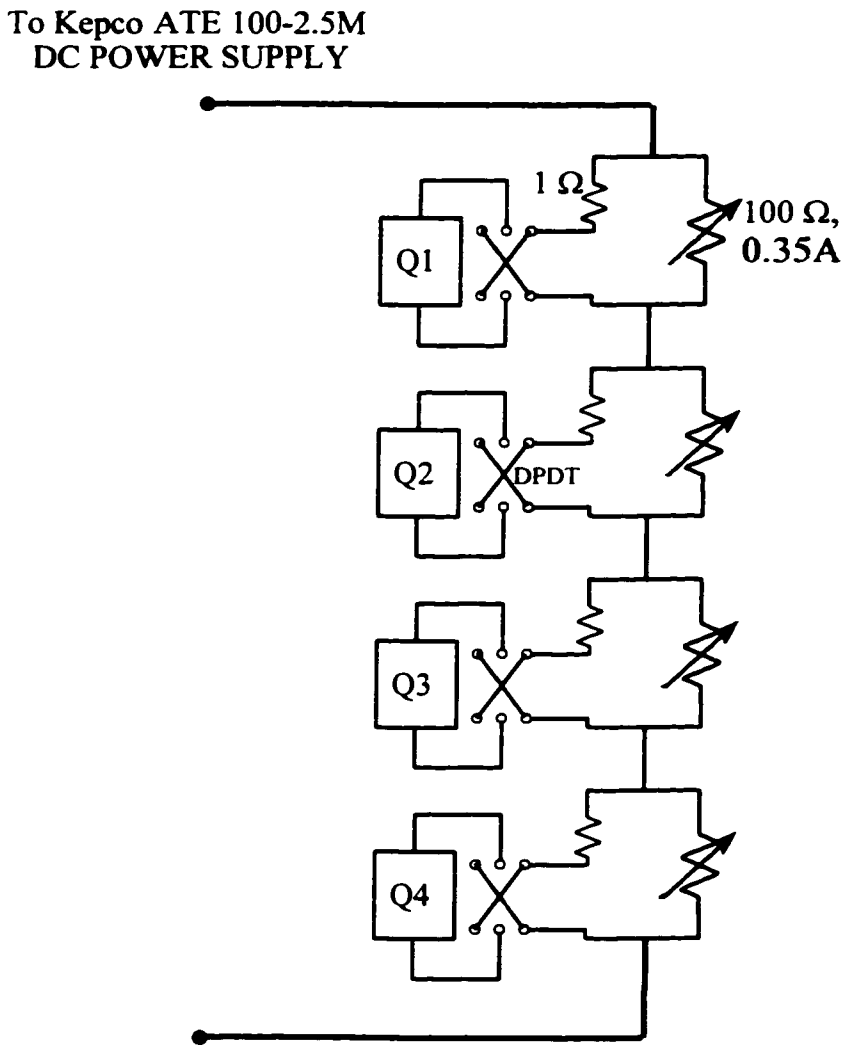

Fig. 5.8. Layout of PC-quadrupole connections. Each quadrupole is about 10 Ω at room temp. DPDT stands for "double pole - double throw" switch; it's used for inverting the quadrupole currents. The latter are read as voltages across the 1 W, 1% resistors.

the printed-circuit temperature is about 60 ^{0}C. Since the heat is limited to the extent of the quadrupole, and significant heat dissipation occurs through the quadrupole aluminum mount itself, there is no noticeable effect on the system's pressure.

Finally, quadrupole focusing is observed sequentially, with special attention paid to quadrupole angular placement to correct for any beam rotations relative to the quadrupole principal axes. Fortunately, rotations of the principal axes of the beam cross section arising from rotated quads are decoupled from centroid motion so they can be easily corrected in the experiment without introducing additional errors. Initially, the quadrupoles are oriented using a simple tool to find the midline on the transport pipe; the error in this operation is about one degree. To correct for a rotated beam, as observed at the midplane of a given quadrupole, only the nearest upstream quadrupole is slightly rotated. The magnitude of these correcting rotations is typically about one degree, or a 0.5 mm displacement off the midline on the pipe. The orientation of the camera is also important when judging beam rotations; normally the back of the camera (where the CCD sensor is located) sits flat on the hardened-steel rods that support the phosphor screen transport (Fig. 3.5, Chapter III), so consistent orientation of the sensor is possible. A discussion of the combined effects of space-charge and rotated quadrupoles is deferred to Appendix C.

Beam alignment was kept within about 0.5 mm through the use of the PC steering dipoles described in Chapter III. The Helmholtz coils, also mentioned before, helped in fine tuning the alignment. A final check of the alignment was done through switching of the quadrupole polarities. The alignment achieved using this method was good only in an

average sense, since space allowed us only one steering dipole between quads to correct for beam centroid position at the midplane of each quadrupole.

5.4 Results

Figure 5.9 shows a partial sample of pictures taken in one run, corresponding to $\sigma_0=85^0$ in the ideal FODO lattice; Figure 5.10 presents the beam profiles in the transverse directions. Pictures and beam profiles corresponding to the $\sigma_0=76^0$ case are shown in Figures 5.12 and 5.13, respectively. The effective beam sizes in the transverse directions are calculated as twice the rms value of x and y using the pixel coordinates and gray scale values (0 to 255) as representation of the beam particle density distribution. Additional details of the image processing involved are given in Chap. III.

The experimental beam envelopes are compared with solutions of the K-V envelope equations obtained with MATHEMATICA. The optimized lens strengths from SPOT are implemented in MATHEMATICA; this code is preferable to SPOT for final calculations because it completely avoids the problem of truncated lenses inherent in the control algorithm which is the basis of SPOT (App. B).

As can be judged from Figs. 5.11 and 5.14, the agreement between experiment and calculations is good, specially at the "midpoints" where the X and Y envelopes intercept. An obvious discrepancy occurs, however, in the X envelope near the midplane of Q4 for both $\sigma_0=85^0$ and $\sigma_0=76^0$. By contrast, the agreement for the Y envelope is near perfect, with the exception of one point (near Q3) for $\sigma_0=76^0$. The difference between the

calculated X envelope and the experiment at Q4 [Figs. 5.11 (a)-(b)] cannot be explained by uncertainties in the image processing used to determine the beam size: beam size calculations with different degrees and types of noise reduction yield essentially the same result. A more likely explanation for the discrepancy is the effect of the Pearson transformer located between the solenoid and Q1 (Fig. 5.1). The increased (7 %) strength used for Q1 in Fig. 5.12 (b) is an attempt to effectively take this into account, and, at the same time, an illustration of the sensitivity of the envelopes to variations in one parameter. The error bars in the plots (± 0.25 mm) are estimated from the calibration error of the digitized beam pictures (Eq. [3.6]) and the small uncertainty resulting from noise reduction in the image processing.

Concerning the beam profiles in Figs. 5.10 and 5.13, the asymmetry observed in both X and Y profiles, specially near the solenoid or first quadrupole, has little effect on the effective beam size. A more important consideration is the situation when the beam size in either X or Y is obviously larger than the phosphor screen, as can be seen near Q2 and Q3 in Fig. 5.12. In this case, the "oversized" beam is manually "fitted" by drawing an ellipse having a minor axis of the right size (as determined in the normal way); the oversize dimension is then found visually by measuring the major axis. Naturally, many ellipses could "fit" the oversized beam, so the operation is relatively crude and subject to an error larger than the error bar in the plot.

Particle-in-cell calculations with WARP show that, for the parameters of the matching experiments, the solenoid and quadrupole nonlinearities have very little effect on the beam envelopes. (The implementation of lens nonlinearities is briefly described

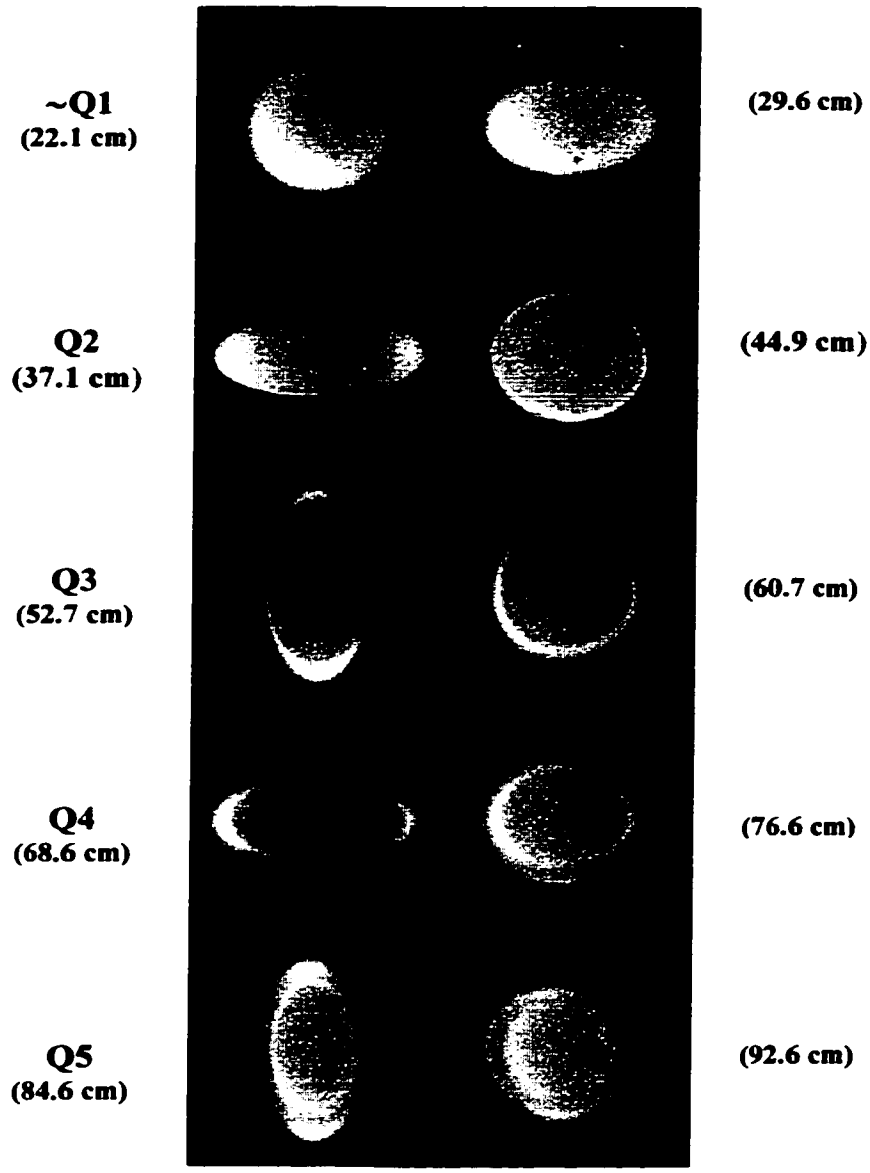

Fig. 5.9. Phosphor screen pictures - partial sample - for the experiment corresponding to $\sigma_0=85^0$ in the FODO lattice. The distances indicated are measured from the aperture. Actual quadrupole locations are given in Table 5.2.

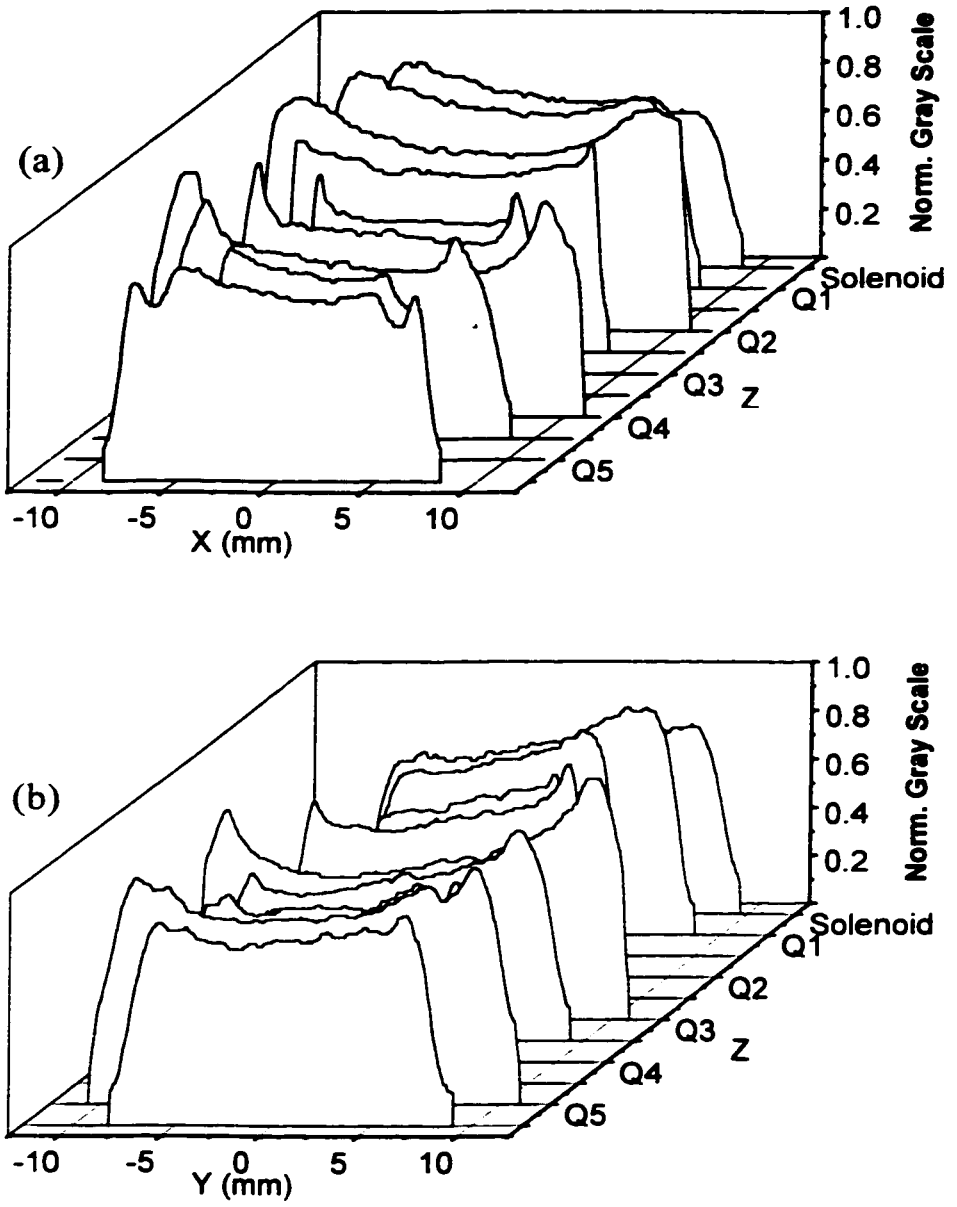

Fig. 5.10. Beam profiles corresponding to the phosphor screen pictures of Fig. 5.9. (a) Horizontal, (b) Vertical.

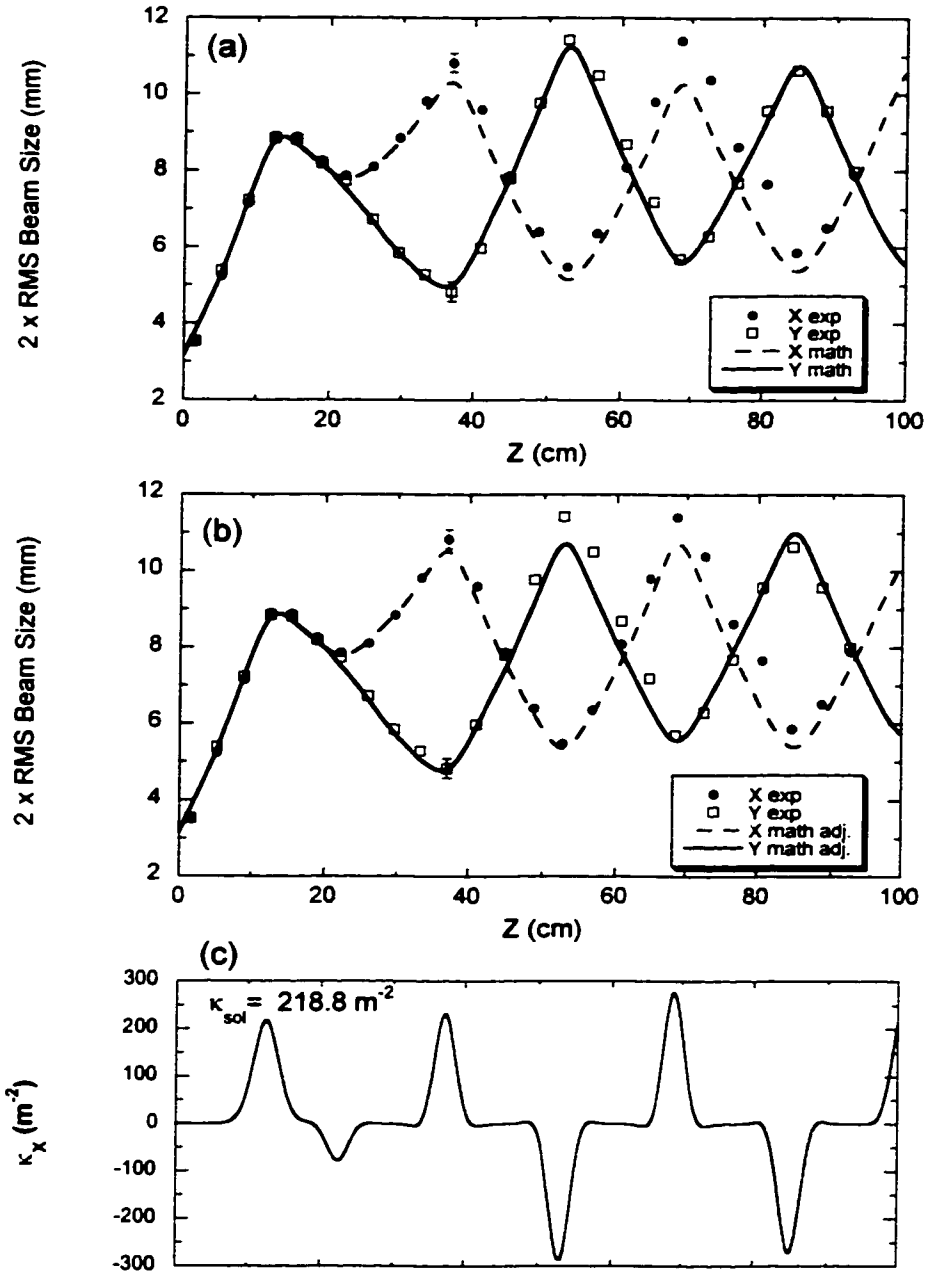

Fig. 5.11. Experiment vs. solution of K-V envelope equations for $\sigma_0=85^0$: (a) Envelope data, (b) Envelope data with the strength of Q1 adjusted by +7%, and (c) Focusing function (horizontal).

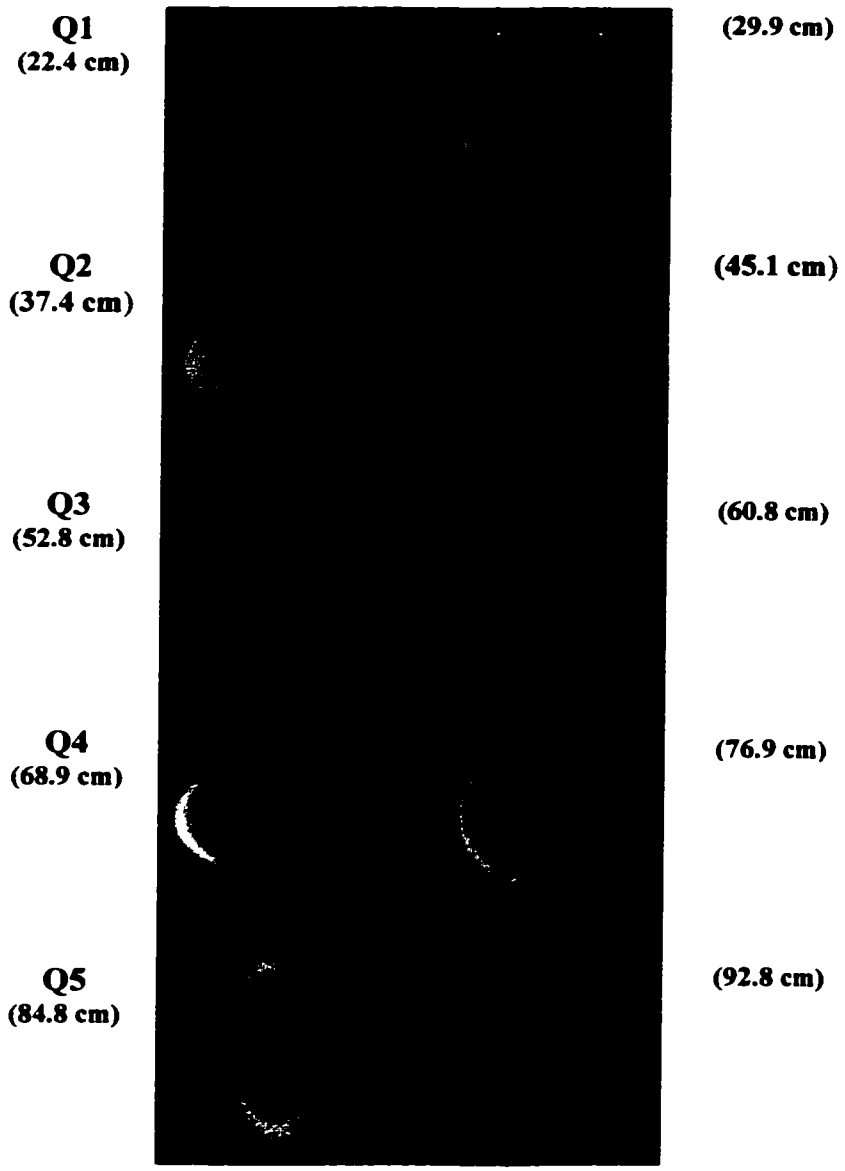

Fig. 5.12. Phosphor screen pictures - partial sample - for the experiment corresponding to $\sigma_0=76^0$ in the FODO lattice. The distances indicated are measured from the aperture.

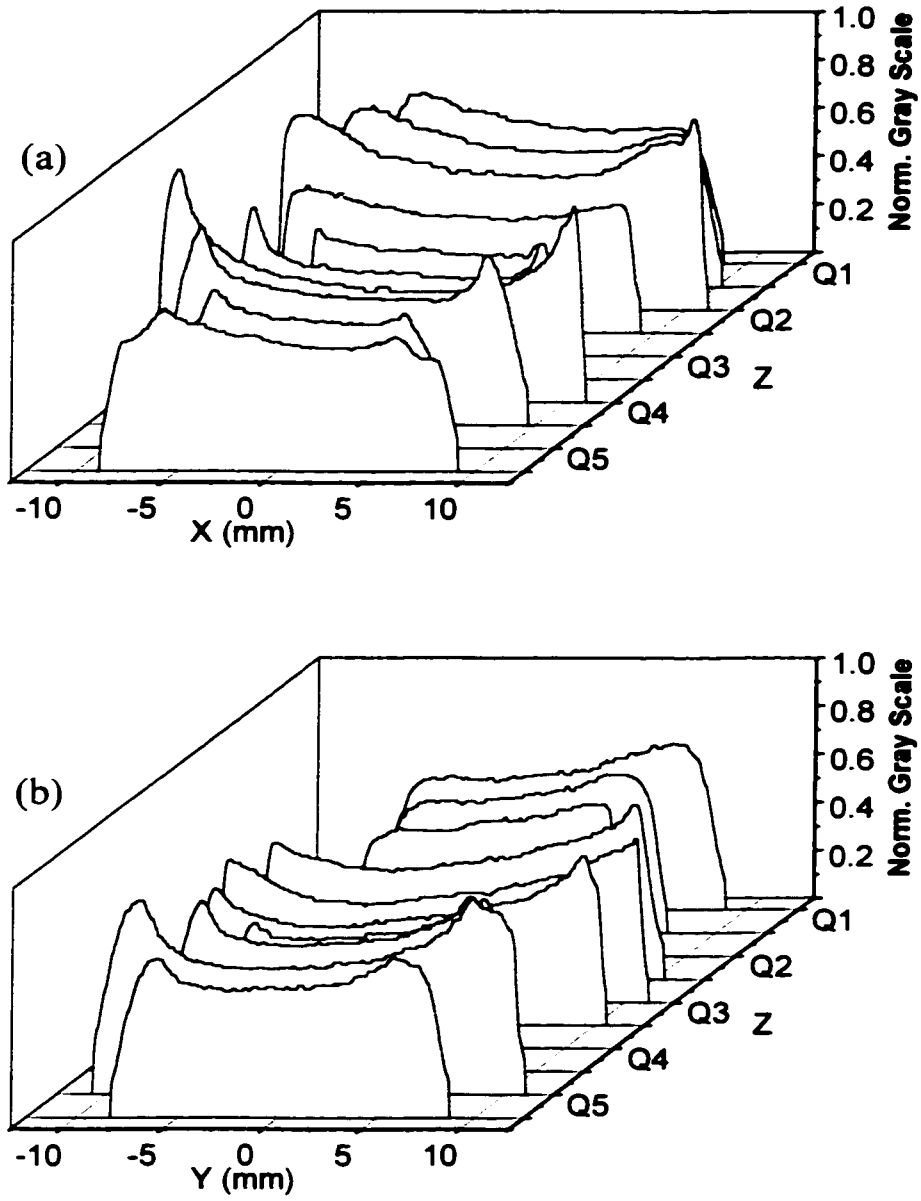

Fig. 5.13. Beam profiles corresponding to the phosphor screen pictures of Fig. 5.12. (a) Horizontal, (b) Vertical.

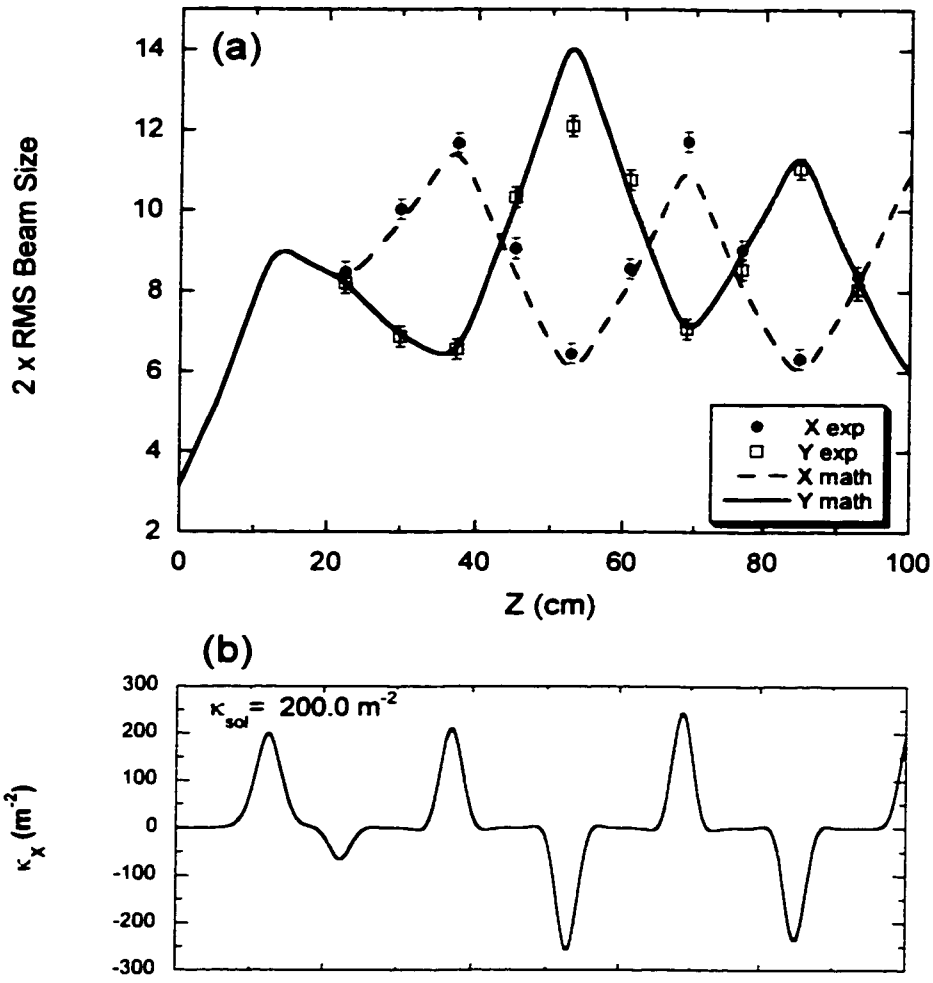

Fig. 5.14. Experiment vs. solution of K-V envelope equations for σ_0=76^0: (a) Envelope data, (b) Focusing function (horizontal).

in App. B.) A factor that is likely to play a more important role than the quadrupole nonlinearities, specially in an extended matching experiment and in *UMER*, is the error in the orientation of quadrupoles. Although we made every effort to correct manually for these errors, through mechanical means and consistent use of the camera, the beam orientations were judged visually. In the future, fiducial marks on the phosphor screen should help in providing a reliable reference for beam orientation. Lastly, a recent development is the realization that errors in the assembly of the two halves of each quadrupole introduce a strong sextupole component (Chapter IV); the evaluation of effects on the quadrupole field gradient itself is under study.

To conclude, general better agreement of theory with experiment can be obtained if the solenoid peak field, initial beam slope, and emittance are slightly adjusted within experimental errors. Instead of making adjustments of this sort, we prefer to adopt a simple criterion for judging matching calculations in a short channel: agreement at "key" points such as the middle plane of the solenoid, at Q1 and at the mid-drift points between quadrupoles (especially the last two).

5.5 Summary and Conclusions

We have used a linear code to design a matching section consisting of a short solenoid and five printed-circuit (PC) quadrupoles. The results for the effective beam size in the channel agree reasonably well with calculations in a linear model as well as with particle-in-cell simulations involving more realistic focusing elements. In this way we have demonstrated linear focusing of a space-charge dominated electron beam in a

solenoid-PC quadrupole system. Furthermore, approximate matching in a root-mean-square sense has been achieved, so the straight matching section can be used for injection into a FODO lattice, as described in the next Chapter.

Also, the use of short-aspect ratio quadrupoles has been validated: it has been shown, within experimental uncertainties, that the design of small aspect-ratio magnetic quadrupoles to focus intense beams can be based on the same criteria used for single particles, i.e. for "zero" current beams.

Finally, some disadvantages of the solenoid-quadrupole system have been made apparent. First of all, solenoid alignment and accurate determination of its strength are two obvious problems. The first one is mostly mechanical in nature and should be solved with an improved design of the mount that allows all degrees of freedom to be adjusted independently and accurately. A solution to the second problem requires more careful handling of powering of the solenoid, possibly following the hysteresis curve, or trying demagnetization of the solenoid, or even direct, in-site measurement of the field. The use of an all-quadrupole matching section, as presented in the following Chapter, will offer an opportunity to contrast two section designs.

CHAPTER VI

Additional Matching Experiments: 20^0 Bend and All-Quadrupole Sections

6.1 Introduction

A natural test of the matching section of Chapter V involves the addition of two periods of quadrupoles as in the *UMER* FODO lattice. The next section describes the 20 deg. bend section used in the extended experiment. Besides testing of the new *UMER* quadrupoles, already introduced in Chapter IV, the experiments employ two bending dipoles based on flexible printed circuits. Their characterization and field properties are presented in Section 6.3, using some of the ideas discussed in Chapter IV. Another important part of the tests is to explore the use of correcting schemes for the beam centroid in the presence of bends and the Earth's field. This is briefly discussed in Section 6.4. The last part of the chapter deals with an all-quadrupole matching section, tested, as the solenoid-five quadrupole lattice of Chapter V, for $\sigma_0 = 85^0$ and 76^0. The advantages/disadvantages of all-quadrupole matching are contrasted with those of the solenoid-quadrupole system.

6.2 20^0 Prototype Bend Section

Figure 6.1 illustrates the setup for the bend experiments. After the experiments with the straight matching section in Chapter V were completed, the transport pipe was "clamped" in place and all quadrupoles and steering dipoles left unchanged. The bend

section, mounted on a post firmly bolted to the floor, was attached to the straight section, and a shorter version of the phosphor screen diagnostics described in Chap. III (Fig. 3.5) added to the other end. A second diagnostics chamber, in the center of the bend section, midway between two pairs of *UMER* quads, was fitted with a slide-seal fixture similar to the one used in the long phosphor-screen transport. The movable pipe had an attached fixture at the end to accommodate a single-surface mirror and a 1-1/4" phosphor screen (Figure 6.2). In this way, it was possible to observe the beam after the first 10^0 bend, by means of a CCD video camera placed vertically over the diagnostics chamber. Despite all attempts to accurately attach the bend section to the straight one, the distance between Q5 and Q6, i.e. between the last small-aperture (SA) quad and the first *UMER* quad, turned out to be off by 0.5 cm: Q5-Q6=15.5 cm. Another issue was the plane of the *UMER* quads, as defined by the support plate (see Fig. 6.1), in relation to the plane of the quads in the straight section. Although the support plate was leveled, and the SA quadrupole rotation angles in the straight section fixed so that they defined an "average" plane, no means to correct for possible relative rotations of these two planes was available. Despite these shortcomings, a successful transport experiment was done, whose results shed some light on possible improvements for the *UMER* design.

Besides the difference in beam parameters between *UMER* and the prototype experiments, bending is done in opposite directions relative to the action of the Earth's field: *UMER* is designed for bending with the "assistance" of the Earth's field, while the prototype experiments require stronger bend dipoles to compensate for that action. Table 6.1 summarizes the differences between *UMER* and the experiments of this work.

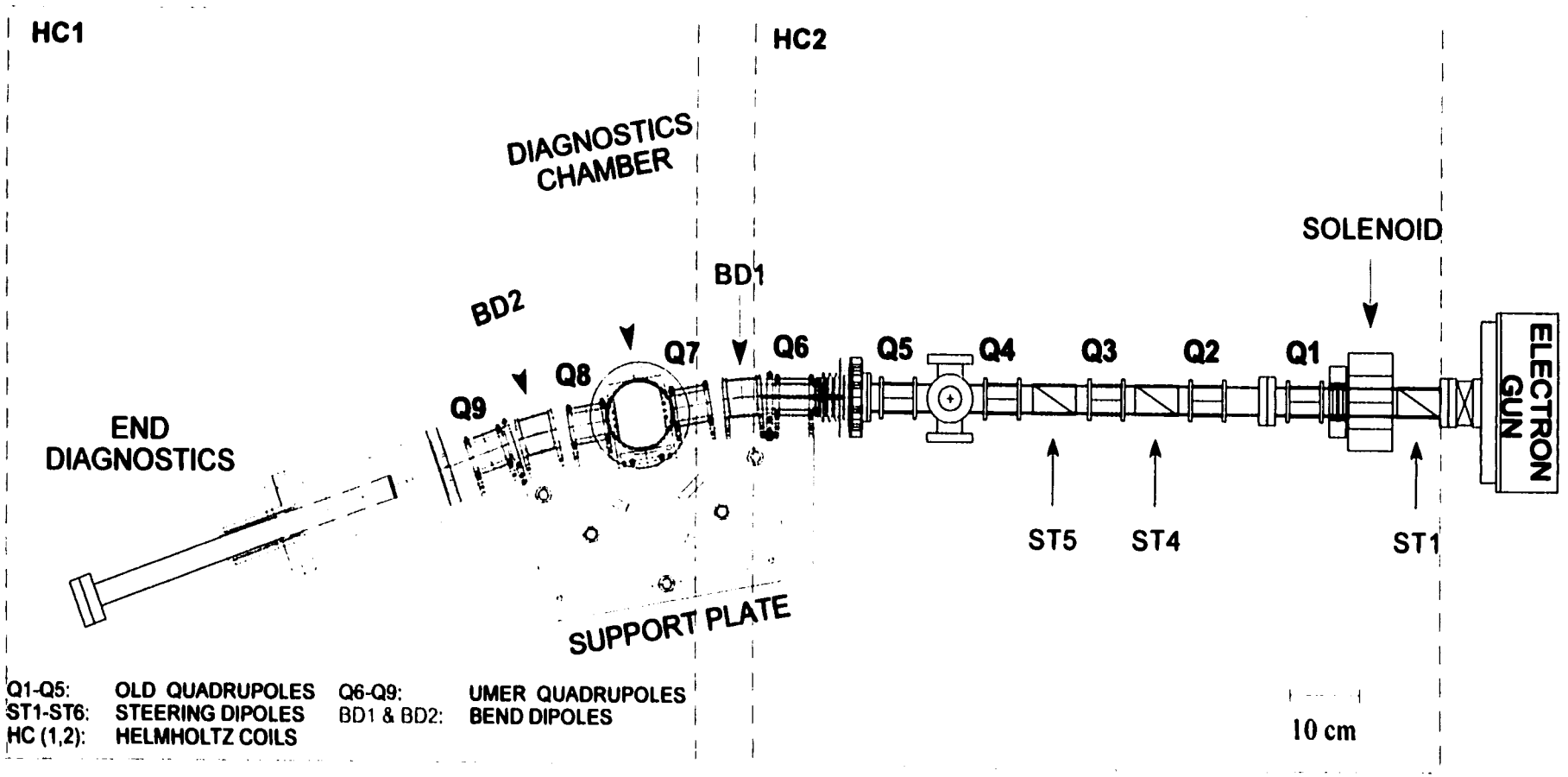

Fig. 6.1. Top view of 20 deg. prototype bend section for *UMER* and matching section. The direction of bending is opposite to the action of the Earth's magnetic field.

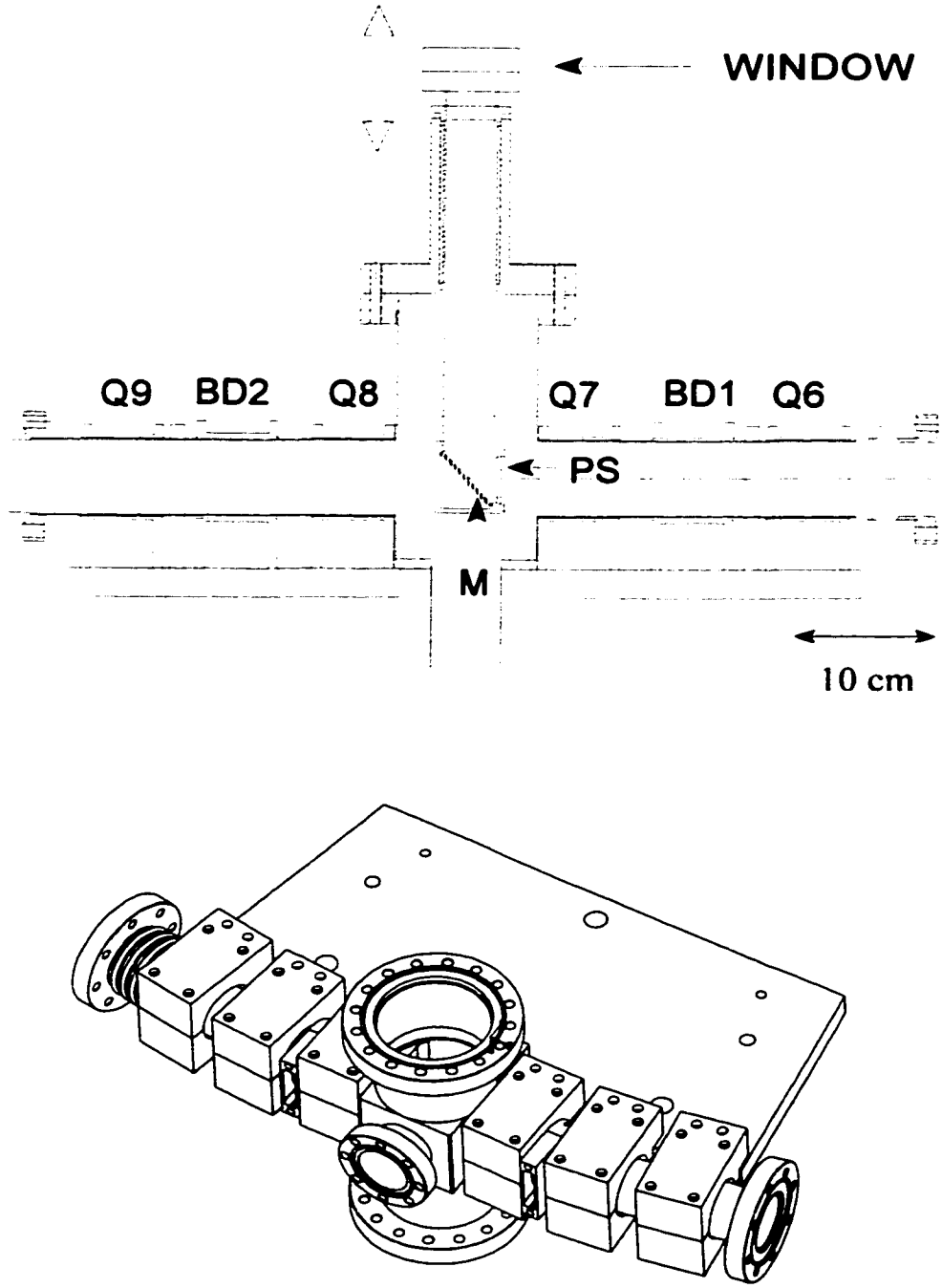

Fig. 6.2. Side and 3D views of the 20-degree bend section in Fig. 6.1. PS represents the phosphor screen, and M a single-surface mirror.

Table 6.1: Prototype Experiment vs. UMER

	PROTOTYPE EXP.	UMER
Beam Energy, Current	4 keV 17 mA	10 keV 100 mA
Full-lattice Period, *S*	32 cm	32 cm
Cyclotron Radius *R*[a]	4.27 m	6.78 m
Orbit Deviation per *S/2* (Eq. [6.1])	3 mm	1.9 mm
Ideal[b] Bend Dipole Current	1.9 A	3.0 A[c]
Experimental Bend Dipole Current	2.15 A	N.A.
Bending	Against action of Earth's field.	Earth's field assisted.

[a] For $B_{Earth} = 0.5$ G.
[b] If $B_{Earth} + B_{corrections} = 0$ G.
[c] If bending is assisted by the Earth's field, the current is reduced to about 2.0 A.

The orbit deviation (Δ), per half-lattice period *S/2*, resulting from the Earth's field is given approximately by

$$\Delta \cong \frac{1}{8}\frac{S^2}{R}, \tag{6.1}$$

where R is the cyclotron radius.

Before presenting detailed results of the bend experiments, we give a brief description of the bend dipoles, the new elements in the transport experiments.

6.3 Characterization of Bend Dipoles

Figure 6.3 (a) shows, close to actual size, the printed-circuit design of the bend dipole for *UMER*. The number of active conductors per quadrant is 20, and the conductor pattern follows an algorithm similar to the one used for the *UMER* quadrupole (Eq. [4.23]), with θ substituted for 2θ:

$$\sin(\theta_i) = 1 - \left(\frac{2z_i}{k'l}\right)^2. \tag{6.2}$$

The spacing between return conductors is constant and equal to $l/42$, with l=44.37 mm. Figure 6.3 (b) shows the measured and calculated on-axis field profiles per amp. Table 6.2 summarizes the main parameters and calculated quantities from MAG-PC. The integrated field is 19.61 G/cm A; for comparison, Eq. [4.20], valid in the continuous surface-current distribution limit, yields an integrated field equal to 19.9 G cm for a two-layered dipole. A detailed study of the multipole content of the bend dipole is presented in Ref [7], and a first report of measurements with the rotating coil was published recently [55].

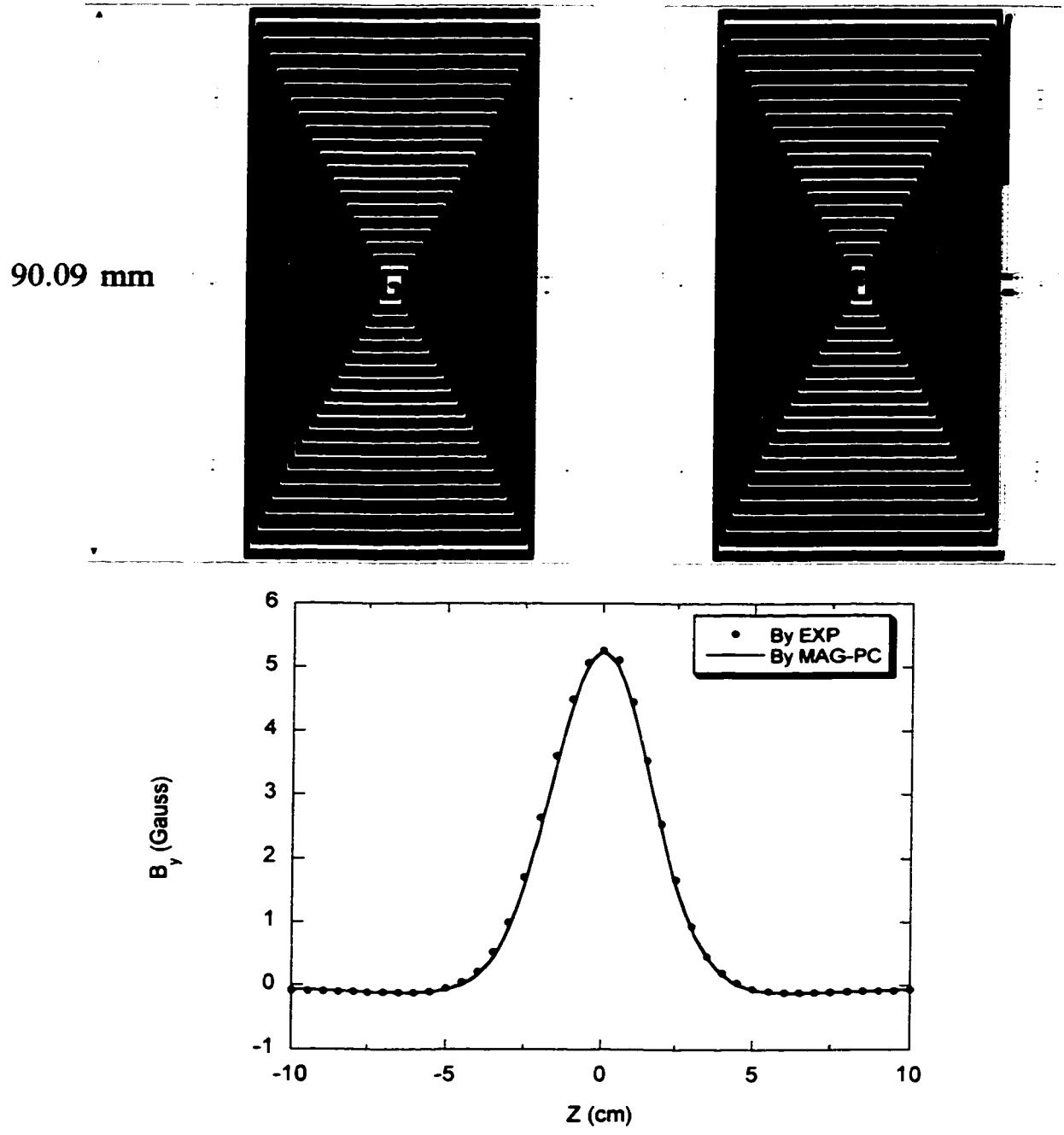

Fig. 6.3. Upper side (top, left), and underside (top, right) of UMER printed-circuit bending dipole (to scale), and transverse (x=0=y) field profile per amp.

Table 6.2: Parameters of UMER Bend Dipole.

Design	20 active conductors/quadrant [61]
Algorithm	Equation [6.2]
Radius and Length, r_0 , l	28.72 mm; 44.37 mm
Aspect Ratio (length : diameter)	0.772 : 1
Effective Length, l_{eff}	3.76 cm
On-axis Peak Field Per Amp:	5.22 G / A
Integrated Field Per Amp: $B_0 \times l_{eff}$	19.61 G cm / A
Peak Field, Current for a 10^0 bend in UMER[a]	15.76 G, 3.02 A
Peak Field, Current for a 10^0 bend in Prototype Exp.[b]	9.93 G, 1.90 A

[a]10 keV electron beam, assuming complete shielding of Earth's field.

[b]4.0 keV electron beam, assuming complete shielding of Earth's field.

The bend dipole, like the quadrupole, is dominated by fringe fields [see Fig. 6.3 (b)]. As a consequence, the effective length of the dipole (3.76 cm) is significantly different from the physical bend length (4.4 cm). However, single-particle calculations with MARYLIE [62], which include the field components through 5^{th} order in the radial coordinate, show a small deviation of the reference trajectory relative to the transport pipe center. Interestingly, the negative tail of the dipole field, at a distance from the center of the dipole roughly equal to the aperture size, starts bending a particle in a direction opposite to the intended direction, so the particle crosses the dipole center with an offset of about 0.1 mm in the outward direction. Further, the PC dipoles are mechanically mounted so that their centers do not coincide with the pipe center, but are displaced about 1.5 mm in the inward direction. The geometry of bending is illustrated in Figure 6.4; in (a) it is assumed that the action of the Earth's field is shielded or balanced by an external field from Helmholtz coils. In practice, beam misalignment, in addition to any residual field from imperfect balancing of the Earth's field, determine the dipole current to be used. Other possible, and, hopefully, minor factors that affect bending come from image forces and field distortions from small magnetization of welds in the bend.

Another important issue is the focusing properties of the bend dipole. The PC dipole can be considered as a rectangular magnet where net focusing in the deflecting plane, i.e. the horizontal or x-plane, is zero [63, 64]. The magnet can be modeled with three elements: two thin lenses and a central sector magnet. For a rectangular magnet, the rotation angle of the "pole" faces relative to the incoming (or exiting) particle is one-

(a)

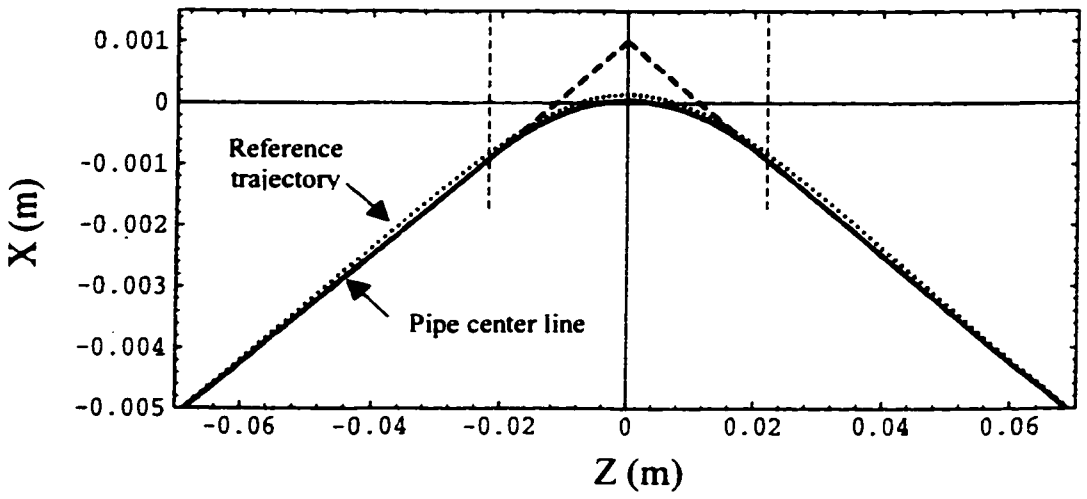

(b)

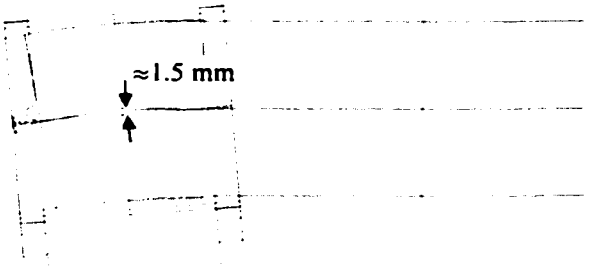

Fig. 6.4. (a) Reference orbit in UMER PC bend dipole (dotted line), from Ref [62], and (b) actual bend dipole setup in UMER.

half the net deflection angle Θ (10^0 in our case). Small defocusing occurs in the vertical plane, with a focal length equal to [63, 64]

$$\frac{1}{f_y} = -\frac{1}{\rho}\tan(\frac{\Theta}{2} - \Psi), \tag{6.3}$$

where ρ is the radius of curvature of the bend (21.48 cm), and Ψ is a *fringe-field* correction angle. This angle can be estimated using a linear model for the fringe field, in terms of the extension of the fringe field (of the order of the effective length, l_{eff}), the magnet gap (the aperture diameter of the PC dipole, $2r_0$), and the bend radius ρ. The result is [63, 64],

$$\Psi = \frac{l_{eff}}{12r_0}\frac{2r_0}{\rho}\left[\frac{1+\sin^2(\Theta/2)}{\cos(\Theta/2)}\right] \approx \frac{l_{eff}}{6\rho} = 1.7^0. \tag{6.4}$$

Thus, the focal length in the vertical plane is, from Eqs. [6.3] and [6.4], $|f_y| \cong 3.7$ m. To compensate for the small dipole focusing in the vertical direction, it is necessary in principle to readjust the strengths of the quadrupoles in the FODO lattice. No such adjustment was tried in our experiment, however, as it involved only two lattice periods in the bend section, insufficient to produce measurable effects of bending on beam rms envelope matching.

6.4 Results of Bend Experiments

Figure 6.5 shows a series of beam pictures starting at the center diagnostics chamber. The beam distortions observed are most probably due to image forces caused by beam misalignment, in combination with accumulated effects from small quadrupole

rotations throughout the straight and bend sections. No beam diagnostics were available just upstream of Q7, the second quadrupole in the bend section, or just downstream of Q5, the last quadrupole in the straight section (a condition that will remain in *UMER*), that could have been used for beam centroid and angle corrections. As mentioned before, since bending was against the action of the Earth's field; careful adjustment of the two Helmholtz coils currents was necessary. The experimental current of 2.15 A for the bend dipoles, compared to 1.9 A expected for a 10^0 bend , indicates that balancing of the Earth's field was not perfect, or that beam misalignment from injection was a factor. Despite these problems, the envelope calculations (Fig. 6.6), which do not include the bends, show reasonable agreement with experiment. Finally, FODO lattice calculations with TRACE 2D (App. B) that include bends and space charge, show a very small effect from dipole vertical focusing over two full periods. The bends are implemented as rectangular magnets, i.e. a sector magnet surrounded by thin lenses with 5^0 pole face rotations. If matching over one FODO period is done with bends included, the original phase advances $\sigma_{0x}=85.0^0=\sigma_{0y}$ are shifted to σ_{0x} =84.9 and $\sigma_{0y}=84.2^0$. These, however, are preliminary calculations that implement the simple linear model presented above for the effect of the fringe fields. Extended experiments and particle-in-cell simulations are obviously needed for a systematic study of bending of space-charge dominated beams.

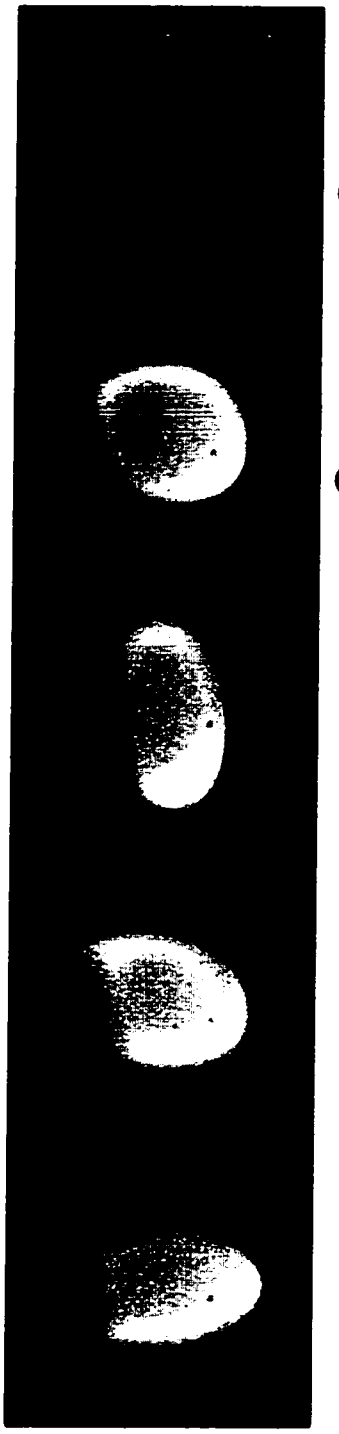

Fig. 6.5. Phosphor screen pictures in the prototype bend section.

"Z" is the linear measure from the aperture, as in Fig. 6.6.

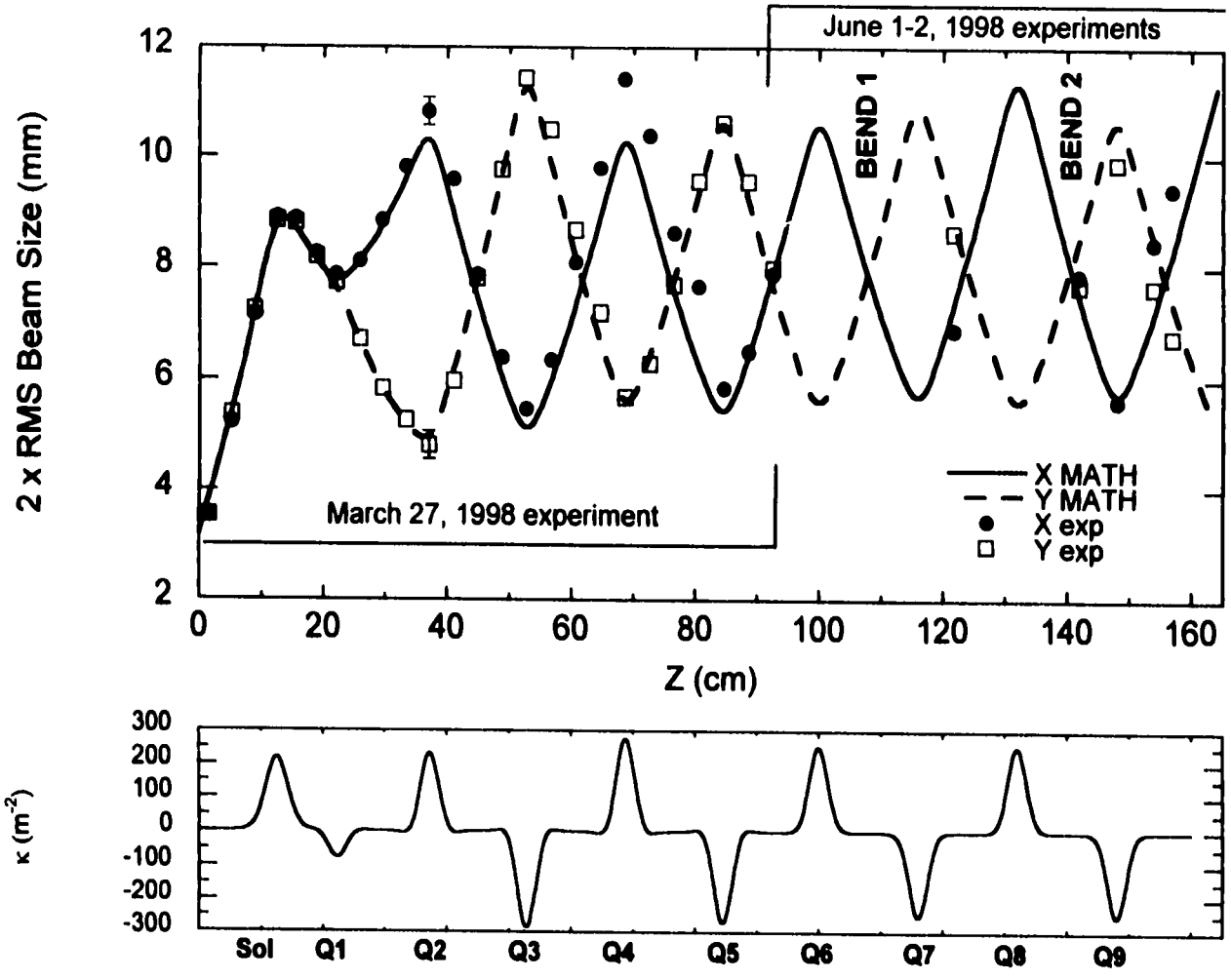

Fig. 6.6 Summary of results of matching experiments in the straight section and the 20-deg. prototype section for σ_0=85 deg.

6.5 Matching with an All-Quadrupole Section

An alternative scheme to the matching lattice of Chapter V is the use of PC quads exclusively, as in most low-energy injectors. Transport experiments with an all-quad lattice were conducted after experiments with three solenoids were completed (to explore the wave phenomenon described in the next Chapter). The special setup illustrated in Figure 6.7 was implemented: two PC quadrupoles were placed as close as possible to each other and to the aperture plane, and steering dipoles based on *UMER* bending dipoles were wrapped around the quadrupole mounts. In addition, a third quadrupole had to be located inside a (unpowered) solenoid. The matching parameters obtained with SPOT (App. B) are given in Table 6.3. Noteworthy from the Table are the currents required for the first two quads; these currents are so high that the quadrupoles had to be operated for short periods and cooled with a fan (see Fig. 6.7).

Figures 6.8 (a)-(b) show the beam pictures corresponding to rms matching at $\sigma_0=85^0$ and $\sigma_0=76^0$. The beam size data vs. envelope calculations are shown in Figures 6.9 and 6.10 for $\sigma_0=85^0$. The original calculations with SPOT use hard-top representations of the quadrupole focusing functions, as in Fig. 6.9 (b). When a smooth representation is employed (Fig. 6.10), the envelopes obtained are different especially near the fourth quadrupole. Since the smooth profiles are a good approximation to the actual fields only in an integrated sense, the overlapping of the actual gradient profiles of the first two quads may not be modeled with sufficient accuracy; the use of hard-top profiles, on the other hand, does not represent the overlapping at all. Besides, another effect that may account for the discrepancy between observed and calculated envelopes

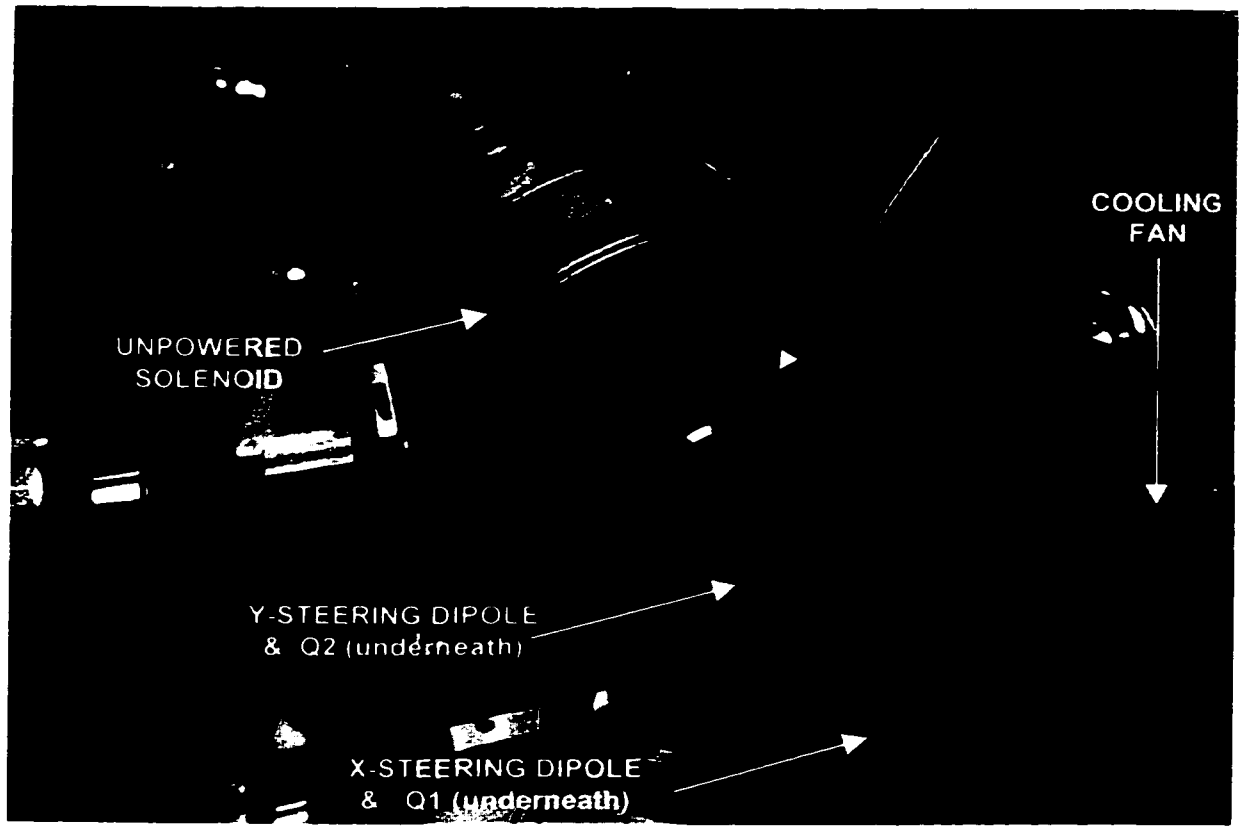

Fig. 6.7. Special setup for matching experiments with six PC quadrupoles.

Table 6.3: Parameters for All-Quadrupole Matching

PC Quadrupole[a]	Distance from Aperture Z (cm)	Peak Focusing[b] (m^{-2}) / Gradient (G/cm) (σ_0=85°, 76°)	Current (A)
Q1	4.70 ± 0.1	464.0 / 9.92, 426.9 / 9.12	1.310 1.205
Q2	10.50	-543.8 / 11.62, -526.9 / 11.26	1.535 1.487
Q3	20.80	360.2 / 7.70, 353.7 / 7.56	1.017 0.998
Q4	32.95	-252.7 / 5.40, -243.7 / 5.21	0.710 0.688
Q5	47.30	254.0 / 5.43, 231.3 / 4.94	0.720 0.653
Q6	63.30	-271.9 / 5.81, -247.7 / 5.29	0.770 0.699

[a]Small-aperture quadrupoles (see Table 4. 1).

[b] SPOT calculations with hard-edge quadrupoles (see Table B.1).

(a)

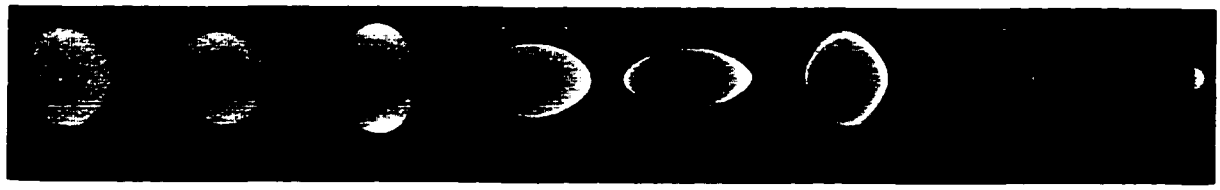

(b)

FIG. 6.8. Partial sample of phosphor screen pictures for six PC-quadrupole experiments: (a) σ_0=85^0, and (b) σ_0=76^0.

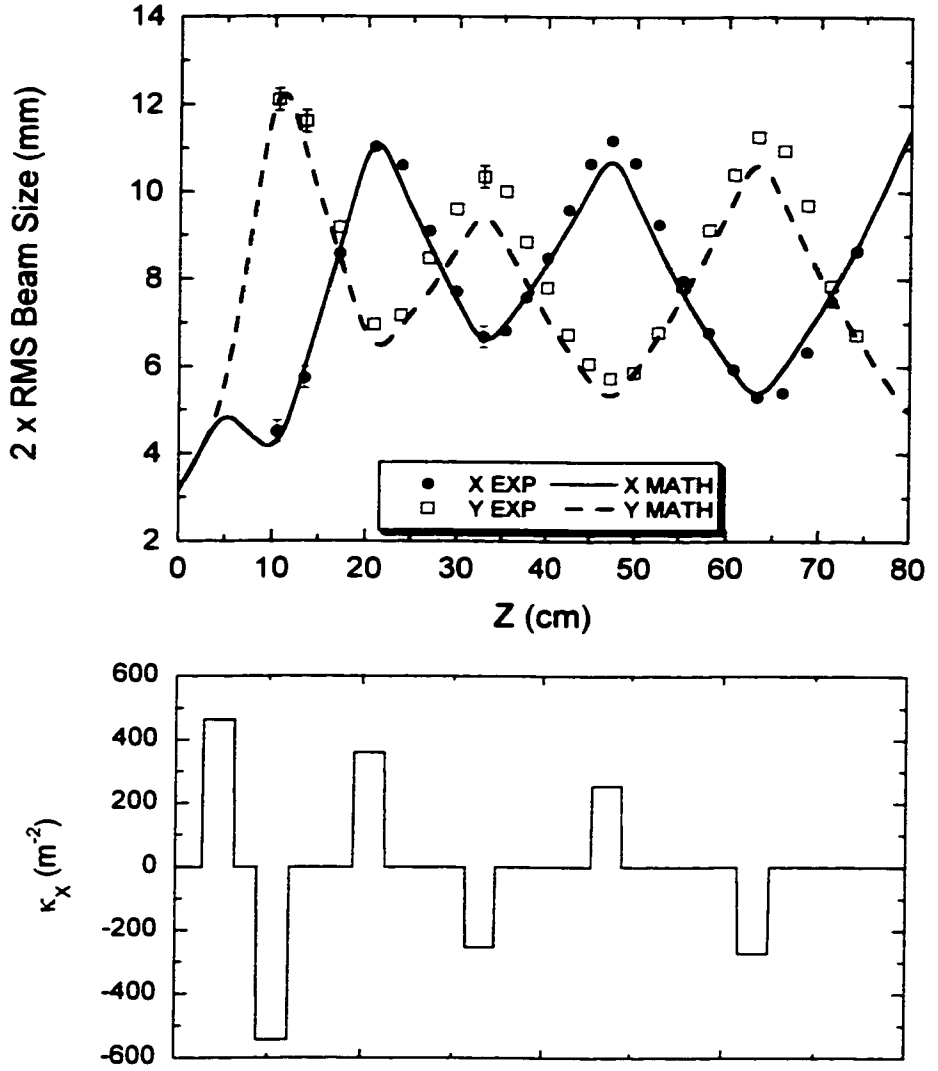

Fig. 6.9. Results of matching with six PC quadrupoles for $\sigma_0=85^0$: (a) Envelope data, and (b) hard-edge representation of horizontal (i.e. "x") focusing function.

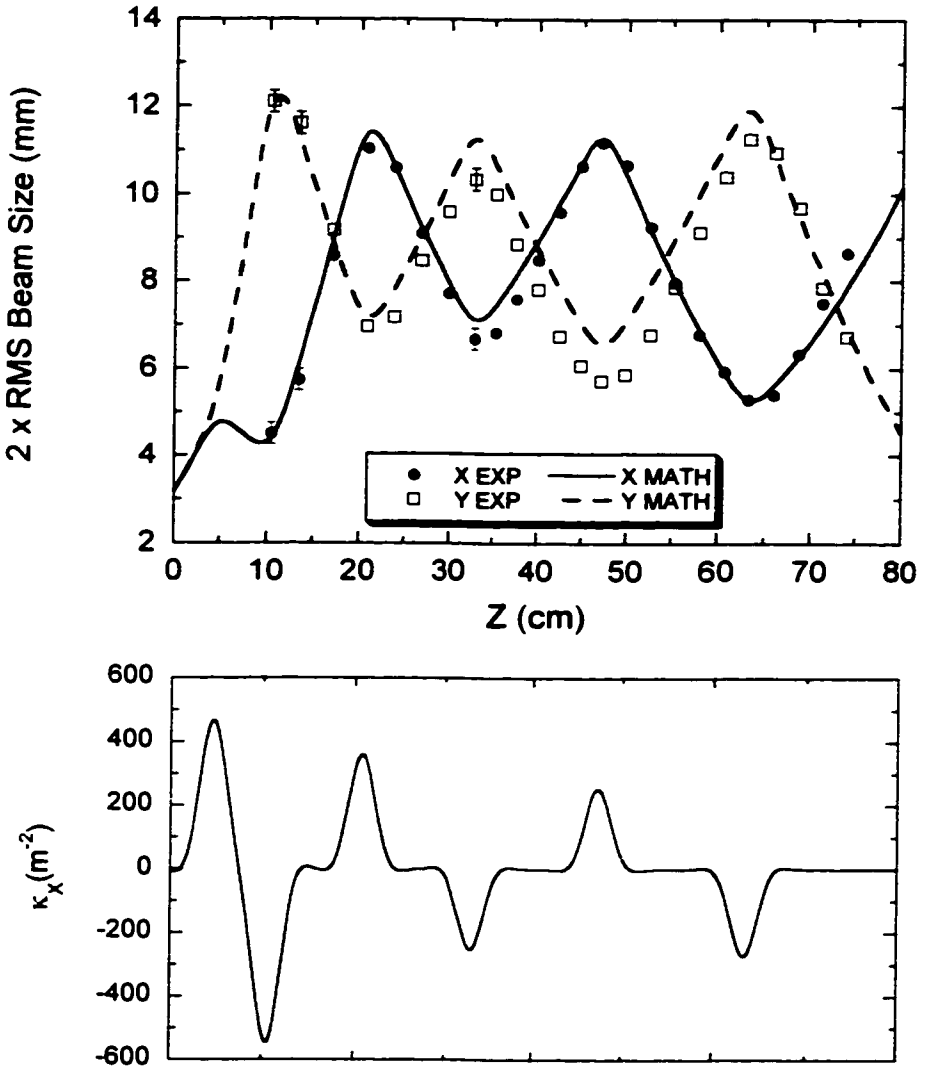

Fig. 6.10. Results of matching with six PC quadrupoles for $\sigma_0=85^0$: (a) Envelope data, and (b) smooth representation of horizontal (i.e. "x") focusing function.

is the action of the solenoid surrounding the third quadrupole on its gradient profile. In any event, there is good agreement between experiment and calculations at the crossing points of the X and Y envelopes, indicating a basically correct scheme for matching with an all-quad lattice.

6.6 Additional Calculations

6.6.1 Matching with $\sigma_{0x} \neq \sigma_{0y}$:

It is of interest to explore the case of a matched beam with different zero-current phase advances in the x and y directions. First, a slight difference is required in any case to compensate for the small vertical focusing from the bend dipoles, and to avoid resonances. However, the case of significantly different phase advances is worth studying in itself because of possible new effects from the enhanced beam anisotropy (see Chapter II, section 2.4.2). Now, instead of the usual four "knobs" for matching the X and Y beam sizes and slopes, an additional four "knobs" are required for the second phase advance. We present in Fig. 6.11 a SPOT calculation for $\sigma_{x0}=76^0$, $\sigma_{y0}=85^0$, in a FODO lattice of small-aperture PC quadrupoles. SPOT (App. B) only allows the specification of four constraints at an exit plane, besides the reference trajectories shown in Fig. 6.11. For the calculation shown, (X,X',Y,Y')=(11.1mm, 0, 4.92 mm, 0) at the midplane of Q6. Trial and error iterations of the calculation may be required for an improved solution.

6.6.2 Round-to-Round Transformation:

It is also of practical interest to study focusing where an initially round beam is transported with a quadrupole channel and brought back to a round shape that will remain so after a drift. This case, of course, does not correspond to matching into a FODO lattice; instead, the geometry and lens strengths in the solenoid-quadrupole system are optimized to yield, after a certain distance, a specified beam size and the same horizontal and vertical envelope slopes. This situation is useful, for example, to simplify a measurement of beam emittance. Figure 6.12 shows the results of a SPOT calculation for the solenoid-PC quadrupole system. The five small-aperture quadrupoles form a symmetric arrangement around the third quadrupole: $(\kappa_1, \kappa_2, \kappa_3, \kappa_4, \kappa_5) = (+110, -250, +305, -250, +110)$ m^{-2}. This *quintuplet* geometry was achieved by simple trial and error with the geometry described in Ref. [57] as the starting point. To our knowledge, no systematic study of similar configurations has been done for focusing of space-charge dominated beams, either in theory or experiment.

6.7 Summary and Conclusions

Transport experiments were successfully completed over about 1.5 m including a 50 cm, approximately, section of two *UMER* FODO periods with two 10^0 bends. A beam-centroid correction scheme based on large Helmholtz coils for Earth's field (vertical component) compensation throughout the channel and steering dipoles in the straight section worked very well. The tests constitute a validation of the matching section design of Chapter V, as well as checks on the *UMER* PC quadrupoles (Chapter

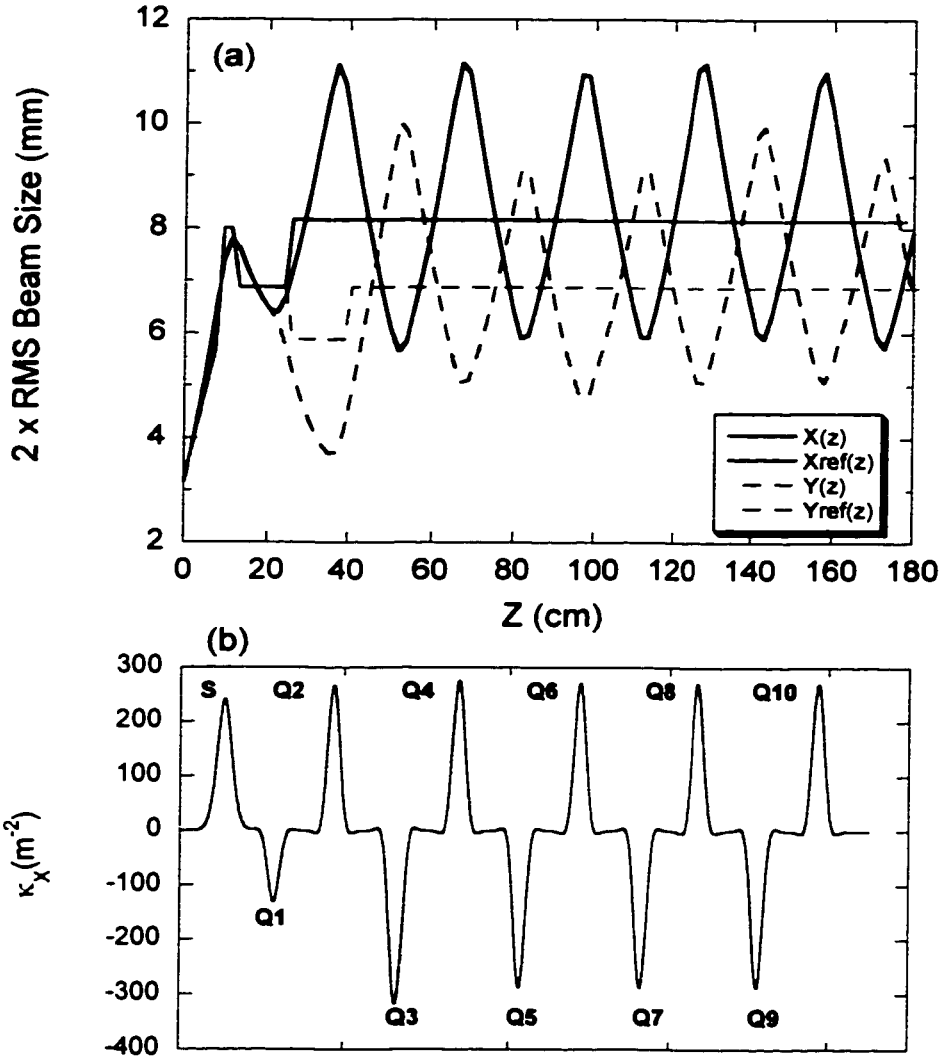

Fig. 6.11. SPOT calculation for $\sigma_{0x}=76^0$, $\sigma_{0y}=85^0$: (a) Envelopes, and (b) Focusing function in the horizontal plane. The quadrupoles are of the small-aperture type.

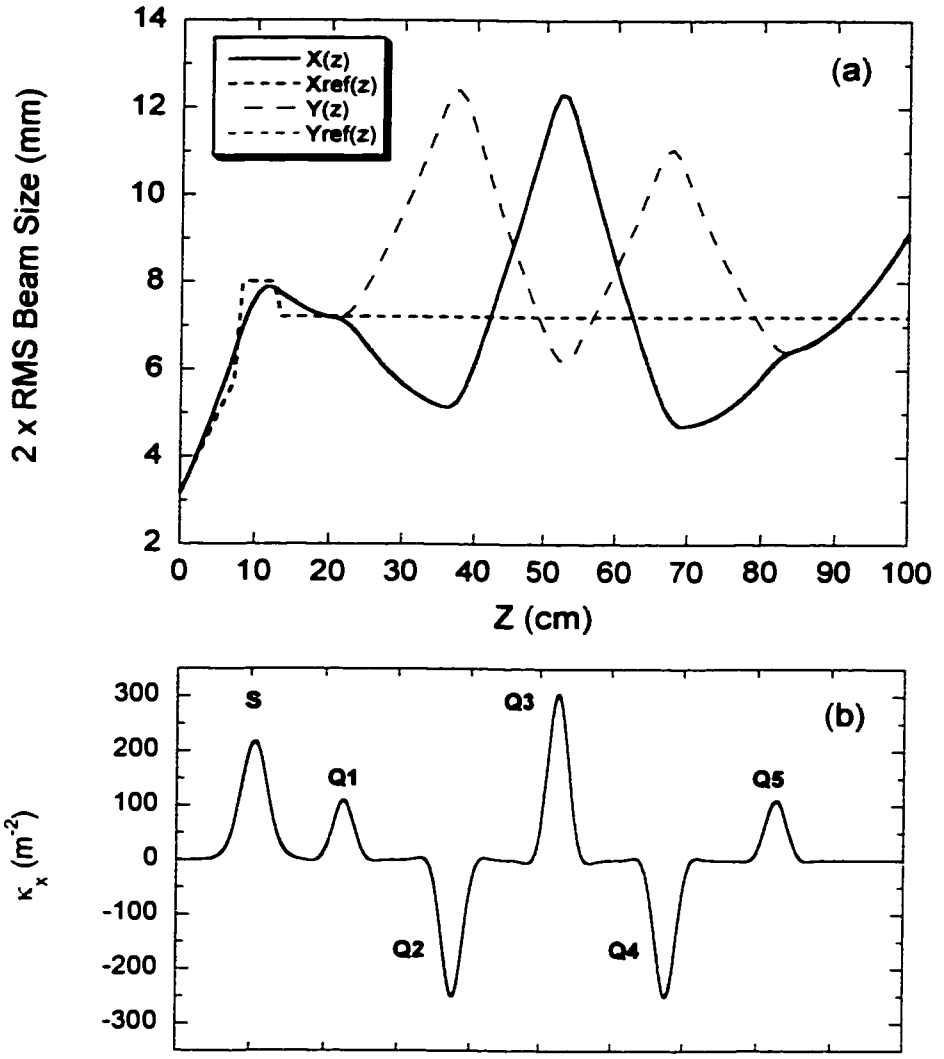

Fig. 6.12. SPOT calculation for a round-to-round transformation. (a) Envelope, and (b) Focusing function of solenoid-quad quintuplet in the horizontal plane.

IV) and bend dipoles. Additional experiments with more bend sections, and particle-in-cell simulations are needed for a systematic study of bending of intense beams.

To conclude, the all-quadrupole lattice provides additional checks of the PC quadrupoles, the initial conditions of the electron beam determined from previous measurements, and the SPOT calculations for matching. Although quadrupoles are known to be inherently more linear than solenoids, substituting a quadrupole doublet for a solenoid introduces new problems like overheating, space availability, and uncertainty in the representation of the doublet field for matching calculations (if strong field overlapping is unavoidable, as it appears to be the case with fringe-field dominated quads). At the same time, the use of a quadrupole doublet as the first focusing element is attractive for two important reasons: first, the alignment problem is simpler than in the case of a solenoid, and second, no hysteresis is present (for air-core quads). From the viewpoint of beam dynamics, on the other hand, the presence of an initially large split of the X and Y envelopes (at Q2 - see Fig. 6.9 or 6.10), must be contrasted with the initial envelope "neck" that appears from the action of a solenoid and a quadrupole (see e.g. Fig. 5.11). More on this issue will be presented in the next Chapter.

CHAPTER VII

Evolution of Particle Distribution in a Collimated Beam

7.1 Introduction

The appearance of a wavelike perturbation in the beam density was discovered during the course of the matching experiments described in Chapter V. To study this phenomenon further, a number of experiments were designed, starting with a single solenoid. To extend the transport distance to about one-meter, two solenoids were added. Finally, experiments were conducted in an all-quadrupole channel; for these tests, the beam is initially focused by a quadrupole doublet right after the aperture. As in Chapter V, the experiments aim at rms envelope matching corresponding to $\sigma_0=85^0$, and $\sigma_0=76^0$ in the ideal periodic systems following the matching sections. When the beam is intentionally mismatched, interesting patterns are seen in the beam transverse density. The results of all these tests prove conclusively that the appearance and main features of the beam perturbation are independent of focusing system.

The discussion in Sec. 7.3 begins with consideration of factors that were originally thought to be plausible explanations for the beam perturbation observed. Next, we motivate the use of a semi-Gaussian (S-G) distribution with a temperature profile to model the beam particle distribution downstream of the aperture. Particle-in-cell (PIC) simulations with the WARP code (App. B) that employ the S-G distribution compare favorably with the observations. The simulations show how the aperture located near the source gives rise to an initial phase-space particle distribution that, under the action

of linear external focusing, evolves to produce the wavelike perturbation. Furthermore, the results of a simple particle-tracking model are presented that reproduce well the onset of the perturbation in all experiments. In this model, the bulk of the beam follows a K-V distribution and the onset of the perturbation is accounted for by the convergence of a number of beam-edge particle trajectories starting at the aperture. It is also shown that this model is consistent with the special trace-space of the collimated beam and the initial S-G distribution of the simulations.

To conclude, the results are examined in the light of the discussion in Chapter II of emittance growth mechanisms, the question of reversibility and entropy change, and Gluckstern modes.

7.2 Experimental Results

7.2.1 Single Solenoid:

The onset and evolution of the density perturbation was studied for two locations of a short solenoid (the same one used in the matching experiments of Chapter V), 12.5 cm and 7.5 cm from the aperture, as a function of solenoid strength. Figure 7.1 shows the phosphor screen pictures corresponding to focusing with the solenoid located at 12.5 cm. For each value of peak axial field of the solenoid, pictures at seven locations from the aperture are shown, starting at about 20 cm from the latter and extending to almost 50 cm. The peak field is varied from about 63 G to 82 G. From the pictures, it is seen that a bright ring appears near the beam edge in every case of solenoid strength, not far from where the beam waist occurs; furthermore, the stronger the solenoid is, the closer

to the beam waist the bright ring first appears. Also, for a given solenoid strength, the size of the bright ring evolves with axial distance from the aperture at a rate that is different from the rate of change of beam size. Similar behavior is seen at a fixed distance from the aperture and varying solenoid strength; in particular, at 40.0 cm from the aperture (fifth row from top in Fig. 7.1), the beam envelope size is nearly constant over a broad range of solenoid peak axial fields (from 70 to 80 G, approximately), but the perturbation clearly evolves from the edge to the beam center.

7.2.2 Three Solenoids:

Two solenoids were added to extend the transport distance to almost one meter. Tables 7.1 and 7.2 summarize the relevant parameters for these experiments and the corresponding matching calculations. Figures 7.2(a)-(b) show the phosphor screen pictures corresponding to σ_0=85^0 and 76^0 in the periodic solenoid system that would ideally follow the third solenoid.

The first picture on the left-hand side in Figs. 7.2(a)-(b), top, is taken between the first two solenoids, and the second one is taken near the plane of the second solenoid. At these two planes, the beam is fairly uniform; the ring perturbation is first seen at about 45 cm from the aperture, after roughly 15 cm from the first beam waist. Further downstream, the ring moves inwards relative to the beam's edge, and a second ring emerges around 86 cm from the aperture.

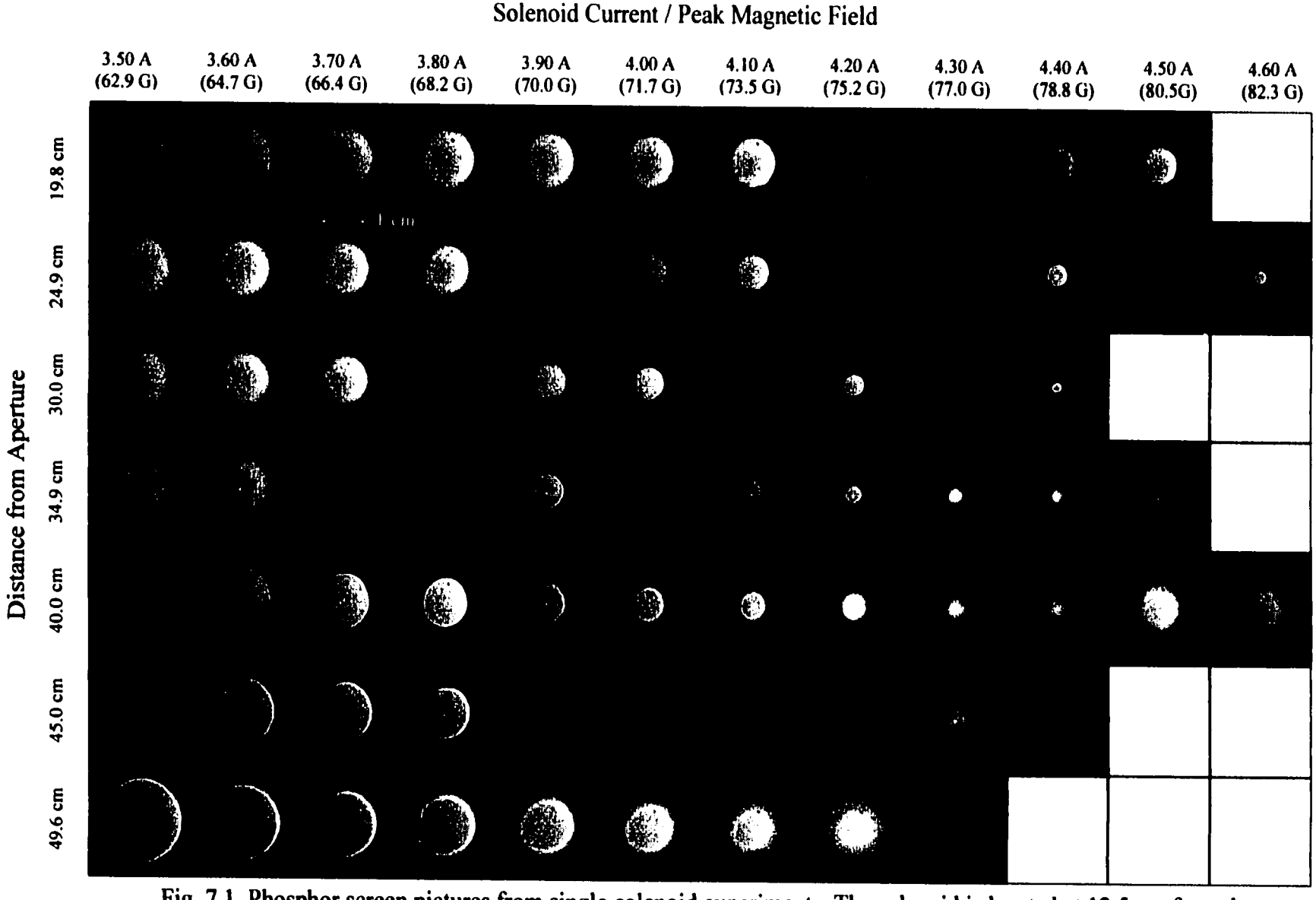

Fig. 7.1. Phosphor screen pictures from single-solenoid experiments. The solenoid is located at 12.5 cm from the aperture; the solenoid parameters are given in Table 3.1.

Table 7.1: Solenoid Parameters

Solenoid	Fit Coefficients (Eq. [3.1])	Effective Length
S1	d = 4.82 cm, b = 3.43 cm, C_0= 0.017.	4.50 cm
S2	d = 3.90 cm, b = 3.53 cm, C_0 = 0.029.	3.99 cm
S3	d = 3.98 cm, b = 3.14 cm, C_0 = 0.019.	3.87 cm

Table 7.2: Matching Parameters from SPOT calculations

Solenoid	Distance from Aperture	Peak Focusing / Peak Field (σ_0=85^0, 76^0)
S1	Z = 12.5 ± 0.1 cm	215.6 m^{-2} / 62.8 G 201.0 m^{-2} / 60.6 G
S2	Z = 36.5 cm	115.5 m^{-2} / 45.9 G 99.1 m^{-2} / 42.55 G
S3	Z = 66.5 cm	175.4 m^{-2} / 56.6 G 138.1 m^{-2} / 50.2 G

(a)

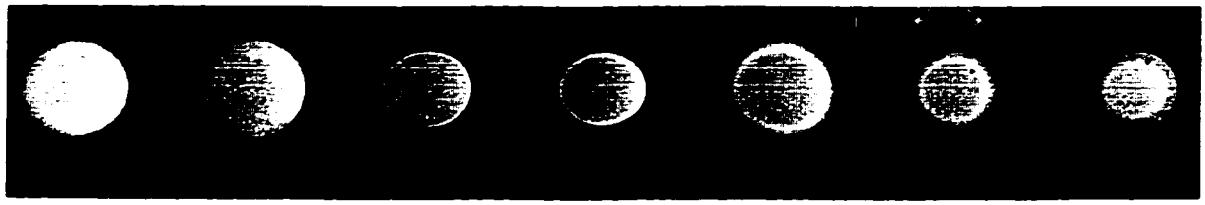

(b)

FIG. 7.2. Partial sample of phosphor screen pictures in three-solenoid experiments: (a) σ_0=85^0, and (b) σ_0=76^0.

7.2.3 Experiments in Quadrupole Channels

As shown in Figs. 6.8(a)-(b) (Chapter VI), the perturbation rings are also observed in alternating-gradient focusing systems. As in the three-solenoid case, the ring appears at about 45 cm from the aperture, near the plane of quadrupole 5; furthermore, the ring is well defined, initially, but evolves so it is brighter in the horizontal direction (x-direction) at a distance of about 70 cm from the aperture. The beam, so to speak, keeps memory of the initial strong focusing in the horizontal direction.

7.2.4 Mismatched Beams:

The quadrupole equivalent to the single-solenoid tests would employ a quadrupole doublet; however, the beam sizes in the two perpendicular directions change very rapidly with axial distance if only the doublet is used. Thus, tests involving different doublet strengths require the presence of the rest of the quadrupoles.

The beam envelope in the all-quad section is especially sensitive to the strength of the second quadrupole, i.e. the one that provides vertical focusing after the large envelope split produced by the first quad (see Fig. 6.9). A change of only 5% in the current yields not only a mismatched beam, but also one where the X and Y envelopes are "disconnected", as seen in Fig. 7.3(c) and 7.3(d). The corresponding beam pictures in Fig. 7.4 (last two columns) show that the perturbation pattern is completely altered, with no closed ring being observed. These results can be contrasted with Figs. 7.5 and 7.6, where the current of the first quad is varied.

The beam near the middle plane of Q5 in Fig. 7.4 has a high degree of anisotropy, with $T_y >> T_x$. As seen in the last three pictures on the same column, the particle density displays features that lack quadrupole symmetry: the internal structures exhibit hour-glass shapes that suggest strong x-y cpoupling. These observations constitute a preliminary test for more systematic studies of beam anisotropy in matched beams with $\sigma_{0x} \neq \sigma_{0y}$, or $\epsilon_x \neq \epsilon_y$; they have been reproduced in recent WARP simulations that are not included here. These last experiments

To conclude this section, we point out that the experiments in the 20 degree bend section reveal the persistence of the perturbation through more than 1.5 m from the aperture (Fig. 6.5). Unfortunately, beam distortions make difficult to study the phase of the perturbation in relation to the observations in the straight section.

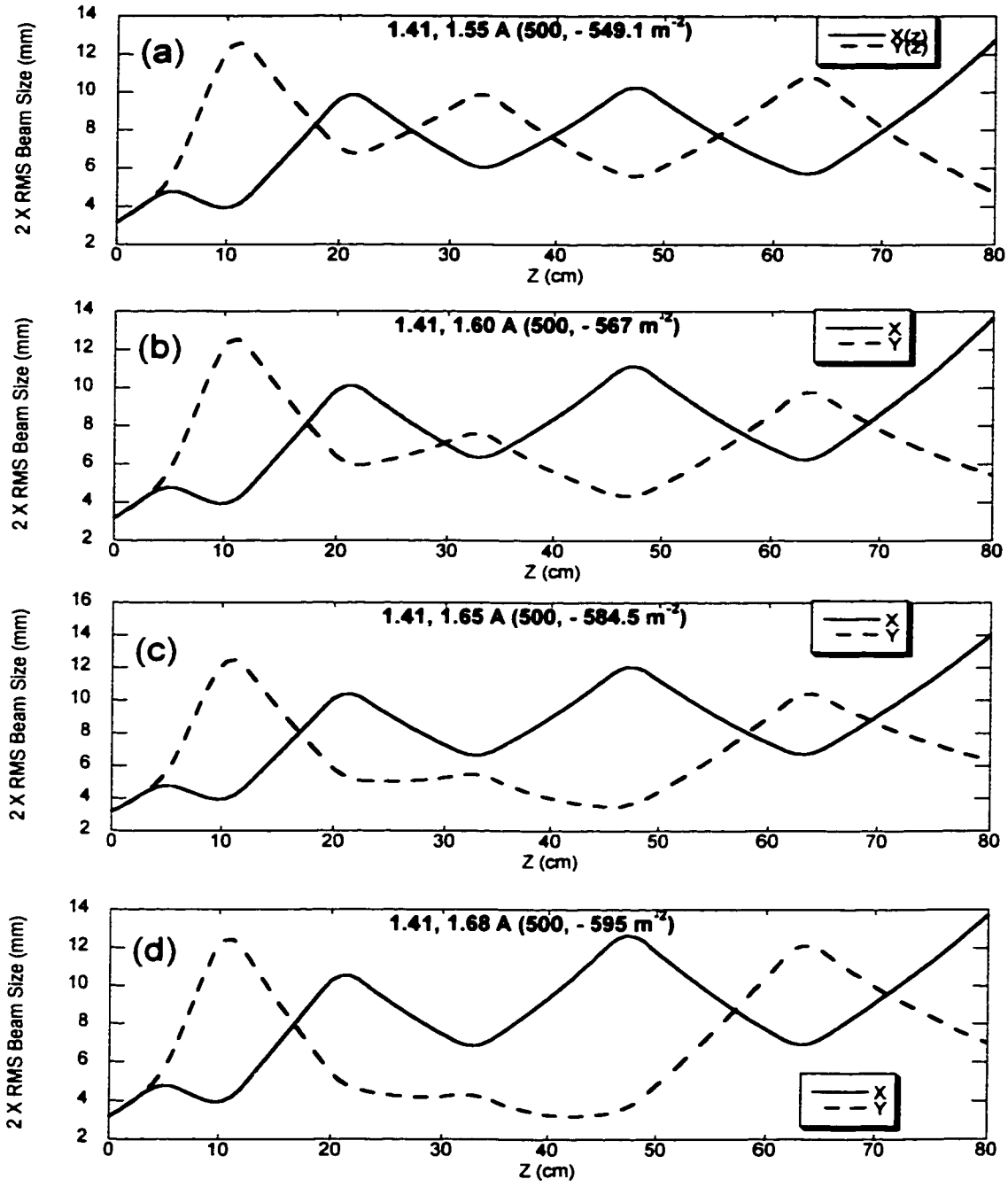

Fig. 7.3. Mismatched beam envelope in six-quadrupole section. The strength of Q2 increases from (a) to (d), while the other quadrupole strengths remain the same (Table 6.3). Fig. 7.4 shows a sample of pictures.

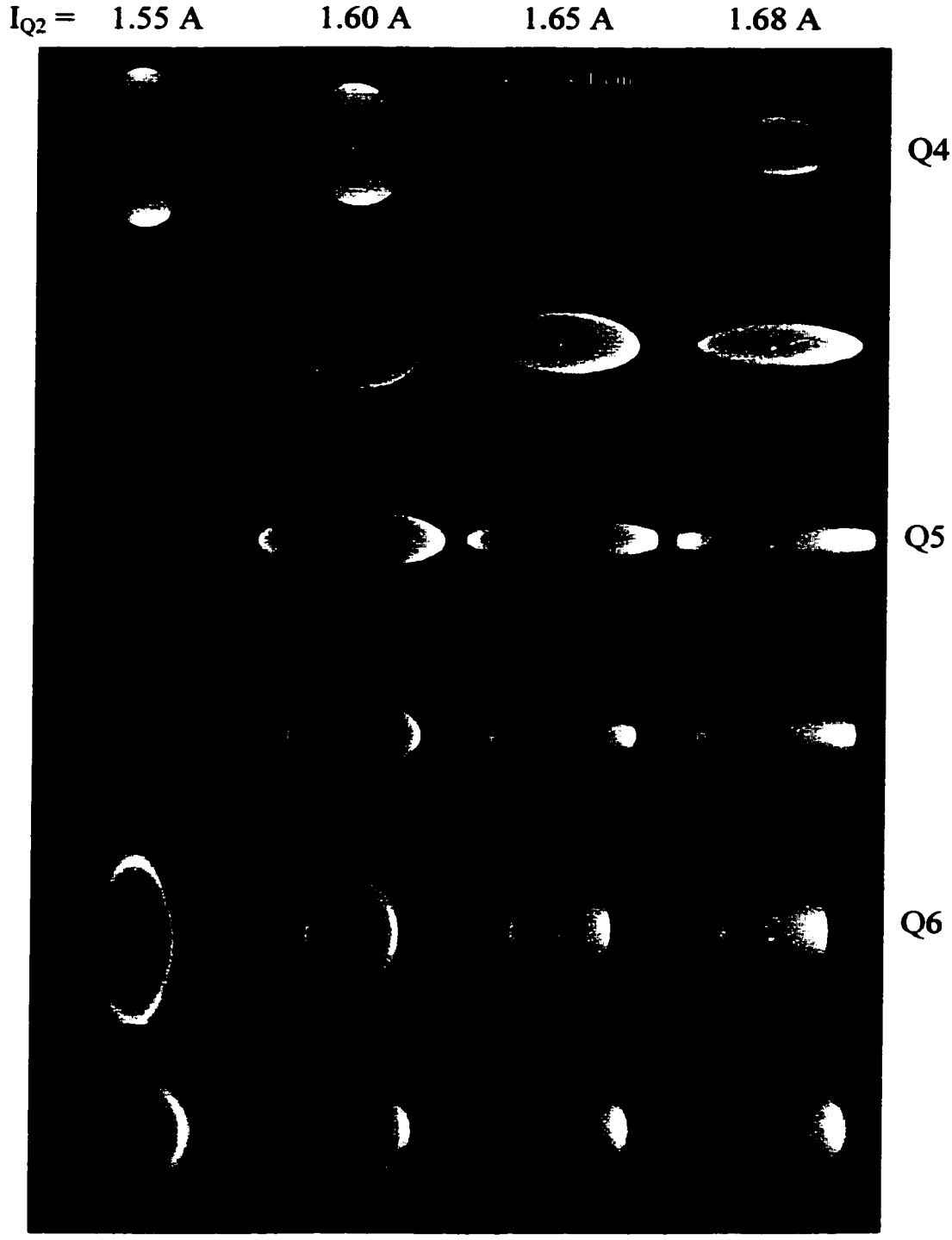

Fig. 7.4. Sample of beam pictures for mismatch conditions illustrated in Fig. 7.3. Note how the perturbation ring "breaks" apart for the mismatch conditions of the last two columns, corresponding to "disconnected" envelopes in Fig. 7.3 (c)-(d).

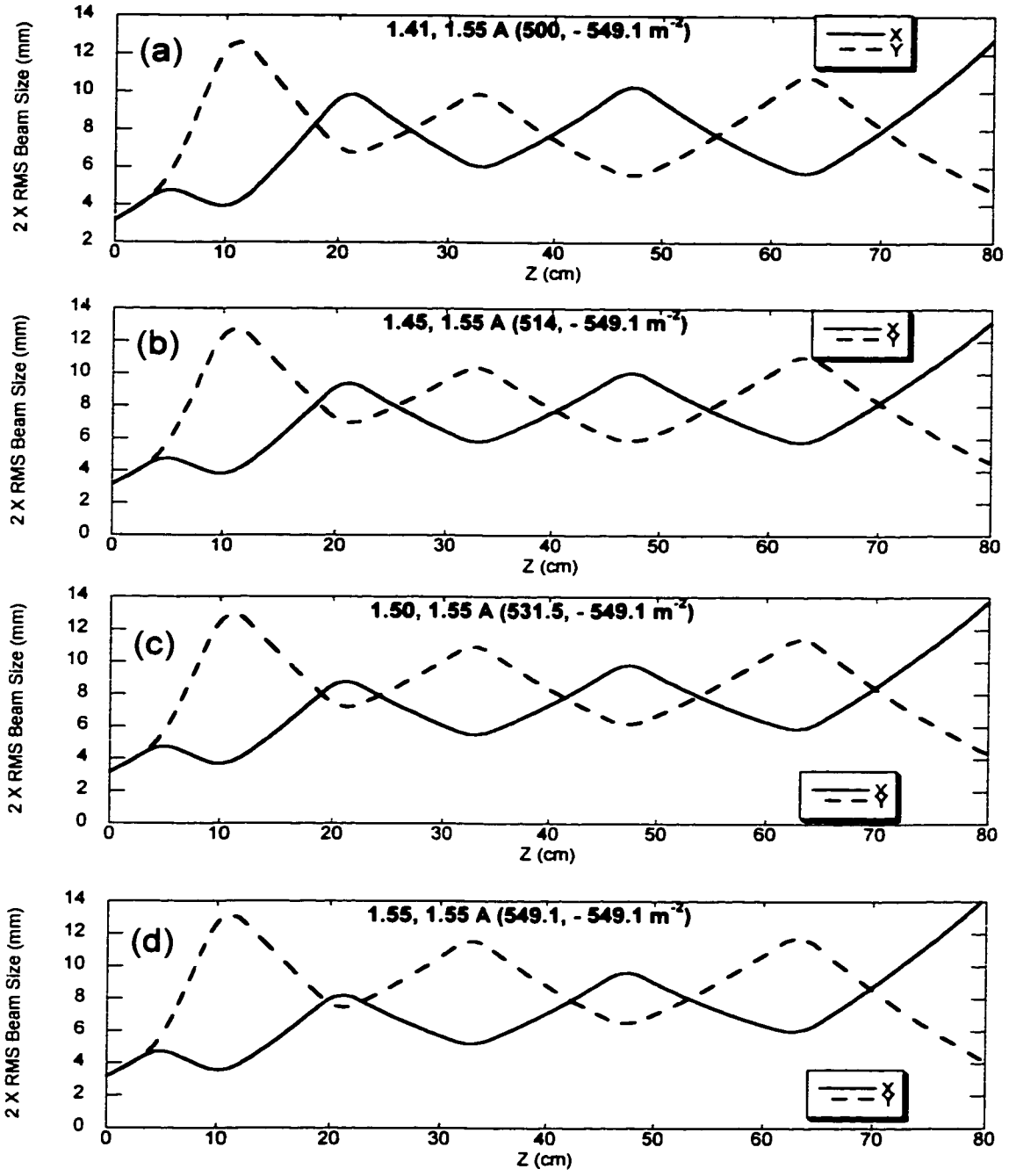

Fig. 7.5. Mismatched beam envelope in six-quadrupole section. The strength of Q1 increases from (a) to (d), while the other quadrupole strengths remain the same. (Fig. 7.6 shows a sample of pictures).

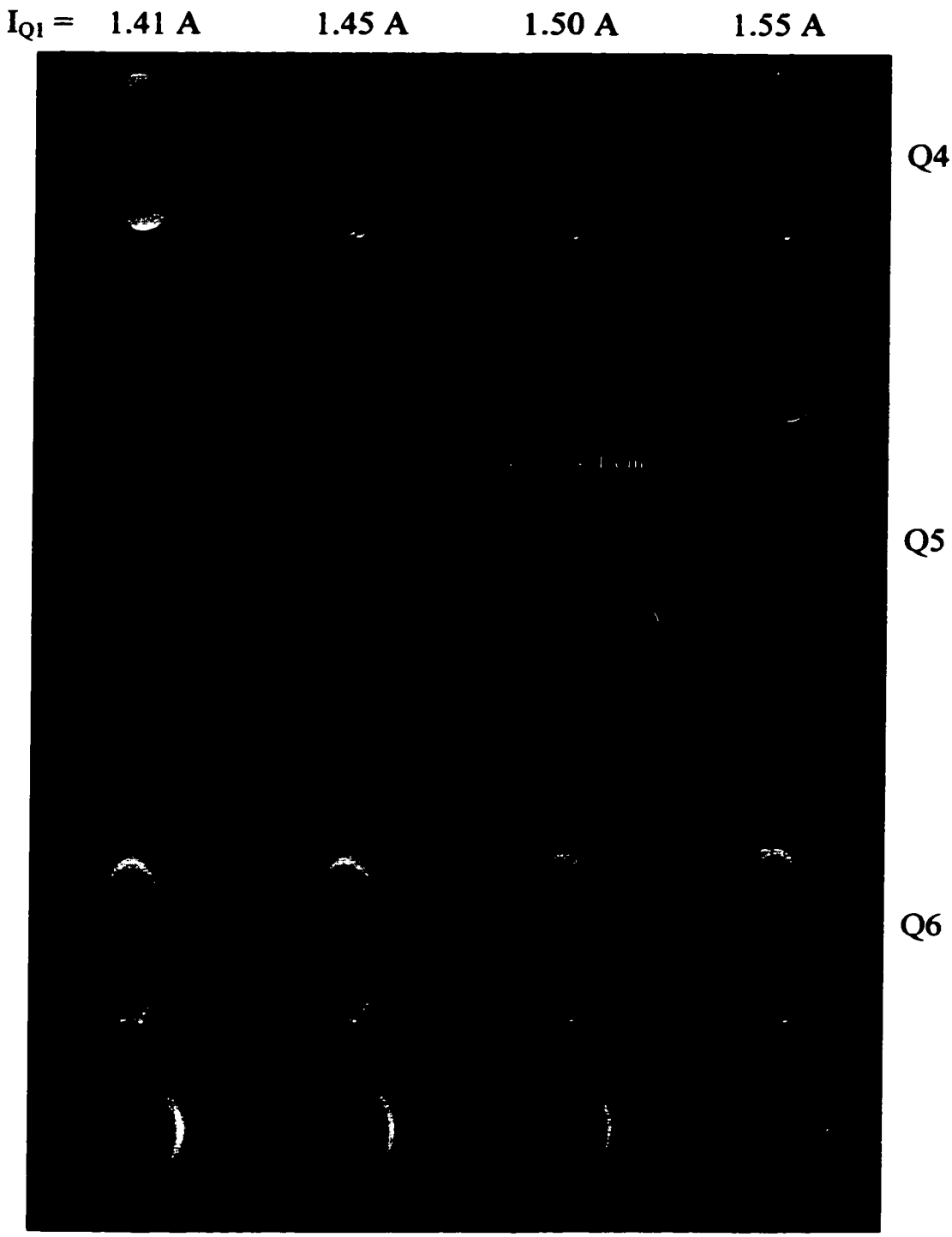

Fig. 7.6. Sample of beam pictures for mismatch conditions illustrated in Fig. 7.5. Compare with mismatch pictures in Fig. 7.4.

7.3 Discussion

We have considered several factors in trying to understand the appearance and evolution of the ring of charge. We show that possible effects from the electron gun and from solenoid or quadrupole nonlinear focusing are not determining factors; furthermore, we argue that "aperture imaging" is not a proper description of the observations. We conclude with arguments to support the idea that the perturbation is mainly the result of nonlinear space charge forces acting on a sheath around the beam edge, a condition that is created by a drastic change in the beam caused by the aperture outside the electron gun. The trace-space of the collimated beam has two main features: the removal of the M-B thermal tails, and the appearance of a population of particles with relatively large transverse velocities near the aperture edge. Since the PIC simulations with WARP provide an important tool, we also devote a significant part of the discussion to the semi-Gaussian distribution, and contrast its properties with those of other more commonly used distributions. The results for the collimated trace-space distribution motivate the use of a simple particle-tracking model that we apply to all the experimental situations presented in the second section of this Chapter and in Chapter VI. Next, we consider emittance growth in the simulations and relate the results to previous calculations by other authors and to the phenomenological theory reviewed in Chapter II. Further, the lack of net emittance growth is contrasted with the clear irreversible character of the evolution of the perturbation, a situation that suggests that the relation between emittance and entropy is far from trivial. We conclude with a brief

comment on other perturbation mechanisms, and the possibility of a unified description in terms of Gluckstern modes in the beam.

7.3.1 Electron Gun Aberrations:

It is known (App. I in Ref. [5]; [45]) that electron guns with a Pierce-type geometry introduce nonlinear focusing (spherical aberration) at the anode aperture, and that this effect is responsible for a large increase in transverse emittance, from a few mm mrad (intrinsic unnormalized effective emittance) at the thermionic cathode to a few tens of mm mrad at the gun exit aperture. Furthermore, the beam profile observed is hollow, resulting in additional emittance increase as the beam relaxes towards equilibrium in a transport channel.

Less known are the observations by Brewer more than 40 years ago [65] of special electron flow patterns coming from convergent-flow guns of the Pierce type. The patterns were observed in studies of conditions for Brillouin flow (Chap. 5 in Ref. [5]); they consist of laminar and "translaminar" flow components. The laminar component is formed by the electron trajectories in the bulk of the beam, while the "translaminar" stream is formed by electrons that cross the beam edge in a periodic fashion. According to Brewer, the translaminar flow is the result of "unequal compression of the beam" due to "spherical aberration in the anode lens of the gun".

Typical parameters of Brewer's experiments are T=1 keV beam energy, 1 to 2 μs pulses at 300-1000 pps, R=2 mm average beam radius, and K=0.02 generalized perveance. The thermionic cathode is shielded, and a drift tube of about 12 cm is fitted

with diagnostics, (a movable phosphor screen and a pinhole for beam current profiling). Brewer presents plots of beam diameter (loosely defined), "outer edge" and on-axis current densities as functions of axial distance, for various values of magnetic field used for uniform focusing. Interestingly, the on-axis current density oscillates with decaying amplitude, and Brewer advances an explanation in terms of "interfering" laminar and translaminar oscillations, and an alternative explanation from another author in terms of "energy conversion to space-charge waves on the beam". Even more suggestive are his calculations of laminar and translaminar trajectories using an analog computer.

The observations in Brewer's experiments have some similarities to our rings, but the basic mechanisms behind the phenomena are different. We argue that the rings observed in our experiment have little or no connection to gun aberrations, specially since the collimating aperture masks most of the "outer" part of the beam that emerges from the anode aperture. Besides, in Brewer's guns, as in most high intensity sources, the combined effects of spherical aberration and strong space charge may lead, with the addition of strong uniform focusing, to beam phenomena similar to the observations of Loschialpo with a single solenoid and a home-made electron gun [50].

7.3.2 External Focusing:

Another question to consider in trying to understand the observations is the possible role of nonlinear focusing in the transport channels. Comparison of envelope calculations based on a K-V model with experimental data shows very good agreement in all cases presented above. Figure 7.7(a) shows an example of results for single-solenoid focusing when the solenoid current is 4.40 A, for a peak field of about 79 G.

Figure 7.7(b) illustrates the corresponding beam profiles in the vertical direction (the beam pictures were shown in Fig. 7.1, third column from right). The beam profile near the waist (at z = 35 cm, labeled "4") is bell-shaped; however, comparison with a profile near the aperture (Fig. 5.3 -Chapter V), where the beam is similar in size (about 4 mm radius) reveals a significant difference. The bell-shaped profile in Fig. 7.7 results from the perturbation which is made visible by focusing; it is not a signal of an emittance-dominated beam. A similar comparison was made in Fig. 5.5 between beam profiles near the midplane of the solenoid and downstream at about 45 cm from the aperture

In conclusion, a linear model fits well the observations even when significant differences in beam profiles exist for the same 2×rms beam size. A simple calculation using Eqs. [3.1] through [3.3] corroborates that the solenoid field is not strong enough to produce significant nonlinear off-axis field components for the beam sizes of the experiments. Additional K-V envelope calculations vs. experiment are presented in Fig. 7.8, for the three-solenoid experiment corresponding to $\sigma_0 = 85^0$. The discrepancies observed can be explained from uncertainties in the solenoid fields. Finally, the results presented in Chapter VI for all-quadrupole matching prove that a linear model in this case is also perfectly adequate.

7.3.3 Aperture "Imaging":

The beam-edge particle tracking model, to be introduced below, originated from the idea that the beam perturbation was somehow an *image* of the aperture. However, it was soon realized that simple "imaging" was not the mechanism involved for at least two reasons. First, a point in the image plane results from the convergence of particle

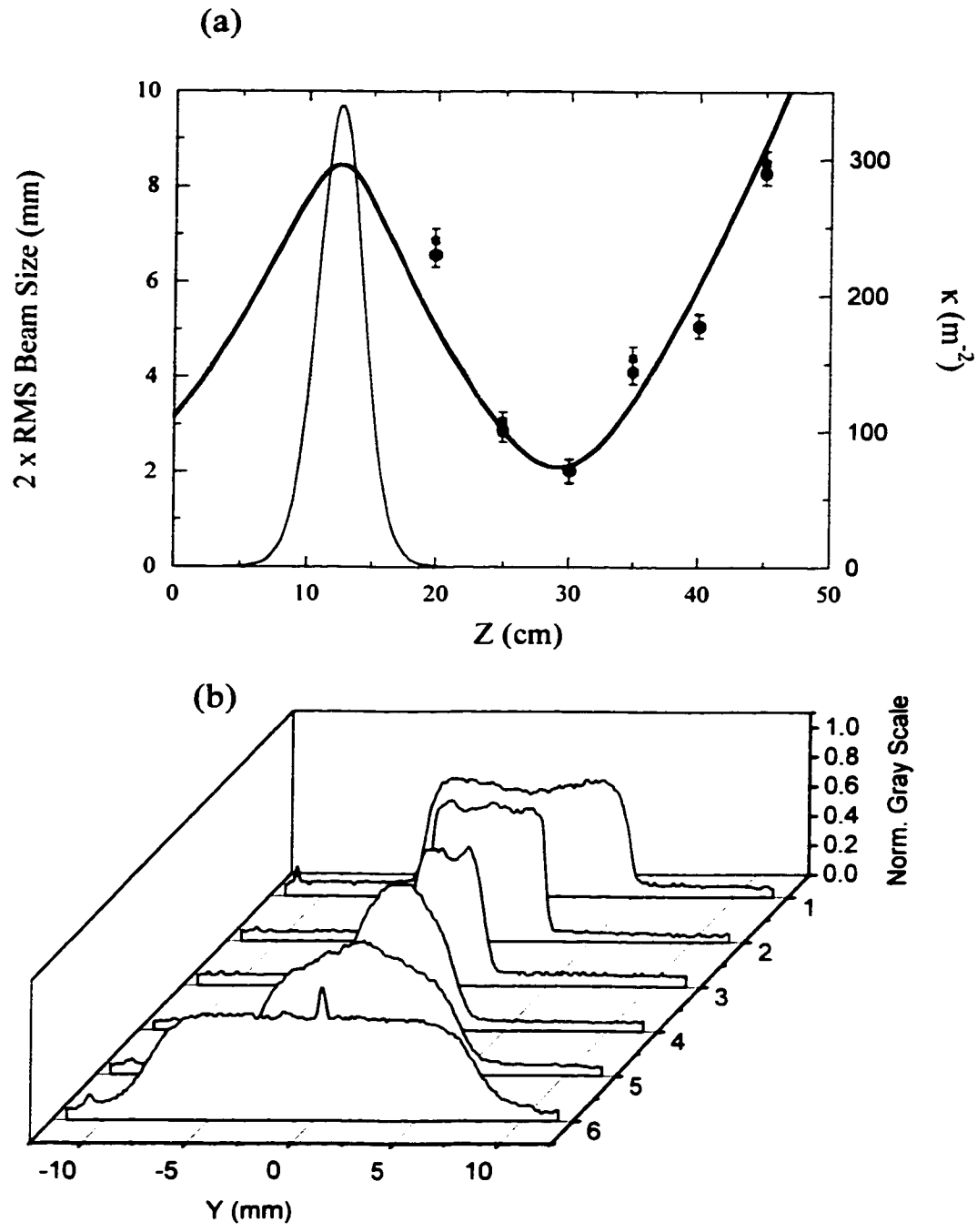

Fig. 7.7. Single-solenoid at 12.5 cm, 4.40 A: (a) K-V envelope calculations from SPOT vs. experimental *x* and *y* beam sizes, and (b) Corresponding beam profiles in the *y*-direction (see also Fig. 7.1).

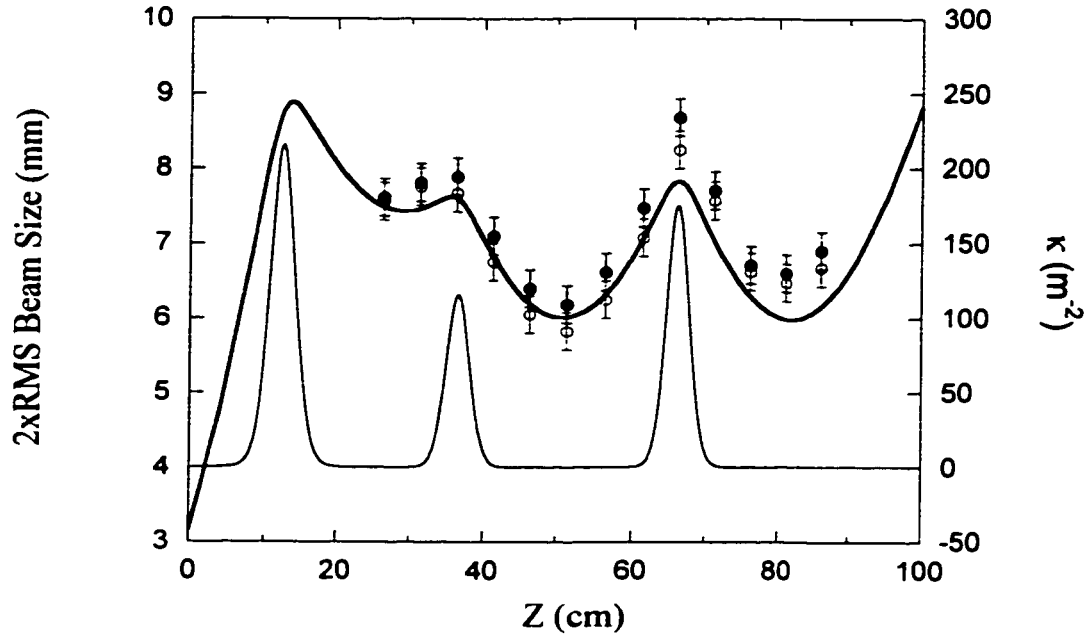

Fig. 7.8. K-V envelope calculations vs. x and y effective beam sizes for the three-solenoid experiment of Fig. 7.2(a) (σ_0=85^0).

trajectories originating from a given point in the object plane, *regardless* of initial slope. This is not the case in the beam perturbation, since only particle trajectories with relatively large initial slopes converge to a point (see Sec. 7.3.5 below). The second reason has to do with the length scale for image formation. For a periodic system with full-lattice period S, the first image appears at a distance from the object equal to one-half the depressed betatron wavelength [45], i.e., at $z_1 = \pi S/\sigma$, where σ is the depressed phase advance per period. If $S = 32$ cm and $\sigma_0 = 85^0$, one gets $\sigma = 24^0$ (Eqs. [1.16] and [1.17] applied to a 4 keV, 17 mA, 67 mm mrad electron beam), so $z_1 = 2.4$ m, almost one order of magnitude larger than the distance for the observation of the first rings. It could be argued that the above calculation does not apply to a non-periodic system like a matching section; however, it should provide at least a correct order of magnitude estimation for the imaging distance.

7.3.4 Semi-Gaussian Distribution and WARP simulations:

To aid in understanding the experiments, we have conducted 2D and 3D PIC simulations using the code WARP. Details of the numerics and modeling are described in the last section of Appendix B and references. The simulations especially address the role of initial conditions. In the simplest approximation, the beam emerging through the aperture is modeled with a semi-Gaussian (S-G) distribution. The normalized S-G distribution is

$$f_{S-G}(x,x',y,y') = \frac{n_0}{2\pi m T_\perp}\Theta\left[a_0 - \left(x^2+y^2\right)^{1/2}\right]\exp\left[-\frac{m\upsilon^2}{2T_\perp}\left(x'^2+y'^2\right)\right], \quad (7.1)$$

where the step function Θ represents a beam of uniform particle density n_0 for $r \le a_0$, a_0 is the beam size at the downstream plane of the aperture, υ is the axial velocity, and

$$T_\perp = \frac{1}{N}\int dx dy \int dp_x dp_y \left(\frac{p^2}{2m}\right) f_{S\text{-}G}, \tag{7.2}$$

is the transverse kinetic temperature in energy units, with $N = n_0 \pi a_0^2$, the total number of particles per unit length. The S-G distribution is an initial, *non-equilibrium* state. It represents a uniform beam with a radially uniform temperature. (Of course, the idea of "temperature" is extended here, in an *ad hoc* way, to a non-equilibrium distribution.) We now use the equivalent K-V beam at the aperture to estimate $T_\perp$: we assume that we can use the *on-axis* temperature of the equivalent K-V distribution (we can identify this temperature with H_0 - see Eq. [2.13]) for the *width* of the transverse kinetic energy part of the model S-G beam in WARP. The transverse kinetic temperature, in Eq. [7.2] appears to be given by $\langle P_\perp^2/2m \rangle = m\upsilon^2 \langle x'^2 \rangle$, since $\langle x'^2 \rangle = \langle y'^2 \rangle$ for an axisymmetric beam. However, it is necessary to subtract the *flow component*, proportional to $(x_m)'^2$, where $(x_m)'$ is the envelope slope at the beam edge, which is non-zero at planes other than the beam waist plane. From $\hat{\beta}\hat{\gamma} - \hat{\alpha}^2 = 1$ for the equivalent beam ellipse, and Eqs. [1.7], we find $\langle x'^2 \rangle = (1/4)\left[\varepsilon^2/x_m^2 + (x_m)'^2\right]$, so the temperature is

$$T_\perp = \frac{1}{4} m\upsilon^2 \frac{\varepsilon^2}{x_m^2} = 0.9 \text{ eV}, \tag{7.3}$$

for a 4 keV electron beam ($\upsilon = 0.125\ c$) with an estimated emittance $\epsilon_{eff} = 4\epsilon_{rms} = 67$ mm mrad, beam size $a_0 = 3.18$ mm, and measured slope at the beam edge $(x_m)' = 32$ mrad.

When the PIC simulations are run with the simple uniform-temperature S-G, only fair qualitative agreement with experiment is observed. The agreement is judged not by comparing the detailed beam profiles in simulations and experiments but by the *phase* of the perturbation, i.e. the radial advance of the bright ring of charge at a given plane along the focusing channel. To facilitate this comparison, the output particle densities from WARP are used to simulate phosphor screen pictures. The simulated pictures are a better reference than simple 1-D profiles because the former provide automatic "averaging" of the full beam profile, i.e. the effects of noise are "spread out", in exact analogy with the information provided by the phosphor screen pictures.

The simulations depicted in Fig. 7.9, bottom series in (a)-(c), also use a uniform-temperature S-G distribution, but start 6.9 cm upstream of the aperture, at the beam waist inside the electron gun. (We note that a M-B distribution at this plane is a better choice; however, since the tails of this distribution are cut off by the aperture, a S-G distribution seems an adequate substitute.) The simulated particle distribution through the aperture has a non-uniform temperature profile that we interpret as the result of collimating an expanding beam. (Two different implementations of the aperture, one of which includes image forces, yield essentially the same results.) Alternatively, a S-G distribution with a parabolic temperature profile right after the aperture produces similar results. As is evident from the figures, the agreement between simulations an experiments is good, despite a difference in the phase of the perturbation, more noticeably in the three-solenoid and solenoid-quadrupole cases. This is most probably due to inaccurate representation of the actual solenoid strengths, and, to a lesser degree, errors in beam parameters, especially the emittance.

(a)

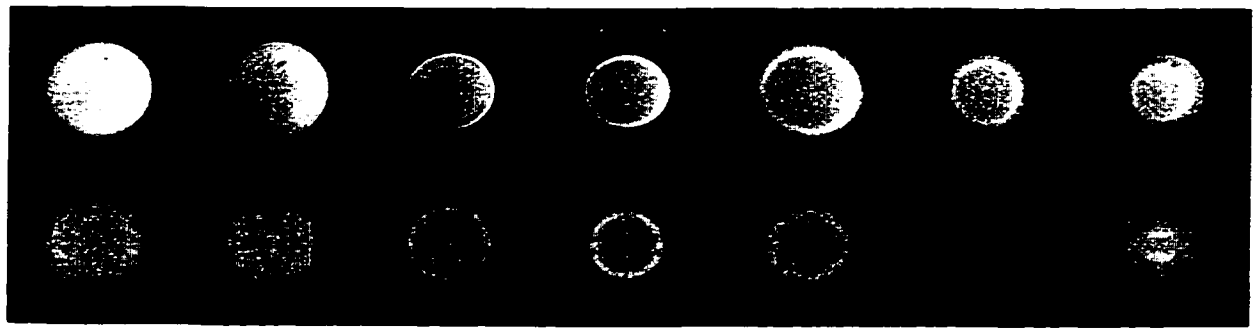

(b)

(c)

Fig. 7.9. Summary of experiments and simulations [26,66] - phosphor screen pictures are on top and PIC simulation pictures on bottom, in (a)-(c): (a) three-solenoid experiment, (b) solenoid - five PC quadrupole experiment, and (c) six PC-quadrupole experiment. In all cases $z = 0$ is the location of the aperture plane, and lens strengths correspond to matching at σ_0=85^0. The scales of experimental and simulation pictures are slightly different.

We gain additional insight for understanding the density perturbation when we replace the truncated distribution in the simulation with an rms equivalent K-V distribution. In that case, no rings appear whatsoever, and the beam distribution remains K-V for the rest of the channel. This leads us to believe that the wavelike perturbation is the result of a force imbalance or lack of equilibrium in a sheath at the beam edge, right after the aperture. As seen in Fig. 7.10(c), the phase space is trapezoidal and tilted, with anomalous particle populations with relatively large transverse velocities near the beam edge. In addition, the distribution lacks the spatial tails of an equilibrium thermal distribution (M-B), which are of the order of a Debye length. In our case, the Debye length is 0.74 cm, which is non-negligible when compared to the beam radius near (and downstream of) the aperture, so the fraction of "missing" particles in a sheath one Debye length is significant. In fact, by assuming a uniform density, a simple calculation shows that close to half of all particles are in a cylindrical shell one Debye-length thick at the beam edge ! However, as we will see, only those particles with sufficiently high initial transverse velocities contribute to the perturbation.

As seen in Fig. 7.11(a), the range of slopes in the equivalent K-V beam at the aperture is $32 \leq x' \leq 38$ mrad, approximately, for particles within about 0.5 mm of the beam edge; the simulated trace space in Fig. 7.11(b), on the other hand, indicates that particles near the beam edge may exist initially with slopes larger than 40 mrad. Furthermore, tracking of particles near the tips of the trapezoidal distribution of Fig. 7.11(b) or Fig. 7.10(c) shows that the radial locations of the particles correlate well with the location of the rings in pictures from experiments or simulations, in the initial stage,

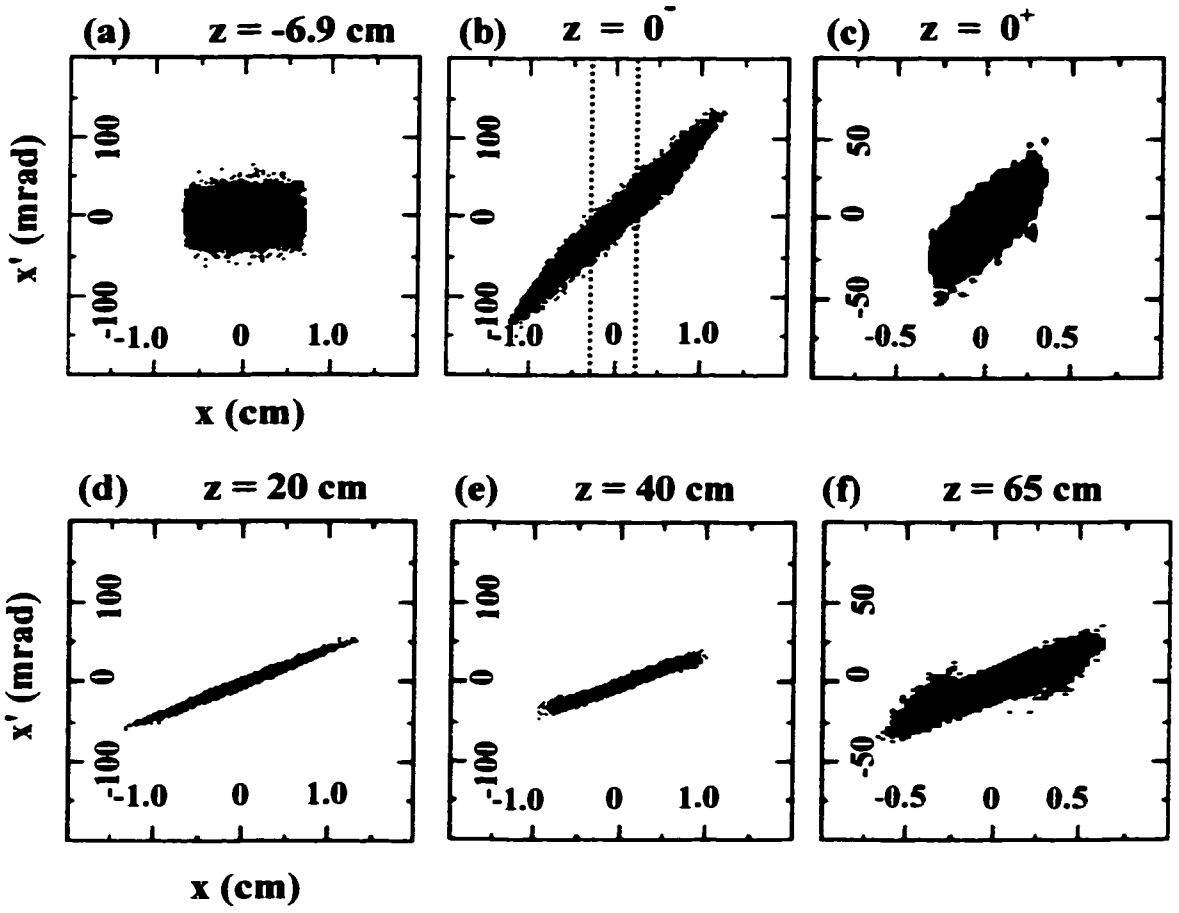

Fig. 7.10 [26]. Horizontal projection of trace space at (a) the beam waist, 6.9 cm upstream of the aperture, (b) the upstream plane of the aperture - the dotted lines indicate the 0.32 cm (radius) aperture, (c) the downstream plane of the aperture, and (d)-(f), evolution in the all-quadrupole lattice (Fig. 6.8a) - note the blown-up scales in (c) and (f).

(a)

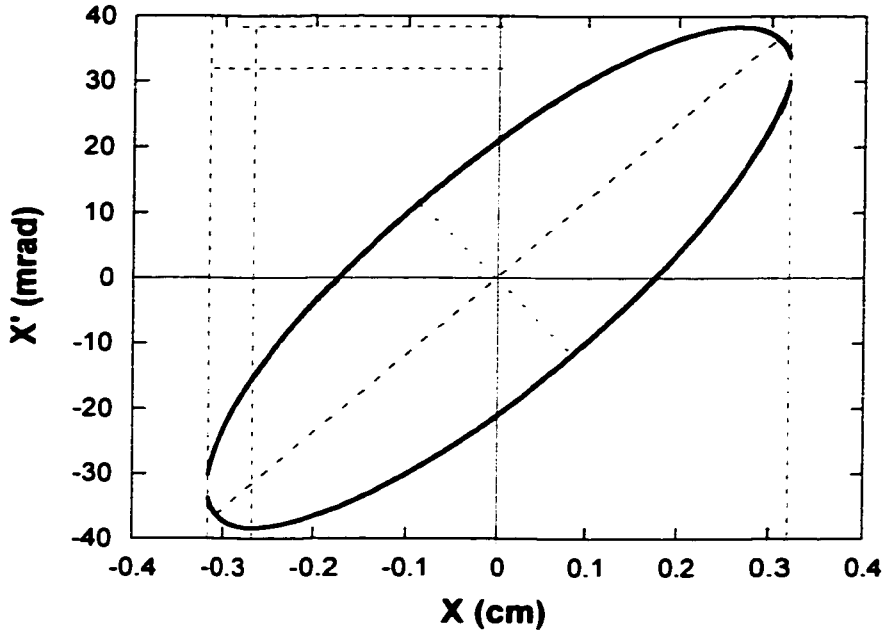

(b)

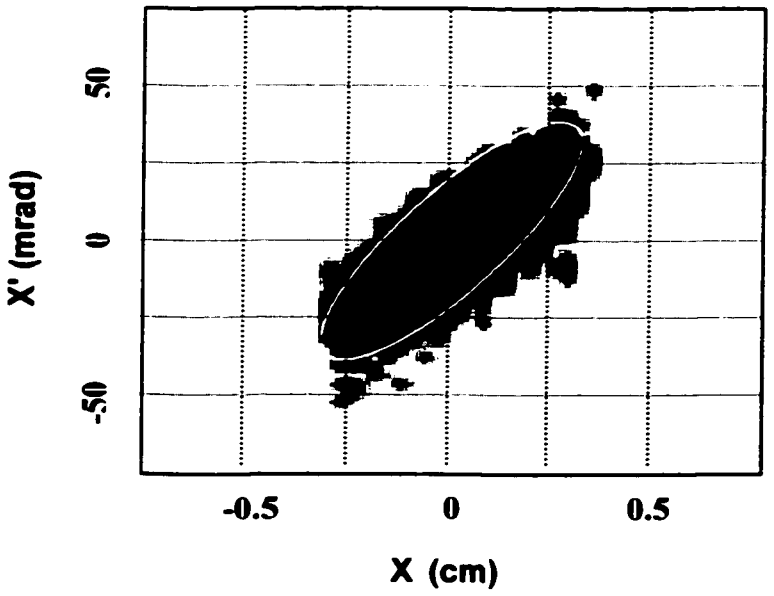

Fig. 7.11. (a) Equivalent K-V beam ellipse at downstream plane of aperture and (b) Trace space from WARP simulations [same as Fig. 7.10(c)]. The Twiss parameters from experiment are $\hat{\alpha} = 1.52$, $\hat{\beta} = 0.151$ mm/mrad, and $\hat{\gamma} = 21.9$ mrad/mm.

i.e. over a few cm from the aperture. This provides the justification for the trajectory calculations based on a K-V beam model that we present next.

7.3.5 Beam-Edge Particle Tracking:

The observed onset and initial evolution of the beam perturbation can be reproduced well with a simple calculation involving a K-V distribution for the bulk of the beam, and a special family of particle trajectories that start at the aperture near to and inside the beam edge, with relatively large initial slopes, and converge inside the beam with the use of external focusing. For the solenoid experiments, the relevant equations are the differential equation for the beam envelope of an axisymmetric beam and the associated single-particle trajectory equations:

$$R''(z) + \kappa(z)R(z) - \frac{K}{R(z)} - \frac{\varepsilon^2}{R^3(z)} = 0, \tag{7.4a}$$

$$r''(z) + \kappa(z)r(z) = \begin{cases} \dfrac{K}{R^2(z)}r(z), & \text{if } r(z) \le R(z), \\ \dfrac{K}{r(z)}, & \text{if } r(z) \ge R(z), \end{cases} \tag{7.4b}$$

where the different symbols have the same meanings as in Eqs. [1.14], and the generalized perveance K and effective emittance ϵ are given in Table 5.1.

The initial conditions for the solution of the equations are *R(0)=0.318 cm* (i.e., the aperture radius), *R'(0)=32 mrad* (experimentally determined beam slope - see Chapter V), *r(0)=0.300 cm*, and *r'(0)≥30 mrad*. The results of solving the equations for focusing with one and three solenoids are shown in Figures 7.12(a)-(b). Three test trajectories

have initial slopes larger than the initial beam slope; the motion observed can be described as being "translaminar" as opposed to the approximately laminar trajectories calculated for particles starting with slopes that are smaller than the initial beam slope. The choice of slope values is justified for purposes of illustration only; the population of "translaminar" particles has initial slopes that are only in the immediate vicinity of 40 mrad, approximately, as discussed above.

Remarkably, the location on the *z-axis* of the ray crossings in Fig. 7.12(a)-(b) agree, within reasonable experimental errors, with the location of the phosphor screen where the bright rings first appear; there is also agreement between the ring sizes in the phosphor screen pictures and the values of r at the crossings. The comparison between calculation and experiment is shown in Fig. 7.13 for three cases of single-solenoid focusing. The same particle-tracking procedure was repeated for the set of observations made with the solenoid at 7.5 cm from the aperture, and the same focusing strengths as in Fig. 7.13; reasonable agreement with experiment was found again.

The ray tracing technique described provides a visual understanding of the onset of the perturbation, but must be examined in some more detail. The starting radial distance $r = 3.0$ mm (0.18 mm inside the beam at the aperture) is arbitrary to some degree; if $r =$ 2.8 mm is tried, for example, with the same initial slope values (still consistent with the trace-space - Fig. 7.11 -, the crossing of trajectories is displaced downstream about 2 cm (axial direction) and radially to a point very close to the beam edge. This is easily understood, as particles that leave the beam, but originate deeper inside it, are affected more by nonlinear defocusing from the bulk of the beam. Of course, at even smaller

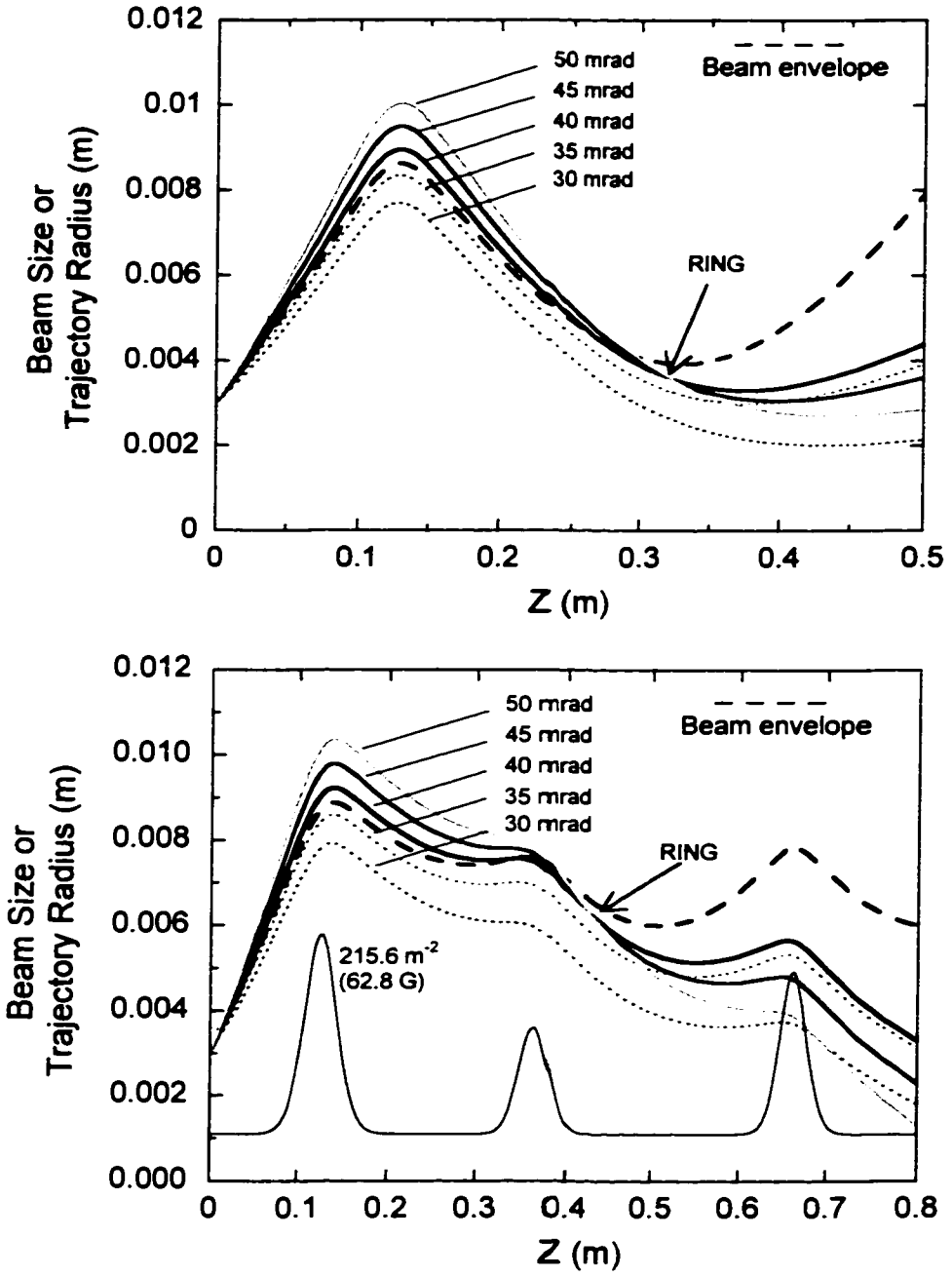

Fig. 7.12. Particle-tracking for: (a) single solenoid at 12.5 cm and 281.7 m^{-2} (4 A), and (b) three solenoids for $\sigma_0=85^0$. The beam slope at z=0 is 32 mrad; all 5 trajectories shown start at r=3.0 mm.

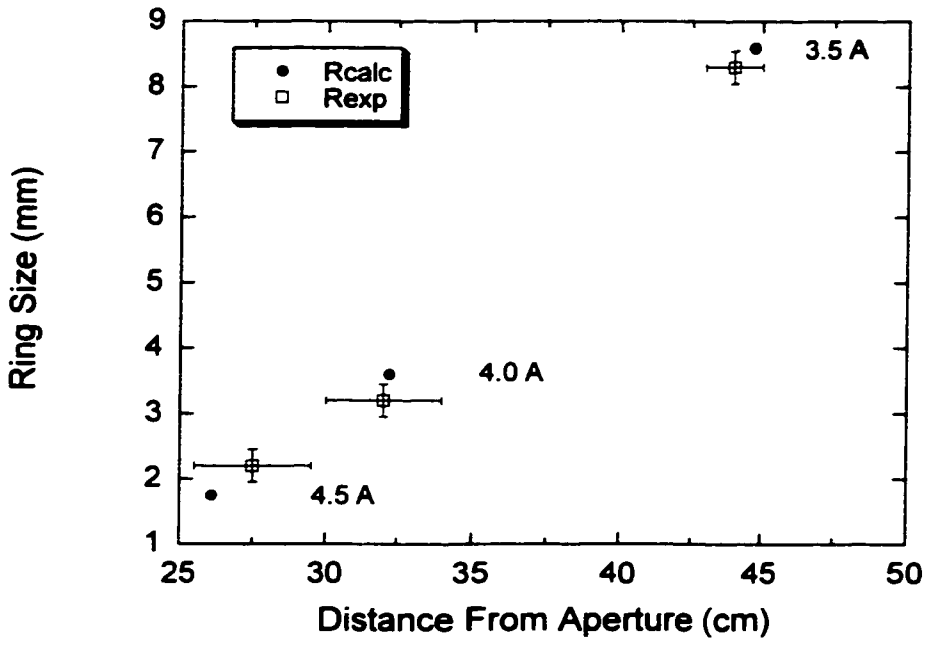

Fig. 7.13. Size and location of first ring perturbation, estimated from experiments and track-particle calculations for three cases of single-solenoid focusing (see Fig. 7.1).

initial values of r for particle tracking, the choice of initial slopes must be adjusted to conform with the available trace space, but then all resulting motion is close to laminar when the slopes are smaller than the beam slope at the aperture. In summary, the beam-edge particle tracking model reflects the existence of a strong correlation between particle radial location and transverse velocity near the beam edge at the aperture; the onset of the perturbation, as signaled by trajectory crossing, gives way to collective phenomena that cannot be accounted for by the same model.

Another feature of the observed beam profiles can be related to the trajectory calculations: in Fig. 5.5 (Chapter V) the beam profile near the midplane of the solenoid has a distinctively different character at the edges when compared with the profile downstream when the beam has the same size. From Fig. 7.12(a), the fuzziness of the beam at the midplane of the solenoid can be understood in terms of the translaminar particles moving "outside" the beam edge.

The beam-edge particle tracking calculations for the all-quadrupole case are shown in Figures 7.14 and 7.15, for the horizontal (x) and vertical motions (y), respectively. The calculations are based on an extension of Eqs. 7.4(a)-(b) to non-axisymmetric beams [35]:

$$X''(z) + \kappa_X(z)X(z) - \frac{K}{X(z)+Y(z)} - \frac{{\varepsilon_X}^2}{X^3(z)} = 0, \tag{7.5a}$$

$$x''(z) + \kappa_X(z)x(z) = \begin{cases} \dfrac{K}{X(z)[X(z)+Y(z)]}x(z), & \text{if } x(z) \le X(z), \\ \dfrac{2K}{x(z)[x(z)+\sqrt{x^2(z)+Y^2(z)-X^2(z)}]}x(z), & \text{if } x(z) \ge X(z), \end{cases} \tag{7.5b}$$

$$Y''(z) + \kappa_Y(z)Y(z) - \frac{K}{X(z)+Y(z)} - \frac{\varepsilon_Y^{\,2}}{Y^3(z)} = 0, \tag{7.6a}$$

$$y''(z) + \kappa_Y(z)y(z) = \begin{cases} \dfrac{K}{Y(z)[X(z)+Y(z)]}\, y(z), & \text{if } y(z) \le Y(z), \\ \dfrac{2K}{y(z)[y(z)+\sqrt{y^2(z)+X^2(z)-Y^2(z)}]}\, y(z), & \text{if } y(z) \ge Y(z), \end{cases} \tag{7.6b}$$

where $\kappa_Y(z) = -\kappa_X(z)$, and it is assumed that $\epsilon_X = \epsilon_Y$. The initial conditions for the solutions of the equations are the same as for the solenoid cases. To simplify the calculations, however, it is implicit in Eq. [7.5b] that a particle starts on the horizontal plane (y=0); similarly, Eq. [7.6b] is valid for a particle initially located on the vertical plane (x=0).

7.3.6 Emittance Change in Simulations

Finally, to examine the long term evolution of the beam, simulations were done in a uniform focusing channel over a distance of 20 m. The simulations are a smooth approximation version of the three-solenoid case; i.e., the beam has the same generalized perveance, and it is matched so its radius is constant, comparable to the average beam size in the experiments. Figure 7.16 shows the simulated pictures for the first 2.5 m from the aperture plane; as seen in the figure, the perturbation appears at a distance of about 70 cm from the aperture, and the oscillations persist for a few plasma periods ($\lambda_p \sim 1$ m) and eventually diminish in amplitude as the beam evolves towards equilibrium. The doubly-peaked profile at 70 cm evolves into a broad hollow profile at 90 cm and then into a relatively uniform profile with a small central peak at 150 cm;

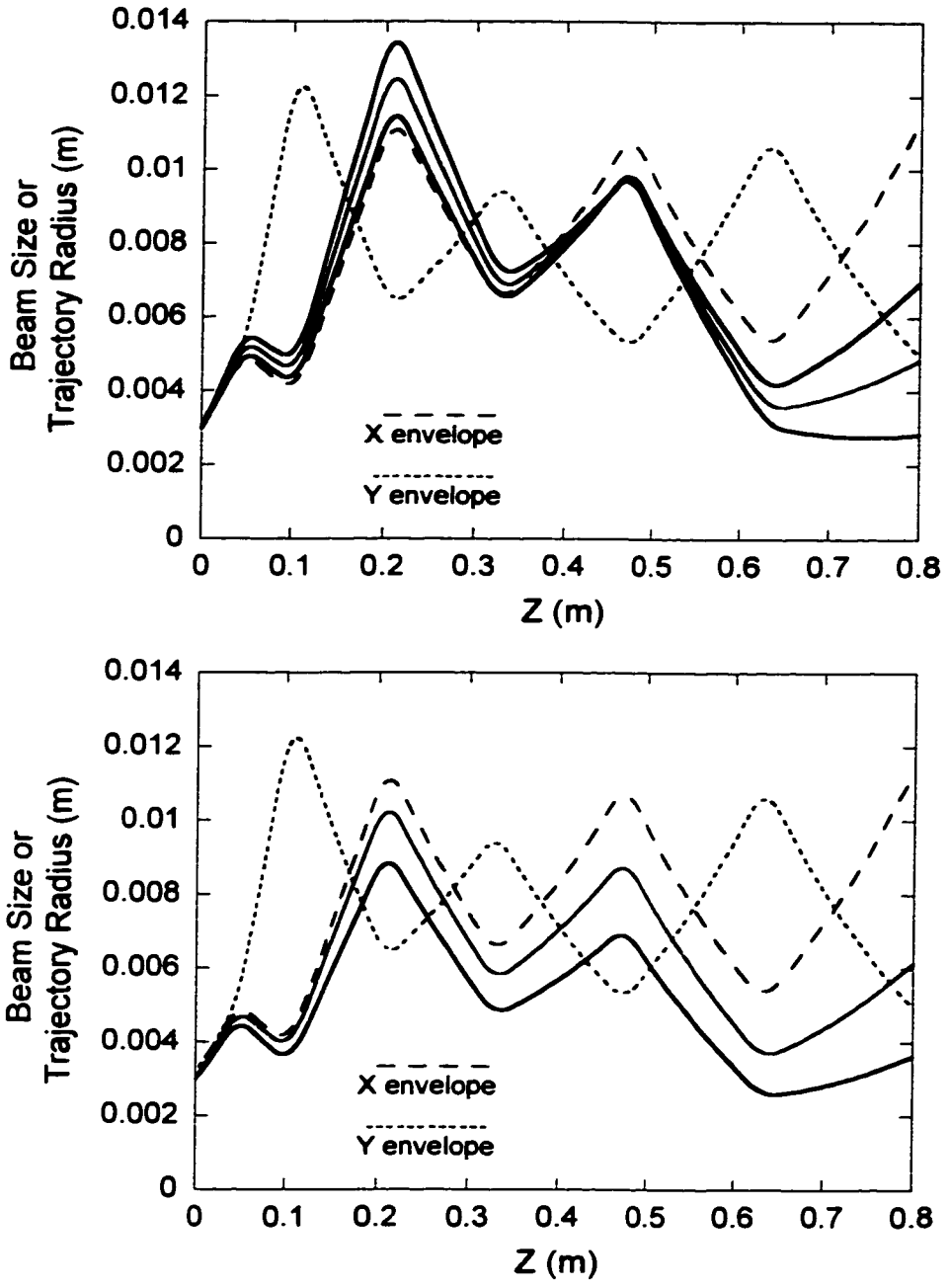

Fig. 7.14. Particle-tracking calculations for the horizontal motion in the six PC-quadrupole experiment (σ_0=85^0). In (a), the initial slopes are 40, 45 and 50 mrad, while in (b) the slopes are 30 and 35 mrad.

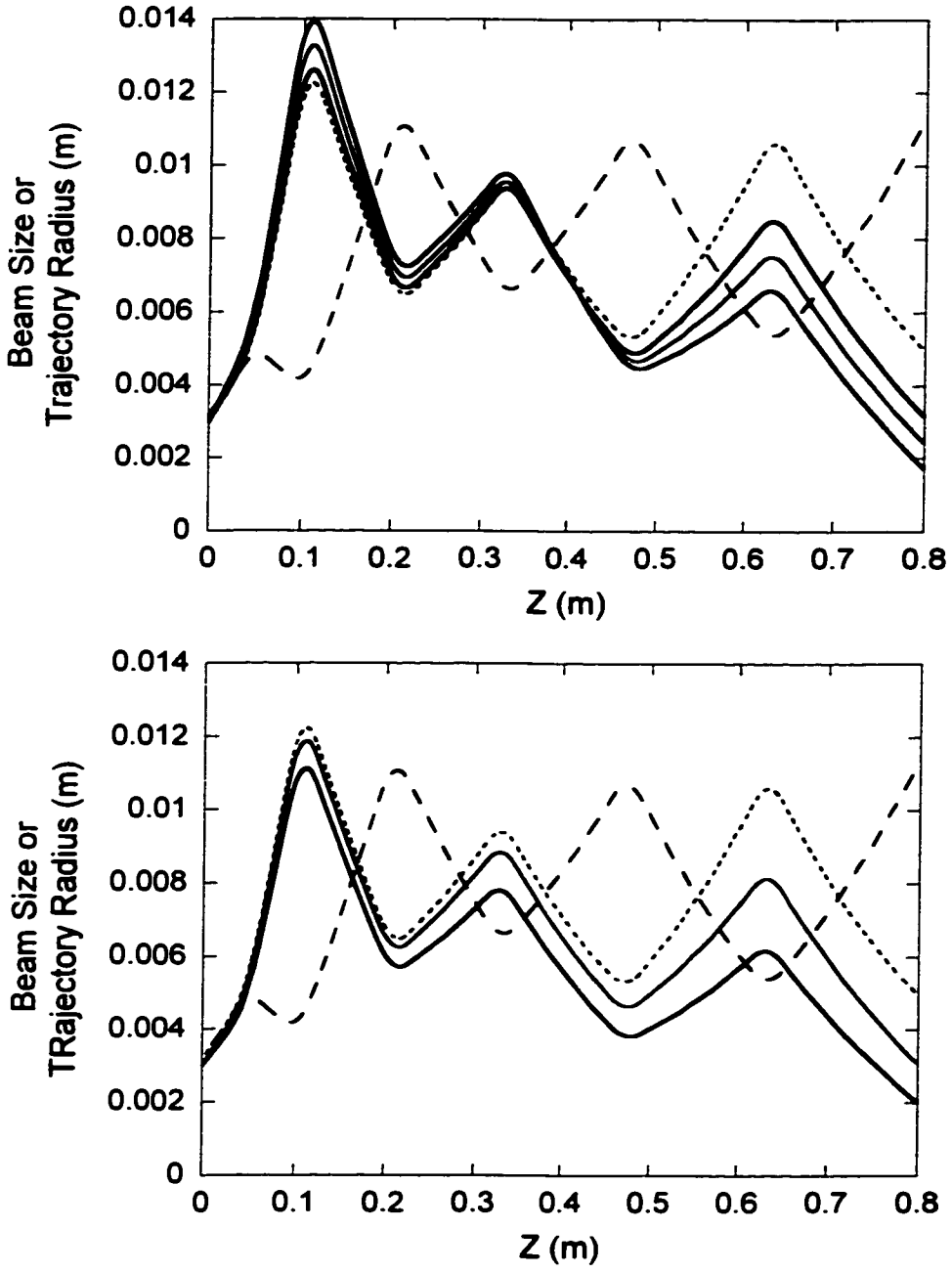

Fig. 7.15. Particle-tracking calculations for the vertical motion in the six PC-quadrupole experiment (σ_0=85^0). In (a), the initial slopes are 40, 45 and 50 mrad, while in (b) the slopes are 30 and 35 mrad.

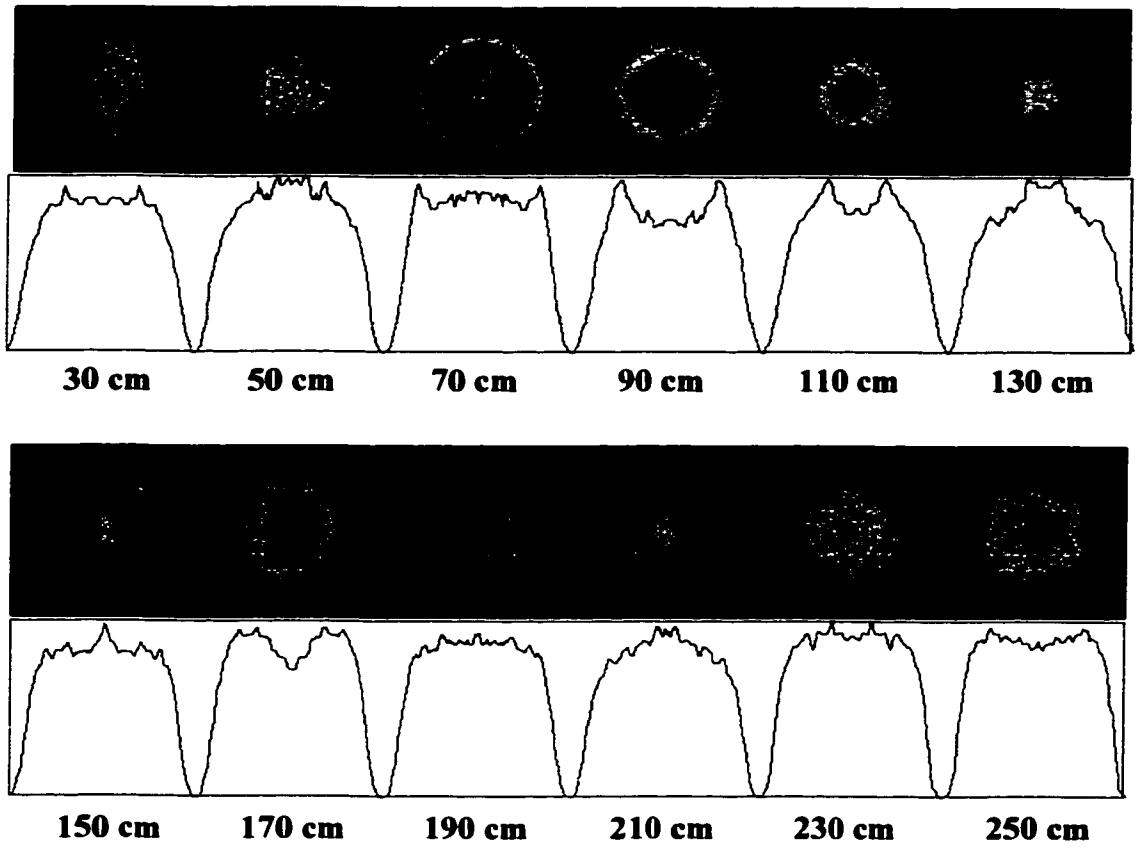

Fig. 7.16 [26]. WARP simulation pictures of evolution of (initially) S-G distribution in uniform focusing channel. The (matched) beam radius is constant and equal to 0.8 cm The distances are measured from the plane of the "aperture".

this is followed by a new hollow profile (or a new broad ring) at 170 cm, and a moderately peaked profile at 210 cm. At 250 cm, the distribution has again become hollow but is much shallower than at 170 or 90 cm; this indicates a "fundamental period" of about 80 cm (also the distance for collapse of the first ring), i.e. a distance close to a plasma period. We recall that the second ring in the experiments also appears around 80 cm from the aperture (Figs. 5.9 and 7.2).

Over the extent of the simulations, we observed no rms emittance growth associated with the perturbation, unlike the situation with the relaxation mechanisms discussed in Chapter II. Instead, as Fig. 7.17 shows, the rms emittance oscillates about its initial value, then levels off to a slightly smaller value as the perturbation damps out. This seemingly counterintuitive result, where an irreversible change in the beam does not ensue a growth in rms emittance, is consistent with previous simulations (p. 496 in Ref. [5], and Ref. [17]) with S-G distributions over a few plasma periods.

In Ref. [5], the simulation with the S-G distribution is done in the third-order instability regime of a FODO channel (σ_0=90^0 and tune depression of 0.46), while in [17] only the tune depression is specified (0.25). In both cases the emittance decreases initially, before the completion of one plasma period, but only in [5] does the emittance eventually increase and saturate to the same value (about 20% increase) obtained for the full Gaussian distribution; this is attributable to the instability regime of the simulation. In addition to plots of emittance evolution, Ref. [17] presents plots of the nonlinear energy $U(z)$ defined in Chapter II (section 2.4.2); this quantity oscillates

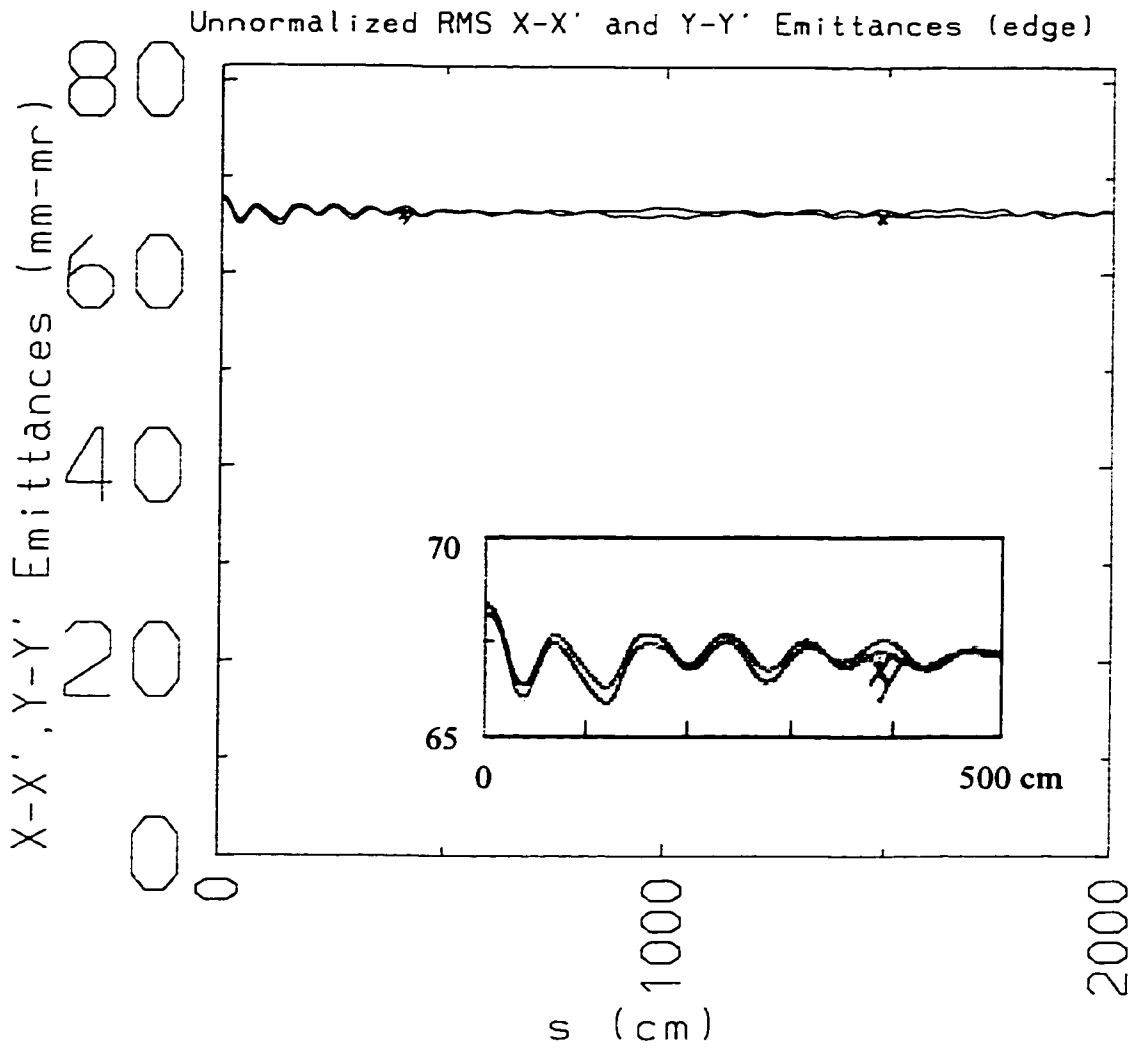

Fig. 7.17. WARP calculation (courtesy of R.A. Kishek) of unnormalized transverse emittances over 20 m in the uniform focusing case (pictures of Fig. 7.16).

initially with a frequency roughly equal to the plasma frequency, corresponding to an initially uniform distribution (U_i=0) that peaks and then relaxes again to a more uniform distribution, before the process repeats itself with decaying amplitude; after 10 plasma periods, the distribution has almost saturated to a distribution *less* uniform than the initial one. Wangler *et al.*'s conclusion is that emittance increases as the beam becomes *more* uniform, and, conversely, decreases as the beam becomes *less* uniform; this is clearly seen by the 180^0 "phase difference" between the plots for $U(z)$ and ϵ/ϵ_i in Fig. 2 of the paper [17]. However, the real issues are the "final" values of nonlinear energy and emittance. If we try to apply the phenomenological theory for emittance growth to a S-G distribution, we find that since U_i =0 (see Eq. [2.24]), or, equivalently, h=0 (Eq. 6-14 in Ref. [5]), *no emittance change* is expected, regardless of the intervening mechanisms. Conservation of energy arguments can still be invoked to understand the relaxation of the S-G distribution and the accompanying reduction in emittance, as shown by Lund *et al.* [67], and N. Brown [68].

Lund *et al.* consider the relaxation of a non-relativistic continuous beam, with an initially S-G distribution, in a uniform focusing channel (represented by the wave number k_0). Equivalent K-V and M-B (thermal) distributions are defined as having the same number of particles per unit length, N, and longitudinal energy per unit length, $Nm\upsilon^2/2$, as the initial S-G distribution. Additionally, all three distributions are assumed to be "matched" in an rms sense, so the equilibrium K-V distribution represents an equivalent uniform distribution for the non-equilibrium S-G. The results for the fractional change in emittance, i.e. $(\epsilon_{M\text{-}B} - \epsilon_{S\text{-}G})/\epsilon_{S\text{-}G}$, as a function of tune depression

indicate that emittance decreases about 2.5% for a tune depression equal to 0.3 as the initial S-G distribution relaxes to a M-B thermal distribution.

In understanding the results, we observe that the equilibrium M-B distribution must have more energy associated with the self fields than the S-G because of the thermal tails that extend beyond the "zero-temperature" radius (see curve labeled "7" in fig. 5.12a in Ref. [5]); the non-equilibrium S-G distribution, on the other hand, has more thermal (kinetic) energy than the equivalent M-B. Thus, upon relaxation to a M-B distribution, conservation of energy forces the S-G distribution to build up self-field energy at the expense of thermal energy, the net result being a *less* uniform distribution (M-B at $T_\perp \neq 0$), with *less* emittance.

7.3.7 An Irreversible Process with no RMS Emittance Growth:

There is no question that the evolution of the perturbation described above is an irreversible process. However, since emittance does not grow, and in fact may actually decrease, no beam degradation is associated with the decaying oscillations. This is consistent with a collisionless system where the energy of an initial perturbation goes into collective modes or waves in a way similar to the phenomenon normally associated with Landau damping.

Another way to understand the lack of emittance growth is by recalling O'Shea's generalization of Wangler *et al.*'s differential equation, or the generalized free energy function (Chapter II). The M-B distribution is associated with higher entropy than an rms equivalent S-G distribution, on account of the fact that the latter is confined (or

more "ordered") in space. This difference in entropies is balanced, or almost balanced, by the action of non-linear space-charge forces, so the generalized free energy, which "drives" emittance growth is nearly constant.

Yet another way to look at the question of emittance growrh vs. irreversibility is through the beam-edge particle tracking model. Figure 7.18(a) illustrates the particle tracking results corresponding to the uniform focusing simulations in Fig. 7.16, or the "smooth approximation" version of the three-solenoid experiment. The undepressed and depressed betatron wavelengths are 1.53 m and 6.0 m, respectively. Further, Figure 7.18(b) presents the results for an emittance dominated beam with the same perveance and emittance as in Fig. 7.18(a); the (uniform) focusing strength has been increased more than 30 times to produce a beam size four times smaller (2 mm radius). In this latter case, the undepressed and depressed betatron wavelengths are 0.27 m and 0.375 m, respectively.

A strong correlation between particle transverse velocity and radial location at the aperture and crossing plane inside the beam in Fig. 7.18(a) indicates an "ordered" or deterministic situation. The trajectory crossings initiate the perturbation, but the tracking model fails to account for the observed evolution after a short distance (e.g. a second ring.) The original single-particle dynamics gives way to collective phenomena that can only be reproduced with PIC simulations. For the space-charge dominated beam, the distance to the crossing plane is roughly half the *undepressed* betatron wavelength, while the distance for thermalization is about half the *depressed* betatron wavelength (this from Fig. 7.16). For emittance dominated beams, on the other

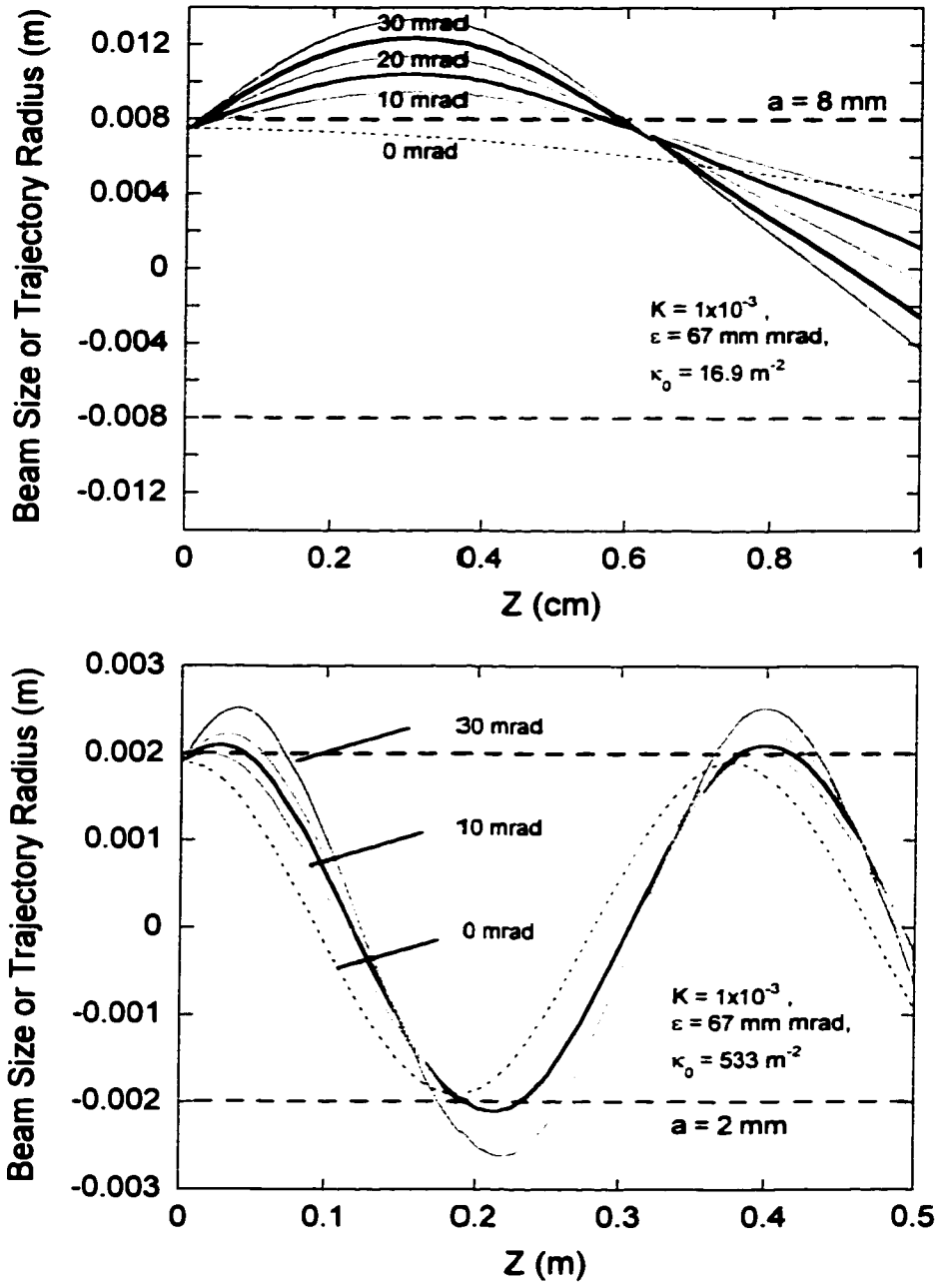

Fig. 7.18. Particle-tracking calculations for uniform focusing channel: (a) Space-charge dominated beam, and (b) emittance dominated beam.

hand, the density oscillations are not well defined (no sharp rings are observed) and follow approximately the undepressed betatron wavelength [see Fig. 7.18(b)], indicating that the phenomenon is, in this case, almost entirely kinematic. This latter observation is confirmed in PIC simulations with WARP.

Ultimately, the description of the beam perturbation must be analyzed in a rigorous fashion through a kinetic analysis of beam oscillation modes. However, since an initial *particle flow* seems to be responsible for the onset of the internal density oscillations, it appears as though a transition region from single-particle motion to collective dynamics exists, and whose extent may have to be determined for a complete understanding. Of course, perturbation mechanisms other than the one studied here are possible, so we turn our attention to a brief overview of these and a possible unified picture for beam oscillations in terms of Gluckstern modes.

7.3.8 Other Perturbation Mechanisms and Gluckstern-Mode Analysis:

Recent computer simulations by Lund *et al.* [69], relating to experiments with an electrostatic-quadrupole injector at Lawrence Berkeley National Laboratory (LBNL), exhibit density oscillations similar to Gluckstern modes. The WARP simulations start at the diode exit with an rms equivalent S-G distribution; perturbations to this initial distribution are introduced in the form of altered charge density profiles (uniform, peaked, or hollow), or temperature profiles. For both types of perturbations, and depending on the exact launching conditions, different wave patterns are observed; common to all simulations, however, is the slow relaxation rate of the perturbation and

the lack of net rms emittance growth. In particular, the simulations with an initial peaked charge distribution agree well with the observed hollowing of the beam profile at the injector exit. It was later realized that the initial peaked distribution was caused by a "hot spot" in the alumino silicate ion source [70].

Although the beam transport parameters in the LBNL experiments are similar to our experiment parameters, the optics of the LBNL source is completely different, and yet simulations suggest the appearance of similar wave phenomena in both experiments. This leads us to conclude that different types of perturbations are responsible for similar collective phenomena. When looking for physical causes of initial beam perturbations, the first candidate is the source, either because of its finite size and inherent non-uniform emission and/or because of the Pierce geometry (not present in the LBNL source) and accompanying aberrations at the anode. Another factor that may change the details of the wave evolution, rather than be their cause, is the presence of large envelope splits or excursions in the matching section, as in the all-quadrupole experiments of Chapter VI, or envelope "necks" as in the solenoid-quadrupole experiment of Chapter V or in the LBNL injector experiment. A discussion and summary of these effects for space-charge dominated beams can be found in a recent paper by I. Haber *et al.* [71].

Finally, and as demonstrated in this thesis, an aperture outside the source can also be the determining factor of the initial beam perturbation. Again, details of the "launching" conditions, i.e. aperture size and location, beam size and slope, just upstream of the aperture, are all important factors. If the beam size is slightly larger

than the aperture, or if the aperture is placed at the beam waist, the effect on the beam temperature profile will not be as pronounced as if the aperture acts on a relatively large and expanding beam. The study of the initial perturbation in this case is simpler than in the other cases mentioned above, though, and allows the use of simple pictures like the particle-tracking model presented before.

Lund has suggested [72] the decomposition into Gluckstern modes (see Chapter II, Section 2.4.4) of the beam oscillations of our experiments. A complication that arises for the decomposition of the waves is the presence of an initial (near where the first ring occurs) transverse particle flow. We speculate that there is a region of transition between particle dynamics and collective phenomena (see previous subsection), so only when true waves are set in could the mathematical decomposition be tried. A relatively simple analysis in terms of axially symmetric, i.e. radial, modes for the ideal case of a perturbation (simulated) in a uniformly focused beam should provide information on relative amplitudes and decay rates. This would, in turn, guide us for the design of experiments intended to test the model by introducing special apertures to attenuate certain modes, or accentuate some others to induce instabilities. However, these ideas should be implemented only after new experiments, over longer lengths, are designed for additional studies of general properties of the waves, as well as for emittance measurements. Furthermore, the role of additional, improved PIC simulations should be emphasized.

7.4 Conclusions and Suggestions for Future Work

A perturbation mechanism involving collimation of an expanding, space-charge dominated beam has been identified. The evolution of the density perturbation has been shown in both experiments and simulations to be essentially independent of the type of focusing.

The beam particle distribution at the aperture can be modeled approximately with a semi-Gaussian particle distribution: a non-equilibrium distribution characterized by a uniform density profile and a Gaussian velocity distribution. Better agreement with experiment is obtained when a temperature profile (e.g. parabolic) is used. Furthermore, the onset of the perturbation can be reproduced well with a simple particle tracking model consistent with the picture of an initial S-G distribution.

Finally, simulations show that the collective, irreversible phenomenon involves a mechanism for relaxation to equilibrium without an accompanying growth in rms emittance. Energy conservation considerations can be used to understand the reduction in effective emittance, while entropy increase in the relaxation of a S-G distribution into a thermal distribution accounts for the irreversible character of the process.

Some suggestion for future work could be listed, perhaps in the order of lower to higher complexity of the experiments involved. All experiments would use a straight system extending at least 3 meters from the source, i.e. including at least 10 full-lattice periods in a FODO configuration.

1. Check of RMS envelope matching, and additional experiments with special combination of quadrupoles like the symmetric *quintuplet* for round-to-round transformation (Section 6.6.2).
2. Study of radial space-charge waves with different collimation schemes (apertures of different sizes, shapes and at different locations). Emittance measurements in two planes.
3. Systematic study of effects of quadrupole rotations on rms envelope matching, emittance and reversibility, and possible corrections with skew quadrupoles as suggested by R. Kishek.
4. Study effects (Hofmann instabilities, emittance growth and equipartioning) of high beam anisotropy produced by implementing significantly different focusing in the two transverse directions, i.e. σ_{0x} appreciably different than σ_{0y}. Another experiment could use a beam with two different initial emittances, $\epsilon_x \neq \epsilon_y$, a condition produced, for example, with a wire mesh in one direction.
5. Five-beamlet or "n-beamlet" experiments in FODO channels.
6. Detailed experimental comparison between "equivalent" all-solenoid and all-quadrupole FODO lattices in the 3-meter channel.
7. Bend experiments with a single *variable* bend near the middle of the 3 meter channel to explore effects from straight-bend-straight transition. Also study the possibility of measuring longitudinal energy spread and *dispersion.*
8. Define and design an experiment to look for instabilities leading to *chaotic* phenomena. If chaos is identified, devise a way to control it.

Appendix A

Effects of an Aperture - General Considerations

A.1 Effect on Tune Depression:

In the prototype injector experiments of this work, an aperture is used to reduce the generalized *perveance* of the beam produced by the Hughes gun in order to obtain a value similar to the *UMER* design value. Naturally, the aperture also reduces the beam *emittance*. The combined changes in perveance and emittance yield, in general, a shift in the tune depression, as shown in the discussion that follows.

The tune depression in a periodic focusing channel, in the smooth approximation, is given by Eq. [1.16], which we write again for easy reference:

$$\frac{\sigma}{\sigma_0}=\frac{k}{k_0}=\sqrt{1-\chi}, \quad \chi\equiv\frac{K}{k_0^{\,2}a^2}. \tag{A.1}$$

where χ is the intensity parameter.

An aperture will have an effect on the beam generalized perveance K, and effective emittance ϵ, which, together with the external focusing given by $k_0=\sigma_0/S$, will determine the "average" beam size a. Within the smooth approximation we can write

$$a=a_0\left(u+\sqrt{1+u^2}\right)^{1/2},\ u\equiv\frac{K}{2k_0\varepsilon}, \tag{A.2}$$

which is also Eq. (1.17). The quantity a_0 is the "zero-current" beam radius given by $a_0 = \sqrt{\varepsilon/k_0}$. The parameters χ and u are related through the expression

$$\chi = 2\left[1 + \sqrt{1 + u^{-2}}\right]^{-1}, \tag{A.3}$$

which can be easily obtained from Eqs. (A.1) and (A.2).

For constant focusing, as given by k_0, the tune depression will depend on the ratio ϵ/K. The "average" beam size, on the other hand, is given explicitly by

$$a = \frac{1}{k_0}\left(\frac{K}{2} + \sqrt{\varepsilon^2 k_0^{\,2} + \left(\frac{K}{2}\right)^2}\right)^{1/2}. \tag{A.4}$$

If a beam is still space-charge dominated after collimation, in the periodic focusing channel following the matching section, i.e. if $K >> \varepsilon^2/a^2$, or $K >> \varepsilon k_0$, the tune depression will hardly be affected by the aperture. This can be seen from Eq. (A.1) and (A.3), for $u>>1$. In this case, the "average" beam size, from Eq. (A.4), will be proportional to the aperture size, since K is proportional to the aperture size squared.

In general, the emittance scales linearly with the aperture size (see next section), so the ratio ϵ/K scales inversely with the aperture size, leading to a dependence of the tune depression on the aperture size.

As an example, consider the case of *UMER*. The electron gun has a rotating aperture plate located near the beam waist; the plate contains four circular apertures, in addition to a pepper-pot for emittance measurements and a five-beamlet mask. From

calculations with EGUN [43,73], the waist radius at 10 keV is 4.0 mm approximately, while the 4×rms, unnormalized, emittance at the same plane is estimated to be 50 mm-mrad. The aperture diameters are 16 mm, 0.5 mm, 3.0 mm and 6.0 mm. We calculate the tune depression and beam size as functions of aperture radius, using Equations [A.1] through [A.4], for a zero-current phase advance $\sigma_0=72^0$. The beam emittance downstream of the aperture is calculated using the expression derived in the next section. Figure A.1 (a) illustrates the results for the tune depression and average beam size, while Fig. A.1 (b) compares the space and emittance terms in the smooth-approximation envelope equation:

$$k_0^{\,2}a-\frac{K}{a}-\frac{\varepsilon^2}{a^3}=0. \tag{A.5}$$

Table A.1 summarizes the results for the existing apertures as well as some additional hypothetical ones.

A.2 Scaling of Emittance

With reference to Fig. A.2, the *area* of the shaded region is easily calculated:

$$\Delta A=2\varepsilon\left[\frac{b}{X_{\max}}\sqrt{1-\left(\frac{b}{X_{\max}}\right)^2}+Sin^{-1}\left(\frac{b}{X_{\max}}\right)\right], \tag{A.6}$$

where ϵ is the emittance *upstream* of the aperture, b is the aperture radius, and $(X_{\max})^2=\varepsilon\hat{\beta}$. The emittance downstream of the aperture can be approximated as

$$\varepsilon_{new}=\frac{\Delta A}{\pi}. \tag{A.7}$$

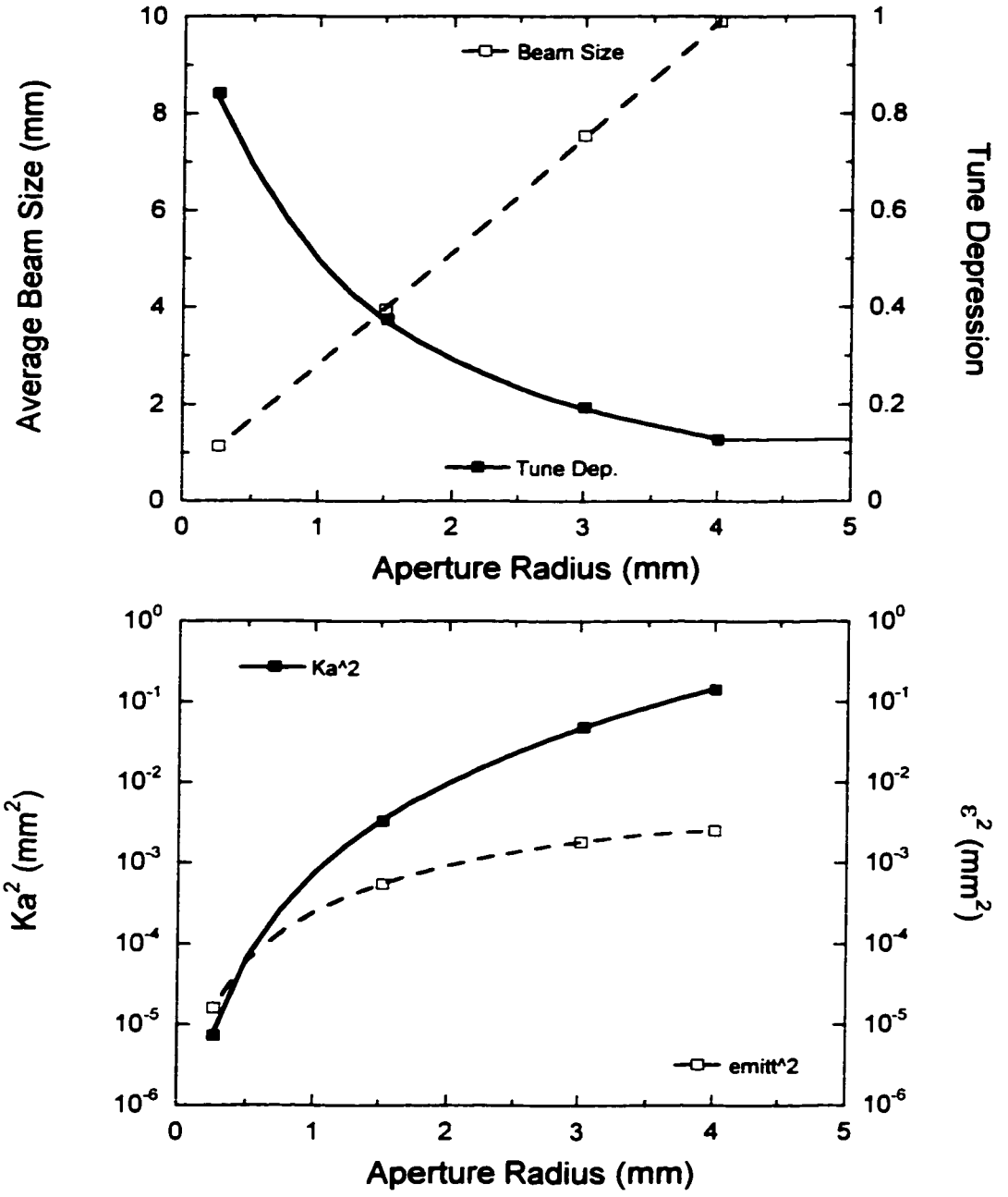

Fig. A.1. (a) Effect of aperture size on tune depression and average beam size in UMER, for constant focusing (σ_0=72^0); (b) space charge and emittance terms in smooth envelope equation (see Eq. [A.5]).

Table A.1.: Effects of aperture size on UMER's 10 keV, 100 mA, 50 mm mrad (4×rms, unnormalized emittance) electron beam. Constant focusing corresponding to $\sigma_0=72^0$ is assumed. The data in the shaded rows represent hypothetical apertures.

Aperture Radius/ Current	K	ϵ (mm mrad)	σ_0/σ	a (mm)
0.25 mm, 0.4 mA	5.8×10^{-6}	4.0	0.83	1.1
0.5 mm, 1.6 mA	2.3×10^{-5}	7.9	0.69	1.7
1.0 mm, 6.25 mA	9.3×10^{-5}	15.7	0.50	2.8
1.5 mm, 14 mA	2.1×10^{-4}	23.3	0.38	4.0
2.0 mm, 25 mA	3.7×10^{-4}	30.4	0.29	5.1
3.0 mm, 56 mA	8.4×10^{-4}	42.8	0.19	7.5
≥ 4.0 mm, 100 mA	1.5×10^{-3}	50	0.13	9.9

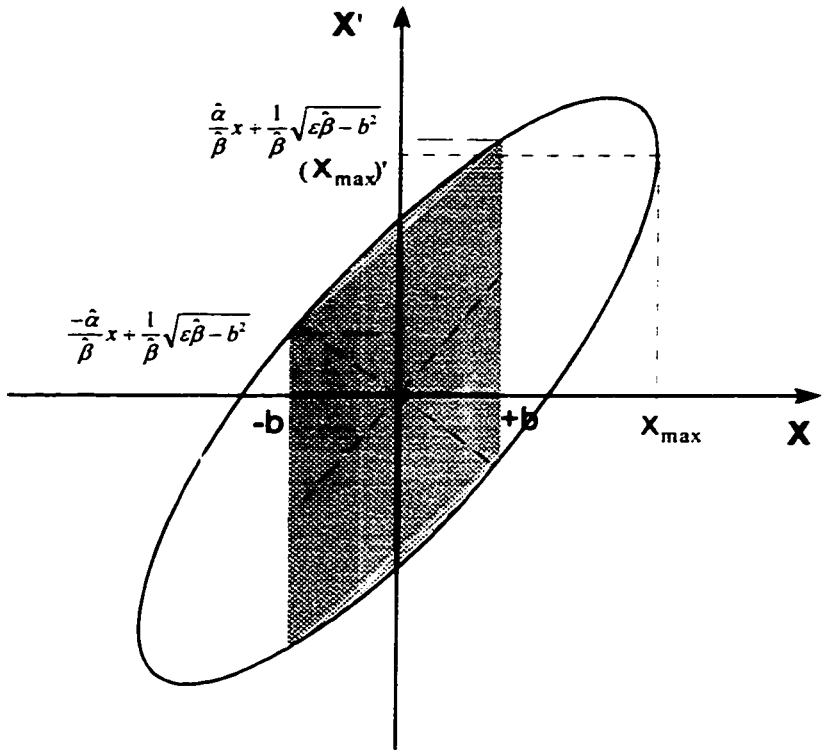

Fig. A.2. K-V beam horizontal trace-space ellipse upstream of aperture (radius b), an model of collimated region. The equation of the ellipse is $\hat{\gamma}x^2 - 2\hat{\alpha}xx' + \hat{\beta}x'^2 = \varepsilon$.

Application of Eqs. [A.6] and [A.7] to our experiments, with b=3.18 mm, X_{max}=8.65 mm, ϵ=106 mm mrad (the last two figures from envelope calculations and D. Kehne's data [45]) yields an emittance of 48 mm mrad downstream of the aperture. Indirect measurements from beam free expansion and rms envelope matching (Chap. V) give 67 mm mrad. The discrepancy highlights the approximate nature of the model and also reflects errors in beam size data upstream of the aperture as well as possible small differences in the physical condition of the thermionic cathode between our experiments and those of D. Kehne's.

A.3 Representation of Collimated Beam Distribution

The exact calculation of emittance downstream of the aperture would require detailed knowledge of phase space upstream. Assuming that the beam just upstream of the aperture can be replaced by the equivalent K-V beam, the calculation of the truncated distribution is made difficult by the fact that the K-V distribution is not separable, i.e., $f_{K\text{-}V} \neq f(x,y)g(x',y')$. The case of a one-dimensional K-V, however, can illustrate the effect of an aperture. The particles populate the *contour* of an ellipse in x-x' space; the action of an aperture (small compared to x_{max}) produces two sets of particles with velocities in opposite directions. Therefore, the initial uniform distribution is split and evolves so that 100% hollowness results downstream of the aperture. Of course, the situation is much more difficult to visualize in four-dimensional trace space (for a continuous beam), but we can infer that the collimated K-V is highly non-uniform in velocity space, if the aperture size is sufficiently small. This leads to a non-uniform distribution in space as the beam propagates in a focusing channel.

Simulations with the code WARP (App. B) confirm that the collimation of a K-V distribution and subsequent focusing lead to non-uniform density patterns. However, the patterns are very different from what is seen in the experiments. A more realistic approach, as we described in Chap. VII, is to model the distribution on the *downstream* plane of the aperture as one with uniform density in space but non-uniform density in velocity. A semi-Gaussian distribution with a uniform temperature profile is the simplest choice, with the temperature derived from the experimental beam parameters for the equivalent K-V distribution *after* collimation.

Appendix B: Computer Codes

B.1 K-V Envelope Code SPOT

The matching of the electron beam into an ideal FODO straight lattice of the PC quadrupoles is calculated using the code SPOT [74], which is based on the solution of the KV envelope differential equations reviewed in Chapter I. SPOT has two types of optimization routines for the strengths of focusing elements in a lattice: the first one is based on minimization of the square-distance (or "cost functional" in Ref. [74]) between the beam envelope and a predetermined reference trajectory; the second one optimizes the focusing strengths to produce the beam parameters (sizes and slopes in the two transverse directions) that best approximate a predefined "target state" at the end of the channel. In addition, SPOT has a "matcher" routine for obtaining the matched beam envelope in a periodic lattice.

B.1.1 Matcher Solutions:

In the first step in the calculations, SPOT's "matcher" feature is used to find the matched beam envelope in one period of the ideal FODO geometry of the UMER PC quadrupoles with the parameters of the prototype experiments (Table 5.1). The peak strength of the PC quadrupole κ_p, its effective length l, and the half-lattice period $L=S/2$ are the input parameters for this calculation. As mentioned in Chapter I, the trace of the matrix for a FODO unit cell is proportional to $\cos\sigma_0$, where σ_0 is the zero-current phase advance. A transcendental equation in $\theta \equiv \kappa_p^{1/2} l$ (Eqs. [1.8]) can be solved to obtain the

required κ_p. Table B.1 summarizes the results; Figure B.1 shows the matched envelope solutions in one FODO cell.

Table B.1: Results of "matcher" calculations (see also Tables 4.1, and 5.1).

$\sigma_{0x} = \sigma_{0y}$	κ_p, g_p	$X_{avg}=Y_{avg}$	X,Y_{max}, X,Y_{min}	$\|X'\| = \|Y'\|$, $z=L/2$
85^0	252.7 m^{-2}, 5.40 G/cm	7.60 mm	10.6, 5.3 mm	36.9 mrad
76^0	230.2 m^{-2}, 4.92 G/cm	8.33 mm	11.2, 6.1 mm	36.4 mrad

A *hard-edge* model for the quadrupoles was used for the "matcher" calculations. If *smooth* quadrupoles with the same effective length as the hard-top versions are used, the average, maximum and minimum beam sizes are about 0.2 mm larger. The matcher solutions with *smooth* quadrupoles agree with envelope calculations using MATHEMATICA, when *either* smooth or hard-edge elements are implemented in the latter; therefore, SPOT's handling of piece-wise focusing functions is not as accurate as when the functions are smooth. Nevertheless, the difference between solutions with smooth and hard-top focusing elements in SPOT is smaller than the errors involved in determining beam size from experiment. Implementing hard-top lenses, on the other hand, is simpler and more convenient when defining a control problem, as it avoids "truncation" problems which are unavoidable when the smooth profiles of neighboring lenses overlap at the tails. This is the case with the solenoid and first quadrupole in the matching problem of Chapter V, which we consider in the next Section.

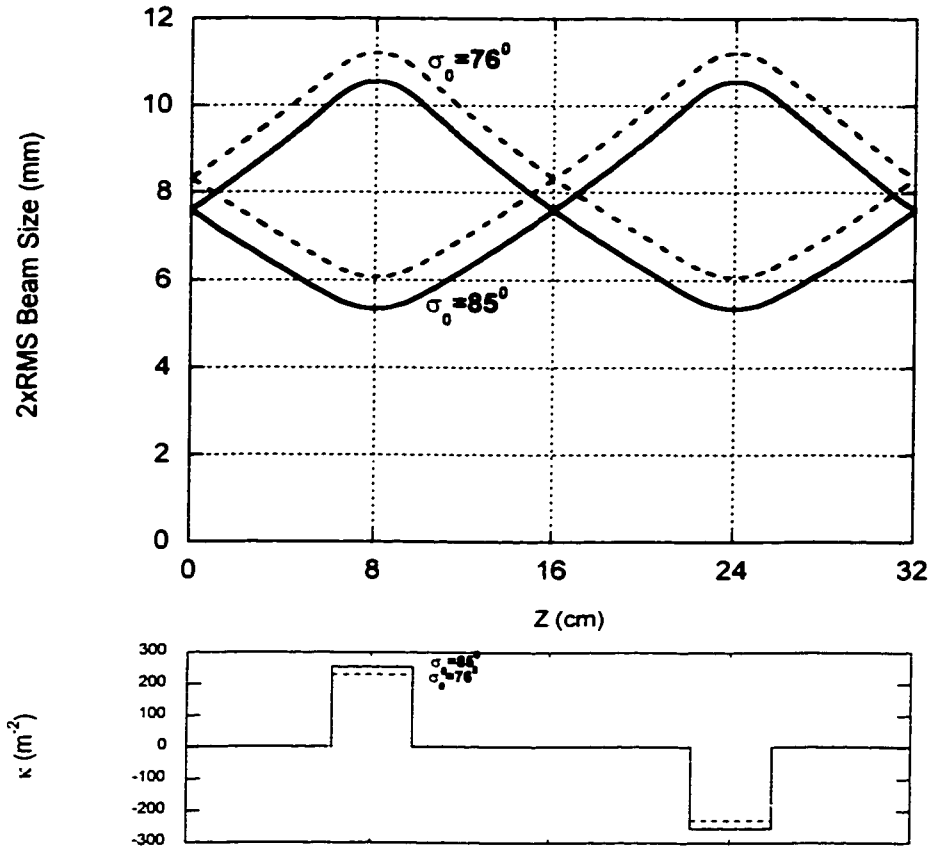

Fig. B.1.Matched envelope in a unit FODO cell of UMER quadrupoles for the parameters in Table 4.1.

B.1.2 Optimizer for RMS Envelope Matching:

The matching problem with a solenoid and five PC quadrupoles of the old design is implemented in SPOT with hard-edge focusing elements. A reference trajectory is defined so that it traces the envelope solution "on average". Further, the strengths of focusing elements, or control parameters, are given initial values. These starting values are guessed from general knowledge of solenoid and quadrupole focusing, though ultimately result from trial and error. The locations of all elements, on the other hand, are decided on the basis of general considerations, as described in Chapter V, and are also refined with simple trial and error.

After optimization of the strengths of all focusing elements to minimize the cost functional, the program is set to optimize the solution one more time so that a target state is approached as closely as possible. The first optimization utilizes the "Local Optimizer", with "Target State" disabled. The local optimizer finds a local minimum to the cost functional, i.e. a solution for the control values in the vicinity of the starting values. The target state, on the other hand, can be defined midway between the fifth quadrupole (old type quad) and the first *UMER* quadrupole (not included in the calculation). The numbers in Table B.1 for $X_{avg}=Y_{avg}$ and $X'= -Y'$ define the target state. Alternatively, the target state can be defined at the midplane of the first *UMER* quad, in which case this quadrupole is included in the calculation (actually one-half of it) but kept at the constant strength required in the FODO lattice. The target state at the quad is defined so $X=X_{max}$, $Y=Y_{min}$, (or $X=X_{min}$, $Y=Y_{max}$), $X'=0=Y'$. Figure B.2 shows typical windows from SPOT. The solution shown corresponds closely to the beam

envelope in Fig. 5.11(a). The maximum number of steps per control stage (drift, solenoid or quadrupole) is 400, so a typical step size is 0.5 mm.

B.2 Matrix Codes TRACE 2-D and 3-D

Another useful linear code that includes space charge is TRACE. Bends of different types can be implemented in the two-dimensional version (TRACE 2-D), while additional capabilities are available in the three-dimensional code TRACE 3-D. Most useful for our purposes is the possibility of setting rotated or displaced quadrupoles, and the calculation of mismatch factors.

B.2.1 Background:

TRACE [64,75] calculates the evolution of the beam envelope through a linear transport system by propagating two 6×6 matrices (TRACE 3-D) or two 4×4 matrices (TRACE 2-D): the *transport* or *transfer matrix* $\boldsymbol{R}$, and the *beam matrix* σ. The elements of the $\boldsymbol{R}$ matrix depend on the transport elements and on the beam size (used for computing space-charge forces). The σ matrix in TRACE 3-D is decomposed into nine 2×2 matrices whose elements can be written in terms of the Twiss parameters reviewed in Chap. I. As an example, the first submatrix of the σ matrix is

$$\sigma_{xx} = \begin{bmatrix} x_m^2 & x_e x'_m \\ (x_m)' x_m & (x'_m)^2 \end{bmatrix} = \begin{bmatrix} \beta_x \varepsilon_x & \alpha_x x_{\text{int}} x'_m \\ \alpha_x x'_{\text{int}} x_m & \gamma_x \varepsilon_x \end{bmatrix}, \tag{B.1}$$

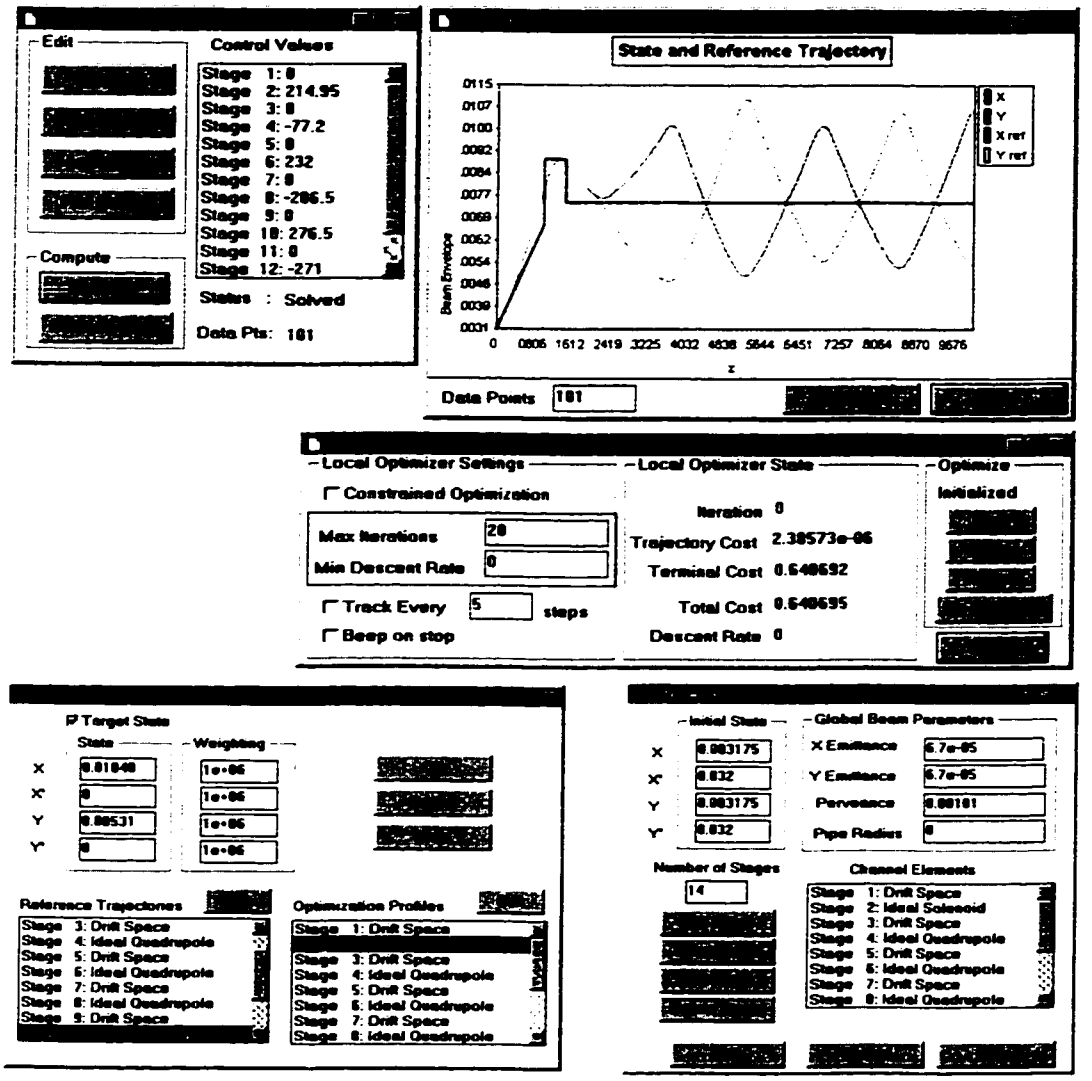

Fig. B.2. Windows from SPOT: the reference trajectory is represented by the solid dark line tracing the "average" beam envelope (top right); the trajectory and terminal costs (middle) are mismatch measures.

where all symbols refer to the beam ellipse of Fig. 1.4, and equations [1.6] and [1.7] defining the Twiss parameters.

The sigma matrix is propagated between two points as $\sigma(s_2) = R\sigma(s_1)R^T$, where R propagates the particle coordinates $\vec{x}^T = (x,x',y,y',z,\Delta p/p)$ as $\vec{x}(s_2) = R\vec{x}(s_1)$. Starting with a sigma matrix at s_1, the transfer matrix obtained from the external forces is used to propagate sigma across a small interval s_2-s_1. The size of the beam is calculated from $\sigma(s_1)$ and the space-charge forces are computed from this information. Next, a space-charge impulse matrix R is obtained, and from this a new sigma matrix follows, etc.

B.2.2 Results of FODO Matching:

Beam matching calculations in the ideal FODO lattice were performed with both TRACE 2-D and 3D for comparison with SPOT's matcher results of Table B.1. Table B.2 summarizes the results obtained with TRACE2D with a maximum step size of 0.1 mm. Virtually the same results are obtained in TRACE 3-D.

Table B.2: Results of FODO matching with TRACE 2-D, 3-D.

$\sigma_{0x} = \sigma_{0y}$	κ_p, g_p	β_{avg} $X_{avg}=Y_{avg}$	$(\beta_{x,y})_{max}$, $(\beta_{x,y})_{min}$ X,Y_{max}, X,Y_{min}	$\lvert\alpha_{x,y}\rvert$ $\lvert X'\rvert = \lvert Y'\rvert$, z=L/2
85^0	252.7 m^{-2}, 5.40 G/cm	2.52 mm/mrad 7.34 mm	4.85, 1.26 mm/ mrad 10.2, 5.2 mm	12.1 35.2 mrad
76^0	230.2 m^{-2}, 4.92 G/cm	3.07 mm/mrad 8.09 mm	5.56, 1.64 mm/ mrad 10.9, 5.9 mm	13.3 35.0 mrad

The beam envelopes from SPOT and TRACE 2-D are shown in Figure B.3. The small difference between the solutions, about 0.2 mm, is most probably the result of details in the numerics used to find the periodic solutions, and/or limitations of the space-charge force calculations in the matrix code.

B.2.3 Matching Section and Mismatch Factor:

Different types of matching are possible with TRACE. As we saw above, an equivalent to the "matcher" option in SPOT yields the beam envelope given the basic unit FODO cell. Furthermore, the strengths of focusing elements in a given geometry can be found for different specifications of the beam ellipse at the end of the channel. In our case, we use $\alpha_{x,y}$, $\beta_{x,y}$ from the periodic solution, specified at the midplane of the last quadrupole (e.g., $\alpha_x=0=\alpha_y$, and $\beta_x=\beta_{xmax}$, $\beta_y=\beta_{ymin}$ from Table B-2). The matching problem is set as four (from the four conditions) nonlinear, simultaneous equations, which are solved iteratively using the method of *regula falsi* (or "false position"), starting with guessed values for the focusing strengths. For an initial guess that is not too far from the solution, the convergence is usually much faster than in SPOT (based on minimizing the "cost functional"). In addition, and as a guide in judging the matching solution, TRACE can provide the resulting *mismatch factor* (MF), a measure of the breathing amplitude of the mismatched envelope relative to the matched solution [64]: for example, if $MF_x = 0.1$, the beam envelope excursions in the x-direction can be about 10% larger than in the matched case.

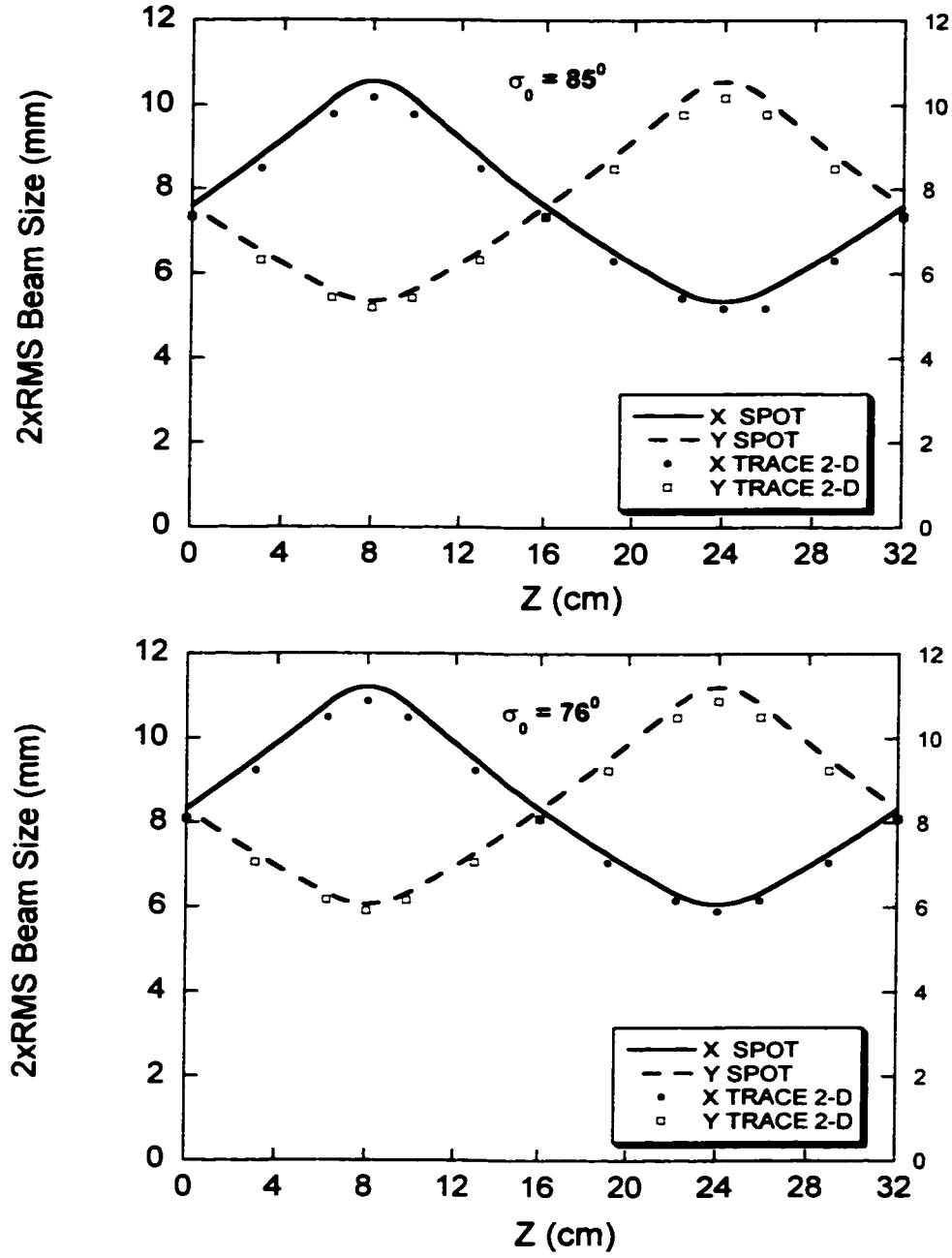

Fig. B.3. FODO matching with UMER quads:
SPOT vs. TRACE 2-D.

As an illustration of the use of TRACE3-D for matching, we solve the matching problem for the solenoid - five quadrupoles section of Chapter V (σ_0=85^0). Figure B4 compares the results with those of SPOT, before optimizing and after optimizing the solenoid strength (only). The mismatch factors before matching in TRACE are rather large: MF_x=0.37, and MF_y=0.48, with an initial solenoid peak field of 63.2 G. After matching (step size = 0.5 mm), we get MF_x=0.03, MF_y=0.024, with a solenoid field equal to 62.24 G. We conclude that SPOT and TRACE yield virtually the same results if the representation of the solenoid in the latter is adjusted. Lastly, optimizing the *location* of the solenoid gives a value within the error of the original location.

B.2.4 Special Considerations for Use of TRACE 3-D:

When using TRACE 3-D to model 2-D problems, i.e. continuous beams, special care is needed in specifying the beam current and longitudinal Twiss parameters [76,77]. Since TRACE 3-D relates the *z-coordinate*, i.e. the particle's location relative to the bunch center, to the phase of the motion in an RF cavity, it is important to specify a RF frequency even if no RF cavities are present. The bunch half-length is made long and equal to the RF wavelength; therefore, a frequency *Freq.* = c/L_s must be defined that satisfies L_s>>*beamline length.* In this case, the effective bunched beam current I is related to the continuous beam current I_b by

$$I = \frac{4}{3}\frac{1}{\beta} I_b, \tag{B.2}$$

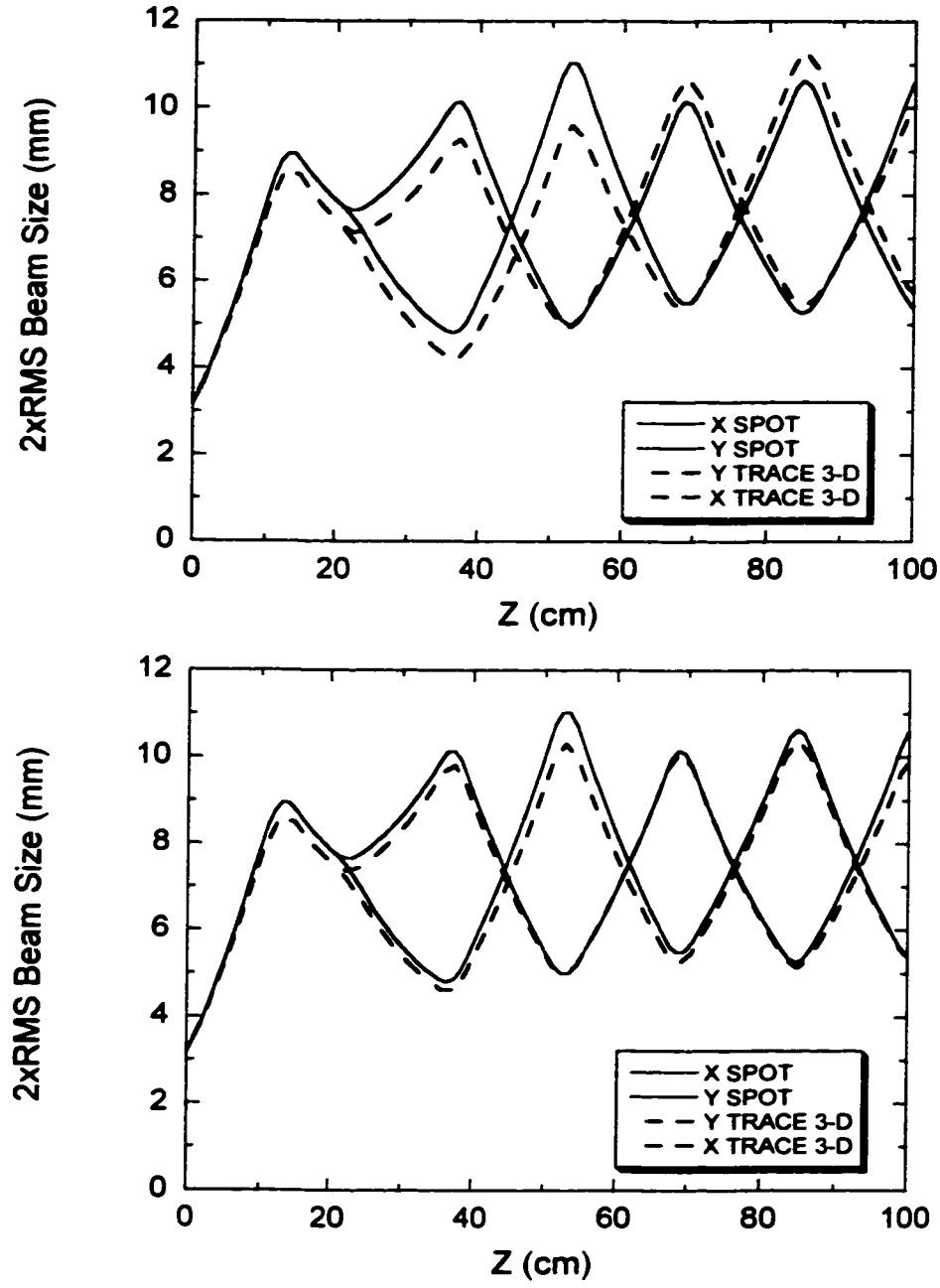

Fig. B.4. Matching with SPOT vs. TRACE 3-D: (a) Solutions with identical geometries and focusing parameters (see Fig. B.2), and (b) After optimization of solenoid's strength (only) in TRACE 3-D.

where β=v/c, not to be confused with the Twiss parameter. Furthermore, the longitudinal emittance must be

$$\varepsilon_z = L_s \frac{\Delta p}{p}, \tag{B.3}$$

where $\Delta p/p$ is the fractional momentum spread.

B.3 Particle-in-cell (PIC) Code WARP

The code was developed by A. Friedmann and D. P. Grote [78] from Lawrence Livermore National Laboratory for studies of high intensity beam transport with applications in heavy-ion inertial fusion and others. The name WARP derives from "warped Cartesian", referring to the use of a special coordinate transformation particularly fitted for the simulation of bends in accelerators.

The code uses BASIS, an interpreted FORTRAN-based language, that facilitates modular development of programs as well as an interactive user interface. WARP consists of several packages: a fully 3-D program, a "2-1/2"-D or single-slice program (i.e. a 2D code that includes all three particle-velocity components), a package for beam envelope calculations, and other packages. WARP was originally implemented to run in CRAY supercomputers, but can now run in UNIX-based machines, including PC's with the LINUX operating system.

The focusing and bend elements can be entered in three different ways: as hard-edge elements, as more realistic 3-D maps obtained with other programs (MAG-PC, for example), or in multipole form. The "leapfrog advance" technique is employed to

advance each particle's velocity by using the applied and self fields in the Lorentz force equation. The self-field is assumed to be electrostatic in the beam frame, moves with the beam and is updated at each time step. A number of initial particle distribution can be implemented, including K-V, semi-Gaussian with uniform or radially-varying temperature profile, and self-consistent Maxwell-Boltzman.

For simulations of the matching sections (Chapters V and VI), the single-slice version of WARP was found to be adequate. A typical simulation uses a grid of 128×128 cells over the transport pipe cross section (3.8 cm diameter), so the cell size corresponds to about 1/3 of one Debye length. To minimize numerical collisions, i.e. to "smooth out" the multi-particle potential function, 40,000 macro particles per slice are employed. A typical run uses a step size of 2.5 mm.

The field of the solenoid is entered, including nonlinearities to fourth order, through the field profile equation and its derivatives, as explained in Chapter III. The quadrupole field, on the other hand, is calculated with the iron-free code MAG-PC and specified on a 3-D grid. Special situations, like solenoid-quadrupole or two-quad field overlapping, are treated by creating single focusing elements by superposition.

WARP constitutes an essential tool for understanding the role of the initial particle distribution on the beam evolution in all experiments. Finally, although not used to design any particular focusing channel, WARP proved to be valuable in "pre-testing" or exploring the merits of several experiments in this work.

Appendix C

Rotated Quadrupoles and Matching

As mentioned in Chap. II, particle-in-cell calculations with WARP (App. B) have shown that random errors in the orientation of quadrupoles in *UMER* produce a significant increase in emittance after a few turns; this emittance growth is much larger than if systematic errors are assumed. The simulations start with a perfectly matched beam on injection. However, the error from rotated quadrupoles in the straight matching section can lead to the injection of a mismatched beam, which compounds the problem of rotated quadrupoles in the main lattice, not to mention the effects of bends. We review here the effects of rotated quadrupoles for low-current beams and also present results of calculations that include space charge. The code TRACE3D (App. B) is used for a simple analysis of the solenoid - five PC quadrupole system described in Chap. V and Chap. VI.

C.1 Single-Particle Effects

If a quadrupole is rotated by an angle α, relative to the x-axis in the lab frame, the single particle equations of motion are [79]:

$$x'' = -\kappa_{x0}\left[\cos(2\alpha)x + \sin(2\alpha)y\right], \tag{C.1a}$$

$$y'' = \kappa_{x0}\left[\cos(2\alpha)y - \sin(2\alpha)x\right], \tag{C.1b}$$

where κ_{x0} is the focusing function in the x-direction, defined in Eq. [4.10]. Equations [C1](a)-(b) describe the effects of a normal quadrupole with strength $\kappa_{x0}\cos(2\alpha)$, superimposed with a skew quadrupole at 45^0 with strength $\kappa_{x0}\sin(2\alpha)$. The ratio of the two strengths is $\tan(2\alpha) \cong 2\alpha$ (small α), so α must be smaller than about 0.3^0 if this ratio is to be less than 1%. In terms of linear dimensions, this corresponds to < 0.11 mm error at the edge of a small-aperture (SA) quadrupole, or < 0.14 mm for a *UMER* quad. In practice, the quadrupoles for the matching experiments are oriented using a level with an estimated error of $\pm\ 1^0$. Rotation errors of this order are used in calculations that also include space charge.

C.2 Matching Section with Rotated Quadrupoles

Figure B4 (b) showed the envelope solution from TRACE3D (and SPOT) when no rotation errors are present. The mismatch factors were quoted before as 0.03 and 0.024 for the X and Y envelopes, respectively. To study effects of rotated quadrupoles, we take the axes of the first quadrupole as the reference, i.e. we assume that the elliptical cross section of the beam coming out of Q1 defines the principal axes for measuring angles of other beam cross sections as well as envelope sizes along the lattice. With this reference, it is implicit that the CCD camera sensor is also oriented so the beam from Q1 (e.g. midway between Q1 and Q2) is seen as the *zero-angle* case.

We start by setting an angle error equal to -1.0 degrees about the quad axis for all SA quadrupoles, except for Q1; this corresponds to an arc-length deflection at the SA quadrupole edge of 0.4 mm, which is a reasonable figure for the actual experiments

described in Chap. V and VI. With these errors, TRACE3D gives mismatch factors at the midplane of Q6 (a *UMER* quad) equal to 0.073 and 0.045 in the x and y directions, respectively. Figure C1 shows the envelope solutions with and without rotation errors, and beam cross sections at the quadrupole middle planes. The envelope solutions are extended to three more *UMER* quads (Q7-Q9) with no rotation errors. As Fig. C1 shows, the beam envelope mismatch is small; the beam cross section at Q9 is rotated about 5 degrees.

When the rotation errors have alternating signs, but the same magnitude of 1.0 deg., the envelope solution from TRACE3D is very different, as seen in Figure C2. It is qualitatively clear why the mismatch is much more severe in this case. After the principal axes of the beam cross section are rotated by Q2 in one direction, the beam encounters a quadrupole (Q3) with an orientation, relative to the beam principal axes, that is even worse than before: it is larger than 1.0 deg. and in the wrong sense. By the time the beam reaches Q6, the beam cross section has rotated about 10 degrees relative to the normal case; the rest of the quadrupoles have no orientation errors, but are seen by the beam as rotated. The beam cross section at the midplane of quadrupoles oscillates about the normal, non-rotated position with no change in the amplitude of the oscillations if no more quadrupole orientation errors are present. Naturally, this is accompanied by envelope oscillations of the mismatched beam, but no relaxation could take place in a simple linear model where all that linear space-charge forces provide is additional linear coupling of x and y motions.

In a more realistic situation, the injected beam encounters at least some small rotation errors of the main FODO quadrupoles. If the errors are random, the beam cross section will rotate in a "random walk" fashion, until it relaxes to a stationary orientation brought about by collective factors not included in the linear model of TRACE3D. We speculate that the relaxation takes longer than for a simple envelope mismatch (without beam rotations), because of the extra degree of freedom represented by the angle of the principal axes of the beam cross section.

As implied above, all forces, internal and external, are linear in the matrix treatment of TRACE3D, so the only additional effect is the extra *linear* coupling of x and y motions from linear space charge (the fact that the beam cross section remains elliptical throughout reflects the linearity of the beam dynamics). This coupling, however, is enough to destroy the constancy of the emittance as measured relative to the (non-rotated) laboratory axes; furthermore, as shown in Ref. [24], it is still possible to define a conserved, generalized emittance that includes the effects of *linear* coupling. Under these conditions, the increase in ordinary emittance is *reversible*, i.e., it could be undone with the use of properly powered skew quads mounted over the main quads (R. Kishek). If non-linear forces from space charge and/or focusing are present, however, not even the generalized emittance is conserved, and the process may be irreversible.

The two cases illustrated in Figs. C1 and C2 correspond roughly to situations of "systematic" and "random" errors, respectively. Initial matching experiments with a solenoid - quadrupole channel, where no angle corrections were tried, show qualitative agreement with the ellipses at the top of Fig. C2 (up to Q6): beam cross sections were

observed with rotation angles of $\lesssim 10^0$. Apparently, the visual corrections applied during the matching experiments were sufficient to reduce the effects of rotated quadrupoles considerably; this is clear from the results of the extended experiments that included the bend section (Fig. 6.6). However, a systematic experimental study of the effects of quadrupole rotations on matching would require a new mechanical design of the quadrupole mounts, possibly incorporating precision mechanisms for adjustment of the quad orientation relative to a well defined "lab" plane. In a first step to facilitate the analysis of these effects, R. Kishek has recently extended the MATLAB program for image analysis to include calculations of beam rotations. We foresee that quadrupole rotations will play a major role on the transverse dynamics of *UMER*, so it will be essential to incorporate means to measure these rotations and their effects.

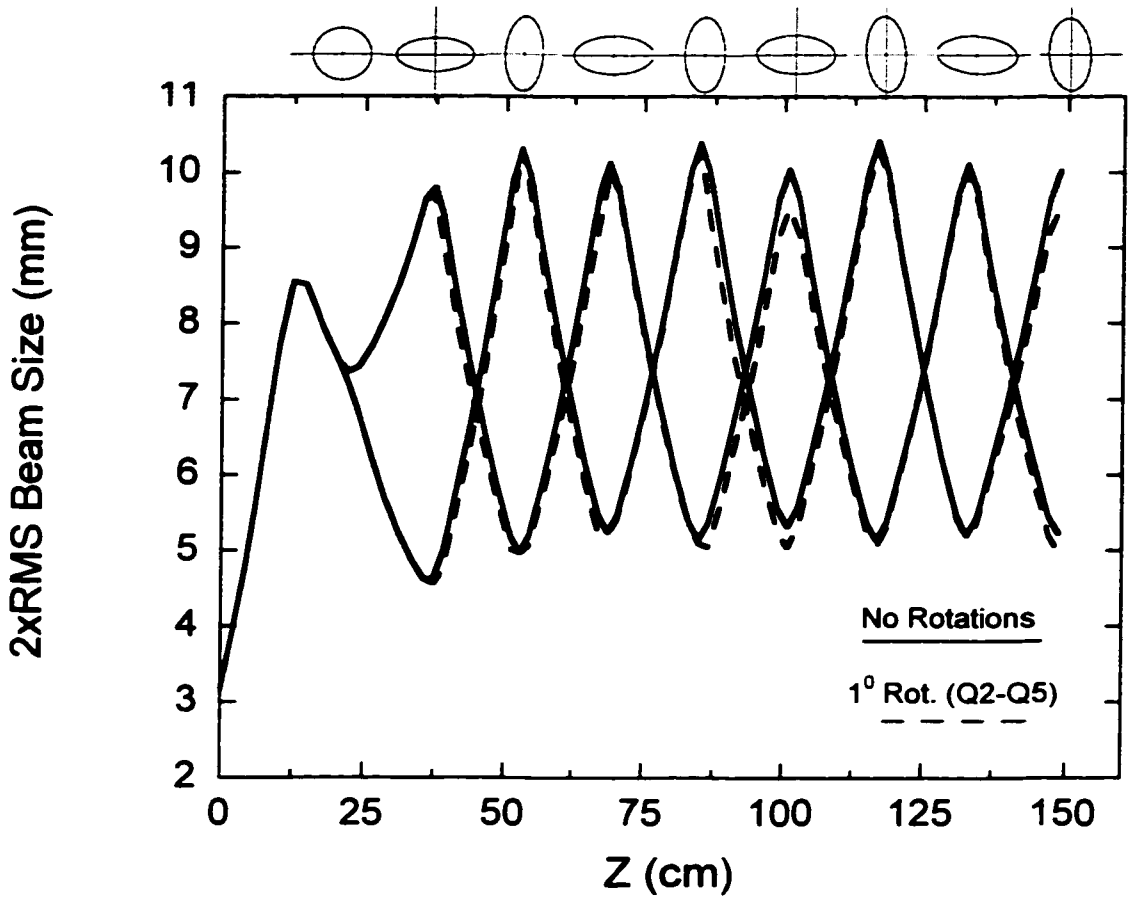

Fig. C1. Effects of quadrupole rotations on matching: the beam envelopes are TRACE3D solutions for a lattice geometry similar to that in Fig. 6.6. The rotation errors are (0.0, −1.0, −1.0, −1.0, −1.0, 0.0, 0.0, 0.0, 0.0) degrees for quads Q1-Q9.

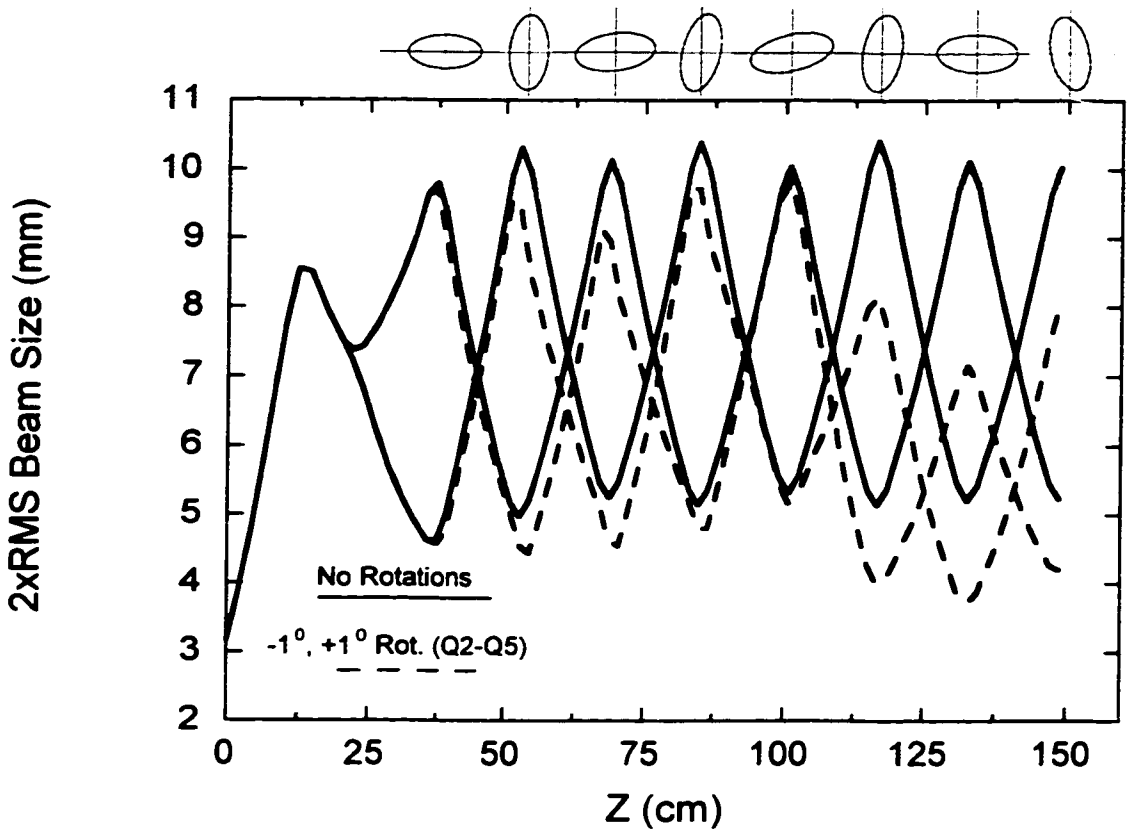

Fig. C2. Effects of quadrupole rotations on matching: the beam envelopes are TRACE3D solutions for a lattice geometry similar to that in Fig. 6.6. The rotation errors are (0.0, −1.0, +1.0, −1.0, +1.0, 0.0, 0.0, 0.0, 0.0) degrees for quads Q1-Q9.

REFERENCES

[1] M. Reiser, S. Bernal, A. Dragt, M. Venturini, J.G. Wang, H. Onishi, and T.F. Godlove, Fusion Eng. Des. 32-33, 293 (1996).

[2] J.G. Wang, *et al.*, Nucl. Instrum. Methods Phys. Res., Sect. A ,415, 422 (1998).

[3] J.J. Barnard, *et al.*, Fusion Eng. Des. 32-33, 247 (1996).

[4] M. Reiser, *et al*, in *Proceedings of the 1999 Particle Accelerator Conference, New York, NY*, p. 234 (1999).

[5] Martin Reiser, Theory and Design of Charged Particle Beams (Wiley, New York, 1994).

[6] Alex J. Dragt, *Lectures on Nonlinear Orbit Dynamics*, AIP Conf. Proc., 87 (1982).

[7] M. Venturini, Ph.D. Thesis, Dept. of Physics, University of Maryland, College Park, 1998.

[8] Ronald C. Davidson, Physics of Nonneutral Plasmas (Addison-Wesley, Reading, MA, 1990).

[9] Thomas M. O'Neil, Physics Today, 52 (2), 24 (1999).

[10] I.M. Kapchinskij and V.V. Vladimirskij, in *Proceedings of the International Conference on High Energy Accelerators*, Geneva, 1959 (CERN, Geneva, 1959), p.274.

[11] Nicholas A. Krall and Alvin W. Trivelpiece, Principles of Plasma Physics, (San Francisco Press, San Francisco, 1986), Chapters 7 and 8.

[12] H.C. Corben and Philip Stehle, Classical Mechanics (Dover, New York, 1977) p.107.

[13] F.J. Sacherer, IEEE Trans. Nucl. Sci. 18, 1105 (1971).

[14] Dragt, A. J., Neri, F., and Rangarajan, G., Phys. Rev. A, 45, 2572 (1992).

[15] M. J. Rhee, Phys. Fluids, Vol. 29, Oct.1986.

[16] M. Reiser, J. Appl. Phys. 70, 1919 (1991).

[17] T.P. Wangler, K.R. Crandall, R.S. Mills, and M. Reiser, IEEE Trans. Nucl. Sci., NS-32, 2196 (1985).

[18] O. A. Anderson, Particle Accelerators, 21, 197 (1987).

[19] I. Hofmann, L.J. Laslett, L. Smith, and I. Haber, Part. Accel. 13, 145 (1983).

[20] J. Struckmeier and M. Reiser, Part. Accel. 14, 227 (1984).

[21] M. Venturini and M. Reiser, Phys. Rev. E, 57, 4725 (1998).

[22] M. Venturini and M. Reiser, Phys. Rev. Lett. 81, 96 (1998).

[23] M. Venturini, R.A. Kishek and M. Reiser, in *Proceedings of the 1999 Particle Accelerator Conference, New York, NY*, p. 3274 (1999).

[24] John J. Barnard, in *Proceedings of the 1995 Particle Accelerator Conference, Dallas, Texas*, p. 3241 (1996).

[25] R.A. Kishek, J.J. Barnard and D.P. Grote, in *Proceedings of the 1999 Particle Accelerator Conference, New York, NY*, p. 1761 (1999).

[26] S. Bernal, R.A. Kishek, M. Reiser and I. Haber, Phys. Rev. Lett. 82 (20), 4002 (1999).

[27] R.L. Gluckstern, in *Proceedings of the Linac Conference* (Fermilab, Batavia, IL, 1970), p. 811.

[28] Robert.L. Gluckstern, Wen-Hao Cheng, and Huanchun Ye, Phys. Rev. Lett. 75 (15), 2835 (1995).

[29] J. Struckmeier, J. Klabunde and M. Reiser, Part. Accel. 15, 47 (1984).

[30] Steven M. Lund and Ronald C. Davidson, Phys. of Plasmas, 5 (8), 3028 (1998).

[31] I. Hofmann, Phys. Rev. E, 57 (4), 4713 (1998).

[32] T.P. Wangler, K.R. Crandall, R. Ryne, and T.S. Wang, Phys. Rev. ST Accel. Beams 1, 084201 (1998).

[33] Edward Ott, Chaos in Dynamical Systems (Cambridge University Press, New York, 1993), p. 9-12.

[34] Chiping Chen and Ronald C. Davidson, Phys. Rev. E, 49 (6), 5679 (1994).

[35] Masanori Ikegami, Phys. Rev. E, 59 (2), 2330 (1999).

[36] J.D. Lawson, P.M. Lapostolle, and R.L. Gluckstern, Particle Accelerators 5, 61 (1973).

[37] J.D. Lawson in *High Brightness Beams for Advanced Accelerators Applications*, William W. Destler, Samar K. Guharay, editors, AIP, College Park, MD (1991).

[38] E.T. Jaynes, Phys. Rev. 106, 620 (1957); E.T. Jaynes, Amer. J. of Phys., 33, 391 (1965).

[39] P.G. O'Shea, Phys. Rev. E 57, 1081 (1998).

[40] Richard C. Tolman, The Principles of Statistical Mechanics, (Dover, New York, 1979), pp. 538-540.

[41] Jürgen Struckmeier, Phys. Rev. E, 54 (1), 830 (1996).

[42] Nathan A. Brown, Ph.D. Thesis, Department of Physics, University of Maryland, College Park, 1995, p. 37-39.

[43] W. B. Hermannsfeldt, "Electron Trajectory Program", SLAC *Report* 226, November 1979.

[44] R. A. Kishek, UMER *Technical Note* E-RING-97-53 , December 16, 1997.

[45] D. M. Kehne, Ph.D. Thesis, Dept. of Electrical Engineering, University of Maryland, College Park, 1992.

[46] P. F. Loschialpo, Ph.D. Thesis, Dept. of Physics and Astronomy, University of Maryland, College Park, 1984, p. 39.

[47] R. A. Kishek and S. Bernal, UMER *Technical Note* E-RING-98-15 , February 25, 1998.

[48] W. G. Davies, Nucl. Instr. and Meth. Phys. Res. A311, 399-436 (1992).

[49] Klaus G. Steffen, High Energy Beam Optics (Wiley, New York, 1965).

[50] P. Loschialpo, W. Namkung, M. Reiser, and J. D. Lawson, J. Appl. Phys. 57 (1), 10-17 (1985).

[51] G. E. Lee-Whitting, Nucl. Instrum. and Meth. 83, 232 (1970).

[52] T.F. Godlove, S. Bernal, and M. Reiser, in *Proceedings of the 1995 Particle Accelerator Conference, Dallas, Texas* (IEEE, New York, 1996), p. 2117.

[53] Robert P. Avery, Glen R. Lamberston and Chester D. Pike, in *Proceedings of the 1971 Particle Accelerator Conference*, p. 885.

[54] Marco Venturini and Alex Dragt, Nucl. Instr. and Meth. Phys. Res. A 427, 387 (1999).

[55] W. W. Zhang, S. Bernal, P. Chin, R. Kishek, M. Reiser, M. Venturini, J. G. Wang, and V. Yun, in *Proceedings of the 1999 Particle Accelerator Conference, New York, NY*, (IEEE, New York, 1999) p. 3372.

[56] H. Li and R. Kishek, Internal *UMER* Report, October, 1999.

[57] S. Bernal, A. Dragt, M. Reiser, M. Venturini, J. G. Wang, and T. F. Godlove, Fusion Eng. Des. **32-33**, 277 (1996).

[58] S. Bernal, P. Chin, R. A. Kishek, Y. Li, M. Reiser, J. G. Wang, T. Godlove, and I. Haber, Phys. Rev. ST Accel. Beams **1**, 044202 (1998).

[59] L. Ahle, *et al.*, in *Proceedings of the 1999 Particle Accelerator Conference, New York, NY*, (IEEE, New York, 1999), p. 3248.

[60] H. Liu and D. Neuffer, in *Proceedings of the 1995 Particle Accelerator Conference, Dallas, Texas*, (IEEE, New York, 1996), p. 1867.

[61] T. Godlove, UMER Technical Note, E-RING-98-16, March 11, 1998.

[62] M. Venturini, Feb., 1998 (unpublished).

[63] Reference 49, p. 96.

[64] K. R. Crandall and D. P. Rusthoi, *TRACE 3-D Documentation, Report* LA-UR-97-886, Los Alamos National Laboratory, May 1997.

[65] George R. Brewer, J. Appl. Phys., 30 (7), 1022 (1959).

[66] S. Bernal, R.A. Kishek, M. Reiser and I. Haber, in *Proceedings of the 1999 Particle Accelerator Conference, New York, NY* (IEEE, New York, 1999), p. 1749.

[67] S.M. Lund, J.J. Barnard, and J.M. Miller, in *Proceedings of the 1995 Particle Accelerator Conference, Dallas, Texas* (IEEE, New York, 1996), p. 3278.

[68] Nathan Brown, Part. Accel. 56, 51 (1996).

[69] S.M. Lund, J.J. Barnard, G.D. Craig, A. Friedman, D.P. Grote, H.S. Hopkins, T.C. Sangster, W.M. Sharp, S. Eylon, T.J. Fessenden, E. Henestroza, S. Yu, and I. Haber, Nucl. Instrum. Meth. In Phys. Res. A 415, 345 (1998).

[70] D.P. Grote, Presentation at the 1998 APS-AAPT Meeting, Columbus, OH (1998).

[71] I. Haber, A. Friedman, D.P. Grote, S.M. Lund, and R.A. Kishek, Phys. of Plasmas 6 (5), 2254 (1999).

[72] S. Lund, Private Communication.

[73] D. Kehne, UMER Technical Note, UMER-031999-DK, March 19, 1999.

[74] C. K. Allen, S.K. Guharay and M. Reiser, in *Proceedings of the 1995 Particle Accelerator Conference, Dallas, Texas* (IEEE, New York, 1996) , p. 2324.

[75] D. P. Rushthoi, W. P. Lysenko, and K. R. Crandall, in *Proceedings of the 1997 Particle Accelerator Conference, Vancouver, BC, Canada,* (IEEE, New York, 1998), p. 2574.

[76] MACcelerator Newsletter, G. H. Gillespie Associates, Inc., Vol. 3, No. 2, April-June 1994.

[77] MACcelerator Newsletter, G. H. Gillespie Associates, Inc., Vol. 5, No. 2, April-July 1996.

[78] A. Friedman, D.P. Grote, and I. Haber, Phys. Fluids B 4, 2203 (1992).

[79] Reference 49, p. 157.